PERFORMANCE OPTIMISATION OF SMALL ANTENNA ARRAYS

A thesis submitted to the University of Manchester
for the degree of Doctor of Philosophy
in the Faculty of Engineering and Physical Sciences

2011

Asim Ali Khan

Microwave and Communication Systems Research Group
School of Electrical and Electronic Engineering

Contents

Word count = 52,044

List of Tables

List of Figures

Abstract

This thesis addresses radiation pattern synthesis problems for small linear periodic phased arrays (with array elements less then 10). Due to the small array size conventional pattern synthesis techniques fail to produce the required results. In the case of practical small arrays, mutual coupling and element pattern asymmetric effect degrade the array radiation performance. The main performance metrics considered in this thesis include sidelobe level (SLL), gain, half power beamwidth (HPBW) and mainbeam scan direction. The conventional pattern synthesis approaches result in sub optimal gain, SLL and HPBW due to the limited number of elements and the mutual coupling involved. In case of difference pattern synthesis these factors resulted in lower difference pattern slope, degraded SLL and difference peak asymmetry. The sum and difference patterns are used in monopulse arrays and a simplified feed that could produce both patterns with acceptable radiation properties is of interest and has been examined (chapter 5).

A conventional technique is applied to small arrays to synthesise a sector beam and there is limited control over the radiation pattern. It is shown that the mutual coupling has significant effect on the array radiation pattern and mitigation is necessary for optimum performance (chapter 6). Furthermore, wideband phased arrays may have a natural limitation of the HPBW in low gain applications and minimisation of the variation becomes important. Also the SLL variations for wideband antenna arrays in the presence of mutual coupling considerably degrade the radiation pattern. The mutual coupling degrades significantly the radiation pattern performance in case of small scanning wideband arrays (chapter 7).

It is the primary goal of this thesis to develop an optimisation scheme that is applied in the above scenarios (chapters 3 & 4). The only degree of freedom

assumed is the array excitation. Optimised amplitude and phase for each element in the array are determined by the proposed scheme, concurrently. The deterministic optimisation techniques reported in the literature for the pattern synthesis may involve complicated problem modelling. The heuristic optimisation techniques generally are computationally expensive. The proposed Intelligent z-space Boundary Condition-Particle Swarm Optimiser (IzBC-PSO) is based on a heuristic algorithm. This scheme can be applied to a wider range of problems without significant modifications and requires fewer computations compared to the competing techniques.

In order to verify the performance of IzBC-PSO antenna array measurements were performed in the receiving mode only using the online and offline digital beamforming setups described in chapter 8. The measurement results show that the proposed scheme may be successfully applied with both online and offline digital beamformers for a practical small array (chapter 8).

Declaration

No portion of the work referred to in this thesis has been submitted in support of an application for another degree or qualification of this or any other university or other institution of learning.

Copyright

The author of this thesis (including any appendices and/or schedules to this thesis) owns certain copyright or related rights in it (the Copyright) and he has given The University of Manchester certain rights to use such Copyright, including for administrative purposes.

Copies of this thesis, either in full or in extracts and whether in hard or electronic copy, may be made only in accordance with the Copyright, Designs and Patents Act 1988 (as amended) and regulations issued under it or, where appropriate, in accordance with licensing agreements which the University has from time to time. This page must form part of any such copies made.

The ownership of certain Copyright, patents, designs, trade marks and other intellectual property (the Intellectual Property) and any reproductions of copyright works in the thesis, for example graphs and tables (Reproductions), which may be described in this thesis, may not be owned by the author and may be owned by third parties. Such Intellectual Property and Reproductions cannot and must not be made available for use without the prior written permission of the owner(s) of the relevant Intellectual Property and/or Reproductions.

Further information on the conditions under which disclosure, publication and commercialisation of this thesis, the Copyright and any Intellectual Property and/or Reproductions described in it may take place is available in the University IP Policy (see http://www.campus.manchester.ac.uk/medialibrary/policies/intellectual-property.pdf), in any relevant Thesis restriction declarations deposited in the University Library, The University Librarys regulations (see http://www.manchester.ac.uk/library/aboutus/regulations) and in The Universitys policy on presentation of Theses.

Acknowledgements

I would like to convey my sincere thanks to my supervisor Prof. Anthony Keith Brown without whom this work would not have been possible. His excellent technical guidance, moral and financial support helped me to complete this research work successfully. His supervision kept my focus on the research problem instead of wavering around.

I would like to thank the CIIT, Pakistan for their funding which supported the major part of this study. I would also like to acknowledge the role of the staff specially Keith Williams at the School of Electrical & Electronic Engineering, University of Manchester for providing all the logistic support. I would like to extend my thanks to Richard Armstrong of Oxford University for his contribution to this work. I would like to appreciate the support provided by Tim Ikin, Chris Shenton, Richard Whitaker, Mathew, Aziz Ahmedsaid and other engineers at the Jodrell Bank Observatory for this project.

I appreciate the motivation and encouragement brought to me by my friends and colleagues; in particular, Hubert, Saad, Laith, Yongwei Zhang, Adnan, Richard and Junaid.

I would like to convey my gratitude to my mother for her love, wisdom, guidance and prayers and my sister for her prayers. I would like to acknowledge my fiancee who has been supportive throughout the completion of this thesis. I also want to extend my acknowledgements to her parents for their patience and prayers.

Abbreviations

HPBW	Half power beamwidth
SLL	Sidelobe level
PSLL	Peak sidelobe level
AUT	Array under test
BDRA	Bowtie dielectric resonator antenna
BECA	Bunny ear combline antenna
PSO	Particle swarm optimiser
IzBC-PSO	Intelligent z-space boundary condition- particle swarm optimiser
UoM-PSO	University of Manchester-particle swarm optimiser
GA	Genetic algorithm
AF	Array factor
TRP	Total radiation pattern
D	Directivity
ESA	Electronically scanned array
MoM	Method of moments
AEP	Active element pattern
OM	Outer mask
IM	Inner mask
FNBW	First null beamwidth
DBW	Difference pattern beamwidth

Chapter 1

Introduction

1.1 Background

Phased array antennas have significant importance in modern day electromagnetic signal transmission and reception systems. Applications include cellular communication, radar, radio astronomy, satellite radio and military applications. An antenna array is a collection of antennas. A single antenna is defined as a "part of a transmitting or receiving system which is designed to radiate or to receive electromagnetic waves" [1].

A single antenna in an array is called an array element or simply an element. Antenna arrays have many advantages over the use of single antennas that mainly include the improvement in gain, half power beamwidth, bandwidth and radiation pattern shape (definitions given in chapter 2). The antenna array properties can be used to modify the radiation pattern. These include the element excitation, inter element spacing, number of elements used and the over all configuration (arrangement of elements in linear, planar, circular geometries etc) of the array. The term phased array is referred to those antenna arrays of which elements are excited with variable phase shift or time delay control to direct the radiation energy in desired direction [2–4]. Depending on the application it is sometimes necessary to increase the radiation energy in a particular direction, suppress the interference in the other directions and jam or block electromagnetic signal(s) approaching form a known direction. These modifications to the radiation pattern can be made through a pattern synthesis process known as the array beamforming [5]. The earlier beamforming applications require analogue systems to be implemented. With the advances in computer technology the analogue beamformers are started to be replaced by their more efficient, flexible and robust digital counterparts.

The work presented in this thesis is concerned with the pattern synthesis of small discrete linear periodic phased arrays in the presence of mutual coupling. This choice of research topic is made on the basis of increasing interest in small antenna arrays in modern communication system. Small arrays are important for low profile radio applications and have advantages over aperiodic arrays for their reduced size and simplicity. In this study array element excitations are chosen to synthesis the radiation pattern. A digital beamformer can be used to readily update the array excitation taper to obtain modified radiation pattern. Finally the measured results are compared with the simulated ones using an array of four elements with digital beamforming setups.

1.1.1 Classical Linear Array Pattern Synthesis Techniques

The basic array pattern synthesis techniques were developed during the World War II (1939-41) and has seen constant improvement since then. The well known techniques of that era are Dolph-Chebychev [6], Taylor $\bar{n}$ distribution [7], Woodward Lawson [8,9] and later $\bar{n}$ Bayliss distribution [10]. All these techniques are based on finding an array excitation taper (vector[1]) to meet the pattern synthesis requirements for a linear periodic array. The techniques developed by Dolph and Taylor were focused on narrow beam sum pattern synthesis [2–4]. The use of Dolph-Chebychev taper provided an optimum compromise between the sidelobe level (SLL) and half power beamwidth (HPBW) of a radiation pattern. When an array is excited with the Dolph-Chebychev taper the resultant pattern has a minimum sidelobe level for the defined HPBW. This technique is derived for discrete arrays and therefore is readily applicable from small to large arrays. However, the Dolph-Chebychev technique is unable to provide optimum solutions for element spacings less then half a wavelength as indicated by H. J. Riblet [11] for a given number of elements.

According to T. T. Taylor, instead of replacing all the patterns nulls (zeros) with Chebychev array pattern nulls only the $\bar{n} - 1$ nulls are required to follow the Chebychev pattern. Far out nulls are taken at the same locations as that of a linear uniformly excited array. This resulted in a radiation pattern with close in

---

[1] In this thesis the term vector is referred to an array of numerical values i.e. $w = [w_1 w_2 ... w_N]$ is a vector consisting of N terms

$\bar{n}$ SLLs almost behaving as the Chebychev pattern whereas far out SLL decaying like the uniformly excited array. The array excitation taper generated by the Taylor′s method has better beam efficiency compared to that of the Dolph-Chebychev taper [7]. Taylor based his work on the assumption of continuous source. The use of Taylor distribution is limited to large arrays due to the taper sampling problem as highlighted in literature [2, 4].

The Bayliss distribution [10] is used to generate difference patterns which are used in conjunction with sum patterns in radar and communication systems for monopulse operations. Bayliss provided the Taylor like $\bar{n}$ distribution where $\bar{n}$ controls the decay rate for SLL. Like Taylor, Bayliss defined the distribution for the continuous line sources. This makes the Bayliss distribution not ideal for the small arrays as indicated in literature [2, 4].

Woodward Lawson technique [8,9] is used to generate the radiation patterns with broader beamwidths. Another conventional method used to generate these patterns is the Fourier transform method [2, 3]. These type of arrays are commonly used in cellular communication systems to illuminate a sector of the cell therefore referred as sector beams. In order to produce such a pattern usually a mask is used to define the required pattern beamwidth and SLLs. Another important parameter used to define the sector beam quality is the mainlobe ripples. It is important to note that both conventional techniques mentioned do not control the ripple level in main beam. As noted by Mailloux these techniques can not be used efficiently for small arrays [2] as the number of elements are reduced the sector beam shape gets out of control.

The general sampling issue with conventional techniques is elaborated in the following section along with other considerable practical issues for small antenna arrays.

1.2 Practical Array Challenges

The above mentioned techniques can not guarantee the optimum array pattern synthesis performance in case of small antenna arrays. In practical small array the effect of mutual coupling changes the radiation pattern significantly. Also these techniques are not suitable for a wideband array performance. The pattern synthesis challenges focused in this study for small antenna arrays are discussed below.

1.2.1 Line Source Sampling

One issue common with all the conventional line source techniques mentioned in the section 1.1.1 is that these can not be used for small arrays to obtain the ideal radiation pattern. It is mentioned by Elliott that even the array radiation pattern for discrete arrays does not follow the ideal Taylor pattern. To solve this problem Elliott introduced the root matching technique to get close to the desired Taylor pattern and this technique still requires an iterative process to reduce the pattern mismatch [4]. Villeneuve presented another discrete version of the Taylor current distribution [12]. He started with the original Dolph-Chebyshev and solved for the discrete elements rather than considering the continuous aperture. His direct approach produced more or less the same patterns as root matching technique [12].

Elliott extended the root matching technique to the Bayliss line source distribution to overcome the same problem [4]. The beam shape performance of Woodward Lawson method is also effected by the number of elements used. Due to the lack of control over the SLL and ripples Woodward Lawson can not be used for high performance arrays. Since this study concerns small arrays therefore the problem of pattern degradation in case of small discrete arrays with elements equal or less then eight while using the line source approximation is taken into account.

Another important phenomenon that reduces the small phased arrays performance significantly is mutual coupling effect as discussed below.

1.2.2 Mutual Coupling

The effect on the array performance due to the element interactions while all the elements in an array are excited is called the mutual coupling effect [3,4]. The mutual coupling effect cause the individual element pattern to alter from its isolated element pattern [2]. The mutual coupling changes element patterns depending on the relative positions of the elements and the element type. For practical small antenna arrays the coupling matrix has its limitations due to the structure scattering effects [13]. In case of finite large antenna arrays the centre element pattern measured in the presence of all other elements terminated at

---

[2] An isolated element pattern for a single element is measured in the absence of other array elements.

matched load can be taken common for all the elements in the array. But in case of small arrays mutual coupling effect is more complex and significant because each element faces nonuniform surroundings. There are two well known methods to model mutual coupling in antenna array systems namely *coupling matrix* [3,4] and *active element pattern* [2,14]. To mitigate the mutual coupling various techniques have been introduced [2,13,15–20].

This study concerns with the mutual coupling effect in small arrays and does not include the feed structure impedance mismatch effects.

1.2.3 Scanned Array Beam Broadening

In low gain applications sometimes it is important to have antenna arrays with stable HPBW. Small arrays are at the disadvantage of having wide beamwidths compared to large arrays. This situation gets worse when the mainbeam is scanned and the natural beam broadening widens the mainbeam of the radiation pattern [2]. One of the goals of this study is to maintain the radiation pattern beamwidth for small antenna array while the array is scanned in the presence of mutual coupling.

1.2.4 Wideband Performance

The wideband array performance depends on the type of the element used. The bandwidth performance metrics used for this study are the half power beamwidth and the sidelobe level of the radiation pattern. Naturally the beamwidth of linear antenna array is sensitive to the frequency [2]. In high resolution systems it may be required to maintain the beamwidth as the system frequency varies. Also it is required to reduce the interference over a band of frequencies. To reduce the interference, low sidelobe levels are preferred to maintain at a target level over that particular band of frequencies. If no mutual coupling is present, sidelobe levels are maintained naturally. However, in the presence of mutual coupling the sidelobe level performance is sensitive to the frequency variation as demonstrated in chapter 7. Therefore it is important to consider the pattern synthesis problem for wideband array. The results presented in this thesis are based on phased arrays only.

In order to overcome these pattern synthesis challenges, an optimisation technique implementing the Particle Swarm Optimiser (PSO) [21, 22] and

Schelkunoff's unit circle [23] is presented in this thesis. The following section covers a brief overview of the existing pattern synthesis techniques.

1.3 Optimisation Techniques: Overview

Optimisation techniques are implemented in order to reduce the computational effort to find an optimum solution in a feasible solution space by exploiting the available degrees of freedom. Conventional optimisation techniques are based on the deterministic approaches. These include typically Newton's Method, Least Squares, Conjugate Gradient also the linear and non linear programming techniques. These techniques have limited usability as they require the fitness (objective) function to be defined analytically, which requires the accurate modelling of the array system. Under practical situations the assumptions made for the analytical model may not hold and lead to a local optimum solution. Another important factor that makes these techniques less attractive is that a user has to make a good initial guess in order to avoid getting trapped in local minima. Significant modification is required in analytical problem model in order to solve a different problem using the same optimisation technique. This adds to the complexity of the optimisation process but the produced solutions are not always satisfactory. Some examples of antenna pattern synthesis solutions implementing deterministic approaches include [24–26]. It is evident from these examples that a complete mathematical system model is required in order to implement these techniques.

The optimisation techniques based on the concept of *black-box optimisation* are becoming increasingly popular [27]. Here the black-box term is referred to the antenna system to be optimised. These techniques require considerably less information of the optimisation problem compared to the deterministic techniques and provide global solutions. These optimisation algorithms are based on the stochastic processes and have been widely used in antenna synthesis problems since the last two decade. Most commonly used algorithms for antenna synthesis problems include Particle Swarm Optimiser (PSO) [21] and Genetic Algorithm (GA) [28, 29]. These algorithms are based on the evaluation of a *fitness function* sometimes referred as cost function. Starting with a random distribution of *agents* in solution space they tend to converge the agent population to the areas of global optimal solutions. Unlike deterministic techniques the stochastic algorithms do not follow a reproducible pattern to reach a global solution, rather they have the ability to jump anywhere in the solution space. This ability gives the stochastic techniques an advantage to avoid trapping in local minima of an optimisation problem. Some examples applying the GA in antenna synthesis problem are given in [30–36]. PSO has been gaining popularity for antenna synthesis problem since the last decade. Here are some examples of PSO based pattern synthesis solutions [37–44]. The performance of these two algorithms is compared quite often and it is found to depend particularly on the optimisation problem [41,45–48]. However, PSO has advantages of its simplicity and less computational complexity over GA.

1.4 Problem Statement & Methodology

The primary objective of this study is to propose a robust optimisation scheme for small linear periodic antenna array pattern synthesis that would ensure the reduced sidelobe levels, narrow beamwitdhs and high gain for narrow band array in the presence of mutual coupling. This scheme is extended to obtain reduced sidelobe levels and stable beamwidths for wide-band array considerations while main beam is at broadside or scanned, in the presence of mutual coupling unless mentioned otherwise. Other objectives include finding a simplified feed for monopulse array using the proposed scheme and to test the optimisation scheme for online and offline digital beamforming. The above mentioned antenna array performance challenges restrict the use of the small antenna array significantly if no rectification is applied. The optimisation solutions available in the literature are mostly focused on large arrays and less attention has been given to small array (number of elements less then ten) pattern synthesis challenges. The element excitation is taken as the only degree of freedom used to solve the pattern synthesis problem for this study. However, there are solutions that modify the array geometry to solve the similar pattern synthesis problems.

To obtain low sidelobe levels, aperiodic separation is implemented among the array elements [49, 50]. For example in order to obtain reduced sidelobe level there are two ways of implementing the aperiodic arrays. One way is to set the element excitations uniformly and find an optimum nonuniform separation between the elements that produce the reduced sidelobe level [51–53]. This array has performance limitations as it may require to find a new optimum non uniform separation to meet a new sidelobe level requirement. This involves the physical rearrangement of the array elements, which makes this system impractical for many applications, especially systems with small assembly and low profile applications. The other way is to obtain the optimum element excitations for each aperiodic geometry considered [54, 55] which adds to the system complexity.

In this thesis, an optimisation solution based on particle swarm optimisation and Schelkunoff's unit circle approach is proposed for all small antenna array pattern synthesis problems considered here. Particle swarm optimiser is chosen because it is computationally less complex compared to its GA counter part and equally able to find a global best solution [48, 56]. The proposed scheme considers the element excitations as the only degree of freedom. For any optimisation problem studied here the only solution provided is in the form of excitation taper. It is well known that the element excitation taper can be represented as an array polynomial [4,23]. This array polynomial is then solved for its roots. The resultant complex roots are taken in z-space and plotted over a unit circle. This z-space unit circle is the solution space for the optimisation procedure. Any modification to the root locations in z-space will reflect its effect through the array polynomial coefficients, which ultimately modifies the antenna array radiation pattern. The root locations in z-space are considered as the optimisation variables for the pattern synthesis problem. The Schelkunoff's unit circle approach is adopted because it offers significant advantages. If there are N number of elements in the array then there are N unknowns for the element excitation taper. If the taper is to be complex then the number of variables become $2N$ (real and imaginary parts to be found for each element). Once the array polynomial for N elements is transformed to its roots in z-space the total number of variables is reduced from $2N$ to $(2N-2)$ (details in chapter 2). This fact may not reduce the computational burden for large arrays but for small arrays it plays a significant role. Also Schelkunoff's unit circle representation allows the implementation of the *Intelligent z-space Boundary Conditions (IzBC)* which is described in detail in chapter 4 and is developed as a part of this study. IzBC allows reduction of the number of variables (root locations) involved and redefinition of the boundary conditions while optimisation is running. The implementation of IzBC significantly improves the convergence performance and the optimum result. Such advantages of Schelkunoff's approach makes it attractive over other approaches.

Particle swarm optimisation coupled with Schelkunoff's unit circle proves a versatile and useful combination [42–44]. After initialisation each particle (agent) contains a set of all root locations considered which are considered as starting at random in solution space. A fitness function is defined in terms of required design parameters and the goal is to minimise the value of the fitness function. The particle with minimum fitness function evaluation is considered as a leader and all particles adjust their variable values to catch the leader [21, 22, 27]. This process results in a set of optimum root locations with minimum fitness function evaluation that corresponds to an optimum radiation pattern. There are various variants of particle swarm optimisation reported in literature [57, 58]. For this study a basic PSO model is developed by the author based on the recommendations given in [56, 59, 60]. Two variants of this basic model based on the definition of solution space boundary conditions are used in this study namely University of Manchester-PSO (UoM-PSO) and Intelligent z-space Boundary Conditions-PSO (IzBC-PSO). For UoM-PSO solution space is divided uniformly among the root locations. Whereas IzBC-PSO considers the sidelobe level topology and compares the root locations in order to define the variable boundaries. This novel scheme has the ability to update the boundaries as required during the optimisation process. The two PSO models are compared for their convergence performance and optimum results to Genetic Algorithm (GA). To make the comparison fair, the solution space used for GA is the same as for UoM-PSO. It is not a study objective to compare the proposed IzBC-PSO with GA or any other optimiser directly.

Schelkunoff's unit circle approach has been coupled with other optimisation algorithms for optimum pattern synthesis as reported in literature [35, 61–66]. In this thesis Schelkunoff's unit circle approach in conjunction with PSO is used to solve a variety of synthesis problems. The proposed scheme has the advantages of stochastic optimisation and the use of novel IzBC-PSO enables reduction of the number of computations required for convergence significantly as compared to UoM-PSO and GA. This work shows the versatility of the proposed scheme as it is applied efficiently to pattern synthesis problems of narrow and wideband arrays in the presence of mutual coupling.

In order to incorporate the mutual coupling effect, active element patterns

[14] and the mutual impedance matrix [3, 4] are used in the problem model. For this study two different antenna elements are considered including Bowtie Dielectric Resonator Antenna (BDRA) [67] and Bunny Ear Combline Antenna (BECA) [68]. The antenna elements are not designed by the author himself. Two antenna arrays are modelled involving these two elements separately using the Computer Simulation Technology-Microwave Studio (CST-MWS®) to determine the active element patterns for BDRA and BECA arrays, as a part of this study. Once the element patterns are known they are incorporated in an array model developed in *MATLAB*®. The proposed optimisation scheme (IzBC-PSO) also developed using *MATLAB*® is then applied to find an optimum radiation pattern. The convergence and optimum result performances of the three optimisers (IzBC-PSO, UoM-PSO, GA) are compared. The GA used for this comparison is provided in *Optimisation Toolbox*™ by *MATLAB*®. The main objective of this study is to compensate for the mutual coupling and produce the radiation patterns having either reduced or desired sidelobe levels with narrow beamwidths.

The simulated optimum performance of the proposed optimisation scheme is compared with the measured results. An array consisting of four BECA elements is used to measure the array radiation patterns in receiving mode having two independent digital beamforming setups namely Interconnect Break-out Board (IBOB) and Data Acquisition (DAQ) board [69, 70]. The IBOB was setup with digital beamforming code developed by Richard Armstrong of Oxford University [69]. The author contributed with the optimum weights obtained using his proposed scheme, IzBC-PSO and performing and setting up the array measurements. The IBOB setup provided the online beamforming. DAQ board was designed and programmed to receive/sample the RF signals by engineers at Jodrell Bank Observatory [70]. There was no beamforming setup provided with DAQ board. An offline software beamformer was developed for the DAQ board by the author of this thesis using *MATLAB*®.

Comparison of the simulated and measured results show that the integration of IzBC-PSO with digital beamformers is of significant advantage. It is shown by the simulated results that the proposed technique has successfully achieved the target SLLs and other objectives for both sum and difference patterns. A simplified feed is also obtained for a monopulse array consisting of eight elements that meets the sum and difference pattern objectives and requires phase only modification. For sector beam synthesis, unlike the conventional technique the proposed technique exhibits better control over the radiation pattern. The use of IzBC-PSO ensured a stable HPBW over a band of frequency. Furthermore the effect of mutual coupling in the small scanning array has mitigated by using the proposed optimisation scheme. It is shown that the preferred technique has significantly improved the SLL when compared with a conventional technique using digital beamformers. The radiation patterns have shown significant improvements after the optimisation in all the above mentioned scenarios. It is essential to use proposed optimisation technique to obtain desired radiation patterns not only under the effect of mutual coupling but also the asymmetric array behaviour.

1.5 Thesis Outline

The thesis structure is as followed. Chapter 2 covers the review of the basic antenna array theory and the array setup used for this work. The mutual coupling models used for this study are also presented. An efficient and fast technique to determine the mutual impedance matrix for dipole array based on the Method of Moment (MoM) is also developed and presented. Chapter 3 describes the implementation of the Particle Swarm Optimiser (PSO). It defines the boundary conditions used in University of Manchester-Particle Swarm Optimiser (UoM-PSO). It also describes the comparative Genetic Algorithm (GA) model.

Chapters 4-9 represent the author's original research contributions. Chapter 4 describes the implementation of the novel concept of intelligent boundary conditions. These intelligent boundary conditions are coupled with the basic PSO and termed as Intelligent z-space Boundary Condition-Particle Swarm Optimiser (IzBC-PSO). Chapter 5 covers the implementation of the IzBC-PSO, UoM-PSO and GA to mitigate the effect of mutual coupling and taper sampling for sum and difference pattern over a narrow frequency band. For monopulse radar operation a simplified feed is also determined. The bulk of simulated results are presented and the optimisation techniques are compared for their convergence performance. The optimised excitation vectors used to obtain the optimised radiation patterns are also given.

Sector beam synthesis is presented in Chapter 6 using the proposed scheme described in Chapter 4. The problem is divided into two scenarios for isotropic and non-isotropic array elements. The simulated results are compared and discussed. Chapter 7 presents the optimisation of wideband phased arrays. The HPBW and in the presence of mutual coupling SLL variation is studied. The proposed scheme is used to determine a single optimised excitation taper that improves the SLL bandwidth performance. The simulated results are presented. Chapter 8 presents the digital beamforming hardware, the measurement setup used for the online and offline beamforming and measured results are compared with simulated results for both beamforming setups. Chapter 9 presents the conclusion and future work recommendations.

Chapter 2

Antenna Array Modelling

2.1 Introduction

In modern radio applications a single antenna element has extremely limited use. Using a single element puts limits on present day radio requirements such as gain, beamwidth, pattern shape, avoiding interference etc. For this purpose a collection of identical elements (in general) is used and called an antenna array. There are many different types of arrays in use these days. These types are mainly based on element placement (orientation), separation between the elements and the methods of excitation. On the basis of the element placement the famous configurations are linear, planar and circular [2–4]. This chapter focuses on the basic theory and mathematical modelling of the linear antenna array considered for this research work.

2.2 Linear Antenna Array

The linear antenna array can be defined as a collection of antenna elements placed along a single dimension. If we consider a Cartesian coordinate system with three axis designated as x, y and z, as shown in Figure 2.1, the linear array elements could be placed along any major axis.

It is assumed for the development of our argument that the radiation point Q is in the farfield i.e. $R > 2D^2/\lambda$ where R is the distance between Q and the observation point and D is the largest dimension of the antenna array structure [3, 4, 71]. This assumption concludes that the electromagnetic waves

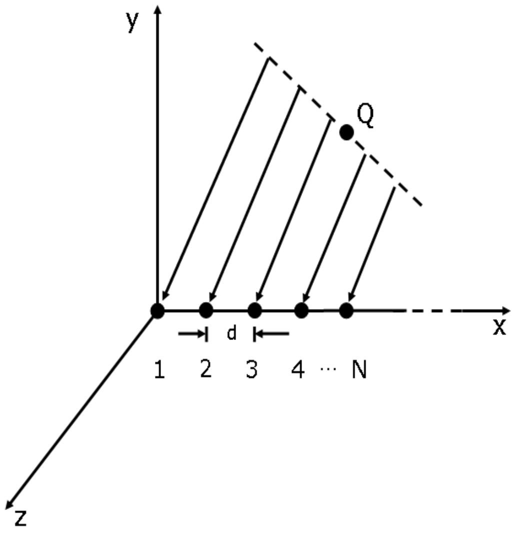

Figure 2.1: Linear antenna array geometry showing the antenna elements laying along $x - axis$

impinging on the linear array would have a planar wavefront. The linear antenna array is a discrete structure. Therefore array actually behaves as a sampler for the electromagnetic radiation energy. As the electromagnetic energy interacts with the individual antenna element it induces a voltage at the terminals of that antenna element. This induced voltage is a function of the antenna element position in the array. The total response of the array is the sum of these induced voltages of each element for a given look direction. If the array response is determined over the entire hemisphere it gives peak where all the received signals add in phase and a null where all the received signals add out of phase. The spherical coordinate system is generally used for the antenna array analysis, shown in Figure 2.2.

The angles θ and ϕ are used for the azimuthal (x-y plane) and elevation (z) plane. The ϕ varies from 0 to 2π (rad) and θ varies from 0 to π (rad) also represented as $-90^o \leq \theta \leq 90^o$. The R gives the distance of the point Q from the centre of the coordinate system.

2.3 Linear Array Factor

For this research work it is assumed that the antenna elements are placed along x-axis shown in the Figure 2.1 unless stated otherwise. The array elements are

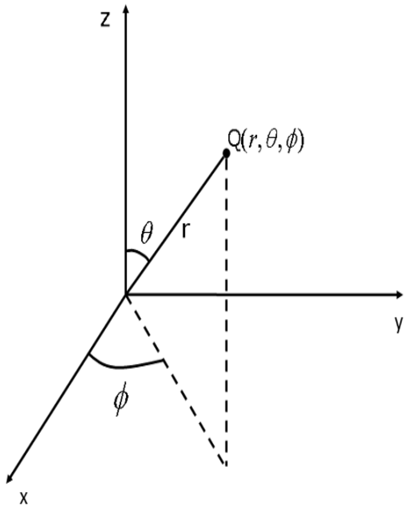

Figure 2.2: Spherical coordinate system used for the antenna array analysis

uniformly spaced with a separation d. It is assumed that the antenna elements are radiating uniformly in all directions i.e. elements are isotropic. For N elements the array factor expression is given below [3](chapter 6);

$$AF(\psi) = \sum_{n=1}^{N} e^{-j\psi_n} \tag{2.1}$$

$$\psi_n = (n-1)kd\sin\theta\cos\phi$$

$$AF(\theta) = \sum_{n=1}^{N} e^{-j(n-1)kd\sin\theta\cos\phi} \tag{2.2}$$

Equation 2.2 represents a special case of uniform element excitation. This means that if the array is in transmitting mode the excitation amplitude is 1 and excitation phase is 0 for each element. On the other hand, if the array is in receiving mode the induced voltage at each antenna element terminal would be the same in magnitude and phase. Generally element excitations are mentioned as *weights* or *taper* in literature. These terms will be used interchangeably for this work.

If each element is weighted arbitrarily (either amplitude or phase or both) then Equation 2.2 will no longer be valid. Assuming that the weighting vector or taper is represented by w_n (a complex vector), where n is for n^{th} element and $\phi = 0^o$ (for considering the xz plane only), then Equation 2.2 becomes;

$$AF(\theta) = \sum_{n=1}^{N} w_n e^{-j(n-1)kd\sin\theta} \tag{2.3}$$

Equation 2.3 gives the form of the AF used for the mathematical modelling in this work. There are three major components of the Equation 2.3 that could be chosen by the designer to meet certain pattern synthesis requirement. These are the degrees of freedom available as given below

1. The number of elements (N)
2. Separation between the elements (d)
3. Weighting vector (coefficients)

For this research work the number of array elements is limited to maximum 8 in most of the examples. The separation between the elements is considered periodic. For any optimisation problem presented in this work the number of elements and the separation between the elements is kept constant. The only degree of freedom exploited for this research is the weighting coefficients or excitation taper.

In practise, isotropic element model can not be fully relied upon for certain array application specially for the small arrays, as the radiation properties of any real antenna element are not uniform in all radiation directions. For an array with identical non isotropic elements, each with radiation pattern $E(\theta)$, the total radiation pattern (TRP) is given by;

$$TRP(\theta) = E(\theta) \cdot AF(\theta) \tag{2.4}$$

However, for small arrays antenna element patterns are not identical as will be shown in the later section 2.11.2 of this chapter. For non identical element patterns Equation 2.4 is modified as;

$$TRP(\theta) = \sum_{n=1}^{N} w_n \cdot E_n(\theta) \tag{2.5}$$

Where E_n refers to the element pattern of the n^{th} element of the array. Equation 2.5 is used to model BDRA and BECA arrays for this research work.

2.4 Array Factor Properties

In this section, properties of the array factor important to the array pattern synthesis will be presented. These properties are used as the pattern goodness criteria for the synthesis problems considered in this thesis.

2.4.1 Radiation Pattern

The AF defined in Equation 2.3 or a trace of the AF as a function of the coordinate system variables is called a farfield radiation pattern or simply the farfield pattern [3]. The plot of Equation 2.3 for eight isotropic elements uniformly spaced with $d = \frac{\lambda}{2}$ and uniformly excited is given in Figure 2.3 for $-90^o \leq \theta \leq 90^o$. Through out this thesis the radiation patterns are plotted against θ values in degrees.

The radiation patterns are plotted usually for normalised values and on dB scale. The radiation pattern shows the proportion of the electric field or the power directed to a particular direction. This radiation pattern helps to define several important antenna array metrics. The metrics presented in this chapter are used for the array pattern synthesis problems dealt in this work.

It is important to note here that the farfield pattern is a discrete Fourier transform of the array excitation [3, 4].

2.4.2 Beamwidth (BW)

The beamwidth of any radiation pattern is its angular width of the main lobe. The beamwidth is measured in degrees. An important relationship exists between the beamwidth and the gain of the antenna array. The larger the beamwidth, the smaller the gain. There are two important beamwidth types used in literature as given below.

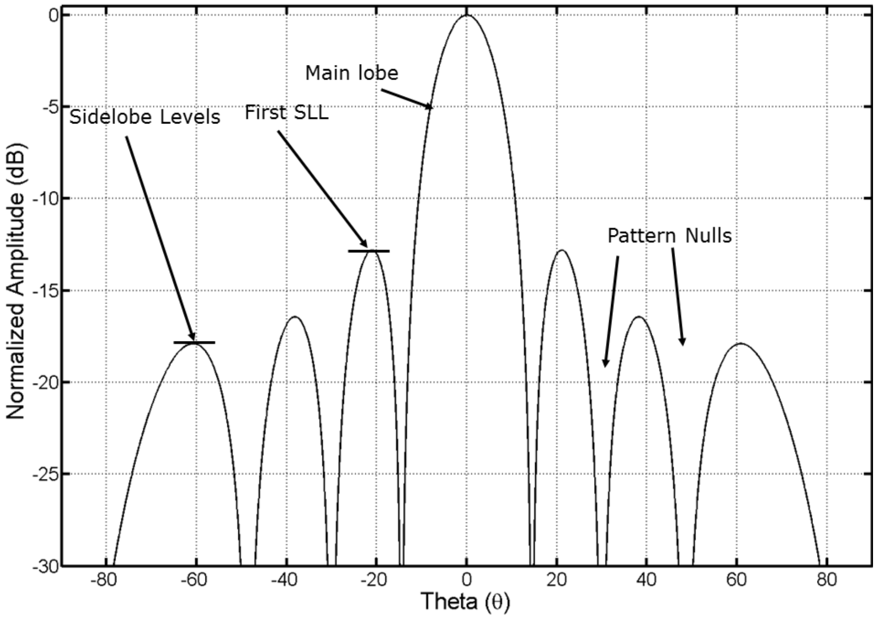

Figure 2.3: Linear array radiation pattern for $N = 8$ and $d = 0.5\lambda$ with uniform taper, θ is in degrees

2.4.2.1 Half Power Beamwidth (HPBW)

The half power beamwidth is also known as the $3dB$-beamwidth. It is defined as the angular separation between the two points on the main lobe where the power is dropped to half or the electric field pattern is $1/\sqrt{2}$ of its maximum value as indicated in Figure 2.4.

2.4.2.2 First Null Beamwidth (FNBW)

This is the angular separation between the first two nulls about the main lobe of the radiation pattern as indicated in Figure 2.3.

The mathematical details and the expressions could be found in [3, 4, 71]

2.4.3 Directivity

The directivity (D) of any antenna is defined as the ratio of the radiation power in a given direction to the radiation power averaged over all directions. In case of the antenna array the mathematical expression for gain is given as [3, 71];

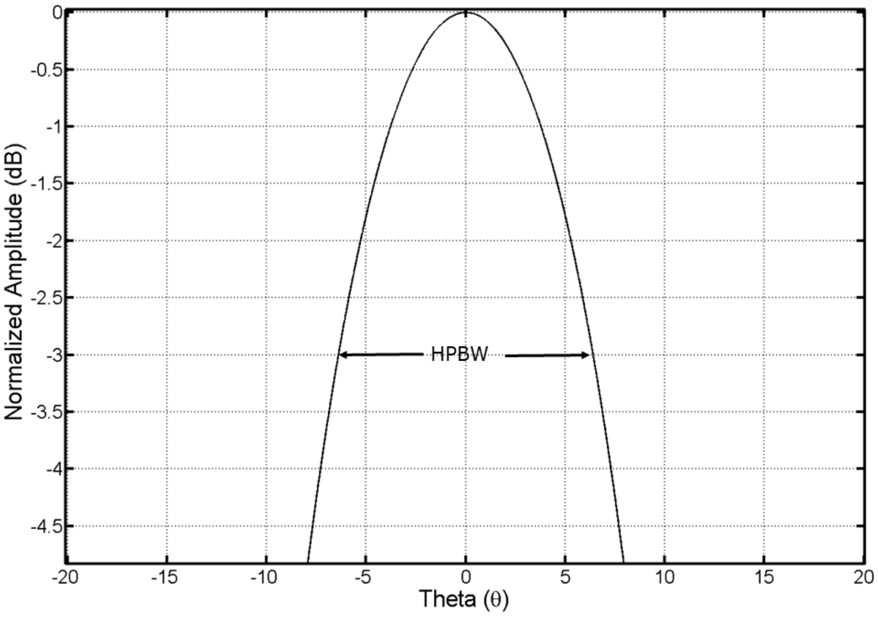

Figure 2.4: Zoomed in linear array radiation pattern shown in Figure 2.3

$$D(\theta) = 4\pi \frac{|AF(\theta)|^2}{\int_0^{2\pi}\int_0^{\pi} |AF(\theta)|^2 \sin\theta d\theta d\phi} \tag{2.6}$$

The antenna gain is an other important term used to characterise. Gain takes into account the efficiency of the antenna. If antenna radiation efficiency is defined as e_{cd} then gain and directivity are related as [3];

$$G = e_{cd} \cdot D \tag{2.7}$$

The gain expression given in Equation 2.7 does not include the impedance mismatch and polarisation mismatch loses. However, these loses are required to be considered for the link calculation of a communication system to determine the received or radiated power, which is not the scope of this work.

The Equation 2.6 can be simplified to the following expression for an array with any arbitrary separation d and directed to θ_o scan direction [72];

$$D = \left| \frac{(\sum_{n=1}^{N} w_n)^2}{\sum_{n=1}^{N}\sum_{m=1}^{N} w_n(n) w_n(m) e^{j((n-1)\beta-(m-1)\beta)} sinc[(n-m)kd]} \right| \tag{2.8}$$

Where $\beta = -kd\sin\theta_o$. Equation 2.8 was further simplified for the arrays with $d = 0.5\lambda$ and the scan direction $\theta_o = 0$;

$$D = \frac{(\sum_{n=1}^{N} w_n)^2}{\sum_{n=1}^{N} (w_n)^2} \tag{2.9}$$

This expression is independent of the scan angle and can be used for the non uniformly excited isotropic arrays.

2.4.4 Sidelobe Level (SLL)

Any radiation pattern in practice with FNBW of 90^o has one or more then one lobes. These lobes appear at the angular directions where received/transmitted signals are added in phase. The principle lobe or the lobe with maximum power or energy content is called main lobe. All other lobes are called sidelobes. These are identified in Figure 2.3. In many applications e.g. mobile communication, Global Positioning System (GPS), radars etc the SLL are undesirable and it is important to meet a certain SLL power level. It is therefore a common goal of the antenna synthesis problem to control the power distribution among the SLLs. The two commonly used terminologies to indicate a SLL in any radiation pattern are the *First Sidelobe Level (FSLL)* & *Peak Sidelobe Level (PSLL)*. The FSLL is the next lobe to the main beam as indicated in Figure 2.3 with a level value of $-13.46dB$ in this case. The PSLL has the highest power or the electric field voltage level among the SLLs but it may not be necessarily next to the main beam. In this example PSLL and FSLL are the same.

In order to meet the SLL requirements for any application a trade off between the SLL and the BW is exploited. If BW is increased then the SLLs get less power. But this increased BW results in low gain in main beam which results in low resolution in imaging applications, weak signal in mobile communications etc. A desirable combination of both is the objective of most pattern synthesis problems and is considered for this work as well.

2.4.5 Radiation Pattern Nulls

The radiation pattern nulls appear at the angular directions in which the received/transmitted signals are added out of phase. The pattern nulls have significant importance in pattern synthesis. They may be used to avoid the interference from any given angular direction. The pattern null synthesis has applications in mobile communications, radars and signal jamming.

2.5 Limitation on Uniform Linear Array

The term uniform array is used to indicate that the elements are equally spaced and the excitation of each element is the same. The mathematical expression of the linear uniform array with N isotropic elements is given by Equation 2.2. Uniform arrays are not flexible in terms of shape of the radiation pattern. By increasing the number of elements in the uniform array one can improve the gain (directivity) of the array but this approach is not feasible in all cases. There are many applications that require a certain radiation pattern for example a null in the direction of a jammer or certain low sidelobe level (SLL) instead of typical -13.46dB (for isotropic array) with uniform excitation. For these applications non uniform arrays are used. These arrays are non uniform in terms of excitation (weight) or separation between the elements or hybrid. The uniform arrays are high gain arrays as compared to the non uniform arrays for same number of elements. But this high gain can be sacrificed for the lower SLL or a particular beam pattern. Under this study arrays with non uniform excitation (weighted arrays) are investigated.

2.6 Electronically Scanned Array (ESA)

The radiation pattern shown in Figure 2.3 has main beam directed to $\theta = 0$. If the array is transmitting then $\theta = 0$ is the angular direction in which it is transmitting maximum power on the other hand in case of a receiving array it receives the maximum power at $\theta = 0$. As it is evident from Equation 2.3 that the phase and the amplitude of any array element can be used to modify the over all radiation pattern. It is required for certain applications to be able to direct the maximum power of the array in a target angular direction. This goal could either be achieved by *mechanical scanning* or *electronic scanning*. The ESA is commonly known as *Phased Array*. If a uniform phase gradient is applied to each of the array element it will result in a radiation pattern with maximum power directed in the target direction in case of the isotropic array. It will be shown in chapters 5 and 6 that the uniform phase gradient is not sufficient to scan the main beam in the presence of coupling and non identical element patterns for small antenna arrays. The required phase shift considered for the mathematical model developed in this chapter is given as [3,4];

$$\beta = -kd\sin\theta_o \tag{2.10}$$

Where θ_o is the target direction. The modified weights can be given as;

$$w_n = a_n e^{jn\beta} \tag{2.11}$$

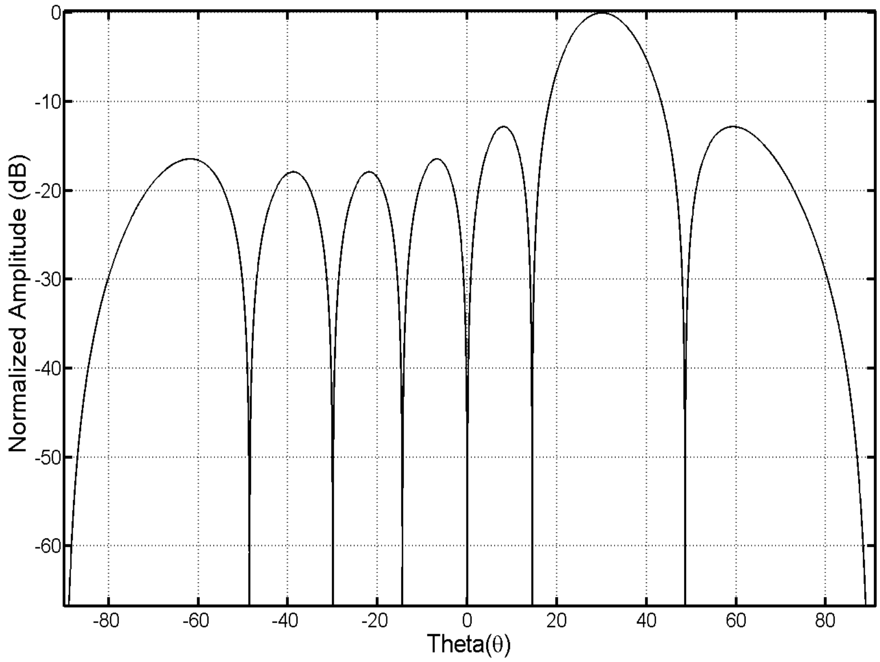

Figure 2.5: Linear array radiation pattern scanned to $\theta_o = 30^o$, $N = 8$, $d = 0.5\lambda$ (plotted using Equation 2.12)

Where a_n is the amplitude applied to the n^{th} element. For the example presented in Figure 2.5 the linear array with eight isotropic elements is scanned to $\theta_o = 30^o$ electronically. For the beam scanning, only phase shift is required therefore the excitation amplitude of all elements would be set to 1. The taper used for the Figure 2.5 is given in Table 2.1.

This modified taper was replaced in Equation 2.12 to find the scanned radiation pattern. Equation 2.12, modified from Equation 2.3, takes element 1 as the reference element and hence with zero phase shift applied.

Number of Element	Amplitude (a_n)	Phase (Degrees)
1	1	0
2	1	−90
3	1	180
4	1	90
5	1	0
6	1	−90
7	1	180
8	1	90

Table 2.1: Uniform taper with linear phase gradient

$$AF(\theta) = \sum_{n=0}^{N-1} w_n e^{j(n)kd\sin\theta} \tag{2.12}$$

It has been presented by Elliott [4] that with the scanning of main beam the main lobe broadens. This was noted by comparing Figures 2.3 and 2.6 for the broadside and scanned patterns that the FNBW were 30^o and the 34^o respectively. This resulted in a 13.33% beam broadening. There was no change to the SLLs. This phenomenon exhibits significant degradation of array radiation pattern with non isotropic elements in small arrays as presented in chapters 5 and 6.

2.7 Schelkunoff's Polynomial

The linear array factor given by Equation 2.12 can be expanded as given below;

$$AF(\theta) = w_0 + w_1 e^{jkd\sin\theta} + w_n e^{2jkd\sin\theta} + ... + w_{N-1} e^{(N-1)jkd\sin\theta}$$

$$AF(\psi) = w_0 + w_1 e^{j\psi} + w_2 e^{2j\psi} + ... + w_{N-1} e^{(N-1)j\psi} \tag{2.13}$$

Letting $z = e^{j\psi}$ results in:

$$AF(z) = w_0 + w_1 z + w_2 z^2 + ... + w_{N-1} z^{N-1} \tag{2.14}$$

S. A. Schelkunoff expressed the antenna array factor in the polynomial form

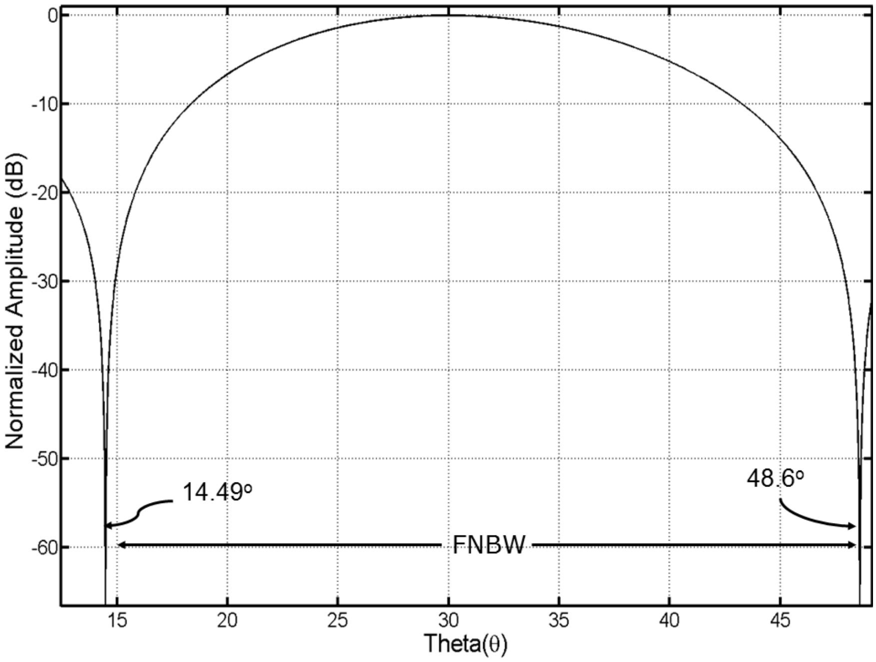

Figure 2.6: Zoomed in linear array scanned radiation pattern shown in Figure 2.5

given by Equation 2.14 [23]. Equation 2.14 is a complex polynomial in variable z. Mathematically any polynomial with order $N-1$ has $N-1$ roots. Assuming that $z_1, z_2, ..., z_{N-1}$ are the roots of the polynomial defined in the Equation 2.14 then the polynomial could be expressed as a product of $N-1$ linear terms given below.

$$AF(z) = w_n(z - z_1)(z - z_2)...(z - z_{N-1}) \tag{2.15}$$

This Equation 2.15 provides an equivalent presentation of array factor to Figure 2.3. Detailed discussion on the Schelkunoff's polynomial can be found in [3,4]. The magnitude of the AF in Equation 2.15 is expressed as;

$$|AF(z)| = w_n|(z - z_1)||(z - z_2)|...|(z - z_{N-1})| \tag{2.16}$$

Clearly the roots of any mono variant polynomial can be mapped on a unit circle. From the earlier example for $N = 8$ isotropic elements and $d = 0.5\lambda$ the rectangular plot (in θ space) is given in Figure 2.3. The same scenario is solved with the Schelkunoff's polynomial approach. Since no beam scanning is applied therefore all the coefficients are unity with zero phase in Equation

2.14. Equation 2.14 then resulted in:

$$AF(z) = 1 + z + z^2 + ... + z^{N-1} \tag{2.17}$$

Equation 2.17 is solved for the roots of z. Equation 2.17 is equated to zero and differentiated w.r.t. z as given by Equation 2.18. After taking the second derivative of the Equation 2.18 the roots of polynomial given in Equation 2.17 were determined. The complex roots ($z_n = x_n + jy_n$) were plotted on a unit circle as shown in Figure 2.7.

$$0 = \frac{d}{dz}\sum_{n=0}^{N-1} z^n \tag{2.18}$$

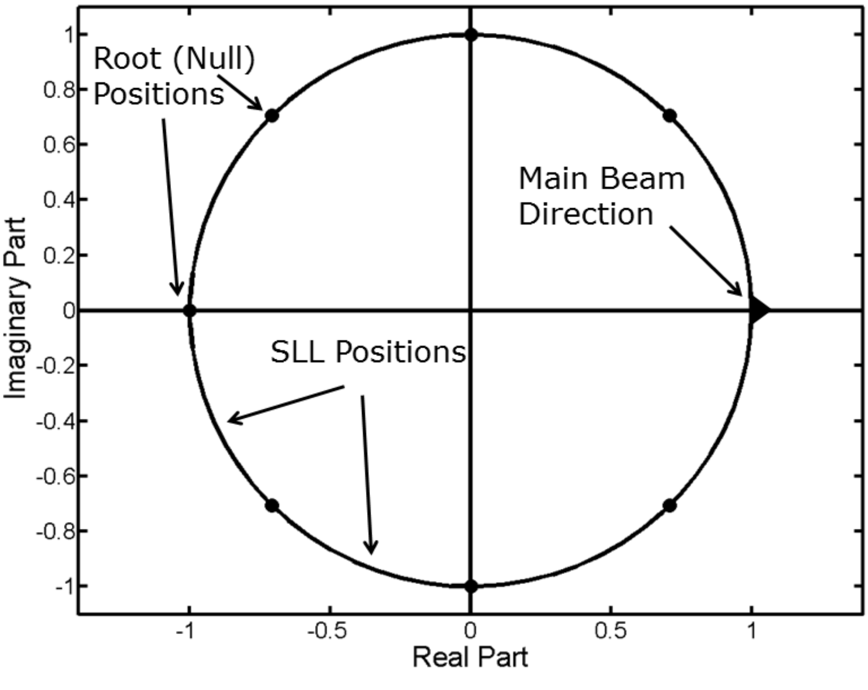

Figure 2.7: Unit circle presentation of the AF defined in Equation 2.17 with $N = 8$ and $d = 0.5\lambda$

As θ varies from -90 to 90 ψ varies from $-kd$ to kd and this makes z vary from e^{-jkd} to e^{jkd}. All the properties of the radiation pattern presented (in θ space) in Figure 2.3 could be traced to the unit circle space. The sensitivity of the unit circle to the separation between the elements and the applied phase shift is presented in [3]. The root positions on the unit circle indicate the pattern nulls and the pattern lobes are located between the nulls. Equation 2.16 could be used to find the magnitude of the AF at any point z on the unit circle. The procedure is elaborated in Figure 2.8 The main lobe is indicated on the unit circle shown in Figure 2.7.

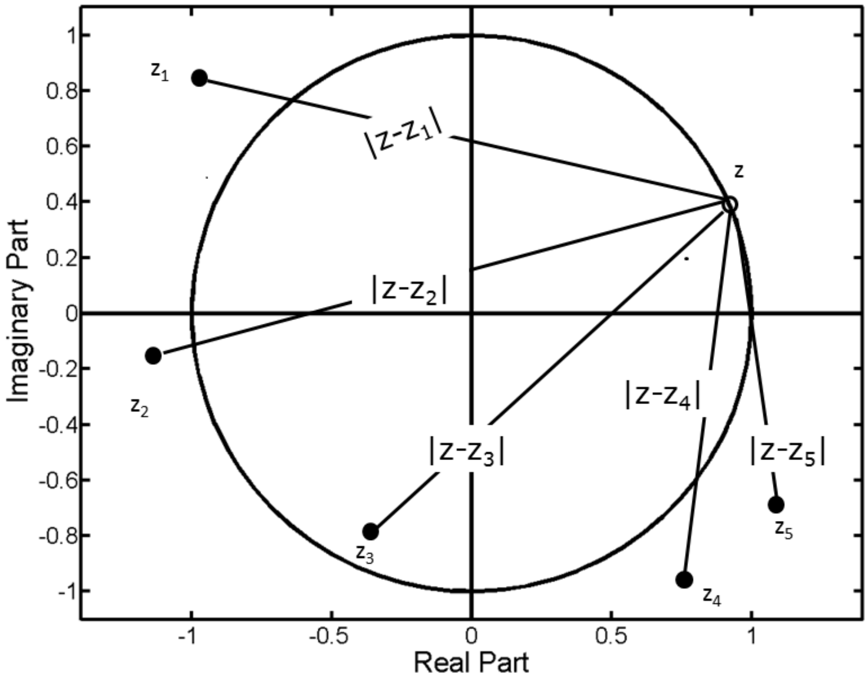

Figure 2.8: The distance between the point z and the roots is calculated and substituted in Equation 2.16

If a progressive phase shift is applied for the beam scanning as given by Equation 2.11 then the modified Equation 2.13 could be given as:

$$AF(\psi) = a_0 + a_1 e^{j\psi+\beta} + a_2 e^{2(j\psi+\beta)} + ... + a_{N-1} e^{(N-1)(j\psi+\beta)} \tag{2.19}$$

The equivalent unit circle plot of the radiation pattern presented in Figure 2.5 is shown in Figure 2.9. The main lobe direction has changed on the unit circle as expected, it reflects the effect of the phase gradient applied. Equation 2.19 is used in the modeling of the linear isotropic antenna array for this research work.

2.7.1 Array Pattern Synthesis

Shelkunoff's polynomial is a powerful tool for the array pattern synthesis [3,4]. In Figures 2.7 and 2.9 the polynomial roots were plotted when the array taper

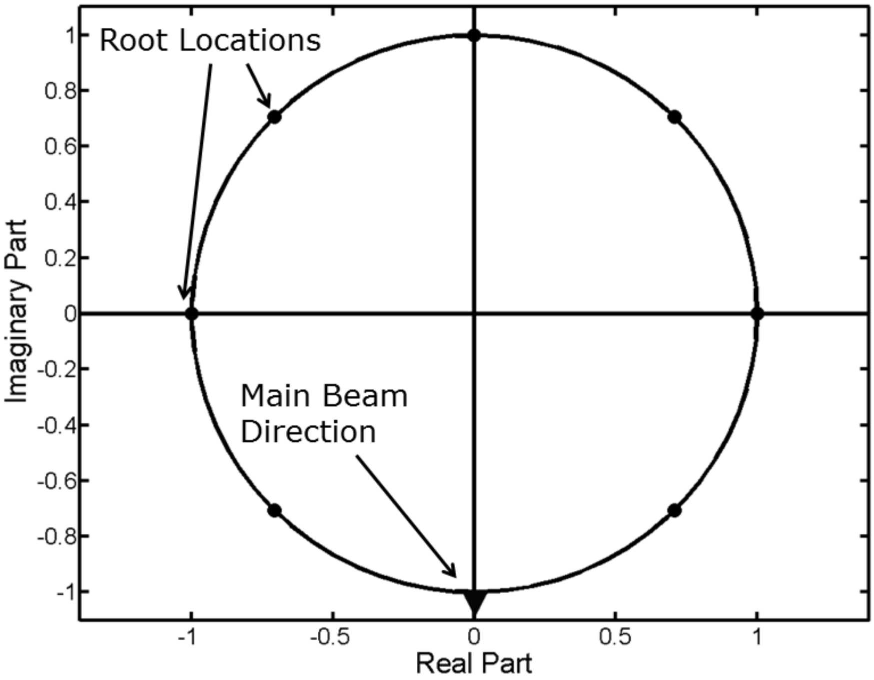

Figure 2.9: The unit circle plot of the roots for scanned pattern with θ_o = 30^o, N = 8 and d = 0.5λ

was known. In order to synthesise a desired array pattern these roots could be relocated on the unit circle to get the desired pattern shape. Once the modified root positions are known Equation 2.16 can be used to determine the AF as depicted in Figure 2.8. The root positions on and around the unit circle define the array pattern. For the examples considered here the roots are placed on the unit circle and resulted in deep pattern nulls in θ space. If the roots are moved away from the unit circle a null free pattern can be obtained. The Schelkunoff's unit circle is extensively used by Elliott for array pattern synthesis [4].

For this research work the Schelkunoff's polynomial based unit circle approach is chosen as the synthesis tool and merged with the Particle Swarm Optimiser (PSO). This optimisation scheme is applied to the pattern synthesis problems for small uniformly spaced arrays as demonstrated in this thesis.

2.8 Mutual Coupling

The mutual coupling in antenna arrays is well known and generally investigated phenomenon [73–83]. In order to make the array model realistic and to test that the developed optimisation tool is capable of dealing with the mutual coupling it was taken into account for this work. In large arrays the effect of the mutual coupling on the antenna element is nearly uniform across the array. Whereas in small arrays ($N < 10$) the mutual coupling effects the radiation characteristics of the array elements non-uniformly. The basic mutual coupling model of the dipole antenna array has been discussed in detail by Balanis and Elliott [3,4].

2.9 Mutual Coupling Models

For this research work two different mutual coupling models are used. Initially an array of the dipole elements is assumed for modelling the mutual coupling. For this a Method of Moment (MoM) based mutual coupling model is developed as the part of this work. The output of this model is a mutual impedance matrix.

The use of element patterns is well known to model the mutual coupling in antenna arrays [2, 14]. For this purpose a Dielectric Resonator Antenna (DRA) designed at the University of Manchester is considered [67]. The DRA array is designed in the Computer Simulation Technology Microwave Studio® (CST MWS) for this project. This second coupling model is based on the determination of active element patterns (AEPs). The array radiation pattern is calculated with these AEPs as they include the mutual coupling effect. No matrix calculation is involved with this second approach. The coupling models used for this research work are described below.

In chapter 8 the antenna array synthesis is presented with the measured active element patterns. The (Bunny Ear Combline Antenna) BECA [68] (designed at the University of Manchester) is used as the array element.

2.10 Dipole Array Model

In order to find the self and mutual impedance of the dipole (a dipole pair) structure the current distribution along the dipole antenna is required. For this purpose Integral Equations (IEs) are defined for the dipole model [3,4]. A dipole is an antenna that consists of a thin wire. The current distribution for a very thin wire is assumed to be sinusoidal. For finite diameter wires

($dia > 0.05\lambda$) the current distribution can be represented as sinusoidal but it is not accurate. Therefore for this work the diameter of the dipole wire was chosen to be 0.01λ. To find the accurate distribution the integral equation must be solved. Generally there are many forms of the integral equations. For time harmonic electromagnetics the two most popular IEs are the electric field integral equation (EFIE) and magnetic field integral equation (MFIE). The EFIE enforces the boundary condition on the tangential electric field where as the MFIE enforces the boundary condition on the tangential components of the magnetic field. The EFIE can be applied to both open and closed surfaces while MFIE can be applied to closed surfaces only. Here only the EFIE will be considered and for radiation problem with wire antenna there are two popular EFIEs, Pocklington's IE & Hallen's IE. The Pocklington's IE is a general type of solution and it is adaptable to many type of feed sources including delta gap and magnetic frill. For this work Pocklington's IE was used to model the dipole.

2.10.1 Pocklinton's IE

For this model the dipole element was assumed along the z-axis and having a length l with a diameter of $2a$ as shown in Figure 2.10. Here the final equation is given (primed coordinate represents the source and otherwise observation coordinate):

$$(\frac{d^2}{dz^2} + k^2) \int_{-l/2}^{l/2} I_z(z')G(z,z')dz' = -j\omega\varepsilon E_z^i \tag{2.20}$$

Where

$I(z')$ = current distribution along the axis of the wire (unknown)

$G(z,z')$, *The Green's Function* $= \frac{1}{2\pi}\int_0^{2\pi} \frac{e^{-jkR}}{4\pi R} d\phi'$

E_z^i = incident electric field

$R = \sqrt{a^2 + (z - z')^2}$; simplified for observations taken along the axis of the wire and $\rho = 0$ for cylindrical coordinates [3]

This equation is also known as Pocklington's Integrodifferential. In Equation 2.20 the only parameter to set is the incident electric field. This field can be produced in case of wire antenna by placing a source at the terminals of the wire. The source used for this model was magnetic frill source proposed by L. L. Tsai [84]. The feed gap of the wire antenna is replaced with a circumferential

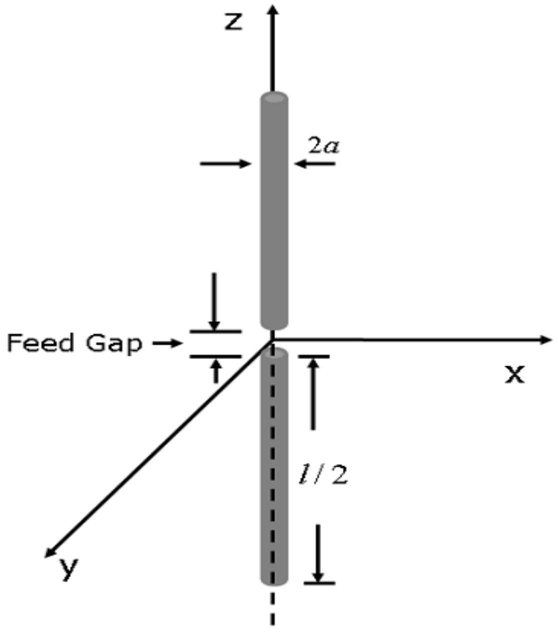

Figure 2.10: The dipole element geometry

directed magnetic current density that exists over an annular aperture. The inner radius of the aperture is taken as a which is chosen as the wire radius and an outer radius b. Assuming that the field is generated along the wire axis by the magnetic frill source then the incident electric E_z^i field equation is given by:

$$E_z^i = -\frac{V_i}{2ln(b/a)}(\frac{e^{-jkR_1}}{R_1} - \frac{e^{-jkR_2}}{R_2}) \tag{2.21}$$

Where
$R_1 = \sqrt{z^2 + a^2}$
$R_2 = \sqrt{z^2 + b^2}$
V_i = input voltage at dipole terminals taken as $1V$
a = radius of the dipole wire
b = outer radius of the equivalent magnetic annular aperture
b= $2.3a$ taken for 50Ω annular [3]

2.10.2 Method of Moments (MoM)

After substituting for the incident electric field in Equation 2.20 various numerical methods exist to find out the $I(z')$. *Method of Moment* (MoM) proposed by

Harrington [85] was chosen because of its simplicity and accuracy. By using the MoM the functional field equation can be converted to matrix form. The matrix form of equation is easy to solve with the use of modern digital computer. The matrix is then inverted to get the final solution. The general form of the MoM is:

$$L(f) = g \tag{2.22}$$

Where L is a known linear operator, g is a known excitation and f is the response function. In this particular case L is integrodifferntial operator of Equation 2.20 and objective is to find f given g. To solve this problem the unknown function f is represented as a linear sum of P terms and given in Equation 2.23.

$$f(z') = \sum_{p=1}^{P} c_p f_p(z') \tag{2.23}$$

Where c_p is a constant and $f_p(z')$ is known function usually called a basis function. Details are given by Balanis [3]. On substituting Equation 2.23 back into Equation 2.22 gives:

$$\sum_{p=1}^{P} c_p L(f_p) = g \tag{2.24}$$

In Equation 2.24 the basis function has the same domain as $f(z')$ and it is chosen so that $L(f_p)$ can be solved conveniently. There are P unknowns and to solve for P unknowns there must be P independent equations. This is accomplished by evaluating Equation 2.24 at P different points. This is referred to as the point matching [3]. By using this method Equation 2.24 is modified as;

$$\sum_{p=1}^{P} c_p L(f_p) = g_q \tag{2.25}$$

Where $q = 1, 2, 3, ..., P$. Equation 2.25 can be written in matrix form as:

$$\begin{aligned} [Z_{qp}][I_p] &= [V_q] \\ [I_p] &= [Z_{qp}]^{-1}[V_q] \end{aligned} \tag{2.26}$$

An important step in the implementation of MoM is the choice of basis function. The basis function must be able to represent the unknown function as accurately as possible. There are many different types of basis functions available and can be subdivided in to two classes, *sub domain* and *entire domain* basis functions. The sub domain basis functions are more flexible as they can be used to represent the function without any prior knowledge of that function. For this work sub domain basis function was chosen. In order to implement the sub domain basis function the dipole antenna was divided into P segments each of length Δz and the basis function was defined over the each segment. More on basis functions could be found in [3, 4]. In order to keep the model simple the basis function of choice was a *piecewise constant* function expressed as:

$$f(z') = \begin{cases} 1 & \text{if } z'_{p-1} < z' < z'_p \\ 0 & \text{elsewhere} \end{cases}$$

But this simple model required a large number of sub segments (≈ 1000) for each segment to numerically evaluate the integral of Equation 2.20 and to achieve the required convergence. In order to improve the computation time following procedure was adopted for this study.

Each segment was divided into Y number of sub segments in order to perform the numerical integration. It is represented as Δz_{py} where y stands for the sub segment number. The number of these sub segments were significantly reduced using the Simpson's rule for numerical integration. The integrand was evaluated at three different points of each sub segment. These points were chosen to be the trailing ($\Delta z_{py(T)}$), middle($\Delta z_{py(M)}$) and the leading ($\Delta z_{py(L)}$) point of each sub segment. If the values determined at these points are indicated as ff_1, ff_2 and ff_3 respectively then the final integration value over that sub segment could be expressed as:

$$\int_{\Delta z_{py(T)}}^{\Delta z_{py(L)}} f(\Delta z_{py}) = \frac{\Delta z_{py(L)} - \Delta z_{py(T)}}{6}[ff_1 + 4ff_2 + ff_3] \tag{2.27}$$

The integration results obtained for each sub segment were summed up and then multiplied by the differential length of the segment. This value was then assigned to that segment. This procedure significantly reduced the number of sub segments required from ≈ 1000 to 5 as used in section 2.10.3.

A MATLAB function is created that takes dipole radius (a) and length (l) as input arguments and solve for Z_{qp} matrix in Equation 2.26. Where Z_{qp} over a single segment p is given as below;

$$Z_{qp} = (\frac{d^2}{dz^2} + k^2)(\frac{e^{-jk\sqrt{a^2+(z-z_p)^2}}}{4\pi\sqrt{a^2+(z-z_p)^2}}) \tag{2.28}$$

This single segment p is subdivided into y sub segments and Equation 2.28 is evaluated at three points as mentioned earlier using Equation 2.27 over each sub segment.

2.10.3 Self Impedance

The mathematical model based on the MoM described in section 2.10.2 was implemented using MATLAB®. The first goal was to determine the self impedance of the dipole antenna to test the software model. The design parameters for the dipole antenna and the MoM model are listed below.

Length of the dipole antenna , $l = 0.47\lambda$
Radius of the dipole antenna wire, $a = 0.005\lambda$
Number of segments, $P = 101$
Number of sub segments per segment, $Y = 5$

The length of the dipole antenna was chosen to be its resonance length. The odd number of segments were chosen to utilise the symmetry of the structure. The optimum number of the segments and the sub segments were found through trial and error for the required accuracy of the result and the computational efficiency. Equation 2.21 was computed to find the incident electric field distributed along P segments of the dipole antenna. This value was replaced in Equation 2.20 and it was solved for P segments. The solution resulted in the matrix $[Z_{qp}]$ shown in the simplified Equation 2.26 and was solved for $[I_p]$ with $[V_q]$ defined as the magnetic frill source from Equation 2.21.

The $[I_p]$ gives the current distribution along the dipole antenna shown in Figure 2.11. The numerically computed value for the self impedance is given for $l = 0.47\lambda$;

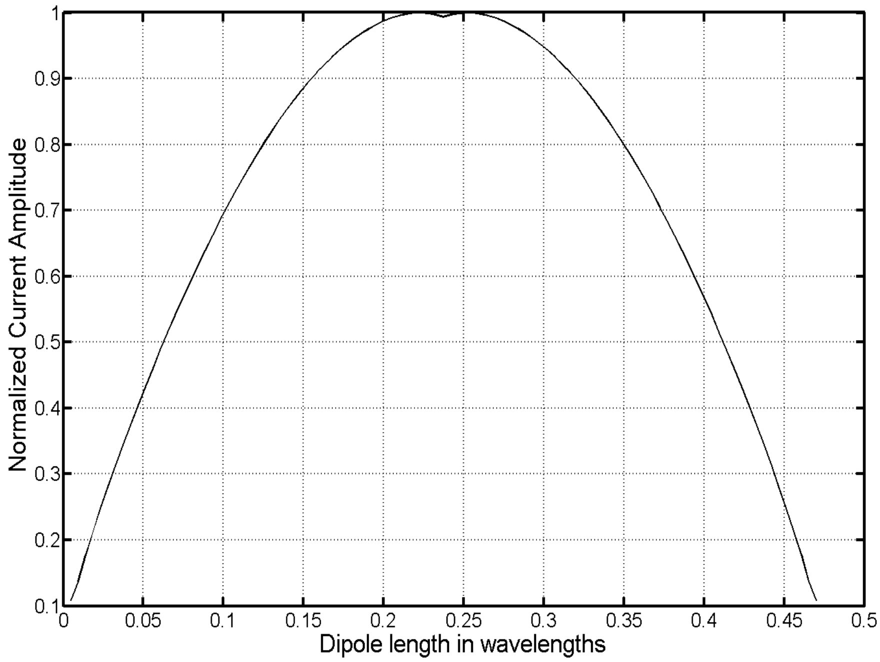

Figure 2.11: Current distribution along the dipole antenna element with $l = 0.47\lambda$ and $a = 0.005\lambda$ found by applying the MoM model developed for this research work

$$Z_{in} = \frac{V_q^{in}}{I_p^{in}}$$

Where V_q^{in} is the voltage value at the feed (centre) segment of the dipole and I_p^{in} is the corresponding current.

$$Z_{in} = 80.0 + j15.2 \tag{2.29}$$

The dipole input impedance determined by the developed MoM model was compared with the one available in the text for $P = 79$ given in the *Table* 8.8 under article 8.5 *Self Impedance* [3]. The value found by the MoM model developed for this research work was $78.9 + j13.2$ and in [3] $78.8 + j12.9$ which was in close agreement. This comparison was made to ensure the accuracy of the developed MoM model.

All other dipole design parameters were the same. The number of segments were increased to find a converging value of input impedance and that is presented in Equation 2.29 for $P = 101$.

2.10.4 Mutual Impedance

The value of the self impedance of a dipole element calculated in the above section holds as long as it radiates in free space. In the presence of any reflecting object or another dipole element the current distribution will be changed. Therefore the self impedance of the dipole element will not remain the same as for free space. In order to overcome this effect it is very important to find out the change in current distribution in the presence of other objects. In this section the attention is focused on the determination of mutual impedance among dipole elements. More theoretical and mathematical background can be found in [3,4].

To find out the mutual impedance between two dipole elements a *MATLAB®* based computer program was developed. The only dipole configuration considered for mutual coupling calculations in this work is the *side by side*. This choice was made because this configuration gives the maximum mutual coupling between the two elements [3,4].

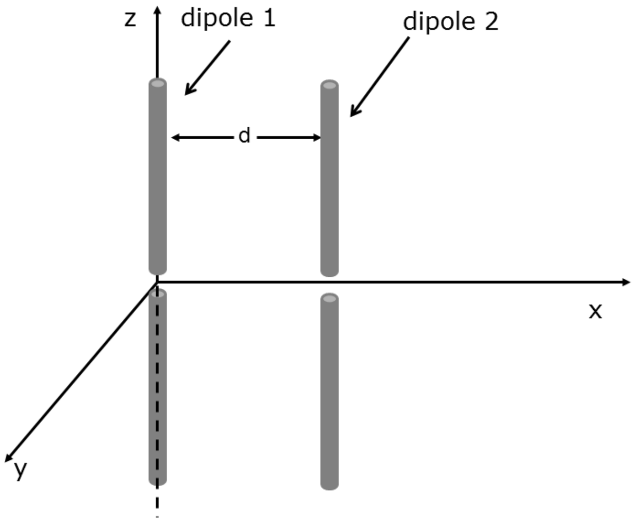

Figure 2.12: Problem geometry considered to determine mutual coupling between two dipoles

It is assumed that dipole 1 and dipole 2 are placed side by side in free space and separated by a distance *d* between their axis as shown in Figure 2.12. No ground and edge effects are considered. At first dipole 1 is energised by a magnetic frill source given by Equation 2.21 and it is assumed that dipole 2 is absent. Then the current distribution over dipole 1, $[I_p^1]$, is determined in the similar way described in sections 2.10.2 and 2.10.3 by using Equation 2.26. Now the electric field due to $[I_p^1]$ is determined at the location of dipole 2 by replacing $I_z(z')$ with $[I_p^1]$ in Equation 2.20. The modified value of R used in Equation 2.20 is given as;

$$R = \sqrt{(a-d)^2 + (z-z')^2} \tag{2.30}$$

The electric field E_{z12} is determined at position of dipole 2 due to a known current distribution, $[I_p^1]$, at dipole 1. After this step dipole 1 is assumed to be open circuited and dipole 2 is placed at its location and energised by the same source as dipole 1. The same field and current distribution as found for dipole 1 is assumed for dipole 2. Due to the presence of E_{z12} the resultant current distribution over dipole 2 is determined by following the procedure described in section 2.10.3 taking E_{z12} as source and denoted as $[I_p^{12}]$. Total current distribution over dipole 2 will become $[I_p^2] = [I_p^1] + [I_p^{12}]$. Now open circuited dipole 1 is segmented into P segments. Due to the induced current distribution, $[I_p^{12}]$, over dipole 2 electric field E_{z21} is determined over the dipole 1.

This electric field then become the source for the dipole 1 which is now terminated [4]. The current distribution across dipole 1 due to E_{z21} is determined using the same computer codes as used in the sections 2.10.2 and 2.10.3. This new current distribution, $[I_p^{21}]$, across dipole 1 gives the value of current distribution resulted by the mutual coupling. With both dipoles energised this new current distribution will be added to their current distributions to reflect the mutual coupling effect. The resultant current due to coupling over dipole 1 will be $[I_p^c] = [I_p^1] + [I_p^{21}]$ and due to reciprocity property on dipole 2 as well. Finally the mutual impedance was determined by using the following expression:

$$Z_{12} = \frac{1}{I_p^1(m) I_p^2(m)} \int_{-l/2}^{l/2} E_{z12}(z') I_p^c(z') dz' \tag{2.31}$$

Where

I_p^c = current distribution across dipole 2 (modified)
$I_p^1(m)$, $I_p^2(m)$ = the input current for dipole 1 and dipole 2 at the feed gap, m

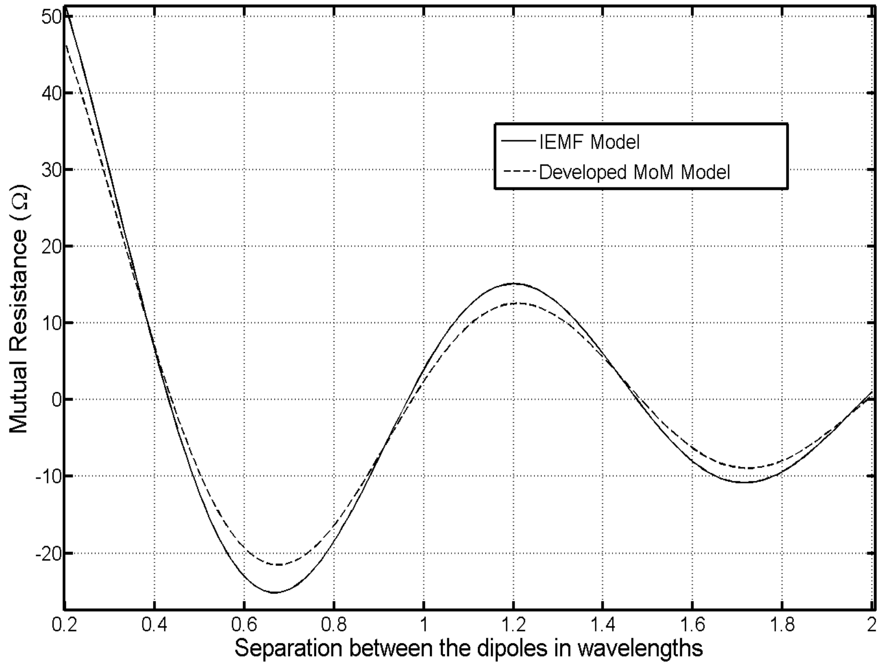

Figure 2.13: Real parts are compared of the mutual impedance determined by the Induced EMF and MoM

The mutual impedance of the two dipole elements over the separation between them is determined by the developed MoM and the procedure described above. The obtained mutual impedance values are compared with the Induced EMF (IEMF) method results. The detailed discussion about the IEMF method is presented in [3,4]. Figure 2.13 compares the real part of the mutual impedance. The imaginary part of the mutual coupling is compared in Figure 2.14.

The IEMF does not allow to select the radius of the dipole antenna wire and the feed gap. The differences between the two results reflect this fact. It is assumed for the IEMF method that the radius of the dipole wire is infinitely thin [3] which is not assumed in this case.

A MATLAB function is developed by the author which takes dipole radius (a), length (l), inter element separation (d) and known current distribution as input ($[I]$). The output of this function is plotted in Figures 2.13 and 2.14 to compare with the IEMF method. The output of this function is the coupled current, $[I_p^{21}]$, and the value of the mutual impedance between the dipoles separated by d. This method is used to determine the array coupling in next section.

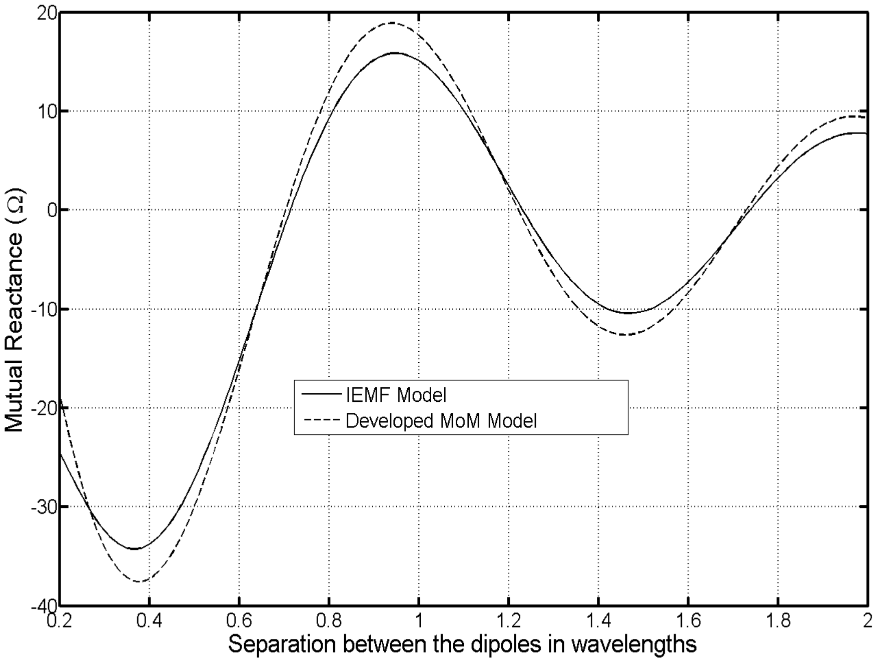

Figure 2.14: Imaginary parts are compared of the mutual impedance determined by the Induced EMF and MoM

2.10.5 Mutual Impedance: Linear Array

The technique developed in section 2.10.4 is extended to an array of linear dipole elements. The procedure is repeated for an array of N elements to find the mutual coupling matrix. For example consider an array of five elements with half wavelength separation between the elements. Generally the impedance matrix for this array would be given as;

$$Z_{mn} = \begin{bmatrix} Z_{11} & Z_{12} & \dots & \dots & Z_{15} \\ Z_{21} & Z_{22} & \dots & \dots & Z_{25} \\ \dots & \dots & \dots & \dots & \\ Z_{N1} & Z_{N2} & \dots & \dots & Z_{55} \end{bmatrix}$$

Where Z_{mn} for $m = n$ is the input impedance of the dipole element and for $m \neq n$ is the mutual impedance between the elements due to current on n^{th} element. If a dipole element is not surrounded by other elements then the input impedance is equal to self impedance. In the presence of other energised elements it does not remain same as the self impedance and it is termed as driving point impedance [3].

It is assumed for this array model that all the elements have sinusoidal current distribution with unit peak value (uniformly excited array). The distribution over n^{th} dipole is given by expression;

$$I_n(z) = \sin(k(\frac{l}{2} - |z - z'|)) \tag{2.32}$$

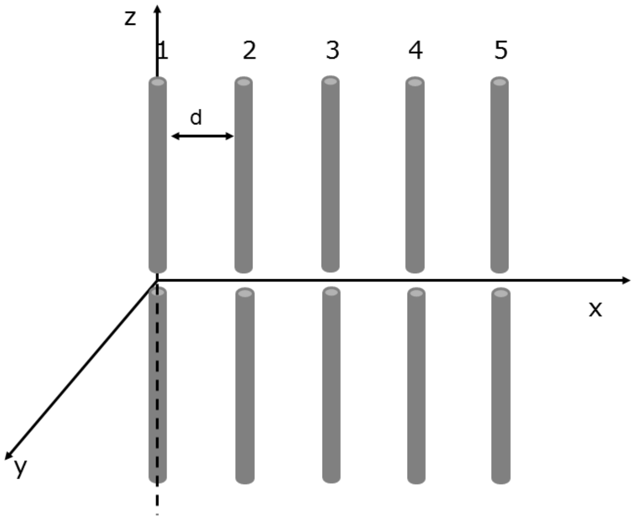

Figure 2.15: Dipole array consisting of five elements (N=5), $d = 0.5\lambda$

The dipole array considered is shown in Figure 2.15. Initially dipole 1 and dipole 2 are considered and mutual impedance is determined using the procedure described in section 2.10.4. The change in current distribution due to coupling, $[I_p^{21}]$, is recorded for dipole 1. Now same procedure is repeated for dipole 1 and dipole 3 and so on. The mutual impedance values and the change in current distribution, $[I_p^{N1}]$ is recorded. After completing this step the modified current distribution over dipole 1 is the sum of initial and coupled distributions. Generally the expression for the modified current distribution for $m \neq n$ is;

$$I_m' = I_m + \sum_n^N [I_p^{nm}] \tag{2.33}$$

Next step is to consider dipole 2 and repeat the similar procedure as done for dipole 1. Dipole 2 is surrounded by dipole 1 and dipole 3 therefore its profile will be different compared to dipole 1 which is evident from Figure 2.16. This consideration is implemented in this array coupling model. Due to the geometrical symmetry only dipole 1,2 and 3 are required to be evaluated. The modified current distribution for the three dipoles is compared with the initial distribution in Figure 2.16. These modified currents are used to determine the driving point impedance for the dipoles by using Equation 2.34 for $m \neq n$.

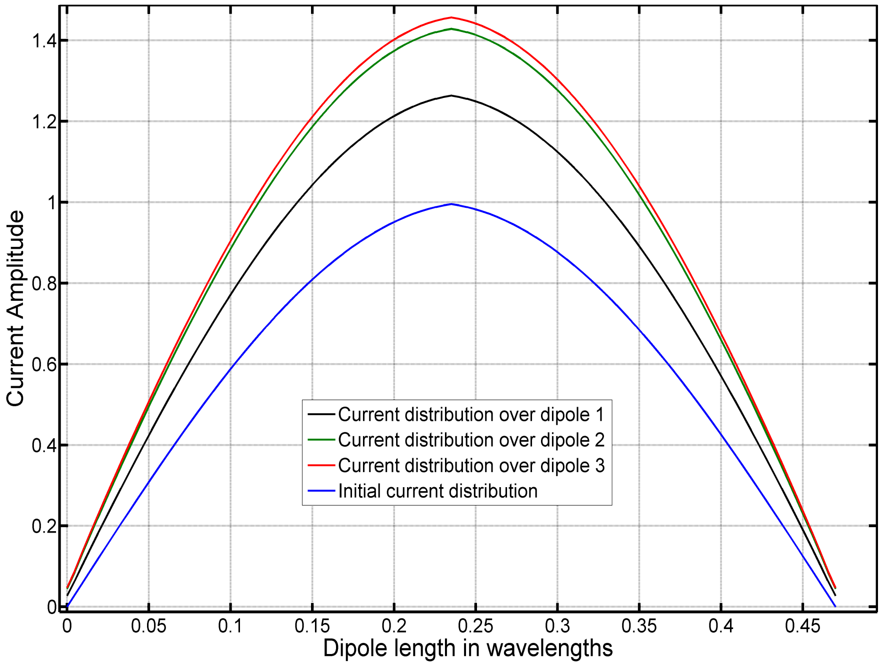

Figure 2.16: Modified current distribution due mutual coupling over dipoles 1,2 and 3 is plotted with the initial current distribution

$$Z_{md} = Z_{mm} + \sum_{n}^{N} Z_{mn} \frac{I'_n}{I'_m} \tag{2.34}$$

Where Z_{md} is the driving point impedance of the m^{th} dipole. The mutual impedance matrix for the linear array of five elements is given below;

$$Z_{mn} = \begin{bmatrix} 78.8 + 13.2j & -9.64 - 27.09j & 2.40 + 15.06j & -0.98 - 10.22j & 0.49 + 7.71j \\ -9.64 - 27.08j & 78.8 + 13.2j & -9.64 - 27.08j & 2.40 + 15.06j & -0.98 - 10.22j \\ 2.40 + 15.05j & -9.64 - 27.08j & 78.8 + 13.2j & -9.64 - 27.08j & 2.40 + 15.05j \\ -0.98 - 10.22j & 2.40 + 15.05j & -9.64 - 27.08j & 78.8 + 13.2j & -9.64 - 27.08j \\ 0.49 + 7.71j & -0.98 - 10.22j & 2.40 + 15.06j & -9.64 - 27.08j & 78.8 + 13.2j \end{bmatrix}$$

A MATLAB based function is developed to find the mutual impedance matrix for N array elements based on the procedure described above. This function is used to determine the mutual impedance matrix in chapter 7.

2.11 Dielectric Resonator Antenna (DRA) Model

The Bowtie Dielectric Resonator Antenna (BDRA) [67] is chosen for this study because of its wide application area mainly due its size, cost and improved bandwidth properties. An array of eight antenna elements is designed and simulated by $CST-MWS$ as given in Figure 2.17. It is reported that this BDRA has a bandwidth of up to 49.4% for the frequency range of $4.194 - 6.944GHz$. For this research work the frequency band chosen was from $4.5GHz$ to $5.5GHz$ and the BDRA reflection coefficient was well under $-13dB$ [67].

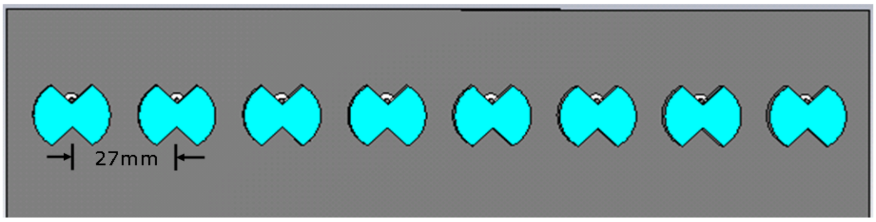

Figure 2.17: BDRA array geometry designed in CST MWS

The array is uniformly separated with the spacing $27.3mm$ which is half wavelength at $5.5GHz$. For this work the time domain solver is used in order to obtain a wideband response of the array and its ability to apply the custom element weights.

In order to find the individual element patterns in array environment the source excitation setting is set to *All Ports* in the time domain solver. With this setup only one element is taken into account while all other elements are terminated with matched loads. This results in the active element patterns for the whole array.

2.11.1 Active Element Pattern (AEP)

In case of infinite arrays it can be assumed that the radiation pattern of a single active element, while other elements are terminated, is enough to model the coupling in the system. This element pattern is called active element pattern.

Since the array is infinite therefore each element "sees" the same environment and hence the coupling faced by each element is the same. There is no need to find individual element patterns to properly model the coupling profile [14]. In practice for finite arrays, as long as the array is large, it is assumed that each element appears as if it was in infinite array except those near the edges. Since edge elements are less in number compared to the other elements in an array, therefore, this argument holds for the large finite arrays. In this case the product of the active element pattern of the infinite array with the finite array factor (provided array is large) models the complete array with mutual coupling. But in small arrays the mutual coupling behaviour is not simple. Each element surroundings differs from the other elements and edge effects play a vital role to effect the array performance. Therefore, each element pattern is required to be determined in the array environment while other elements are terminated with matched loads. The patterns obtained in this manner are different from the *Isolated Element Pattern* (IEP). Isolated element pattern (IEP) is determined in the complete absence of other array elements. Therefore, active element patterns are considered in this study of small antenna array pattern synthesis.

2.11.2 Simulated Element Pattern

The simulation of the array structure shown in Figure 2.17 resulted in the eight individual element patterns. These patterns are presented in Figures 2.18 and 2.19. For comparison purposes Isolated Element Pattern is also shown in both figures.

In Figure 2.18 the radiation patterns for the elements 1 from 4 are compared with the Isolated Element Pattern. The element radiation patterns have significant differences in shape as compared to the Isolated Element Pattern (IEP). The maximum significant difference of $4.8dB$ between the AEPs and the IEP is at $\theta = -58^o$. This implies that the mutual coupling between the array elements has a significant effect. There are no dummy elements and that resulted in the edge effect. This has effected element 1 radiation pattern significantly as compared to the other elements.

Figure 2.19 presents the AEPs for elements 5 to 8. Since the ideal physical conditions are assumed therefore these AEPs are the mirror image of the other half of the array patterns. The maximum difference between AEPs and the IEP in this case is found to be $4.9dB$ at $\theta = 58^o$. The edge effect is clearly visible in

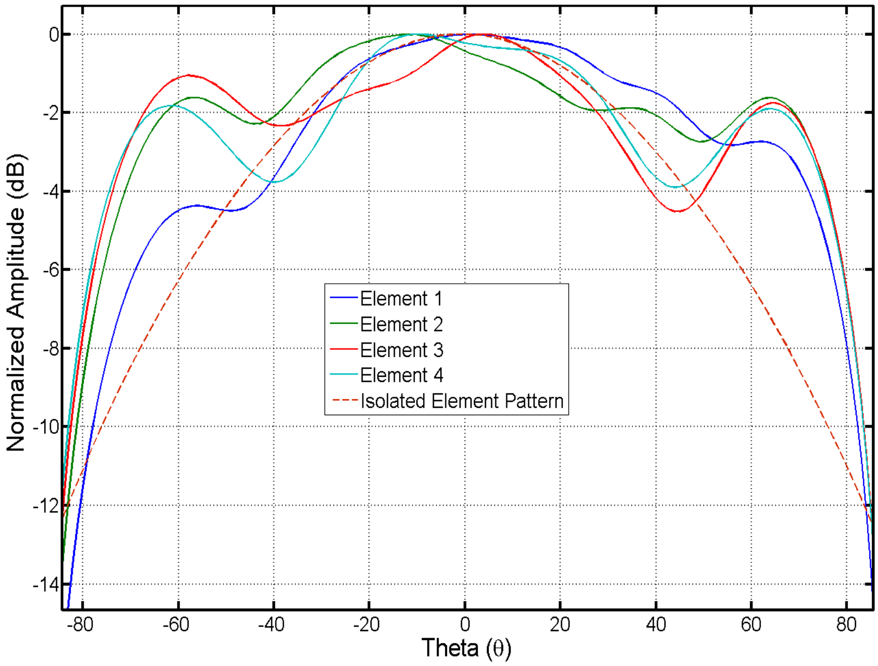

Figure 2.18: Simulated active element patterns for element 1 to 4 of BDRA array at 4.5*GHz*

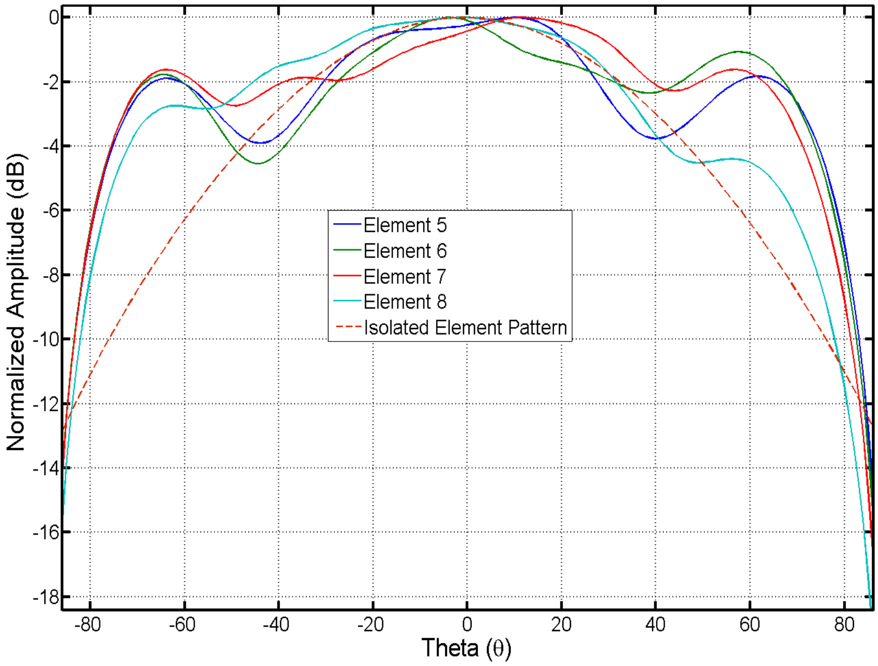

Figure 2.19: Simulated active element patterns for element 5 to 8 of BDRA array at 4.5*GHz*

the pattern of element 8.

From these results it is clear that in case of small arrays individual AEPs are important to consider for antenna array modelling, as the mutual coupling and the presence of edge effect is not uniform over the array.

2.11.3 BDRA Array Pattern

In this section a comparison is presented of the BDRA array patterns and the isotropic array pattern. The Figure 2.20 shows the three instances of the radiation patterns at 4.5*GHz* resulting in the equivalent uniform separation of $d = 0.41\lambda$. The isotropic array pattern is plotted using the Equation 2.3. The isolated BDRA array pattern is plotted using the Equation 2.4. Where $E(\theta)$ is the isolated BDRA pattern in the absence of other antennas. Therefore the isolated BDRA array pattern does not show the effect of mutual coupling or the finiteness of the array. The BDRA array pattern considers AEPs and is plotted using the Equation 2.6. Since it considers the AEPs therefore it models the array close to the physical array. The Table 2.2 summarises the important features of the three patterns.

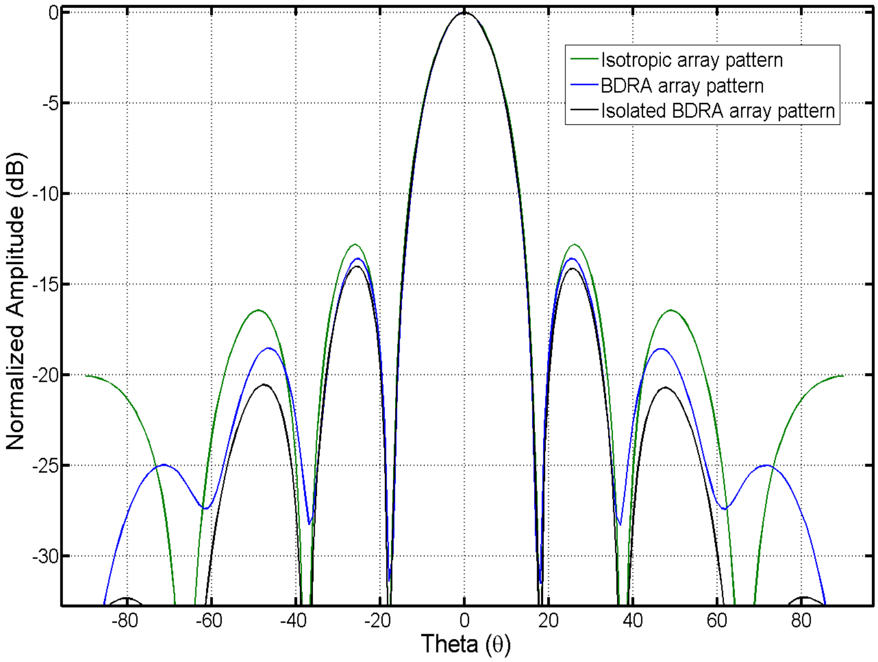

Figure 2.20: Radiation pattern plots for isotropic, isolated BDRA element, and the BDRA arrays at 4.5*GHz*

Array Type	HPBW (Deg)	Peak SLL (PSLL) (dB)	Average SLL (dB)	Gain (dBi)
Isotropic Element	15.5	−12.8	−16.4	8.4
Isolated BDRA Element	15.0	−14.0	−22.1	14.4
BDRA Array	16.0	−13.6	−19.0	12.7

Table 2.2: The summarised results from the Figure 2.20

The effect of the isolated element pattern produces lowest PSLL among the three radiation patterns. In case of the BDRA array pattern obtained by using the AEPs the SLL improvement as compared to the isotropic array is 6.2% in PSLL and 15.64% in average SLL. The comparison of the array gains is worth noting. The AEPs reflect the true array gain once assembled. The array directivity was found using the Equation 2.8 with $\theta_o = 0$. The array gain is shown in Table 2.2. The isotropic array gain was found to be $8.4dBi$ for $d = 0.41\lambda$. The gain of the isolated BDRA element was $6dBi$ therefore the isolated BDRA array gain was $14.4dBi$. The BDRA array gain found by using the *CTS-MSW* was $12.7dBi$ in xz-plane. The array gain reduced by $1.7dB$ as compared to the predicted gain with the isolated BDRA array pattern. The difference in the isolated and the coupled BDRA array gains can be explained if 3D radiation pattern is considered. In Figures 2.21(a) and 2.21(b) the 3D patterns are shown along the xz and yz planes respectively. The radiation pattern optimisation is performed in xz plane only and the effect on the array gain in xz plane due to the radiation in other planes is not considered.

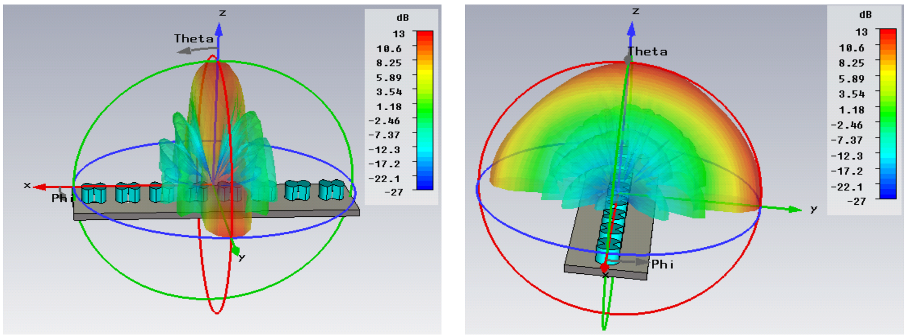

(a) (b)

Figure 2.21: 3D BDRA array radiation pattern at $4.5GHz$

2.12 Chapter Summary

In this chapter a mathematical model of the basic linear array considered for this research work is presented. The array factor properties that are used as the pattern synthesis metric for the optimisation purpose are defined. A pattern synthesis technique based on Schelkunoff's polynomial, that is used in this study, is described and discussed. Two test arrays are presented consisting of dipole and BDRA elements. An accurate and computationally efficient technique developed by the author based on MoM is presented. This technique is used to model the dipole element. The developed model is used to determine self impedance of a single dipole element with unknown current distribution and the mutual coupling impedance between two dipole elements. The same model is then extended to find the mutual impedance matrix for an array of linear dipoles. An array of eight BDRA elements is designed and presented. The active element patterns are determined for the BDRA array using CST-MWS. The isotropic array and BDRA array radiation patterns are compared and discussed.

Chapter 3

Particle Swarm Optimiser: Implementation

3.1 Introduction

Optimisation is a process that finds the optimal solution among the alternatives for any given problem. There are various optimisation techniques available [27]. The Particle Swarm Optimiser (PSO) belongs to a special group of stochastic algorithms that is inspired by the stochastic phenomenon in nature. This group of algorithms is further subdivided into two main categories related to the two natural phenomena namely *evolution* and the *swarm intelligence*. The famous example of the former is the *Genetic Algorithm (GA)*. PSO falls in the category of the swarm intelligence. It was first presented by J. Kennedy et. el. [21, 22] in the year 1995. Since then it has been used widely by the researchers in various applications. A diverse review of the PSO applications is presented by R. Poli [86]. This optimisation technique was introduced to the electromagnetic problem domain by J. Robinson et. el. [47,56].

The PSO was used for the first time to optimise phased arrays [38,45]. Since then it has been reported for pattern synthesis problems. For this research work the PSO was chosen as the optimising tool because of the following reasons.

- At the time this work was undertaken a solution based on the PSO in conjunction with Schelkunoff's polynomial method for the issues related to small antenna array pattern synthesis highlighted in chapter 1 was not reported in the literature.

- Due to its heuristic nature it avoids the need to formulate the problem to be optimised in analytical manner
- No differentiable functions are required to be defined in order to find the global extrema in the *solution space*. Therefore it avoids all shortcomings of the deterministic optimisation algorithms [27].
- It is not necessary to have a detailed model of the problem
- No initial or starting points are required to be defined
- Multiple objective optimisation problems can be solved
- Compared to its famous heuristic counterpart, the GA, it has simple computational structure. Also it has been shown that it outperformed GA in some instances [45, 87]

3.2 Basic Concept

The PSO is based on the social intelligence of a group of individuals e.g. fish school, bird flock etc . Various analogies based on these social groups have been reported in the literature [21, 56]. All these individuals share a common objective while working in the group. An objective could be successfully achieved if every member of the group play its role and share its knowledge about it with the group. This way the group develops its own memory about the surroundings. An intelligent processing of this information is essential in this whole process. This enables the members of the group to attain the best possible state of their role so that the main objective is achieved.

For the array pattern synthesis problem at hand as described in chapter 2 section 2.7 a particle contains all the root (null) locations on and around the unit circle. If $N = 8$ there will be 7 roots as shown in the Figure 2.7. The goal is to achieve an array pattern with the desired characteristics. All particles containing the root locations are the potential solutions. The ″goodness″ of a goal is measured by a *fitness function* whose value is evaluated for each particle. The PSO records the best fitness function values for the individual particle and best of all these as for the group. A root location is defined by its distance from the centre of the unit circle r and its angular position α as shown in the

Figure 3.2. Therefore it is a two dimensional optimisation problem resulting in 14 variables in total for this example. The equal number of particles were assigned to both dimensions each with 7 variables to optimise. The general solution space used for the optimisation purposes has shown boundaries on r and α in z-space, Figure 3.3. The required modifications in the r and α values for each null position are determined independently by *velocity* calculation. The old values of r and α are updated in the form of a *position vector* for each particle. Each particle's personal best value for both r and α (each of 7 variable values) is recorded if it has resulted in a better individual fitness result. Also the particle with the best fitness value is chosen as the leader and all particles follow it. This continues until the termination criteria is met. The flow chart for the PSO algorithm highlighting the basic steps is shown in Figure 3.1.

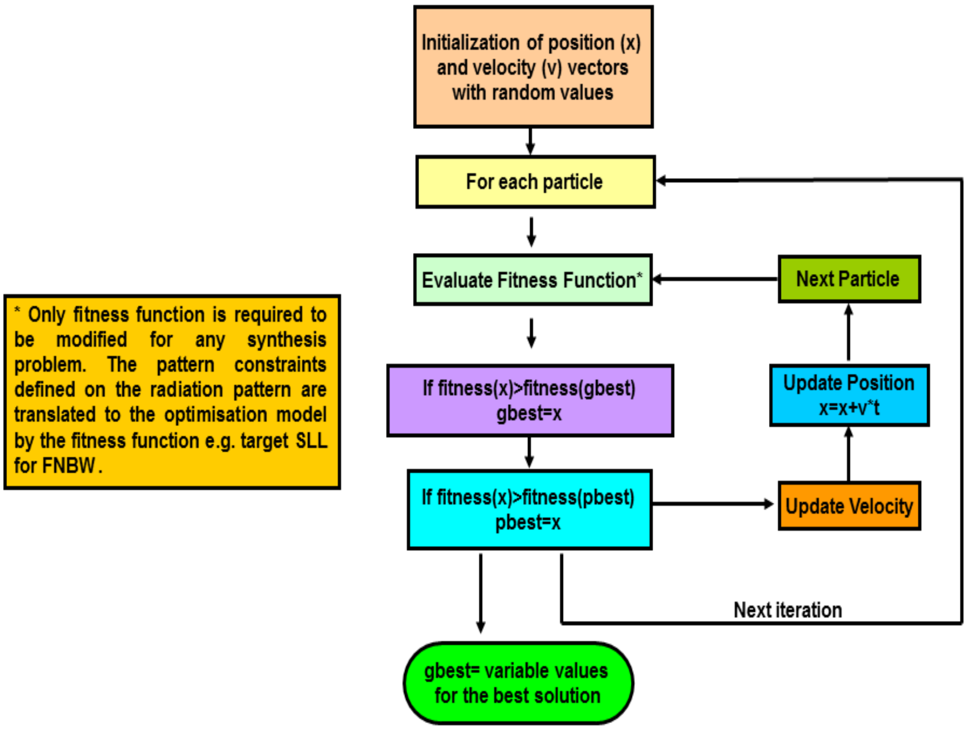

Figure 3.1: Flowchart highlighting the basic steps involved in the Particle Swarm Optimiser (PSO)

In the following the major components of the PSO are described in accordance to the pattern synthesis problem model discussed above.

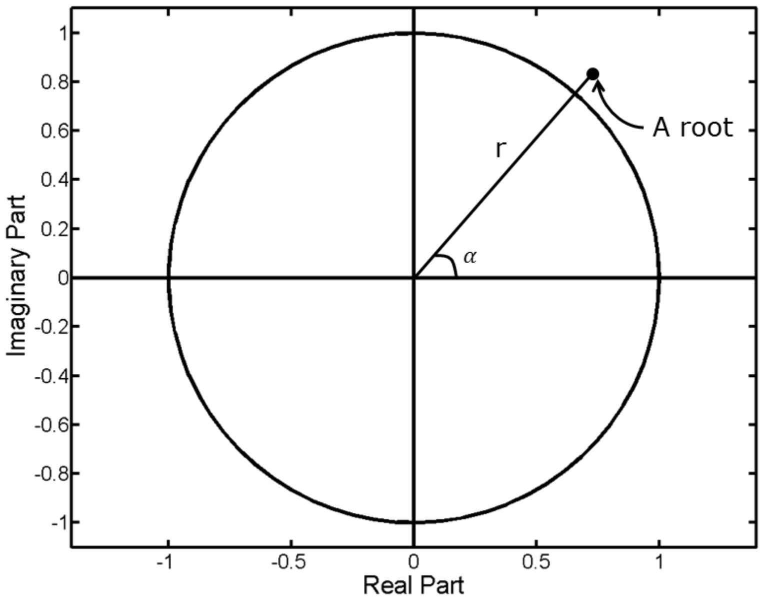

Figure 3.2: A root location (variable) placed in solution space

3.3 PSO Components

In the case of an optimization problem, the individuals represent the variables involved. The objective is to find the variable values that result in the optimum solution to the problem. While searching for these optimum variable values the PSO records the individual best values and the group best values both the corresponding fitness values and the variable values contained by the particle. Some important definitions related to the PSO are given below.

Particle: The term particle comes from the swarm analogies used for individual member of the swarm. In our case each particle in r and α domain when combined give null positions in z-space that represent the resultant array pattern.

Population Size: It is the total number of particles in the swarm. In an optimization problem it depends on the number of variables to be optimized. The population size differs for the various pattern synthesis scenarios considered in this work. There is a tradeoff between the number of particles and the number of iterations required to converge.

Position Matrix: This stores the position or coordinates of each particle in the swarm. The size of the matrix depends on the dimensions of the problem.

In our case the position matrix will hold the values for r and α separately each consisting of 7 values. The size of the position matrix in this problem is 2×7

Velocity Matrix: It represents the amount of the change required to set the appropriate speed so that the swarm could converge to the best solution. In our case it would keep the incremental or decremental values to be applied to the position matrix.

Cost (Fitness) Function: This is the function that represents the goodness of the problem objective. It is a single valued function. Throughout this study, various fitness functions were used depending on the nature of the problem.

pbest: This is the best position of an individual particle in the swarm. Each particle remembers the position vector that results in the best fitness value so far as *pbest*. In our case the values for r and α that resulted in individual particle best fitness evaluation are saved as *pbest*.

gbest: This is the best position known by the whole swarm. Each particle in the swarm remembers this as *gbest*. If the *pbest* for any particle results in a better fitness function evaluation as compared to the current *gbest* corresponding fitness function value then *gbest* will be replaced by the *pbest* of that particle.

Solution Space: In order to implement the PSO defining a solution space is critically important. This requires defining the maximum and minimum boundaries for each dimension involved. This limits the search of the optimum solution in the reasonable range. In order to improve the convergence of the PSO the solution space was intelligently defined for the problems dealt here. In detail description of which shall be given in section 3.4.7.

3.4 Development of UoM-PSO

In the following sections the PSO algorithm developed for this research work named as the University of Manchester - Particle Swarm Optimiser (UoM-PSO) is described.

3.4.1 Initialisation Setup

The initialisation setup of the UoM-PSO includes the antenna array modelling start up. This includes defining the number of antenna array elements (N), the separation between the elements (d) and the uniform taper. A choice among the antenna array models (isotropic, dipole, BDRA) defined in chapter 2 was made at this point. In order to define the cost function later in the UoM-PSO the target values for the radiation pattern metrics are defined. The swarm size (number of particles) and the number of iterations are defined depending on the nature of the problem. The numerical values will be provided while considering the examples.

3.4.2 Defining Solution Space

For the UoM-PSO the solution space is defined in z-space. In case of $N = 8$ the Figure 3.3 shows the defined solution space. As described earlier it is a two dimensional problem to find the root location therefore the bounds are applied to the both dimensions. For r maximum and minimum bounds are the same for each particle. However in case of α maximum and minimum bounds are defined for each null location in a particle individually. The simplistic boundary definition for α works on the idea that unit circle space is uniformly divided among all the roots(nulls). Each root is allowed to roam within the $\frac{360^o}{N-1}$ interval. For example the initial position of each root obtained from the uniform taper as shown in Figure 2.7 is taken as the centre of this roaming interval. A uniform division of the boundaries is depicted in Figure 3.3 where each sector represents a constraint on single root location. This boundary condition is applied to UoM-PSO.

3.4.3 Initialisation of Position and Velocity Matrices

In order to begin searching for the optimum null positions each particle is initialised with random values within the bounds of each dimension. The velocity matrix is also initialised randomly. These randomly generated initial position values for each particle are taken as their *pbest*. The *gbest* is chosen among these values. In Figure 3.4 randomly generated population of 5 particles for $N = 8$ within the defined boundaries of each variable is shown. After the

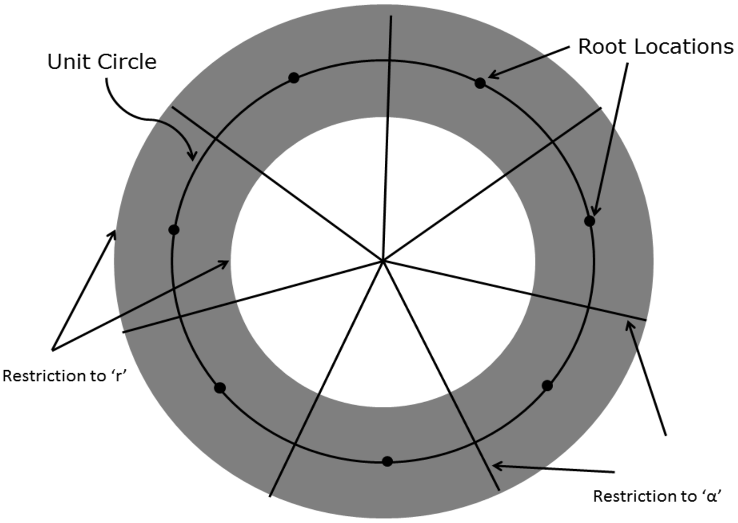

Figure 3.3: Solution space is divided in boundaries. The shaded region shows the bound on r for each root location. The unit circle is divided into 7 sectors to represent the allowed roaming region for each root in α

initialisation each particle starts searching for values of its variables that result in best fitness evaluation.

3.4.4 Updating Velocity Value

The calculation of velocity is critically important and the only major calculation involved in PSO implementation. The velocity value for any particle depends on its relative location in the solution space to its *pbest* and swarm's *gbest* locations. The following expression was used for the velocity calculation of p^{th} particle at g^{th} iteration in h^{th} dimension [56]:

$$v_{ph}^{g+1} = K^g \cdot v_{ph}^g + \gamma_1^g \cdot \zeta_1 \cdot (pbest_{ph}^g - x_{ph}^g) + \gamma_2^g \cdot \zeta_2 \cdot (gbest_{ph}^g - x_{ph}^g) \qquad (3.1)$$

Where K is the *inertial weight* multiplier, γ_1 and γ_2 are the cognitive and social scaling factors, ζ_1 and ζ_2 are the randomly generated values between the interval 0.0 & 1.0 and x_p^g is the current position of the particle.

The velocity expression given in Equation 3.1 differs from the one given in early literature [21]. This inertial weight was added in order to fade the effect of the v_p^g gradually with time [27,56] in order to concentrate the particles around the most promising locations. For UoM-PSO model inertial weight

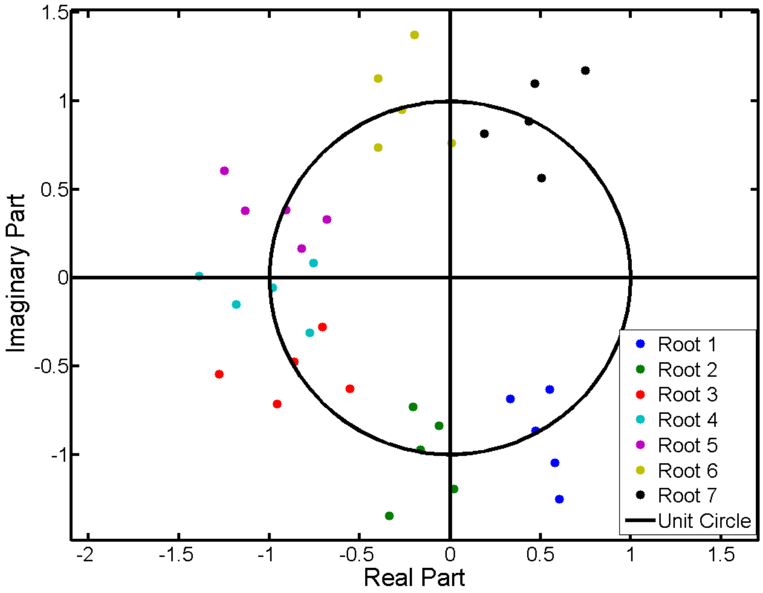

Figure 3.4: Randomly initialised root locations for 5 particles with $N = 8$

value was varied linearly from 0.9 to 0.4 for this purpose [56,88]. This is given mathematically as:

$$K^{g} = K^{max} - \frac{K^{max} - K^{min}}{ite} g \tag{3.2}$$

Where K^{max} and K^{min} are the maximum and minimum values respectively and *ite* is the total number of iterations.

The cognitive multiplier γ_1 decides the pull towards the particle's *pbest* location for each particle. Whereas the social multiplier γ_2 defines the pull towards the *gbest*. It was suggested that at the start of the search procedure particles should follow their own best location *pbest* but as it goes along towards the end of the search the particles should prefer to follow *gbest* [27]. Mathematically this could be achieved by:

$$\gamma_1^{g} = \gamma_1^{max} - \frac{\gamma_1^{max} - \gamma_1^{min}}{ite} g \tag{3.3}$$

$$\gamma_2^{g} = \gamma_2^{min} + \frac{\gamma_2^{max} - \gamma_2^{min}}{ite} g \tag{3.4}$$

Where γ_1^{max}, γ_1^{min}, γ_2^{max} and γ_2^{min} are the maximum and minimum values for the cognitive and social multipliers respectively. The minimum and maximum values for both cognitive multipliers are chosen through trial and error to be 0.5 and 2.5 for this study. These values provide better convergence for the optimisation problems presented in this thesis.

3.4.4.1 Velocity Control

One of the earliest issues with the basic PSO was the swarm explosion effect. Different remedies to this problem have been suggested [27, 56, 59]. In this study the velocity clamping method is used to overcome this issue. For this purpose a maximum value of the velocity $V_{max}^{p_v}$ is set for each variable v in a particle p depending on its dynamic limits. The pseudocode is provided below in Algorithm 3.4.1.

In case of overshoot in variable velocity value in any dimension the Algorithm 3.4.1 is used to set the variable velocity value to its defined maximum.

3.4.5 Position Update

The calculated velocity is then used to determine the new position of the particle in solution space. The mathematical expression is be given as;

$$x_p^{g+1} = x_p^g + \Delta t \cdot v_p^g \tag{3.5}$$

Where x_p is the position vector in one dimension. Since this study concerns a two dimensional problem therefore position vector was determined for both dimensions r and α. Generally Δt is taken as 1 in Equation 3.5.

```
Algorithm 3.4.1: VELOCITY CONTROL($V_{max}^{ph_v}, v_{ph}^{g+1}$)

if $|v_{ph}^{g+1}| > V_{max}^{ph_v}$
  do for $h \leftarrow 1$ to 2
    do
      if $v_{ph}^{g+1} < 0$
        do
          $v_{ph}^{g+1} = -V_{max}^{ph_v}$
          else
          $v_{ph}^{g+1} = V_{max}^{ph_v}$
return ($v_{ph}^{g+1}$)
```

3.4.6 Fitness Function Evaluation

Particles with the updated positions are then used to evaluate the fitness function. In this study each particle in r and α dimension together is used to indicate the candidate optimum root locations. These roots are then used to find out the coefficients of the Equation 2.20. The coefficient values are then substituted into the Equation 2.20 to obtain the resulted pattern. This pattern is evaluated against the desired criteria in terms of root mean square error (in most cases for this study). The pattern evaluation details and different fitness functions used for this study will be provided for the discussed examples in corresponding sections.

3.4.7 Boundary Conditions

In order to constrain the variables within the defined boundaries the V_{max} check and the inertial weight are not sufficient. To obtain faster convergence it is important to implement boundary conditions. There are three commonly implemented boundary conditions namely *absorbing boundary*, *reflection boundary* and *invisible boundary* [56,60]. When a particle hits the absorbing boundary it losses its velocity (set to zero) and eventually pulled back to the solution space. The invisible boundary allows the particles to fly without any physical restriction. Once the particle is outside the defined bounds its fitness evaluation is not considered to determine the *pbest* and *gbest* until it moves back to the solution space. These two boundary conditions result in less diversity and limits the global search. Therefore for this study reflection boundary condition is implemented.

With reflection boundaries each particle that has an impact with the boundary gets its velocity reversed in sign and halved in magnitude and the particle stays in the solution space. This provides the opportunity of utilizing all the defined particles to search the solution space effectively.

3.4.8 Termination Criteria

Various solution search termination criteria have been reported in literature. For this study the termination criteria was set to the number of iterations. The number of iterations vary for various antenna pattern synthesis problems presented here. Further details will be given in the respective sections.

In next section comparative algorithm model is presented that is used to compare the performance of the proposed techniques and algorithms.

3.5 Comparative Algorithm Model

In order to compare the optimisation performance for certain examples Genetic Algorithm (GA) [28] is used as the comparative model. The comparison is made in terms of number of computations required to converge, consistency to achieve an optimum solution and the goodness of the optimum solution. Performance of two PSO variants (UoM-PSO,IzBC-PSO) developed in this research work are compared with the GA. The GA model available with *MATLAB Optimisation Toolbox* is used for this purpose with the default settings for all parameters except number of iterations (generations). There are three major operations involve in GA implementation including fitness function evaluation, gene pool formation and recombination and mutation, details can be found in [29]. It is not the intention of this section to describe and discuss the GA implementation in general, however, the specific GA model used in this study is described.

In order to initialise the optimisation process a random population of 20 individuals is considered. These individuals are used to evaluate the fitness function and are ranked based on the goodness of their fitness evaluation [89]. All the following details are taken from the MATLAB documentation [89]. Based on these ranks parents are selected for the next generation (iteration). The selection criteria is set on Stochastic uniform method. For reproduction in the next generation elite count is set to 2 which ensures the survival of these individuals. The crossover fraction is set to 0.8. To perform the mutation (to make random small changes in the individuals) random numbers from the Gaussian distribution centred at zero are taken. Next step is to perform crossover and generate new individuals. The crossover function used by default is Scattered. It creates randomly a binary vector of the same length as individuals and selects genes from first parent where the vector is 1 and from the second parent where it is 0. With these default settings the GA was used for this study as a comparative algorithm.

3.6 Chapter Summary

This chapter describes the implemented version of PSO used for this research. The PSO with boundary conditions described in this chapter is termed as UoM-PSO. Important components of the algorithm are presented as they are implemented. A description of the comparative algorithm is also presented.

Chapter 4

Intelligent Z-space Boundary Conditions

4.1 Introduction

In this chapter intelligent boundary conditions will be described. This systematic modification to the solution space in z-space (unit circle) has been developed for this research study. The unit circle presentation of the pattern nulls gives an opportunity to modify the pattern by manipulating the root locations. For various array pattern synthesis problems the unit circle approach in conjunction with the UoM-PSO have been presented [42–44]. After studying the null behaviour in z-space it was decided to develop a technique that will enable defining the solution space intelligently so that the required goals could be achieved with the reduced computations of the fitness function. Once the optimisation starts, the boundaries in solution space are re-evaluated, if for a certain number of iterations, no improvement is found in fitness evaluation.

4.2 Initialisation

To initialise this technique a desired FNBW of the sum pattern was defined. For example, consider a linear array with $N = 8$, uniformly separated with half wavelength spacing. The FNBW was defined to be 50^o with $FNBW_1 = 25^o$ and $FNBW_2 = -25^o$. The polynomial given by the Equation 2.17 in section 2.7 was solved for its roots. Once the roots are obtained they are placed in the z-space as shown in Figure 4.1. The value of the required FNBW defined for the pattern in the θ space was mapped to the z-space. This mapping resulted in the displacement of the roots marked as 1 and 7 in Figure 4.1. For root location 1 using $z = e^{(jkd\sin\theta)}$ for $d = 0.5\lambda$ and $k = 2\pi/\lambda$ from section 2.7, $z_1 = e^{(jkd\sin(FNBW_1))} = 0.24 + 0.97j$ is plotted in Figure 4.1. Similarly the root location 7 was determined as $z_7 = e^{(jkd\sin(FNBW_2))} = 0.24 - 0.97j$, indicated in Figure 4.1.

These modified root locations were then used to determine the element excitations (polynomial coefficients). The Equation 2.17 is used to plot the array pattern with the modified FNBW as shown in Figure 4.2.

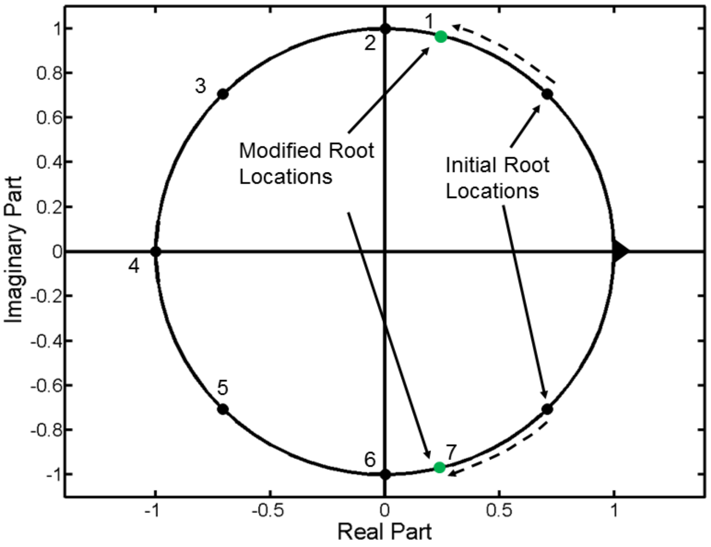

Figure 4.1: The root locations are shown in Black for the uniformly excited array. The modified root locations are marked in Green to setup a defined FNBW. The main beam pointing direction is marked by black triangle.

4.3 Defining Boundaries

In z-space the modified locations of the root 1 and root 7 were locked in α dimension but not in r. That resulted in the 12 variables to optimized in order to obtain a desired pattern instead of 14 as was the case with UoM-PSO with the boundary conditions defined in chapter 3. Before assigning the boundaries in α dimension it was made sure that the α boundaries of roots 2 and 6 do not fall between roots 1 and 7. The arrangement ensured that the particles (containing

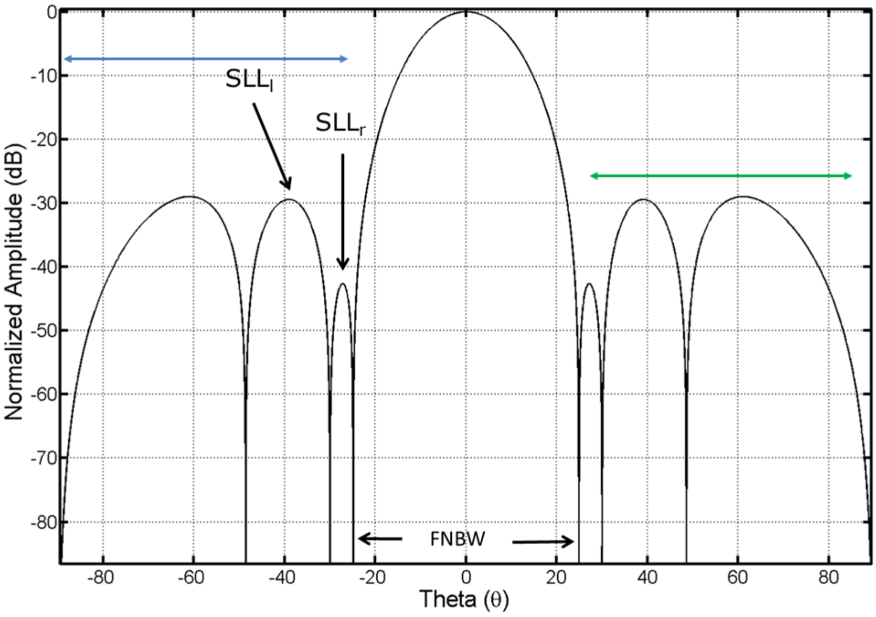

Figure 4.2: Linear array pattern obtained from the modified root locations as given in the Figure 4.3. The FNBW in θ space has been obtained as desired. The pattern regions marked with the Green and the Blue lines shows the sensitivity to the z-space

5 variables in α dimension) stayed in the intelligently defined solution space. The methodology adapted to determine the bounds in α dimension is described below.

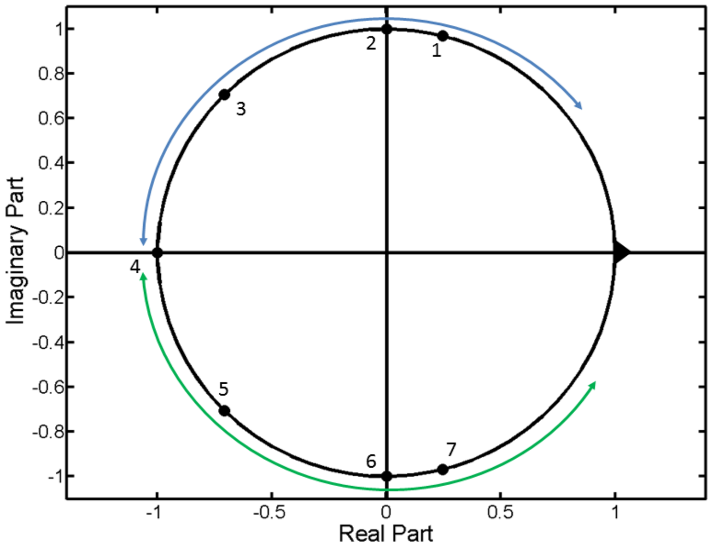

Figure 4.3: Modified root locations with the colored lines highlighting the corresponding roots in θ space

4.3.1 α Bound

In order to define the tentative effective solution space for the variables array pattern in θ space is compared with the target mask. Figures 4.2 and 4.3 show the mapping of the pattern in θ space to the z-space. The consecutive SLLs are compared to determine the bounds on the intermediate root location variable. The variable movement is restricted such as either its upper bound or lower bound was set to its current position depending on the SLL difference signature. If the current variable location is given as α_m for the m^{th} variable and the surrounding SLL peaks as SLL_r and SLL_l marked in Figure 4.2, a pseudocode is used to clarify the process.

Algorithm 4.3.1: α BOUND($\alpha_m, SLL_r, SLL_l, \alpha\_upper\_bound, \alpha\_lower\_bound$)

```
for $m \leftarrow 1$ to $N - 3$
    do
        if $SLL_r - SLL_l < 0$
            do
                $(\alpha\_upper\_bound)_m = \alpha_m + bound\_allowance$
                $(\alpha\_lower\_bound)_m = \alpha_m$
            else
                $(\alpha\_upper\_bound)_m = \alpha_m$
                $(\alpha\_lower\_bound)_m = \alpha_m - bound\_allowance$
return $(\alpha\_upper\_bound, \alpha\_lower\_bound)$
```

Where $(\alpha\_upper\_bound)_m$ and $(\alpha\_lower\_bound)_m$ are the upper and the lower bound values for the m^{th} variable α_m and *bound_allowance* is the allowed span for the variable roaming. In this thesis the used value for the *bound_allowance* is 20% of the $\frac{360^o}{N-1}$.

It is obvious from Figure 4.2 that in order to reduce SLL_l the pattern null in between SLL_r and SLL_l should move to the left. This particular pattern null is indicated as root 2 in Figure 4.3. Its current position in α is set as the lower α bound i.e. α_2. The upper α bound for this root is set to $\alpha_2 + bound\_allowance$. This setting restricts the root's (variable) search in α dimension and increases the chances of finding a best solution in reduced number of computations significantly.

4.3.2 r Bound

The bound on r is defined the same way as before in chapter 3. The r bound is uniform of all the variables in r dimension. The Figure 3.3 shows the r bound on the unit circle.

4.4 Redefining α Boundaries

In order to get to the convergence point in reduced number of iterations it is found beneficent to revisit the Algorithm 4.3.1 while optimiser is running. The fitness values of the best particle is observed for $0.05 \cdot ite$, where *ite* is the total number of iterations, and if there is no other particle with better fitness evaluation then the Algorithm 4.3.1 is called. This resulted in convergence to the minimum value of the fitness function evaluations as shown in coming chapter 5.

4.5 Generalising Intelligent z-Space Boundaries

The technique described in section 4.2 considers an array of isotropic elements and can be generalised to any linear periodic array of non isotropic elements. The initial requirement is to define the FNBW for the desired pattern and then transform it to the z-space. In case of isotropic array the solution of Equation 2.17 gives the roots in z-space and can be modified to reflect that FNBW requirement. But for the non isotropic elements considered in this study the mutual coupling results in a radiation pattern that can not be represented by the roots shown in Figure 4.1 accurately.

A MATLAB code is developed as a part of this study to determine a relationship between the FNBW in θ-space and root locations 1 and 7 in z-space by simultaneously considering the θ and z spaces. The initial root locations for any broadside array would be taken as shown in Figure 4.1. The accurate mapping of the FNBW is achieved. All other root locations are left unaltered at this step. During defining the boundaries for α the roots are adjusted as described in section 4.3.1.

4.6 IzBC-PSO

The basic PSO model developed in chapter 3 is used and no parametric changes are made. The boundary conditions defined in chapter 3 are associated with UoM-PSO model. The intelligent boundary conditions described in this chapter are associated with PSO and the complete setup is called IzBC-PSO (Intelligent z-space Boundary Conditions-Particle Swarm Optimiser). The use of intelligent technique reduce the number of variable to optimise and significantly improve the convergence performance. The IzBC-PSO model is compared with UoM-PSO and GA optimisers described in chapter 3 and comparison results are presented in chapter 5. The details of IzBC-PSO implementation will be covered in respective chapters. A flowchart summarising all main steps involved in implementing the proposed technique is shown in Figure 4.4.

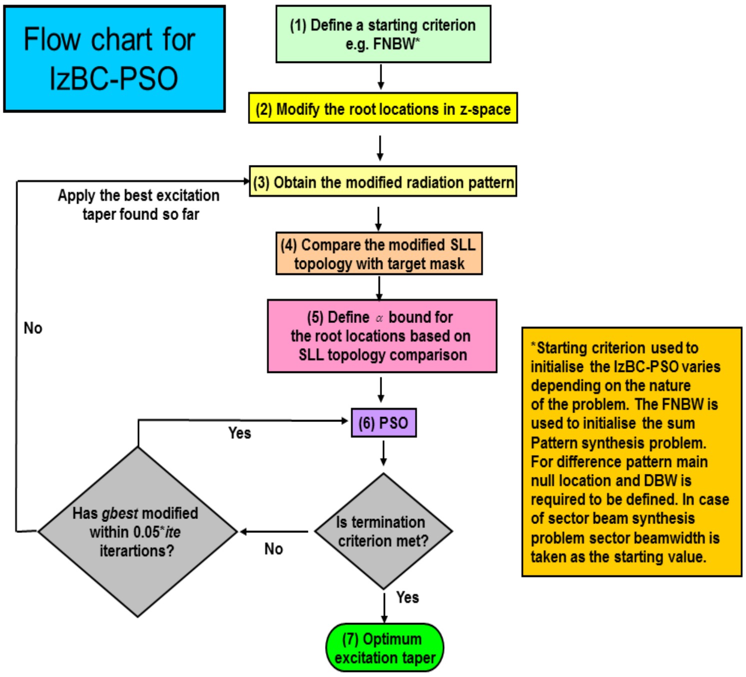

Figure 4.4: Flowchart depicting the process of defining the IzBC and merging with PSO

4.7 Chapter Summary

A novel technique is described in this chapter based on Schelkunoff's unit circle approach for small array pattern synthesis. This intelligent technique defines the problem boundaries for itself based on the SLL topology in θ-space and the root locations in z-space. These boundaries can be updated if no improvement is noted in fitness function evaluation by revisiting the SLL topology in θ-space while optimisation process is running. It is shown that this technique can be easily generalised to arrays of any non isotropic elements.

Chapter 5

Narrow Band Pattern Synthesis

5.1 Introduction

In this chapter the pattern synthesis for narrow beam sum and difference patterns is presented based on the UoM-PSO model and with the proposed z-space (solution space) modifications described in chapters 3 and 4. The array model used in this chapter is based on the BDRA as described in the chapter 2 section 2.11. The small antenna arrays suffer from the effects of edge elements and the finite ground plane in addition to the mutual coupling. Therefore it is critical to model the antenna array accurately in order to propose a practical solution to the pattern synthesis problem. The pattern synthesis problem considered in this chapter is the low SLL for a given FNBW. This problem is treated by the conventional techniques proposed by C. Dolph [6] and the T. T. Taylor [7]. These widely used techniques do not consider the practical array environment and therefore require pattern correction in the presence of mutual coupling.

In order to compensate for the mutual coupling in the array model Kang et al. presented characteristic mode and point matching techniques [15]. A dipole array with eight elements was modelled by the MoM to find the coupling matrix. The characteristic mode method involves matrix inversion and it is dependent on the scan direction due to multimode elements. The point matching technique has a limitation of the number of elements in the array. Another approach for the compensation was proposed by Steyskal et al. [16]. The solution was proposed for the single mode elements. The drawback of this technique was that one has to know the isolated element pattern in order to find the coupling coefficients. Since this technique requires evaluating the Fourier integral, therefore there must be no null in the isolated element pattern over the integration limit. The advantage of this technique was also limited by the spacing between the elements as it should be greater then $\frac{\lambda}{2}$ to keep the integration limits within the visible range. The alternate technique for the spacings less then $\frac{\lambda}{2}$ suffered from the lack of accuracy [16]. It was shown by Gupta et al. that in case of small arrays and in the presence of structure scattering the coupling matrix concept may not be useful [13]. The result was based on the measured and simulated data obtained from the experiments performed over the dipole arrays. Therefore the techniques based on the active element patterns are considered more practical in small arrays.

A more accurate and realistic model of the antenna array was proposed by Kelley and Stutzman [17]. They investigated the antenna array radiation pattern synthesis while using various element patterns to include the effect of coupling and structural non linearity (edge element and finite ground plane effect etc). It was shown that for small arrays the hybrid active element pattern or embedded element pattern would not be suitable. The results presented in the chapter 2 section 2.11.2 for the BDRA array agreed with the published literature. A compensation approach based on the active element patterns was presented by Fletcher et al. [18]. In order to overcome the pattern corruption a point matching technique was proposed. This technique is always limited because of the number of elements in the array and the number of samples required to model the accurate far field pattern. To use this technique maximum samples could not exceed the number of elements in the array. The method adopted in [18] took the pattern nulls and the broadside of the far field pattern as the sampling points. Partial but not complete control over the SLLs was obtained by following this technique. Therefore this technique was only useful to obtain the Chebychev patterns within some error and was not accurate for the scanned patterns or sector beam synthesis. Another approach based on the active element patterns for a linear array of patch antenna was implemented by Salonen et al. [19].

Evolutionary optimisation techniques have been used to compensate for the coupling effect.The differential evolutionary algorithm is used for the optimisation of the antenna array pattern by Yang et al. [90]. The optimisation results were presented for a linear array of sixteen dipole elements and it was shown that the coupling effect were successfully compensated for narrow band. Also active element pattern and PSO are used to compensate for mutual coupling [91].

The goal in this chapter is to show that the proposed optimisation technique has improved the array radiation pattern performance in the presence of mutual coupling for both sum and difference patterns. Also the improvement is shown over the limitations of conventional techniques for sum and difference patterns discussed in chapter 1. Furthermore for monopulse array a single feed is obtained using the proposed optimisation that satisfies the target sum and difference patterns and requires phase only modification.

5.2 Sum Pattern Synthesis

In this section the mutual coupling compensation in small linear periodic arrays is presented. In practical arrays the Dolph-Chebychev taper is affected by the mutual coupling. For the element spacing $d < \lambda/2$ as in this case Dolph-Chebychev does not give the optimum results [72]. An optimum solution in terms of the weight vector is presented to compensate for the pattern errors. Three independent optimization models consisting of IzBC-PSO, UoM-PSO and GA are compared for the optimization problems presented in this chapter.

5.2.1 Problem Setup

An array consisting of eight bowtie dielectric resonator antennas (BDRAs) is considered as described in chapter 2 section 2.11. The separation between the elements is $d = 0.41\lambda$ at $4.5GHz$ resulting in the array length 2.87λ. The array radiation pattern is obtained using the active element patterns determined by the *CST-MWS* as described in chapter 2 section 2.11. The goal in this section is to obtain a $-30dB$ Dolph-Chebychev pattern with this BDRA array. The other objectives are to improve gain and the dynamic range ratio ($DRR = max(|w_n|)/min(|w_n|)$) in the presence of BDRA array coupling. In order to obtain lower SLLs an excitation taper is applied across the array. The taper has the maximum excitation level at the centre and the minimum levels at the corners. This resulted in high dynamic range ratio (DRR), which means that the corner element excitations are more vulnerable to pattern errors (mutual coupling, edge effects, ground plane effect etc). Therefore it is important to get lower SLLs by applying a taper of lower DRR. The Dolph-Chebychev taper has high DRR as will be shown in the next section 5.2.3. For this reason DRR is added to the fitness function for this problem.

It is assumed that the main beam is directed to $\theta = 0$ and no scanning is involved. The θ-space to z-space transformation was performed as described in the section 4.5 of the chapter 4 for initialising IzBC-PSO. In z-space the general boundaries for the seven root locations are defined to implement UoM-PSO based solution as described in the section 3.4.2 of the chapter 3. For the GA the z-space boundaries are taken same as UoM-PSO. In order to compare the performance of the three optimisers the fitness function computations were taken as criterion.

The swarm size is taken as 30 and the number of iterations was chosen to be 300 for UoM-PSO and the IzBC-PSO resulting 9000 fitness function evaluations. In case of the GA since default population size of 20 is used therefore to maintain the 9000 computations the number of iterations is taken as 450.

The fitness function used for this optimization problem is given by;

$$\begin{aligned} fitness &= [\varsigma_1(SLL_{des} - SLL_{patt})^2 + \varsigma_2(FNBW_{des} - FNBW_{patt})^2 + \\ &\quad + \varsigma_3(DRR_{patt})^2 + \varsigma_4(Gain_{patt} - Gain_{iso})^2]^{1/2} \end{aligned}$$

Where

ς_1, ς_2, ς_3 and ς_4 are the weighting multipliers

SLL_{des} = desired (target) SLL, -30dB

SLL_{patt} = obtained SLL in dB, max($patt(\theta')$)

θ' = excludes the radiation pattern between the two first nulls

$FNBW_{des}$ = desired (target) first null beamwidth of the target radiation pattern in degrees

$FNBW_{patt}$ = obtained first null beamwidth of the computed radiation pattern in degrees

DRR_{patt} = Dynamic range ratio of the obtained set of weights

$Gain_{patt} = (\frac{(\sum_n w_n)^2}{\sum_n (w_n)^2})$, an approximation for the obtained set of weights as the array is not half wavelength separated

$Gain_{iso}$ = The gain of isotropic array with $N = 8$

It is a multi-objective fitness function that is solved as a single objective problem. The values of the multipliers (ς_1, ς_2, ς_3, ς_4) are carefully found by trail and error procedure such that all the objectives have same significance. For this purpose the values for all the weighting multipliers are set to 1 in the fitness function and the numeric range is recorded for all objectives individually. Once the numeric variation in objective values is known the multiplier values are set to keep all the objective in the same numeric range as of a single objective value. The goal of this optimisation problem is to obtain the target PSLL ($SLL_{des} = -30dB$) for a desired FNBW while maximising the gain of the array and minimising the dynamic range ratio in order to minimise the fitness function value. The target gain was the one obtained for the isotropic array with $N = 8$. The desired FNBW was set to 52^o. Table 5.1 summarises the parameter values set for the optimization algorithms. The boundary conditions used for the UoM-PSO and the GA are the same.

In case of IzBC-PSO the fitness function reduces to;

$$\begin{aligned} fitness = {} & [\varsigma_1(SLL_{des} - SLL_{patt})^2 + \\ & + \varsigma_3(DRR_{patt})^2 + \varsigma_4(Gain_{patt} - Gain_{iso})^2]^{1/2} \end{aligned} \tag{5.1}$$

Where all terms have their all ready defined meanings. It is evident that IzBC-PSO simplifies the fitness function as setting a desired FNBW is the part of its initialisation process.

Optimiser	Population Size	Number of Iterations	Number of Computations
UoM-PSO	30	300	9000
IzBC-PSO	30	300	9000
GA	20	450	9000

Table 5.1: Tabular summary of the optimisers parameters

5.2.2 PSO Stability

The stability of PSO has been studied and various models have been proposed for the particle motion in solution space [27]:chapter-3. The core behaviour of a single particle is examined by J. Kennedy [92] to address the questions related to the particle trajectories in solution space, optimal parameter values and velocity explosion issue. The effect of the cognitive multipliers (γ_1, γ_2 in Equation 3.1) over the particle trajectory is examined and an artificial limit over the velocity value is suggested to overcome the explosion issue. The optimiser stability study is presented in [59]. The heuristic model is simplified to a deterministic model with constant parameter values. Further details of the stability studies are given in [27]. It is important to note that the study models are simplified to deterministic model and does not represent the heuristic nature of the algorithm. A stability analysis for a stochastic particle model is presented by V. Kadirkamanathan [93]. The stability of the optimiser is studied in conjunction with the parameter value variations. The bounds on the parameter values defined by [27,59] are confirmed by the dynamic model.

The parameter values chosen for this research work are taken according to the guidelines given in [56] to maintain the stability of the optimisation process and no unstable behaviour is observed.

5.2.3 Results & Discussion

In Figure 5.1 the isotropic, isolated BDRA, and the BDRA array radiation patterns are compared for $-30dB$ Dolph-Chebychev taper.

The isotropic array radiation pattern exhibited $-30dB$ PSLL and $-30.9dB$ average SLL for a FNBW of 57^o. The radiation pattern obtained for the isolated BDRA array did not include the mutual coupling effect and other array pattern errors. The PSLL obtained was $-31.9dB$ with the average SLL of $-37.4dB$ for the FNBW of 57^o. The BDRA array radiation pattern included the mutual coupling and other array pattern errors. The effect of the pattern errors resulted in the divergence from the ideal Dolph-Chebychev radiation pattern. The PSLL was $-32dB$ with the average SLL of $-34.2dB$ for the FNBW of 57^o. The results are summarised in Table 5.2.

Figure 5.2 shows the optimised array radiation patterns in the presence of pattern errors. The comparison was made to judge the performance of the

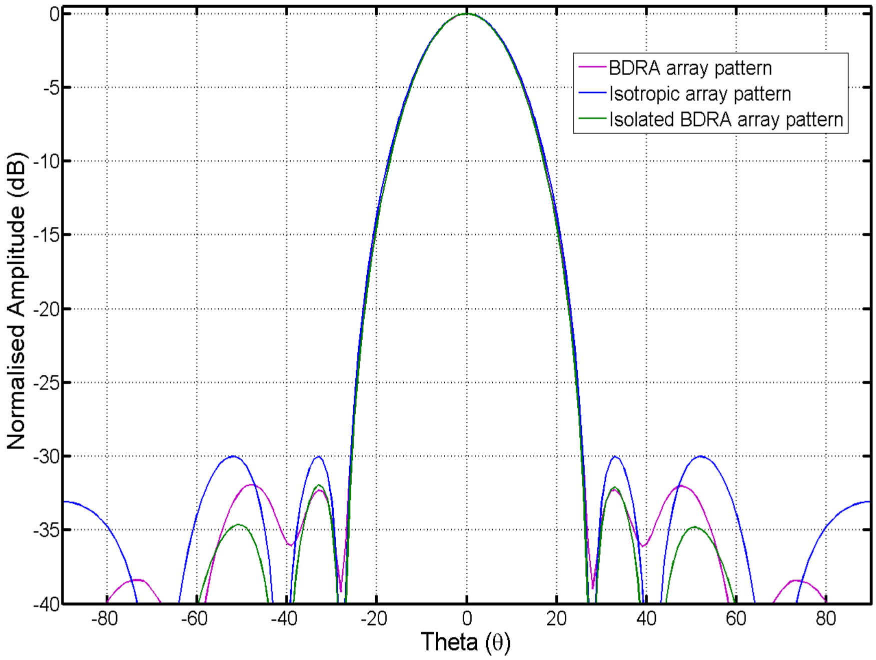

Figure 5.1: Farfield patterns obtained for the isotropic array, BDRA array and the isolated BDRA array while the Chebychev taper of -30dB SLL was applied

Array Type	PSLL (dB)	Gain (dBi)
Isotropic Element	-30	7.6
Isolated BDRA	-31.9	13.6
Coupled BDRA	-32	11.9

Table 5.2: Tabular summary of the Figure 5.1

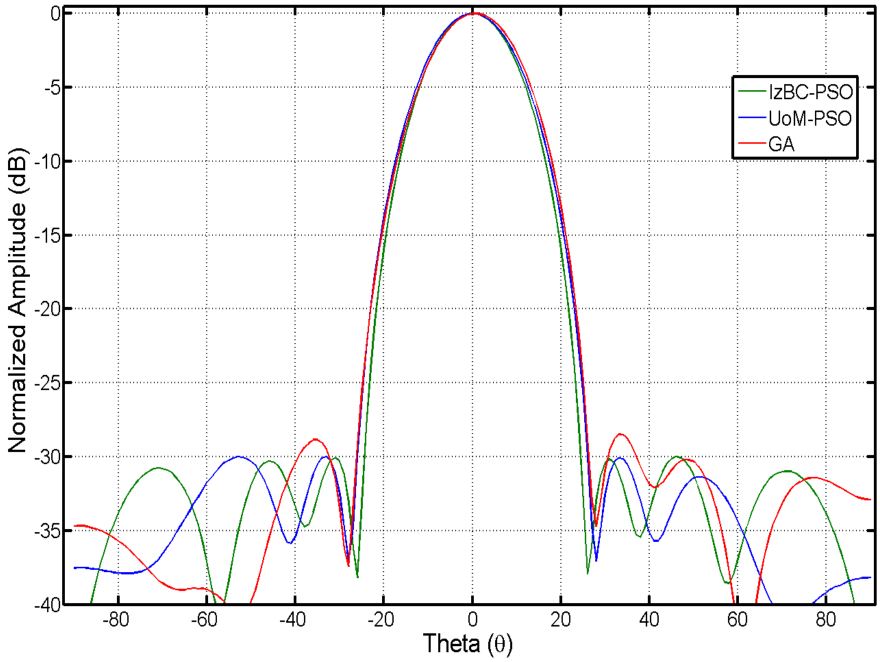

Figure 5.2: Optimised radiation patterns obtained by UoM-PSO, IzBC-PSO and GA

three optimisation techniques used in this study. As described in the previous section that the optimisation problem involved multiple objectives. The effect of coupling in the case presented resulted in the lower PSLL then desired. The objective is to improve the gain and DRR while achieving the target PSLL. The best result obtained out of 10 trials using the IzBC-PSO and the UoM-PSO (shown in Figure 5.2) were meeting the PSLL criterion. However the best out of 10 trials of GA was unable to meet the PSLL within the 9000 fitness function evaluation limit. The PSLL for the GA best solution (in 10 trials) was found to be -28.5. The results are summarised in Table 5.3.

Optimiser Used	PSLL (dB)	Gain (dBi)
IzBC-PSO	-30	12.2
UoM-PSO	-30	11.8
GA	-28.5	11.9

Table 5.3: Tabular summary of Figure 5.2

The results associated with the array weights shown in the Table 5.5 for the objectives defined in the Equation 5.1 are presented in the Table 5.4.

Array Excitation	PSLL (dB)	Gain (dBi)	FNBW (Deg)	DRR
Dolph-Chebychev	−32	11.9	57	3.8
IzBC-PSO	−30	12.2	52	3.1
UoM-PSO	−30	11.8	57	4.3
GA	−28.5	11.9	57	4.8

Table 5.4: Comparison of the optimisation objectives for BDRA array radiation pattern

It is shown that the optimum performance that can be achieved by Dolph-Chebychev for an array with $d = \lambda/2$ is obtained for $d < \lambda/2$ by using the proposed technique.

The IzBC-PSO outperformed the UoM-PSO and the GA in achieving the objectives. The array gain obtained with the IzBC-PSO showed improvement by 2.5% over the Dolph-Chebychev taper. The dynamic range ratio was improved by 22.6% with the IzBC-PSO whereas the UoM-PSO and the GA resulted in the worse values as compared to the Dolph-Chebychev taper. The IzBC-PSO showed the optimum results for the problem at hand. It provided the set of weights that resulted in better gain, reduced DRR, reduced FNBW (9.6% as compared to Dolph-Chebychev) and meeting the target PSLL.

Dolph-Chebychev		IzBC-PSO		UoM-PSO		GA	
Amp	Phase (Deg)	Amp	Phase (Deg)	Amp	Phase (Deg)	Amp	Phase (Deg)
0.26	0	0.32	0	0.23	0	0.21	0
0.52	0	0.53	−2	0.54	0	0.47	24
0.81	0	0.84	−1	0.79	−1	0.80	17
1.00	0	0.98	−1	1.00	0	1.00	22
1.00	0	1.00	−1	1.00	−1	1.00	20
0.81	0	0.84	−1	0.78	−1	0.84	26
0.52	0	0.53	−2	0.54	−1	0.56	19
0.26	0	0.34	0	0.23	−1	0.27	30

Table 5.5: The excitation (weight) vectors used for the radiation plots shown in the Figure 5.1 and Figure 5.2

In order to compare the computational efficiency of the optimisers used for this study convergence curves were investigated as shown in the Figure 5.3

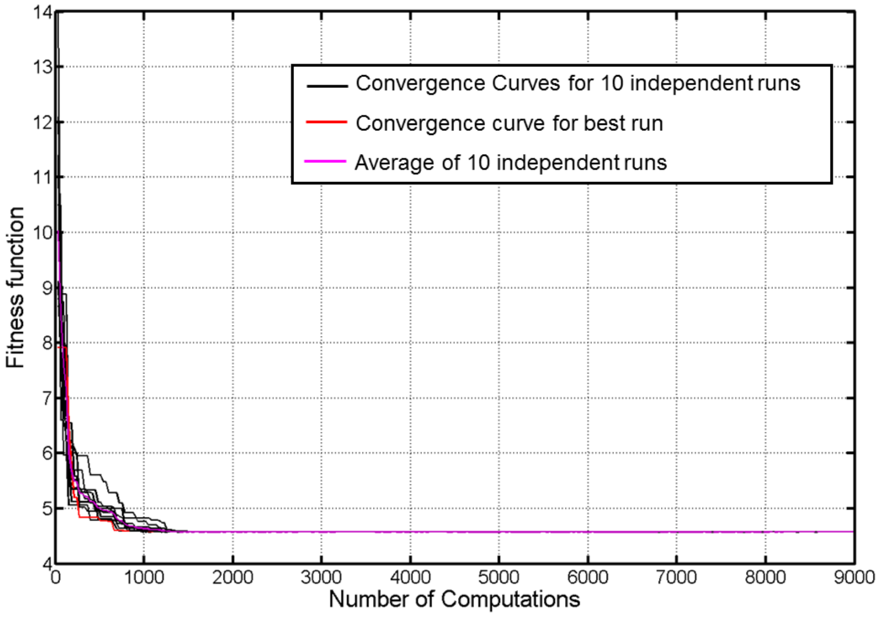

Figure 5.3: The convergence curves obtained for 10 trials of IzBC-PSO

to the Figure 5.6. Figure 5.3 shows the convergence curves for the 10 trials of the IzBC-PSO. The best convergence was achieved within 1050 fitness function evaluations. The worst convergence case took 1980 computations. On average 1260 fitness function evaluations were required to get to the optimum solution.

Figure 5.4 shows the convergence performance of the UoM-PSO. The best and the worse convergences were obtained in 1710 and 4410 fitness evaluations respectively. The average fitness function evaluations were found to be 3660 to get to the convergence. The IzBC-PSO showed improvement of 38.6% and 65.8% for the best and average convergence over UoM-PSO respectively.

In Figure 5.5 the convergence curves for the 10 trials of GA are shown. The best and the worst convergences took 6220 and 8760 fitness function evaluations. The average computations required to converge with the GA were found to be 6960. The IzBC-PSO showed the improvement of 83.1% and 85.7% for the best and the average convergence instances over the GA. Finally in Figure 5.6 a summary of comparison is presented for all three optimisers.

The array performance has significantly improved in the prrsnce of mutual coupling by using the proposed optimisation scheme. It is important to note the simplicity of the optimisation as only fitness function is used to define the objectives and no additional details are required to perform the optimisation. It

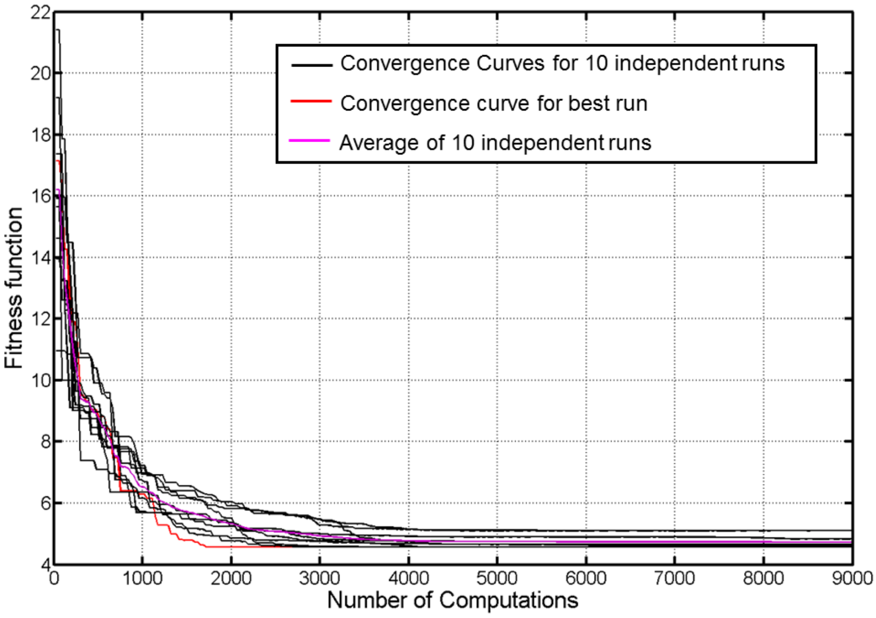

Figure 5.4: The convergence curves obtained for 10 trials of UoM-PSO

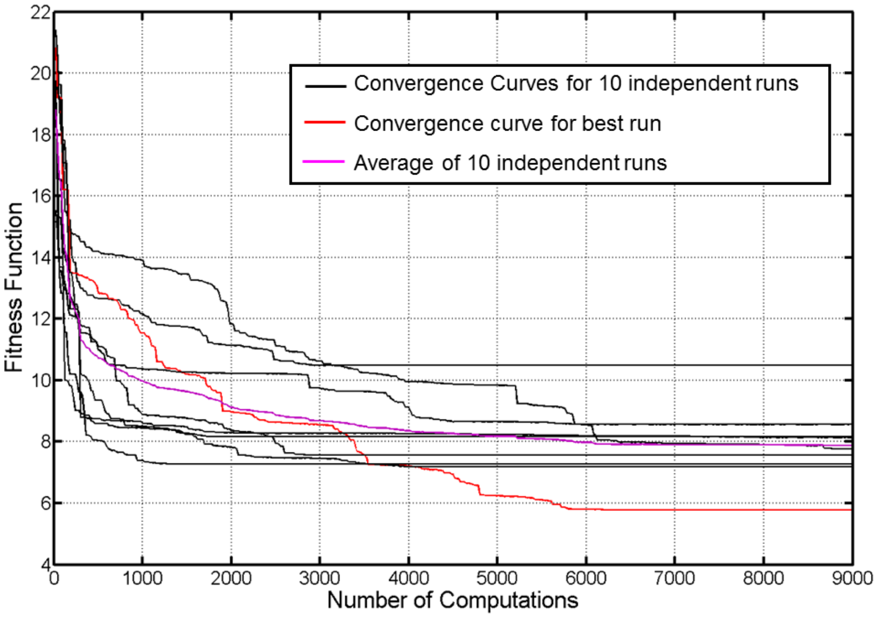

Figure 5.5: The convergence curves obtained for 10 trials of GA

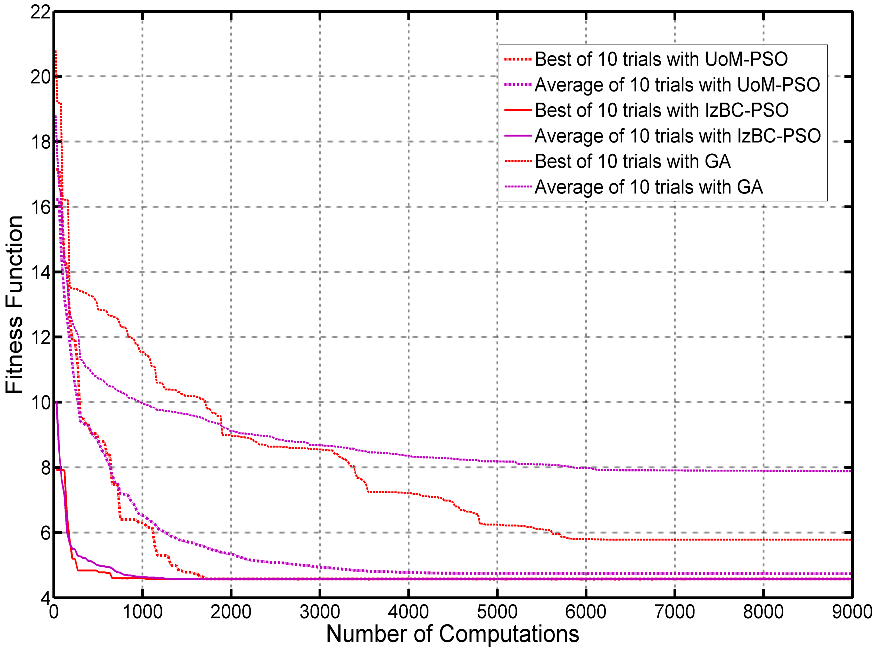

Figure 5.6: The comparison of the best and the average convergence curves obtained by UoM-PSO, IzBC-PSO and GA

is shown that the proposed IzBC-PSO outperformed the UoM-PSO and the GA in minimising the fitness function value and in terms of the fitness evaluation performance. Figures 5.3-5.4 show that IzBC-PSO is consistent in achieving the optimum solution. Whereas, UoM-PSO and GA lack in consistent optimum performce. This is a significant performance improvement in the optimisation by using the intelligent boundary conditions.

5.3 Scanning Array

In this section the array scanning is considered under the presence of mutual coupling. The coupling properties of the array varies as the main beam scans. This study is performed only for one scan direction ($\theta_o = 30^o$) to show the coupling effect over the Dolph-Chebychev weights, and the optimised weights determined in the last section for main beam scanned to $\theta_o = 0^o$. The main beam scanning is achieved by applying a progressive phase shift as described in chapter 2 section 2.6. The effect of beam broadening with scan [4] is studied under mutual coupling environment. The mainbeam gain reduces due to the pattern multiplication effect and the sidelobe levels are raised. The array scanning is also limited by the element pattern of the particular antenna and the impedance mismatch effect [3]:chapter 6.

This study is performed in two parts. In first part array scanning is performed for unity amplitude and progressive phase shift applied to BDRA array. The inherent beam broadening becomes worst in the presence of mutual coupling. The IzBC-PSO is used to improve the FNBW with array scanning. In second part of the study, tapered excitation amplitude is applied and then array is scanned. The array optimisation is performed by all three optimisers and the performance is compared.

5.3.1 Problem Setup

The same array of $N = 8$ BDRA elements is considered as described in section 5.2.1 of this chapter. For the first part of the problem the objective is to keep the same FNBW as with the main beam at $\theta_o = 0^o$. The unity amplitude progressive phase shift excitation as given in the Table 2.1 of chapter 2 section 2.6 is applied to the BDRA array. The fitness function used for this problem is given below;

$$fitness = [\varsigma_1(SLL_{des} - SLL_{patt})^2 + \varsigma_2(Scan_{des} - Scan_{patt})^2]^{1/2} \tag{5.2}$$

Where
$SLL_{des} = -20dB$
$Scan_{des} = 30^o$
$Scan_{patt}$ = the scan direction of the obtained radiation pattern

All other terms have the same meanings as described above. The FNBW is fixed to 36^o which is the FNBW of the BDRA array radiation pattern with main beam directed to $\theta_o = 0^o$ and the IzBC-PSO is used to reduce SLL while maintaining the scan direction. The fitness function weighting multipliers are set such that the objectives have the same significance. This problem is only solved by IzBC-PSO as the objective here is to show that the optimiser is suitable to improve the FNBW with reduced SLL while the main beam is scanned.

The second part of the problem involves the array scanning with the excitation weights given in Table 5.5. It is observed that the FNBW has increased because of the beam broadening effect of the scanning and the SLL has increased as well. The goal is to keep the FNBW same in case of $\theta_o = 30^o$ as in the case of $\theta_o = 0^o$. The other objective is to find out the excitation weight with low DRR and high gain. All three optimisers are used to achieve these targets. The fitness function used by the optimisers is given as;

$$\begin{aligned} fitness = [&\varsigma_1(SLL_{des} - SLL_{patt})^2 + \varsigma_2(FNBW_{des} - FNBW_{patt})^2 + \\ &\varsigma_3(Scan_{des} - Scan_{patt})^2 + \varsigma_4(DRR_{patt})^2 + \\ &\varsigma_5(Gain_{patt} - Gain_{iso})^2]^{1/2} \end{aligned} \tag{5.3}$$

Where
$SLL_{des} = -30dB$, to reduce the SLL for a given FNBW
$FNBW_{des} = 55^o$
$Scan_{des} = 30^o$

All other terms have the same meanings as described in the previous section. This is a multi objective fitness function and the weighting multipliers are set such that SLL performance has more significances then other objectives. The IzBC-PSO, the UoM-PSO and the GA settings are the same as given in Table 5.1. The simulated results and the comparisons are presented in the next section.

5.3.2 Results & Discussion

The Figure 5.7 compares the BDRA array radiation pattern and the optimised pattern. The BDRA array radiation pattern is obtained by applying the uniform amplitude and progressive phase, as given in Table 2.1, to the BDRA array. The FNBW for the BDRA array radiation pattern is found to be 36^o while main beam directs to $\theta_o = 0^o$ as described in the section 2.6 of chapter 2. The main beam is scanned to $\theta_o = 30^o$ and the beam broadening is observed as FNBW becomes 42^o. The IzBC-PSO is used to improve the FNBW while reducing the SLLs and maintaining the target scan direction. The fitness function given in Equation 5.2 is used for this optimisation problem.

The PSLL of the scanned BDRA array radiation pattern is found to be $-11.5dB$ with average SLL of $-15.8dB$. The optimised pattern has the PSLL of

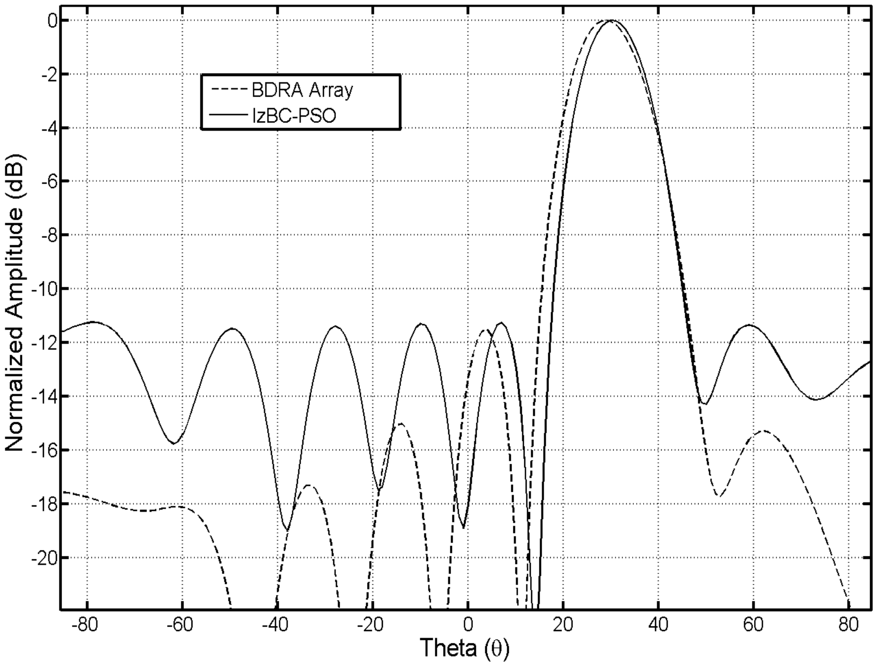

Figure 5.7: The array radiation plots for the BDRA array with the excitation vector given in Table 2.1 applied and the optimized excitation vector given in Table 5.7

Excitation Applied	PSLL (dB)	FNBW (Deg)	Gain (dBi)
Given in Table 2.1	-11.5	42^o	11.0
Optimized (IzBC-PSO) given in Table 5.7	-11.2	36^o	11.3

Table 5.6: Tabular summary of the Figure 5.7

$-11.2dB$ and the average SLL of $-11.3dB$ with FNBW of 36^o. The optimised weight vector is given in the Table 5.7. The results are summarised in the Table 5.6. The FNBW is improved by 14.3% using the IzBC-PSO. As the FNBW is reduced a 3% improvement in the array gain is observed as given in the Table 5.6. It is shown here that IzBC-PSO can be successfully used to counter the beam broadening effect of the array scanning.

IzBC-PSO Weight Vector	
Amplitude	Phase
0.7231	0
0.5908	177.8
0.3329	164.5
0.5882	−126.0
0.6206	−28.8
0.3040	49.7
0.4332	82.1
1	−158.0

Table 5.7: The optimised excitation (weight) vector used for the optimised array radiation plot in the Figure 5.7

The second part of the scanning problem involves the weight vectors given in the Table 5.5. As a starting point a linear progressive phase shift is applied, taking the element 1 as phase centre, to the optimised weights determined at broadside scan. The resultant scanned radiation patterns are shown in the Figure 5.8. The PSLL variation is tabulated in the Table 5.8.

Excitation Applied	PSLL (dB)	FNBW (Deg)	Gain (dBi)
Dolph-Chebychev	−18.0	73^o	10.8
IzBC-PSO	−18.4	67^o	10.7
UoM-PSO	−17.8	74^o	10.8
GA	−18.0	73^o	10.7

Table 5.8: Tabular summary of the Figure 5.8

The PSLL of $-18dB$ is obtained for the Dolph-Chebychev taper after scanning with FNBW of 73^o. The PSLL for IzBC-PSO, UoM-PSO and GA determined optimised weights are $-18.4dB$, $-17.8dB$ and $-18dB$ respectively. The

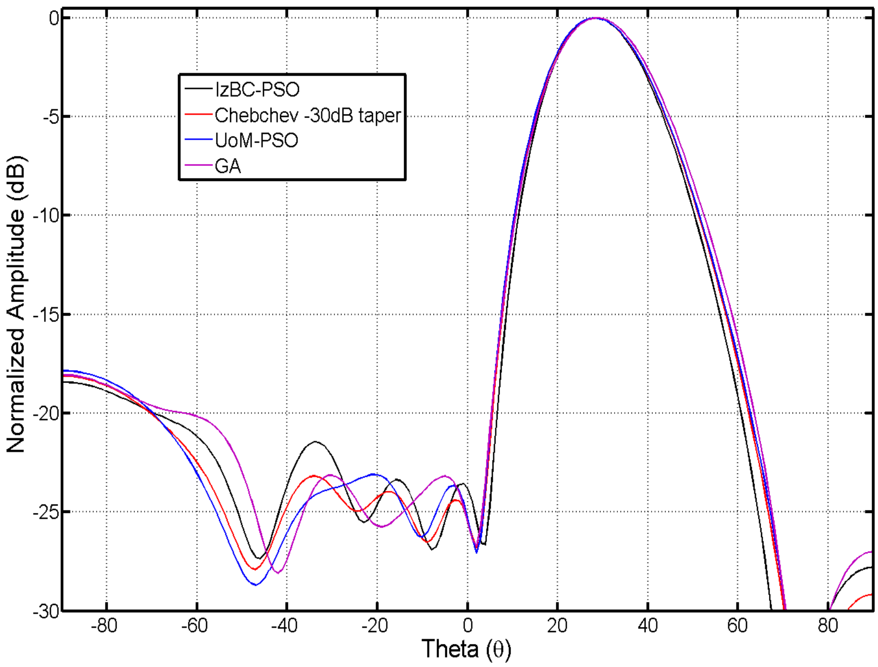

Figure 5.8: The array radiation patterns obtained by applying the progressive phase shift to the excitation vectors presented in the Table 5.5

worst beam broadening of 40% and SLL variation (compared to $30dB$ PSLL) of 40.7% are observed for the UoM-PSO determined optimised excitation vector. The IzBC-PSO determined optimised excitation vector resulted in 21.8% of beam broadening and 38.7% of SLL variation.

The goal is to restore the FNBW of the radiation pattern to 55^o the one obtained for main beam at $\theta_o = 0^o$. A re-optimisation is required in order to meet this goal. Obviously this results in the limitation on the PSLL therefore it can not be maintained at $-30dB$. This goal is achieved by applying the three optimisers while reducing the PSLL simultaneously. The reduced DRR, increased gain and maintaining the main beam scan direction are among the other objectives. The resultant optimised radiation patterns are shown in the Figure 5.9 for the best convergence achieved. A comparison of optimisation objectives is presented in the Table 5.9.

The PSLL obtained for the IzBC-PSO was found to be $-20dB$ for the target FNBW of 55^o and the scan direction of $\theta_o = 30^o$. The best UoM-PSO radiation pattern resulted in PSLL of $-19.3dB$ meeting the target FNBW and the scan direction requirement. The radiation pattern obtained for the GA excitation vector obtained after re-optimisation had PSLL of $-19.8dB$ for the required scan

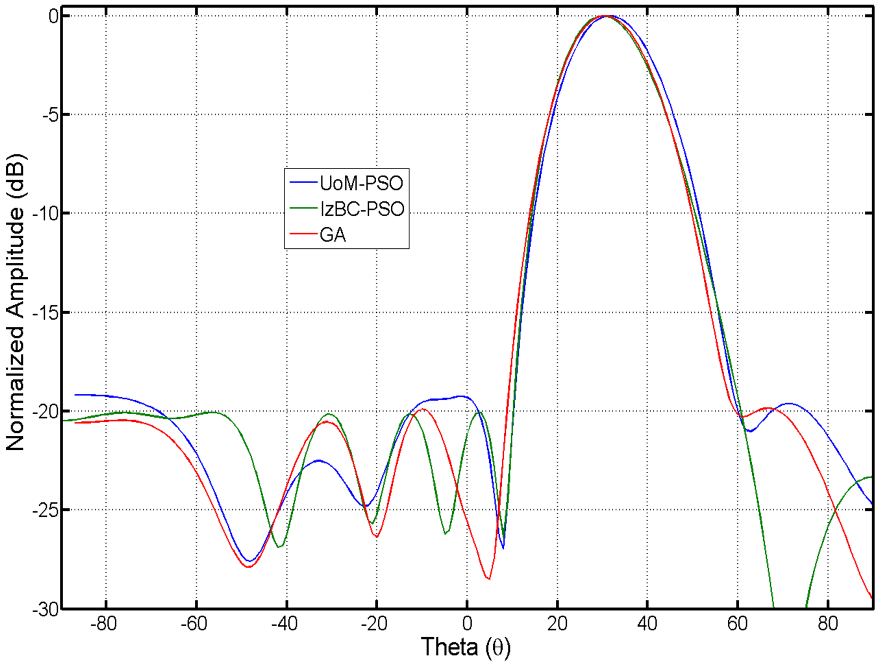

Figure 5.9: The optimised array radiation patterns plotted for the best convergence obtained by the respective optimiser

direction and the FNBW. The re-optimisation resulted in the improvement of the PSLL, FNBW and the array gain. The PSLL improvement in case of the IzBC-PSO was 8.7% for the improvement of 17.9% and 4% in FNBW and array gain respectively. The percentage improvement observed in the case of UoM-PSO for PSLL, FNBW and array gain were found to be 8.5%, 25.7% and 2% respectively. In the case of GA the optimised weight vector resulted in an improvement 10% in PSLL, 24.6% in FNBW and 5% in array gain.

Excitation Applied	PSLL (dB)	FNBW (Deg)	Gain (dBi)	DRR
IzBC-PSO	-20	55^o	11.1	2.2
UoM-PSO	-19.3	55^o	11.0	3.9
GA	-19.8	55^o	11.2	2.6

Table 5.9: Tabular summary of the Figure 5.9 and the summary of the problem objectives

The excitation weight vectors used for the radiation patterns shown in the Figure 5.9 are given in the Table 5.10. The IzBC-PSO resulted in the excitation vector with minimum DRR and the reduced PSLL among the three optimisers. The percentage improvement of 43.6% and 15.4% was found over UoM-PSO and GA DRR values respectively. The GA however offered the best array gain of 11.2*dB*.

IzBC-PSO Weight Vector		UoM-PSO Weight Vector		GA Weight Vector	
Amplitude	Phase (Deg)	Amplitude	Phase (Deg)	Amplitude	Phase (Deg)
0.45	0	0.26	0	0.39	0
0.51	75	0.49	81	0.50	86
0.83	147	0.84	168	0.79	162
1.00	−131	1.00	−122.0	1.00	−133
0.93	−51	0.85	−49	1.00	−64
0.78	18	0.87	17	0.92	−4
0.67	101	0.88	95	0.77	81
0.45	179	0.46	171	0.48	155

Table 5.10: The optimised excitation (weight) vector used for the optimised array radiation plots in the Figure 5.9

Figure 5.10 shows the convergence curves for 10 trials of the IzBC-PSO. The best convergence curve is marked in red color. The best convergence was achieved in 2910 fitness function evaluations whereas worst case took 6000. On average 3930 computations were required to achieve the convergence.

The convergence performance of UoM-PSO is shown in the Figure 5.11 for 10 trials. Th best and the worst convergence were achieved in 3570 and 6630 computations respectively. On average the total of 4560 fitness evaluation were required to converge.

Figure 5.12 shows the convergence performance of 10 trials of the GA. The best and worst convergence was achieved in 1360 and 4040 computation respectively. A total of 2120 fitness function evaluations were required on average. The Figure 5.13 summaries the convergence performance of the three optimisers used for this study as their best and average curves are shown. For this optimisation problem the GA has out performed the other optimisers for the best convergence performance. However GA was not consistent with its convergence as it was evident if a comparison of convergence span was considered. The convergence span is determined by the difference between minimum and maximum convergent values for a given optimiser′s convergence performance. In case of the IzBC-PSO and the UoM-PSO convergence span was 0.08 and 0.3 respectively. For the GA the convergence span was found

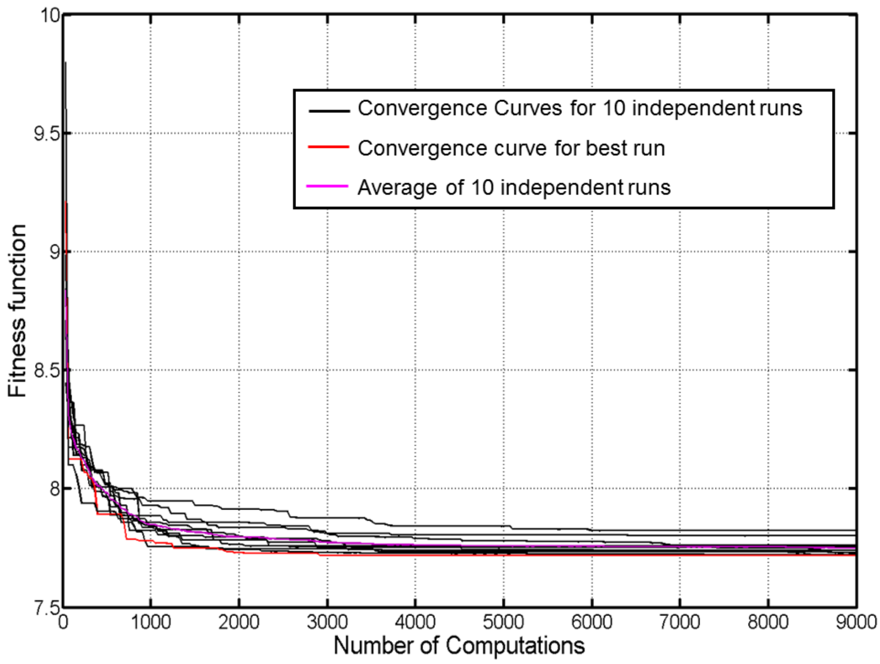

Figure 5.10: The convergence curves for the 10 trials with IzBC-PSO

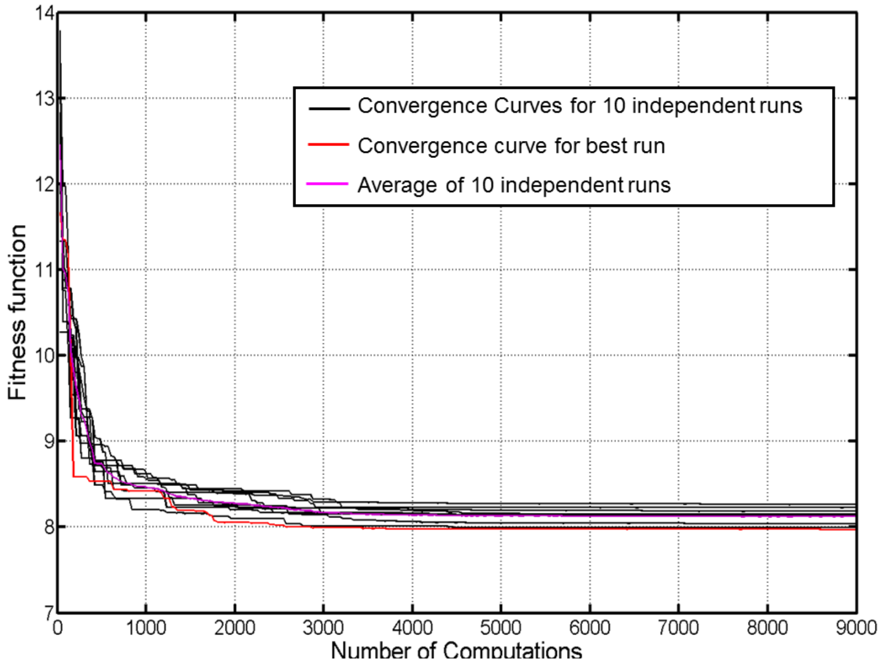

Figure 5.11: The comparison of the best and the average convergence curves obtained by UoM-PSO, IzBC-PSO and GA

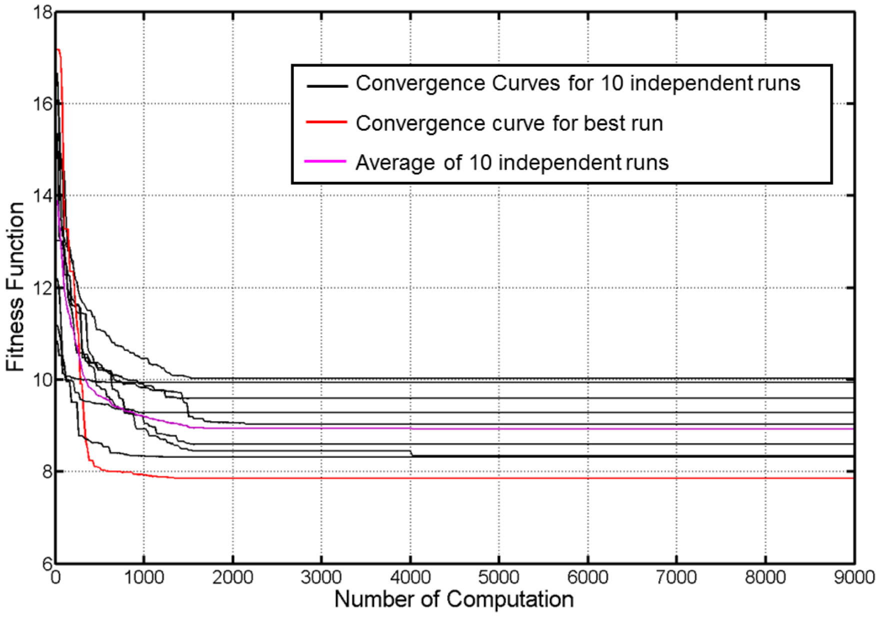

Figure 5.12: The comparison of the best and the average convergence curves obtained by UoM-PSO, IzBC-PSO and GA

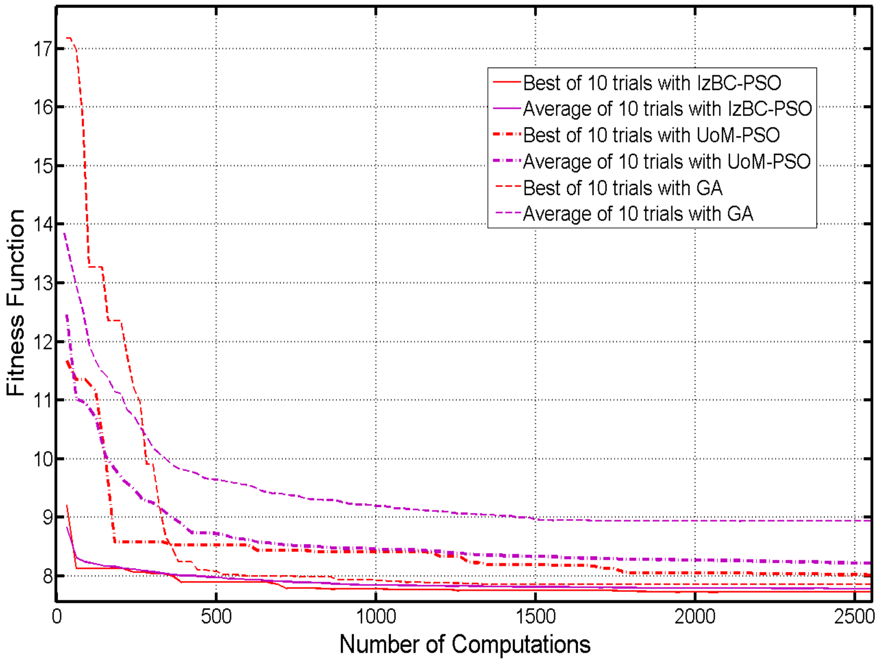

Figure 5.13: The comparison of the best and the average convergence curves obtained by UoM-PSO, IzBC-PSO and GA

to be 2.2. Therefore IzBC-PSO is more reliable as it has better convergence span performance compared to the UoM-PSO and the GA.

5.4 Taylor Taper Sampling Problem

The Dolph-Chebychev taper is defined for the discrete array therefore there is no sampling issue for small antenna arrays with $d > \lambda/2$. Since Taylor distribution is defined for a continuous line source therefore it is required to be sampled far a discrete array. The conventional sampling method that samples the Taylor distribution over the aperture at discrete points separated as the inter element spacings produces satisfactory results for large arrays. But as the number of elements are reduced and less samples are available it is not possible to achieve the ideal Taylor pattern. The root matching technique improves over the conventional sampling method for small arrays [4] but still it has room for improvement [42]. Starting from the root matching technique the improvement in the PSLL is achieved for a given HPBW. The results are presented for the elements from 5 to 12.

5.4.1 Problem Setup

For this work uniformly spaced linear isotropic arrays with $d = 0.5\lambda$ are considered. The objective is to determine the element excitations for the optimised array pattern with low PSLL for a given HPBW and compare it with conventional and root matching techniques. The UoM-PSO is used for the determination of the optimised null positions. The optimiser requires a fitness function to be evaluated for each desired null position. This fitness function is given below;

$$fitness = \sqrt{\varsigma_1(SLL_{des} - SLL_{patt})^2 + \varsigma_2(BW_{des} - BW_{patt})^2} \tag{5.4}$$

Where
BW_{des} = desired HPBW given in Table 5.11
BW_{patt} = HPBW of the obtained radiation pattern
$\varsigma_1 = 10$
$\varsigma_2 = 1$

All other terns have the predefined meanings. The results are discussed below.

5.4.2 Results & Discussion

The optimization technique is applied to different number of elements. Two different cases have been considered. In case 1 the optimised results are compared with conventional sampling and the Elliot's root matching technique on the basis of reduced PSLL for a given beamwidth. The results are shown in Table 5.11.

Number of Elements	HPBW (Deg)	PSLL (dB)		
		Conventional Sampling	Root Matching	UoM-PSO
5	25.95	−21.16	−26.49	−26.53
6	22.59	−23.49	−28.32	−32.94
7	18.66	−23.68	−28.33	−29.24
8	17.52	−27.97	−35.90	−37.19
9	15.46	−28.46	−35.49	−35.74
10	14.74	−32.10	−38.15	−41.36
12	12.62	−35.76	−45.02	−45.61

Table 5.11: Comparison for a given beamwidth

It is obvious from the results obtained that the conventional sampling method is not suitable for arrays with small number of elements. By using the root matching technique lower sidelobe levels can be achieved for the same beamwidth. By using the UoM-PSO on average $1.5dB$ improvement in SLLs is obtained as compared to the root matching technique. It is important to note that an optimal Dolph-Chebyshev pattern can be obtained for odd number of elements by careful selection of $\bar{n}$ with the root matching technique. As the proper selection of $\bar{n}$ for lower SLLs is restricted due to the less number of elements [7, 94]. The UoM-PSO technique was unable to show any significant improvement in the case of odd number of elements as evident from the Table 5.11.

It has been shown that UoM-PSO technique merged with the unit circle representation is an efficient way to control the array pattern. The UoM-PSO technique has shown improvements in the SLL in case of small arrays with even number of elements. In most practical situations antenna arrays with even number of elements are used because of the ease of feed design. The use of the proposed technique proves its advantage over conventional techniques.

5.5 Difference Pattern

This section is dedicated to the difference pattern synthesis using the three optimisation algorithms used so far. The conventional analytical difference pattern techniques for linear arrays include Zolotarev polynomial based approach introduced by McNamara [95] and the Bayliss distribution [10]. The Zolotarev polynomial based approach results in the optimum array radiation pattern in the Dolph-Chebychev manner. For a given number of elements and a defined difference pattern beamwidth (DBW) between the main null and the first null of difference pattern Zolotarev distribution provides a radiation pattern with minimum SLL and the maximum difference pattern slope [96] in the same fashion as Dolph-Chebychev for the sum pattern. The Bayliss distribution is equivalent to the $\bar{n}$ Taylor distribution for sum patterns. The limitations of the conventional $\bar{n}$ Bayliss distribution has been highlighted in case of small discrete antenna arrays by Elliott [4]. The issues related to the discrete array difference pattern synthesis are similar to those of Taylor distribution. The solution provided by Elliott was based on the iterative process to reduce the error in the pattern.

The objective in difference pattern synthesis optimisation is to determine a pattern that has a certain SLL constraint and maximum difference slope. Various optimisation algorithms have been introduced to solve this problem [97–100]. In these cases the medium sized arrays are considered and subarray concept is utilised and no mutual coupling model is considered.

5.5.1 Problem Statement

A linear array of eight BDRA elements is considered for this study. The effective element separation is $d = 0.41\lambda$ at $4.5GHz$. The Bayliss weights [10] are used to obtain an array radiation patterns. For this a MATLAB function was developed based on the data given in [4] to find the required Bayliss distribution. The target SLL and $\bar{n}$ were set to $-30dB$ and 3 respectively. The w_n in the Equation 2.5 is replaced by the Bayliss distribution thus found for a BDRA radiation pattern. For comparison the same Bayliss taper was applied to the isotropic array (the Equation 2.3) with inter-element spacing of $d = 0.41\lambda$.

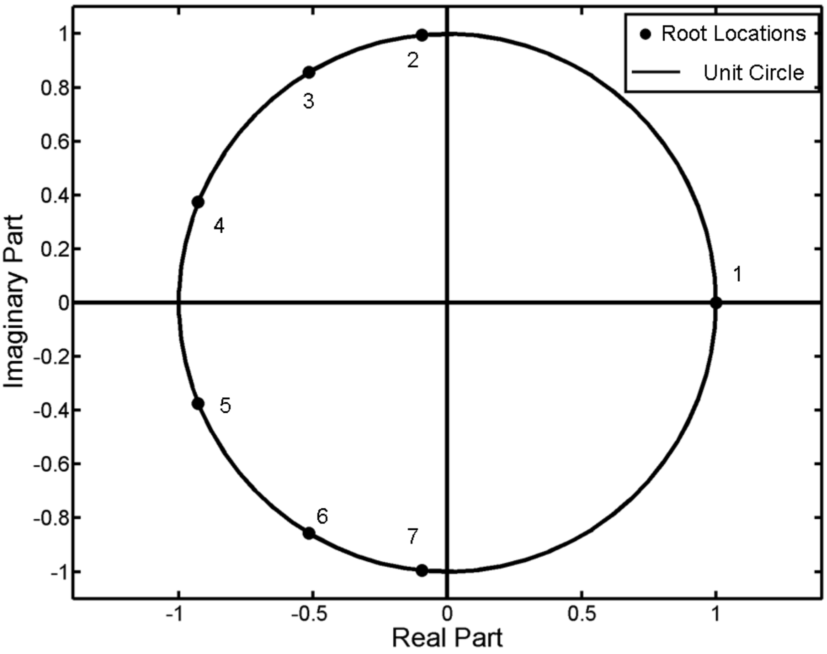

Figure 5.14: The z-space presentation of the Bayliss taper for SLL= $-30dB$ and $\bar{n}$

The root distribution for the Bayliss taper in z-space is shown in the Figure 5.14. As compared to the sum pattern the root at $\alpha = 180^o$ is moved to $\alpha = 0^o$ for difference pattern. In order to implement the IzBC-PSO the target null beamwidth (between the main null and the first null of the difference pattern). The boundaries are set according to the SLL topology as described in the chapter 4. The initial step to the α bound was set to 20^o and if necessary 10^o increments were set. The upper and lower bounds would be $\alpha_o + 20^o$ and $\alpha_o - 20^o$, for a step size of 20^o, where α_o is the current root location in α. The upper and lower bound on r were set to 3 and 0.5.

To implement the UoM-PSO the initial root locations shown in the Figure 5.14 were taken as the starting point and the α bound for each root location was set to $360^o/(N-1)$ with the root location in the centre. This resulted in the upper and lower bounds of $\alpha_o + 360^o/(N-1)$ and $\alpha_o - 360^o/(N-1)$. The r bound stays the same as before. The same α and r bound were used for the GA solution.

The optimisation goal was to improve the radiation pattern under the presence of mutual coupling to meet the required SLL criteria. The issue related to the Bayliss taper for small discrete arrays is resolved simultaneously. The other objectives include the reduced dynamic range ratio, increased excitation efficiency and maximised difference slope.

The fitness function used to achieve a solution for this multi objective problem is given below.

$$\begin{aligned} fitness = [&\varsigma_1(SLL_{des} - SLL_{patt})^2 + \varsigma_2(1 - \frac{1}{DRR_{patt}})^2 + \\ &\varsigma_3(DBW_{patt} - DBW_{iso})^2 + \varsigma_4(1 - \eta)^2]^{1/2} \end{aligned} \tag{5.5}$$

Where
DBW_{patt} = the difference pattern beamwidth of the obtained pattern
η = the excitation efficiency of the obtained excitation set

DBW_{iso} = difference pattern beamwidth of the isotropic array when it is excited with uniform taper

All other symbols have the same meanings as defined earlier. The excitation efficiency is a ratio of the directivities of the difference pattern obtained at one difference peak and that of the uniformly excited sum pattern [101]. The mathematical expression used for this research work is given as;

$$\eta = \frac{D}{D_o} \tag{5.6}$$

Where D_o is the directivity of the uniformly excited sum pattern obtained from the Equation 2.8 for $d = 0.41\lambda$ and $\theta_o = 0^o$ and D is the directivity of the difference pattern obtained with the taper w_n for θ_o set to one difference peak and $d = 0.41\lambda$.

In both PSO models (IzBC-PSO and UoM-PSO) the swarm size was chosen to be 30 and the total iteration were set to 200 resulting in the 6000 fitness function evaluations. For the GA a population of 20 was selected with the total generations of 300 to make the fitness function computations of same number for comparison proposes. All other settings for the GA were left to the

MATLAB default values. The Table 5.12 provides the summary.

Optimiser	Population Size	Number of Iterations	Number of Computations
UoM-PSO	30	200	6000
IzBC-PSO	30	200	6000
GA	20	300	6000

Table 5.12: Tabular summary of the optimisers parameters

5.5.2 Results & Discussion

Figure 5.15 highlights the sampling problem with small discrete array of $N = 8$ isotropic elements while using the Bayliss distribution for target $SLL = -30dB$ and $\bar{n} = 3$.

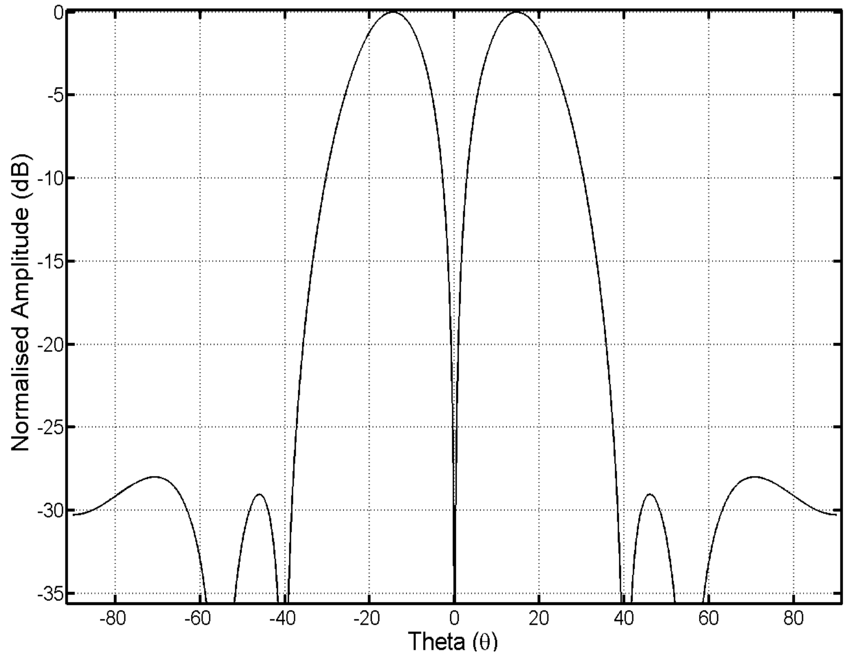

Figure 5.15: The isotropic element array radiation pattern for $d = 0.41\lambda$ Bayliss taper with target SLL= $-30dB$ and $\bar{n} = 3$

The Bayliss distribution used to obtain this radiation plot is given in the Table 5.13. No mutual coupling effect has introduced. In addition the array is not half wavelength separated as ($d = 0.41\lambda$) therefore the Bayliss solution is not optimum. The PSLL for this isotropic radiation pattern was $-28dB$ and the average SLL was $-28.5dB$ with the difference beamwidth (DBW) of 40^o.

Bayliss Weight Vector	
Amplitude	Phase
0.4203	0
0.8712	0
1	0
0.4420	0
0.4420	180
1	180
0.8712	180
0.4203	180

Table 5.13: The Bayliss taper used for the radiation patterns shown in the Figures 5.15 and 5.16, SLL= $-30dB$ and $\bar{n} = 3$

Figure 5.16 compares the radiation patterns of BDRA array and the isolated BDRA element array. The BDRA array radiation pattern includes the mutual coupling and therefore has filled nulls as compared to the isolated element array pattern. The PSLL and the average SLL for the BDRA array radiation pattern was found to be $-29.7dB$ and $-31.7dB$, respectively, with DBW of 42^o. The isolated BDRA array radiation pattern resulted in PSLL of $-32.4dB$ and average SLL of $-34.1dB$ for a DBW of 40^o. Since the target PSLL and average SLL was to be $-30dB$ therefore the error in PSLL and average SLL of the discrete array of isotropic elements was found to be 6.7% and 5.0% respectively. In case of the isolated BDRA element array the PSLL was found to be lower as compared to the isotropic array pattern and the target SLL due to the effect of the element pattern multiplication. The percentage error in case of the isolated BDRA element was 8.1% and 13.8% for PSLL and the average SLL.

In the presence of mutual coupling the PSLL has increased, shown in the Figure 5.16, as compared to the isolated BDRA element array pattern by 7.1%. The percentage error for BDRA array radiation pattern to achieve the target SLL is given by 1% and 6% for PSLL and average SLL respectively. The results presented in the Figure 5.16 include the pattern corruption due to coupling (for BDRA array) and the discrete array sampling. These results are summarised in the Table 5.14.

Figure 5.17 compares the BDRA array radiation pattern and the best optimised radiation pattern obtained by IzBC-PSO out of 10 trials. The mutual

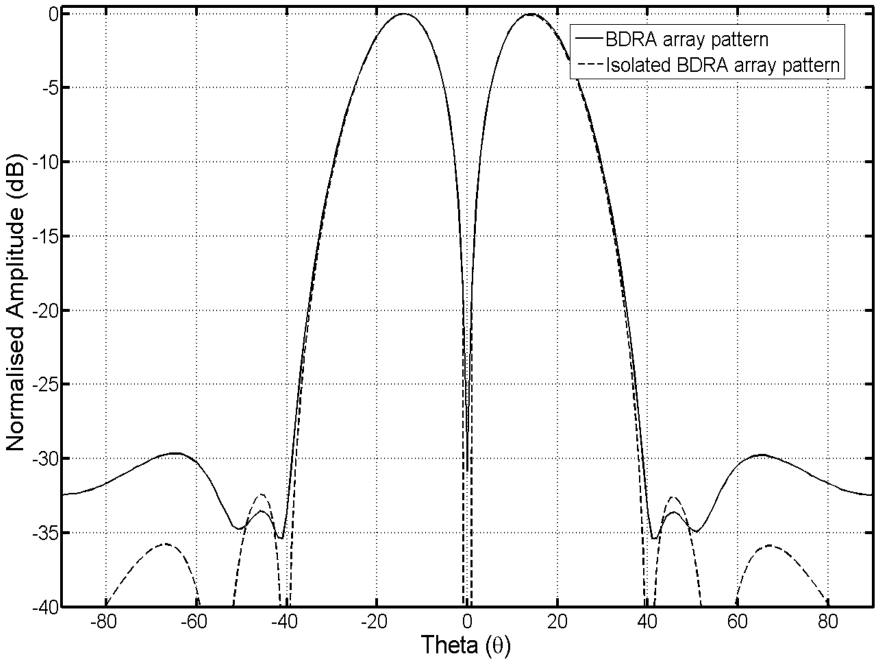

Figure 5.16: The radiation power patterns for the BDRA array and the isolated BDRA element array at 4.5GHz for Bayliss taper with target SLL= $-30dB$ and $\bar{n} = 3$

Array Type	PSLL (dB)	Average SLL (dB)	Difference beamwidth (DBW) (Deg)
Isotropic	-28	-28.5	40
Isolated BDRA	-32.4	-34.1	40
BDRA coupled	-29.7	-31.7	42

Table 5.14: Tabular summary of the Figures 5.15 and 5.16

coupling and the array sampling problem has been tackled simultaneously. The optimised radiation pattern has met the target SLL requirement as both PSLL and average SLL are $-30dB$ with DBW of 39^o. The optimised pattern shows the improvement of 5.4% in average SLL and 7.1% in DBW resulting in increased difference pattern slope over BDRA array radiation pattern.

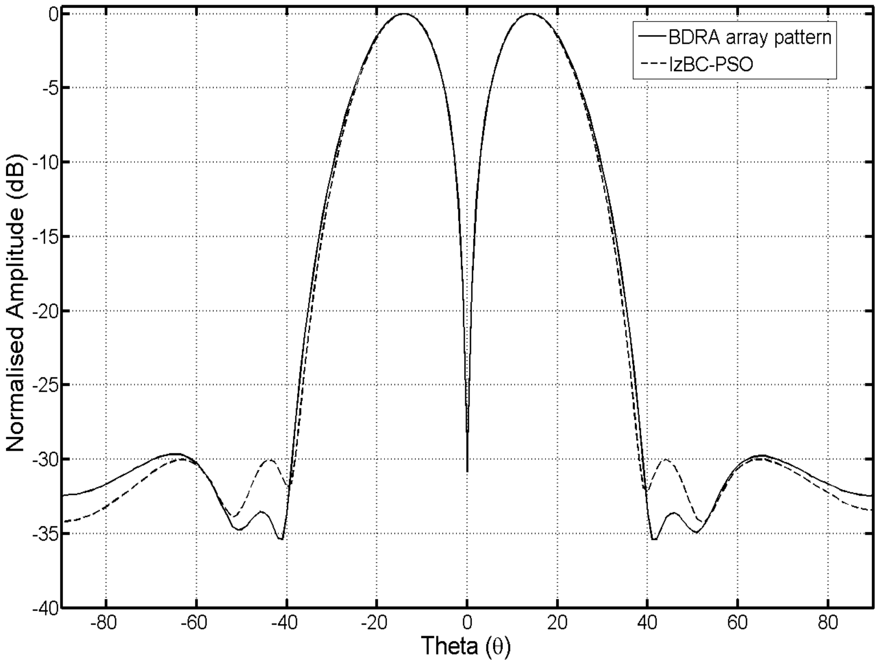

Figure 5.17: The BDRA array radiation pattern is compared to the IzBC-PSO radiation pattern

Figure 5.18 compares the best optimised results obtained by IzBC-PSO, UoM-PSO and GA out of 10 independent trails of each. The three optimised results have met the target SLL. However the optimised pattern obtained with IzBC-PSO has the narrowest DBW compared to UoM-PSO and GA. The percentage improvement is 11.3% and 9.3% over GA and UoM-PSO respectively. The results are summarised in the Table 5.15. The optimised weights used to find the radiation patterns shown in the Figure 5.18 are given in the Table 5.16.

Other optimisation objectives include the dynamic range ratio (DRR) and the excitation efficiency (η). The DRR and η for the weights given in the Table 5.16 are compared in the Table 5.17 with Bayliss distribution. Both IzBC-PSO and UoM-PSO weights resulted in the 7.7% better DRR as compared to GA optimised weight. The IzBC-PSO weight has the maximum efficiency compared to the Bayliss distribution given in the Table 5.13 and the optimised

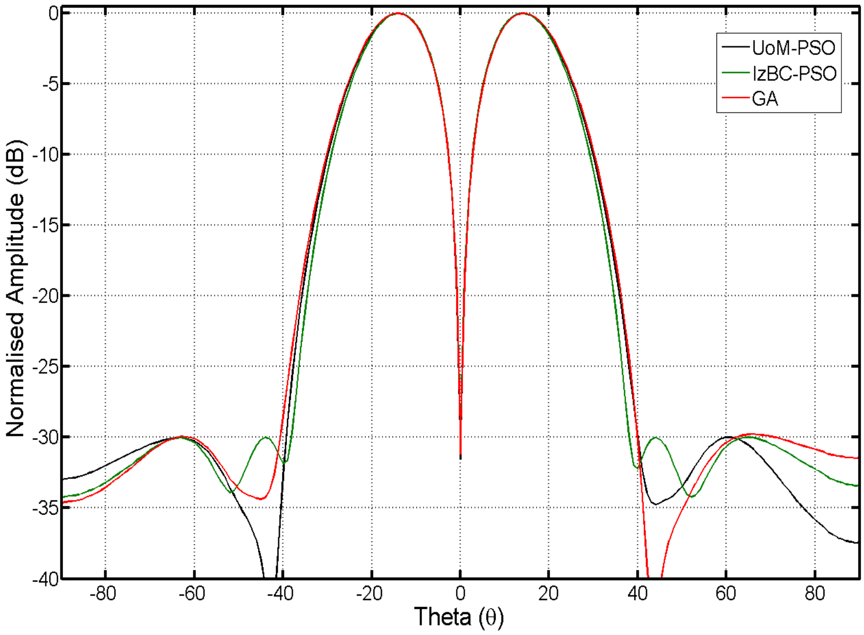

Figure 5.18: The best optimised radiation patterns obtained out of 10 independent trials in each case of IzBC-PSO, UoM-PSO and GA

Array Type	PSLL (dB)	Average SLL (dB)	Difference beamwidth (DBW) (Deg)
IzBC-PSO	-30	-30	39
UoM-PSO	-30	-30	43
GA	-30	-30	44

Table 5.15: Tabular summary of the Figure 5.18

weights obtained with UoM-PSO and GA. The summary of the optimisation objectives achieved is given in the Table 5.17.

IzBC-PSO Weight Vector		UoM-PSO Weight Vector		GA Weight Vector	
Amplitude	Phase (Deg)	Amplitude	Phase (Deg)	Amplitude	Phase (Deg)
0.46	0	0.41	0	0.39	0
0.89	0	0.86	0	0.81	0
1.00	0	1.00	0	1.00	0
0.41	0	0.41	0	0.49	0
0.43	180	0.46	180	0.42	180
1.00	180	1.00	180	1.00	180
0.89	180	0.81	180	0.86	180
0.44	180	0.41	180	0.39	180

Table 5.16: The optimised excitation (weight) vector used for the optimised array radiation plots in the Figure 5.9

Taper Applied	DRR	Excitation Efficiency	Difference beamwidth (DBW) (Deg)
IzBC-PSO	2.4	0.8730	39
UoM-PSO	2.4	0.8697	43
GA	2.6	0.8683	44
Bayliss (Table 5.13)	2.4	0.8723	42

Table 5.17: Optimisation objectives summary and comparison for the BDRA array

It is evident from the Table 5.17 that IzBC-PSO has performed better in achieving the target objectives. The DRR for IzBC-PSO is as low as Bayliss distribution where as the excitation efficiency has been improved. The major improvement can be seen in the DBW value as it has improved by 7.1% compared to the Bayliss distribution. The IzBC-PSO has clearly met all the objectives and the resultant optimised weight gives a difference pattern with target SLL, high excitation efficiency, low DRR and high difference slope.

Figures 5.19 to 5.22 compare the convergence performance of the optimisation algorithms used for this study. The convergence curves for the 10 independent trials of IzBC-PSO are shown in the Figure 5.19 with the best and

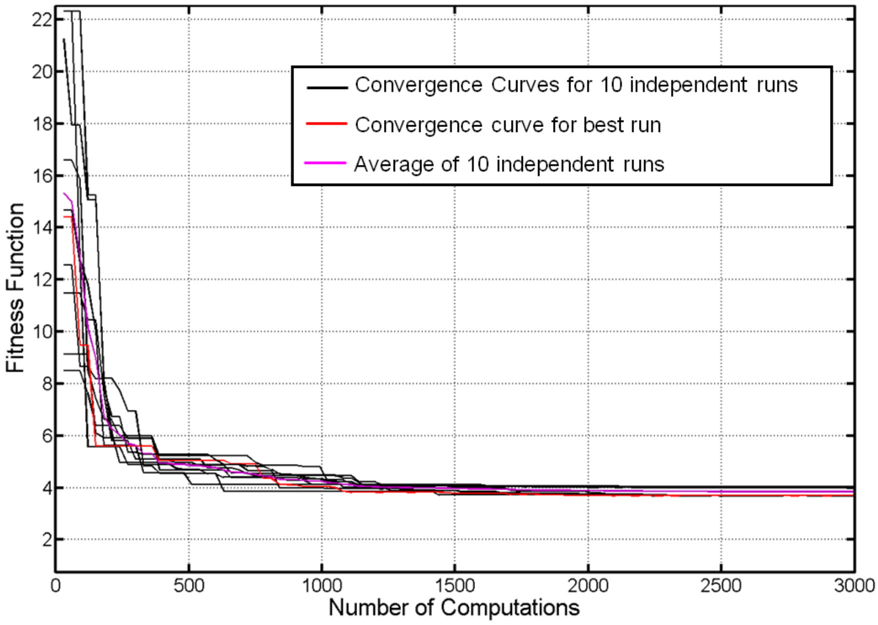

Figure 5.19: Convergence curves for 10 independent trials of IzBC-PSO

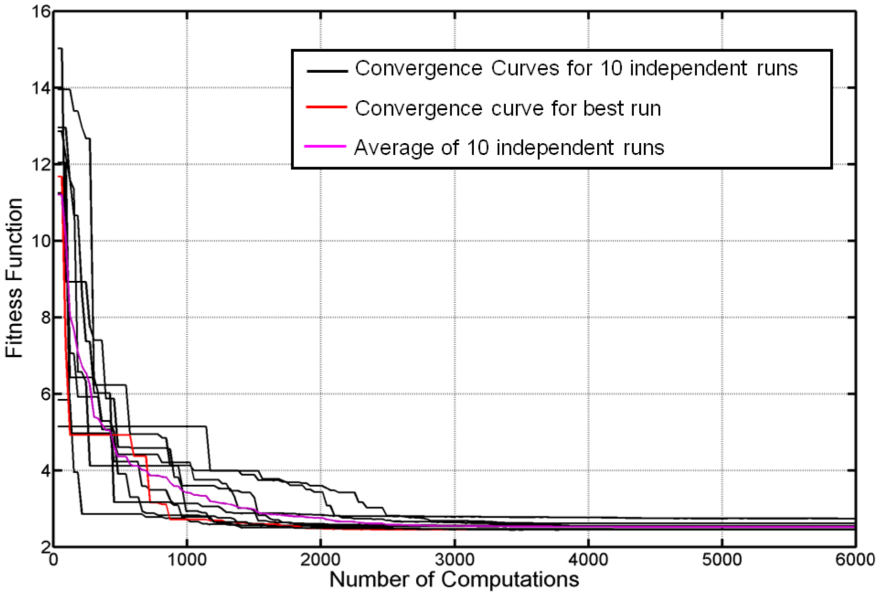

Figure 5.20: Convergence curves for 10 independent trails of UoM-PSO

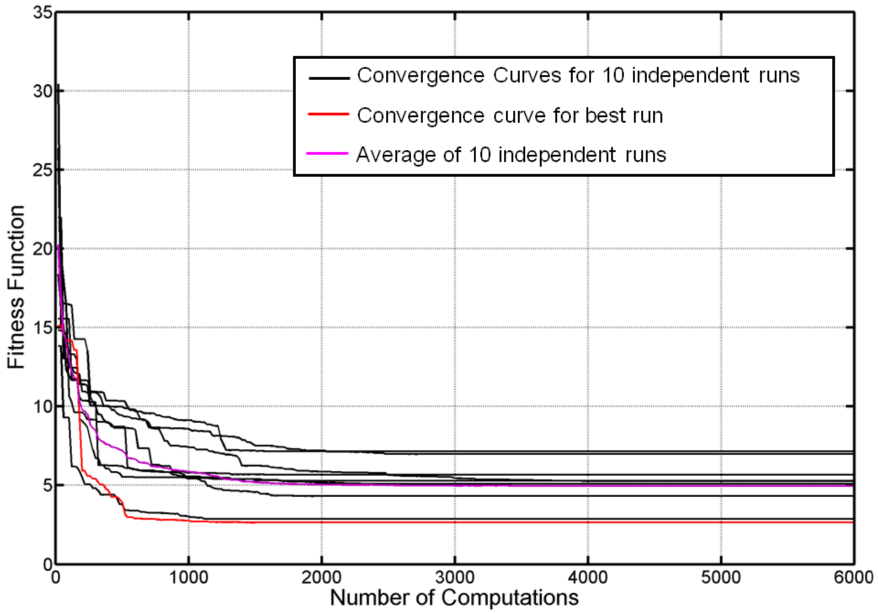

Figure 5.21: Convergence curves for 10 independent trails of GA

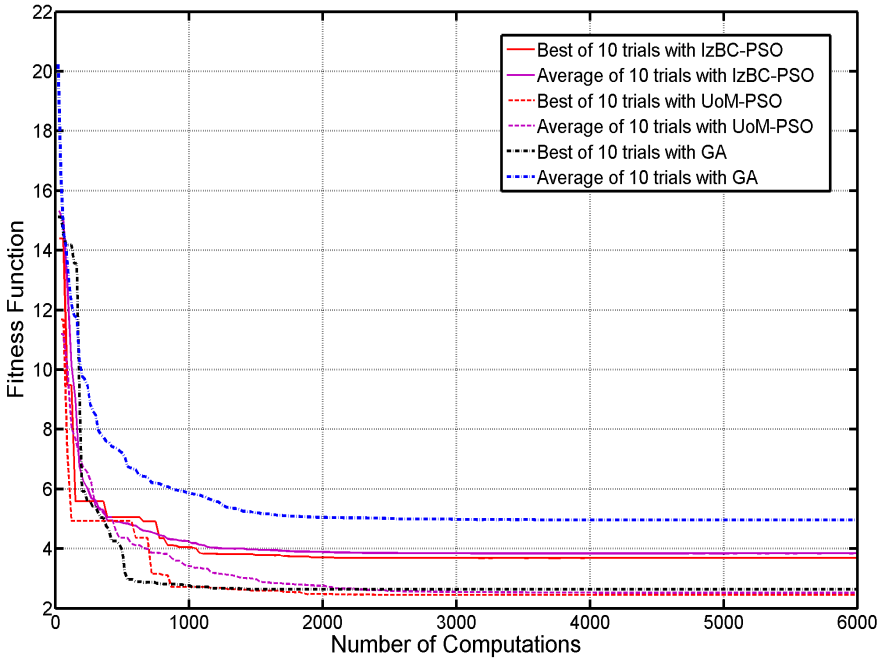

Figure 5.22: A comparison of best and average convergence curves for IzBC-PSO, UoM-PSO and GA

average convergence achieved in 1440 and 2250 computations of the fitness function. The convergence curves for the UoM-PSO are given in the Table 5.20. The best and average convergence was achieved in 1890 and 3360 evaluations of the fitness function. For GA the convergence curves are given in the Figure 5.21 with the best and average convergence achieved in 1600 and 2940 computations. The best and average convergence curves are shown in the Figure 5.22.

The IzBC-PSO has best overall convergence performance compared to UoM-PSO and GA. The improvement in the average number of required computations to solve this multi-objective problem with IzBC-PSO has been noted to 33% compared with UoM-PSO and 23% compared with GA. The GA has outperformed the UoM-PSO for this problem in terms of convergence however it was poor to achieve the problem objectives. Overall convergence performance by IzBC-PSO and UoM-PSO was consistent whereas GA failed to show the consistent convergence.

These multiple performance comparison instances presented in sections 5.5.2, 5.2.3 and 5.3.2 have repeatedly shown that the IzBC-PSO is better in terms of achieving the optimisation goals and the convergence performance consistency. Therefore only IzBC-PSO results will be reported for the remaining optimisation problems in this study.

5.6 Difference Pattern Scanning

This section concerns with the difference pattern scanning of the BDRA array. For scanning purposes the linear phase gradient is applied to the array as discussed in section 2.6 of chapter 2. It is observed that with scanning the array’s important characteristics of the difference pattern get compromised. The difference between the twin beam peaks, SLL, difference pattern slope and the main null depth suffer because of the mutual coupling. Therefore it is necessary to mitigate the effect of mutual coupling and element pattern multiplication in order to achieve a desired performance. In this study IzBC-PSO is used to achieve the desired pattern objectives. To highlight the tradeoff among the pattern features this work is divide into two independent scenarios.

In *Scenario I* the objective is to achieve the difference pattern with deep main null and the difference pattern slope is maximised while minimising the difference between the two difference peaks for a 30^o scanned BDRA array. No restriction is applied to the SLLs. In *Scenario II* the SLL constraint is applied. Lower SLL were obtained for a reduced slope difference pattern. It is further demonstrated that IzBC-PSO is a versatile tool to be used as a multi-objective problem optimiser.

5.6.1 Problem Setup

A linear array with eight BDRA elements is assumed at $4.5GHz$. The array is initially excited with the Bayliss taper shown in the Table 5.13 and a linear gradient is applied to scan the main difference pattern null to $\theta_o = 30^o$. The modified z-space root distribution is shown in the Figure 5.23.

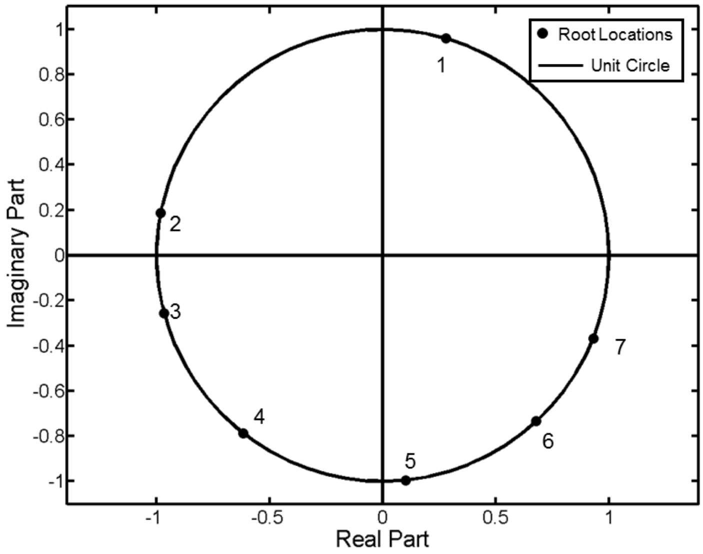

Figure 5.23: The root locations in z-space for $d = 0.41\lambda$ with phase gradient applied for 30^o to Bayliss distribution, SLL=$-30dB$ and $\bar{n} = 3$

The isotropic array pattern is given in the Figure 5.25 for comparison and defining the optimisation parameters. The difference peaks of the pattern are indicated in the Figure 5.24. The difference pattern slope is defined by the slope of a hypothetical straight line passing through the $-10dB$ point and the main null as highlighted in the Figure 5.24 of isotropic array. One of the two points of the straight line are fixed to the *theta*$_o$ and the other end is set to $\theta_o \pm \theta_{-10dB}$.

The expression is given below;

$$Slope = \frac{Patt_{-10dB} - Patt_{\theta_o}}{\theta_o - \theta_{-10dB}} \tag{5.7}$$

Where

$Patt_{-10dB}$ = the pattern value at $-10dB$ point as indicated in the Figure 5.24

$Patt_{\theta_o}$ = main null depth of the difference pattern

θ_{-10dB} = the angle value at the indicated $-10dB$ point

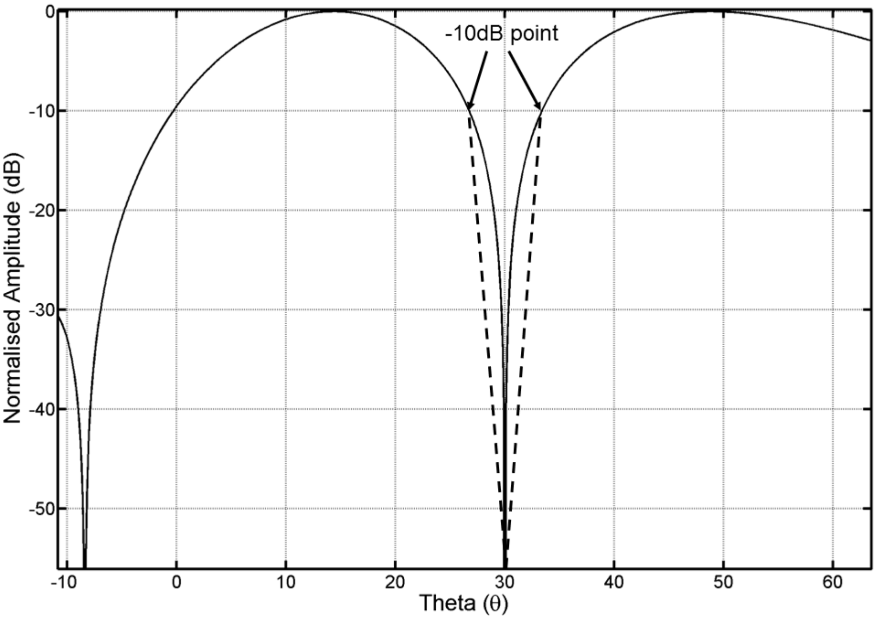

Figure 5.24: Presentation of slope lines defined to calculate the difference pattern slope

The two slope values are determined and compared. The minimum of two is taken as the slope measure and used in the fitness function to maximise the slope. The IzBC-PSO is initialised by the root locations shown in the Figure 5.23 following the similar steps mentioned in the previous problem setup. No additional constraints are applied to the root location bounds.

The fitness function used for the *Scenario I* is given as;

$$fitness = [\varsigma_1(Peak1_{patt} - Peak2_{patt})^2 + \varsigma_2(Slope_{iso} - Slope_{patt})^2 + \varsigma_3(NDepth_{tag} - NDepth_{patt})^2]^{1/2} \tag{5.8}$$

Where
$Peak1_{patt}$ & $Peak2_{patt}$ = are the difference peaks of the pattern
$Slope_{patt}$ = the minimum of the two measured slopes
$Slope_{iso}$ = the slope value determined for the isolated BDRA element array
$NDepth_{tag}$ = target null depth, set to $-60dB$
$NDepth_{patt}$ = obtained pattern null depth
$\varsigma_1 = 12$
$\varsigma_2 = 1$
$\varsigma_3 = 0.5$

For *Scenario II* the SLL constraint is added to the fitness function. The modified fitness function is given below;

$$fitness = [\varsigma_1(Peak1_{patt} - Peak2_{patt})^2 + \varsigma_2(Slope_{iso} - Slope_{patt})^2 + \varsigma_3(NDepth_{tag} - NDepth_{patt})^2 + \varsigma_4(SLL_{des} - SLL_{patt})^2]^{1/2} \tag{5.9}$$

$\varsigma_1 = 12$
$\varsigma_2 = 1$
$\varsigma_3 = 0.5$
$\varsigma_4 = 0.05$

Where all other terms have been defined. The optimisation parameters for IzBC-PSO have been given in the Table 5.18 for *Scenario I* and *Scenario II*.

5.6.2 Results & Discussion

Figure 5.25 shows the isotropic array pattern while main null is scanned to $\theta_o = 30^o$. The PSLL raised to $-26dB$ with average SLL of $-27.8dB$. The difference

Scenario Type	Swarm Size	Number of Iterations	Total Computations
Scenario I	30	200	6000
Scenario II	30	500	15000

Table 5.18: Optimisation parameter values for IzBC-PSO used in *Scenario I* and *Scenario II*

pattern slope calculated using the Equation 5.7 was found to be 87.8 with main null as deep as $-300dB$. In the absence of element pattern multiplication effect and the mutual coupling the difference between the twin beam peaks was negligible.

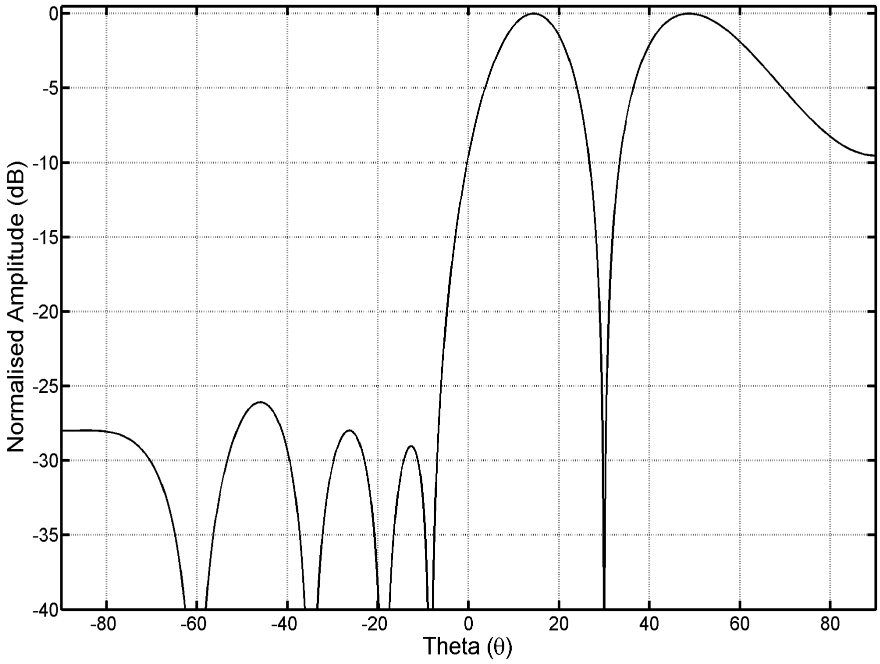

Figure 5.25: Isotropic element array radiation pattern for Bayliss distribution with target SLL= $-30dB$ and $\bar{n}=3$ scanned to 30^o

Figure 5.26 compares the BDRA array and the isolated BDRA element array radiation patterns while main difference pattern null is scanned to θ_0. In case of isolated BDRA element array the PSLL is $-29dB$ with average SLL of $-31.2dB$. The difference between the twin beam peaks was found to be $-3.6dB$ which is not acceptable for monopulse tracking applications. The main null depth was found to be $-70dB$ with the difference slope value of 17.1.

In case of BDRA array radiation pattern the PSLL was raised to $-13.4dB$ with

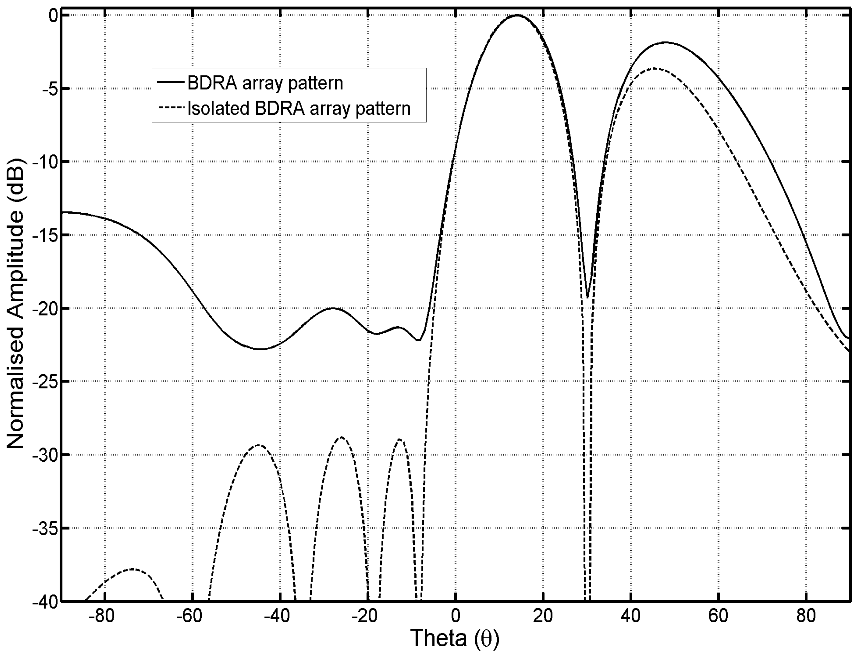

Figure 5.26: Comparison of BDRA array and Isolated BDRA element array patterns for Bayliss distribution with target SLL= $-30dB$ and $\bar{n} = 3$ scanned to 30^o

the average SLL of $-18dB$ as shown in Figure 5.26. The difference between the twin beam peaks was found to be $-1.8dB$. The null depth and the pattern slope was found to be $-19.3dB$ and 3.1 respectively. The mutual coupling has significantly effected the pattern characteristics as it is evident from Figure 5.26 and summarised in Table 5.19.

Array Type	PSLL (dB)	Average SLL (dB)	Null Depth (dB)	Difference Slope	Twin Beam Peaks Difference (dB)
Isotropic element	-26	-27.8	-300	87.8	*N.A.*
Isolated BDRA element	-29	-31.2	-70	17.1	3.6
BDRA array	-13.4	-18	-19.3	3.1	1.8

Table 5.19: Summarising the results from the Figures 5.25 and 5.26

5.6.2.1 Scenario I

In *Scenario I* the IzBC-PSO is used to compensate for the null depth, difference pattern slope and the difference between the twin beam peaks in the presence of mutual coupling. No SLL constraint was applied. The target null depth was set to $-60dB$ and twin beam peaks were required to be at the same level. The difference pattern slope was set to be maximised. The best result obtained out of 10 independent trails of IzBC-PSO is shown in Figure 5.27 compared with that of the BDRA array radiation pattern.

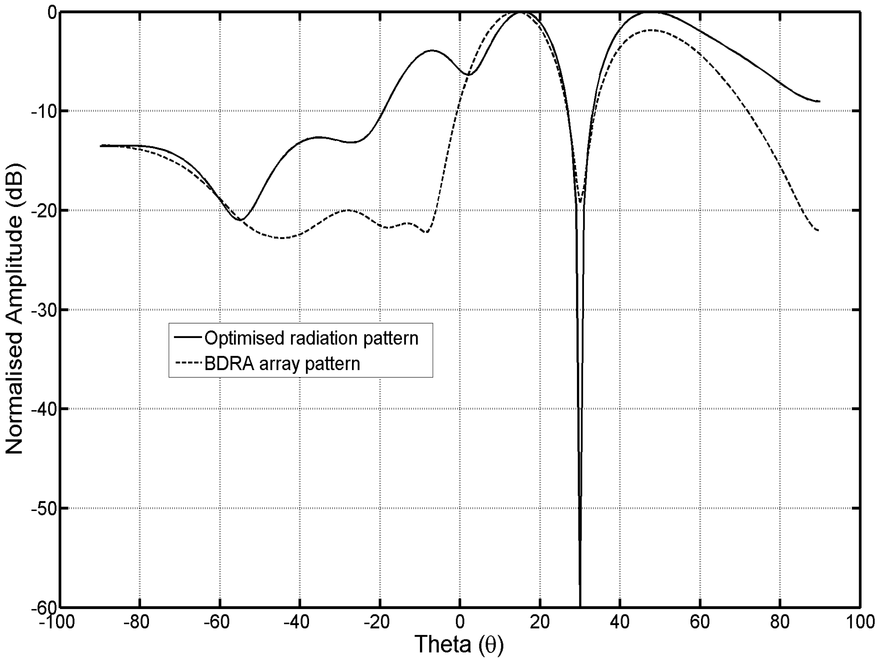

Figure 5.27: Addition patterns for BDRA array before and after the optimisation for *Scenario I*

Array Type	Null Depth (dB)	Difference Slope	Twin Beam Peaks Difference (dB)
BDRA array	−19.3	3.1	1.8
IzBC-PSO	−60	16.7	0.02

Table 5.20: Summarising the results from the Figure 5.27 and comparing the optimised and BDRA array radiation patterns

The optimised pattern has improved the null depth by $47.3dB$ as compared to the BDRA array radiation pattern. The twin beam peaks difference has reduced to $0.02dB$ after optimisation instead of $1.8dB$ before. The difference pattern slope has improved to 16.7 compared to the BDRA array slope value of 3.1, under mutual coupling after using IzBC-PSO. The careful selection of the weighting multipliers used in the *Scenario I* fitness function and the use of IzBC-PSO have significantly improved the difference pattern performs under mutual coupling conditions. The results are summarised in Table 5.20.

IzBC-PSO Weight Vector	
Amplitude	Phase
0.19	0
0.36	52
0.34	120
0.41	−163
0.48	−46
0.10	82
1.00	−104
0.49	−30

Table 5.21: The optimised weight used to obtain the optimised radiation pattern shown in the Figure 5.27

The optimised taper used to obtain the radiation patterns shown in Figure 5.27 is given in Table 5.21. The optimised root locations corresponding to the optimised weight are shown in Figure 5.28. As it can be seen the root locations marked as 1, 2 and 7 are affecting the optimisation goals significantly. Other root locations have minor effect on the outcome of the results. The root location marked as 1 corresponds to the main null of the difference pattern and it has to go off the unit circle to increase the null depth in the presence of coupling.

5.6.2.2 Scenario II

The *Scenario II* added constraint on the SLL. As it can be seen that there are four objectives that are required to meet simultaneously which increases the complexity of the optimisation. The target null depth and SLL were set to $-40dB$ and $-20dB$ for this example, respectively. The result is presented in Figure 5.29 comparing the BDRA array radiation pattern before and after the optimisation.

The radiation pattern performance in the presence of mutual coupling has

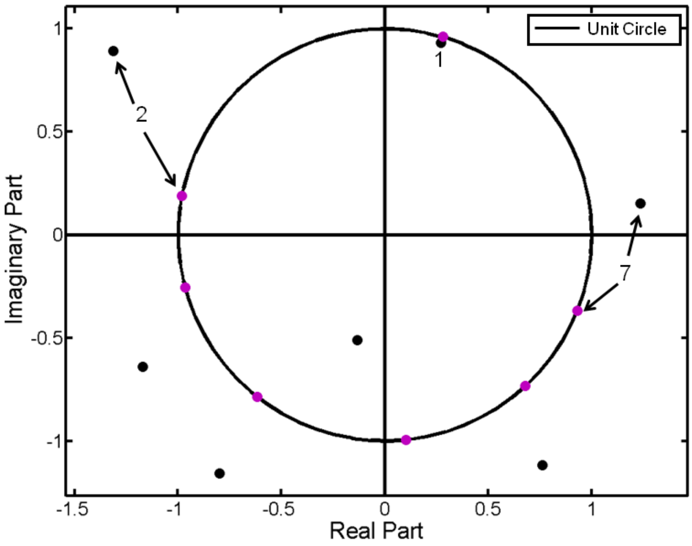

Figure 5.28: The optimised root locations shown in Black compared to that of the initial Bayliss distribution shown in Magenta

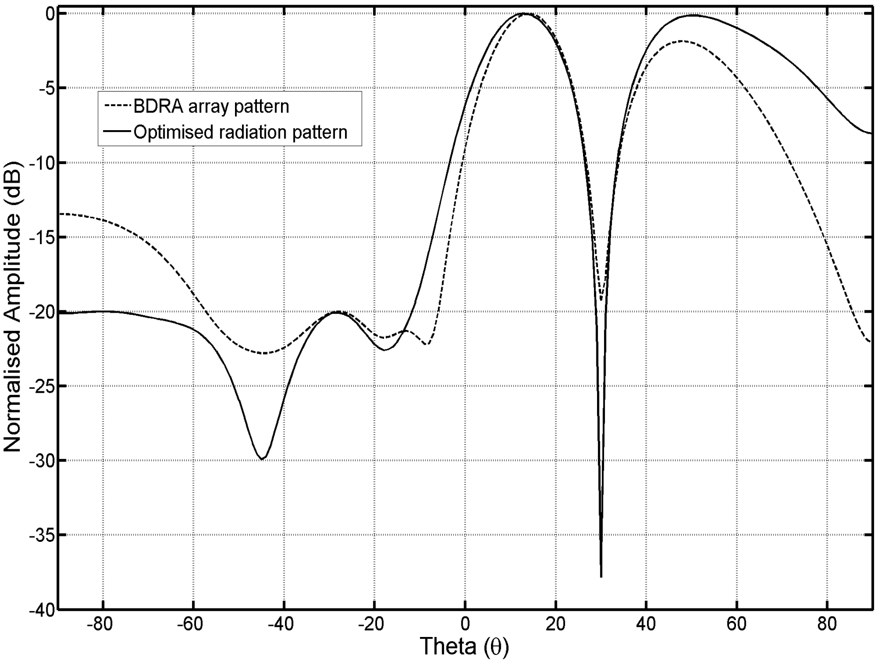

Figure 5.29: Optimised BDRA array radiation pattern using IzBC-PSO

significantly improved after optimisation. The PSLL and average SLL were improved to $-20dB$. The obtained null depth is $-37.3dB$ with the difference pattern slope value of 7.4. The difference between the twin beam peaks has been reduced to $0.1dB$. The PSLL and average SLL has improved by 49.2% and 11.1% respectively comparing with the BDRA array radiation pattern before optimisation. The null depth has improved by $18.5dB$ after using IzBC-PSO. It is evident that optimisation has significantly improved the difference pattern performance. The results are summarised in the Table 5.22.

Array Type	PSLL (dB)	Average SLL (dB)	Null Depth (dB)	Difference Slope	Twin Beam Peaks Difference (dB)
BDRA array	−13.4	−18	−19.3	3.1	1.8
IzBC-PSO	−20	−20	−37.8	7.9	0.1

Table 5.22: Summarising the results from the Figure 5.29 and comparing the optimised and BDRA array radiation patterns

The IzBC-PSO average convergence performance is shown in the Figure 5.30. This multi objective problem requires 8870 fitness function evaluations on average. The Figure 5.31 shows the optimised root locations found after running the IzBC-PSO to meet the objectives defined in the *Scenario II*.

It is clearly sown that IzBC-PSO has improved the radiation pattern performance of the difference pattern in the presence of mutual coupling while the array is scanned. It is also shown that if this technique is not implemented significant pattern degradation is observed. It is also shown that the versatile technique, IzBC-PSO, can be used to meet any desired objectives with mere modification to fitness function only.

5.7 Monopulse Array Synthesis

Both the sum and difference pattern synthesis have been presented in this chapter, so far, in the presence of mutual coupling. It has been shown that optimisation was necessary to obtain the desired pattern properties and conventional techniques (Chebychev, Taylor, Bayliss) suffered from the discrete array sampling and coupling. One of the important uses of sum and difference patterns is in the monopulse array. Monopulse arrays are widely used for the

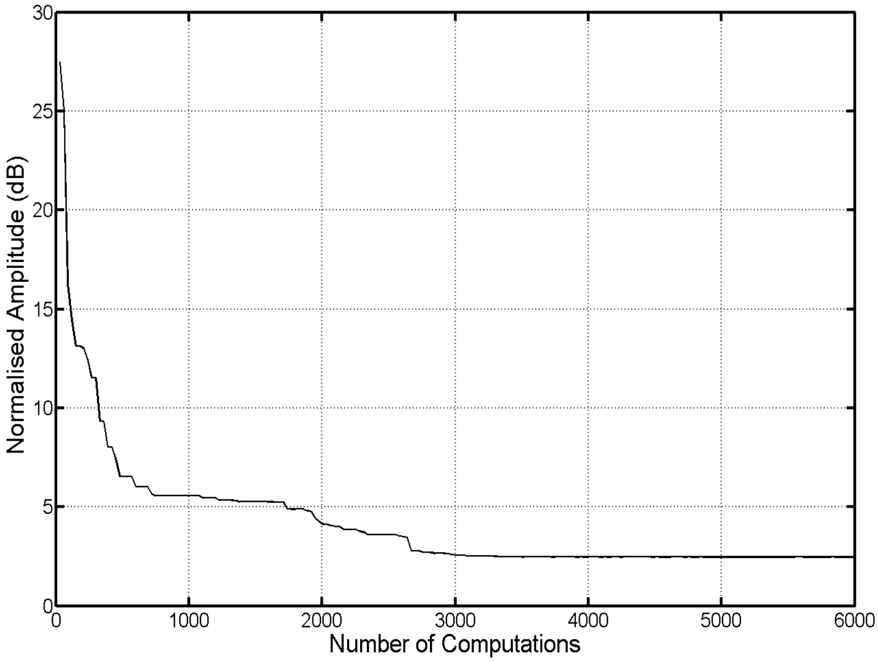

Figure 5.30: The average convergence curve for 10 independent trials of IzBC-PSO

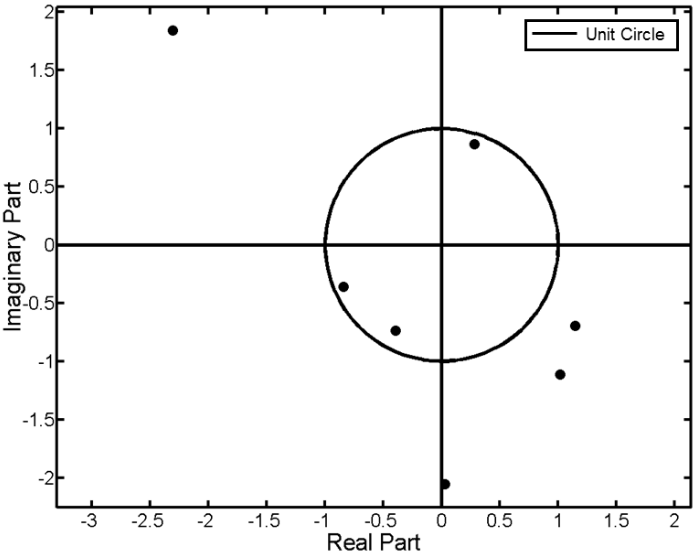

Figure 5.31: The optimised root locations corresponding to optimised weight vector that was used to find the radiation patterns shown in the Figure 5.29

.

source detection and angle of arrival applications. The monopulse operation depends on the sum and difference pattern characteristics. Usually, sum and difference patterns are used in a manner with the sum pattern main beam and the difference pattern null both pointing in the θ_o direction. The difference pattern is used simultaneously with the sum pattern to accurately determine the direction of arrival. For this purpose the difference pattern slope is very important factor to identify the main null of the difference pattern in the presence of noise. Conventionally Taylor distribution [7] is used to determine the sum pattern with the desired SLL characteristics. For the difference pattern Bayliss [10] distribution is used to obtain a difference pattern with desired difference beamwidth and the SLL characteristic. This requires two independent feed structures to support the desired sum and difference patterns which increase the complexity and cost of a monopulse system. It is desirable from the system design point of view to obtain a taper that simplifies the array feed. Ideally same amplitudes across the array for both sum and difference patterns with 180^o phase shift across the half of the aperture.

Several approaches have been reported to achieve this goal. Hosseini et al [102] have reported solutions based on phase only, amplitude only and separation only methods for an array of 100 elements. The methods based on amplitude only and phase only gave low sidelobe levels (SLLs) but required a complex feed structure. The separation only method resulted in simple feed structure but SLLs were comparatively high [102]. An approach based on the subarrayed linear arrays is used to find the optimum sum and difference patterns [103]. The work is focused on the minimizing the sidelobes (SLL) while maximising the slope across broadside direction. The results were presented for the arrays with 20 and 100 elements.

Another approach proposed by M. D'Urso et al [99] based on hybrid optimization technique deals with the problem of simplifying the feeding network for optimal sum and difference patterns. The proposed technique starts with a set of sum pattern excitations. To determine the difference pattern excitations subarray clustering is performed. As a result of this approach different elements have chosen for sum and difference patterns among the subarrays. The drawback of this technique is that one have to have additional elements in the subarrays as not all of them are used in one particular scenario (sum or difference pattern).

To simplify the feed structure it has been proposed to reduce the difference between the Taylor and Bayliss taper using simulation annealing optimiser [104]. The authors were partially successful as up to 50% of a common aperture distribution could be shared between the Taylor and Bayliss distribution. This then uses a common feed structure over half the array, but still requires different weights for sum and difference patterns over the remaining half of an aperture.

The techniques mentioned above consider either arrays with ($N > 10$) or continuous aperture. In this section UoM-PSO is used to simplify the feed structure for the monopulse radar system with small number of elements ($N = 8$). It is a well known fact that a difference pattern can be obtained simply by flipping the phase of the other half of a sum pattern taper. This reduces the complexity of the feeding network but the resultant pattern has high sidelobe levels (SLL). It is a matter of interest here to use a global optimization technique to find a single excitation set that may produce sum and difference patterns with mere phase flipping within acceptable SLL limits. This simple idea was applied to Taylor and Bayliss distributions sampled by Elliott's root matching method to obtain sum and difference patterns respectively. For comparison an 180^o phase difference was introduced over half of the aperture to obtain a difference pattern from Taylor current distribution and sum pattern from Bayliss current distribution. The patterns are given in the Figures 5.32, 5.33 and discussed in the results section. These patterns had SLLs above $-10dB$. A compromise between sum and difference patterns was found by using the particle swarm optimiser.

5.7.1 Problem Setup

An array of eight isotropic elements was assumed along the z-axis. The elements are uniformly half wavelength separated. Since each null position (root location) is defined by two variables r and α. The total number of variables to deal with are 14. Trial and error procedure was adopted to find out the optimum number of agents required to solve the problem. The number of agents used for the optimization problem was 30. These thirty agents were distributed in the solution space randomly. Since each null position has two dimensions therefore the constraint was applied to both r and α . For each null position (variable) the dimension r was bounded between 0.8 to 1.5. The dimension α was allowed to vary along its initial position with in 20^o limit for each variable.

Now a scenario was considered where target average SLL for the sum pattern was taken as $-20dB$. The PSLL for the difference pattern was set to $-15dB$. The target null depth for the main null of the difference pattern was taken as $-40dB$. The fitness function used for this optimisation problem is given below as;

$$\begin{aligned} fitness = [&\varsigma_1(SLL_{des}^{sum} - SLL_{patt}^{sum})^2 + \varsigma_2(SLL_{des}^{diff} - SLL_{patt}^{diff})^2 + \\ &\varsigma_3(NDepth_{des} - NDepth_{patt})^2]^{1/2} \end{aligned} \tag{5.10}$$

Where
SLL_{des}^{sum} = desired average SLL for sum pattern which was set to $-20dB$

SLL_{patt}^{sum} = average SLL obtained for the sum pattern

SLL_{des}^{diff} = desired PSLL of the difference pattern which was set to $-15dB$

SLL_{patt}^{diff} = PSLL for the obtained difference pattern

$NDepth_{des}$ = desired null depth for the main null of the difference pattern which was set to $-40dB$
$NDepth_{patt}$ = main null depth for the obtained difference pattern

The weighting multipliers for the fitness function were chosen such that all the objective get the equal weight. The excitation vector corresponding to a proposed optimum root location (values contained by a particle of swarm) was first used to find the sum pattern for which the average SLL was recorded. Then the later half of the excitation vector was multiplied by -1 and used to find the difference pattern using the same Equation 2.3.

5.7.2 Results & Discussion

A Taylor sum pattern with target $-20dB$ SLL and $\bar{n} = 2$ was obtained. As the objective was to keep the feed network simple and less expensive only phases of the half of the element excitations were flipped to give a difference pattern.

The resultant difference pattern had a SLL of $-10dB$. The results are shown in Figure 5.32.

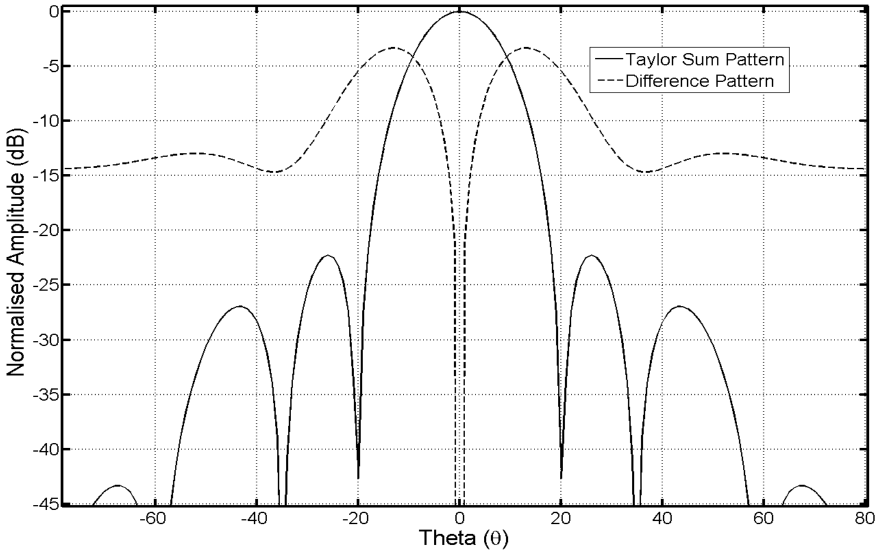

Figure 5.32: Taylor sum pattern for $\bar{n} = 2$ and SLL $= -20dB$, corresponding difference pattern

In Figure 5.33 Bayliss difference pattern for SLL $-15dB$ is shown. The Bayliss pattern was obtained for different values of $\bar{n}$ but since the array was small the SLL requirement met for $\bar{n} = 3$. Once again to meet the objective, only phases of the half of element excitation were flipped to obtain a sum pattern. The resultant sum pattern shown in Figure 5.33 has a SLL of $-7.29dB$.

It is clear from the results shown in Figures 5.32 and 5.33 that the difference pattern obtained from modified Taylor distribution was not acceptable. With the same token sum pattern obtained by the modified Bayliss excitation was not desirable. A compromise between acceptable difference and sum patterns for small arrays was obtained by using the particle swarm optimiser (PSO). The starting point was $-20dB$ sum pattern and then by flipping the sign of the half of the excitation the difference pattern was obtained.

In Figure 5.34 the optimised compromised patterns have presented. All three objectives were achieved within certain error. The sum pattern has the average SLL of $-20.5dB$. The difference pattern has PSLL of $-15dB$ with reference to the difference pattern peak and the null depth of $-40.73dB$. The two patterns were obtained by applying the excitation vectors given in Table 5.23. It is important to note that the magnitude of the excitation taper stays the same

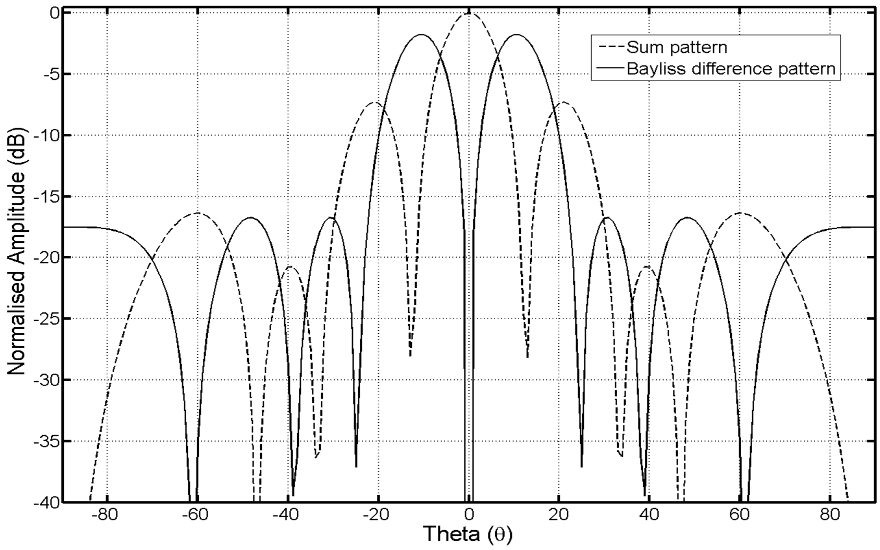

Figure 5.33: Bayliss difference pattern for $\bar{n} = 3$ and SLL $-15dB$ with corresponding sum pattern

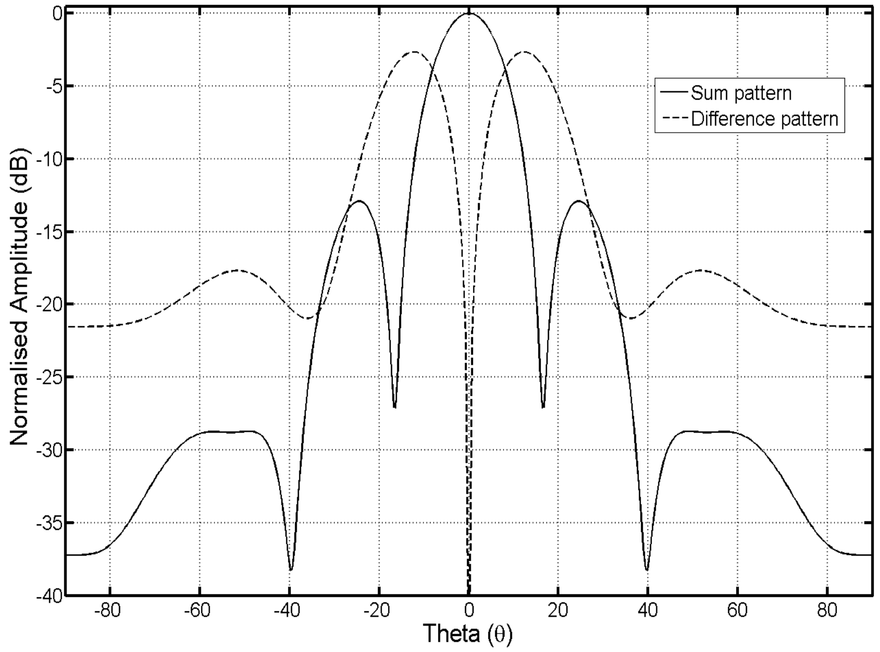

Figure 5.34: Optimised sum and difference patterns

for both sum and difference patterns. Only a phase flip of 180^o was applied to achieve the desired difference pattern properties. The improvement in the sum pattern PSLL is 78% compared to the sum pattern in Figure 5.33. The PSLL of the difference pattern shown in Figure 5.34 has improved by 50% as compared to the one presented in Figure 5.32.

UoM-PSO Weight Vector for Sum Pattern		UoM-PSO Weight Vector for Difference Pattern	
Amplitude	Phase (Deg)	Amplitude	Phase (Deg)
0.29	0	0.29	0
0.77	0	0.77	0
1.00	0	1.00	0
0.71	0	0.71	0
0.70	0	0.70	180
0.78	0	0.78	180
0.76	0	0.76	180
0.41	0	0.41	180

Table 5.23: The weight vectors used to determine the radiation patterns shown in Figure 5.34

It is shown that UoM-PSO is successfully used to find the optimum sum and difference pattern for monopulse operation with a simple array feed structure. As it is shown that if Taylor is chosen desired PSLL could be obtained but if 180^o phase shift is applied to half of the taper the resultant difference pattern has higher SLLs. On the other hand, if a low SLL difference pattern is obtained using the Bayliss distribution and then a sum pattern with high SLL is obtained by applying the 180^o phase shift to the half of this taper. The optimisation method used in this section simultaneously considers the SLL performance of sum and difference pattern for the desired SLL objective. It is shown that the optimisation technique based on PSO and Schelkunoff's approach, developed for this research work, has successfully achieved a simplified feed for monopulse operation with desired SLL profile.

5.8 Chapter Summary

The important results of this chapter are:

- IzBC-PSO and other optimisers are used to find both the amplitude and phase of the optimised excitation taper for all the cases presented in this chapter;

- It is shown that the proposed optimisation scheme, IzBC-PSO, has significantly improved the SLL (target), gain, FNBW and DRR performance of the small antenna array in the presence of mutual coupling and also for non optimal Dolph-Chebychev (as for $d < 0.5\lambda$) concurrently while the main beam is pointing at $\theta_o = 0^o$ (§5.2.3);

- The beam broadening issue associated with the main beam scanning is solved optimally while main beam pointing at $\theta_o = 30^o$, simultaneously achieving reduced SLL, high gain and reduced DRR under mutual coupling (§5.3.2);

- Issues related to the aperture sampling for small discrete array and mutual coupling corruption associated with Bayliss distribution are solved using, IzBC-PSO, while achieving the target PSLL, reduced DRR, better excitation efficiency and improved difference pattern beamwidth (DBW), with difference pattern null pointing in $\theta_o = 0^o$ (§5.5.2);

- Difference pattern degradation associated with the difference pattern main null scanned to $\theta_o = 30^o$ in the presence of mutual coupling has significantly improved in terms of difference pattern slope, twin beam difference, reduced PSLL and main null depth using IzBC-PSO (§5.6.2);

- It is shown that the proposed optimisation scheme, IzBC-PSO, has outperformed the UoM-PSO and GA optimisers and has achieved better optimum results with less number of fitness function evaluations and with better convergence consistency for small array with eight elements in the presence of mutual coupling (§5.2.3, §5.3.2, §5.5.2);

- For monopule operation a simplified feed is determined for the small isotropic array with eight elements, sum pattern (average SLL = $-20dB$)and difference pattern (PSLL = $-15dB$) are produced by mere applying 180^o phase shift across the half of the aperture, the array excitation vector is determined by using the UoM-PSO (§5.7.2);

- It is shown that this simplification (for monopulse array) does not work with the conventional tapers (Taylor and Bayliss) therefore use of the proposed scheme is necessary to achieve the required SLL behaviour (§5.7.2);
- The proposed optimisation scheme, IzBC-PSO, is universally applicable to isotropic and non isotropic arrays (§5.7.2, §5.2.3).

Chapter 6

Sector Beam Synthesis

6.1 Introduction

Sector or shaped beam synthesis has vital importance in various applications. In mobile communications the sector beams are used to provide the wireless coverage to a wide physical area in order to increase capacity. It is required that a certain level of electromagnetic energy is maintained through out the target area whereas reduced interference in unwanted directions. Conventional techniques used to synthesis such patterns include Fourier Transform and Woodward Lawson method discussed in detail by various authors [2–4]. The work presented in this chapter deals with the arrays consisting of small number of elements. A drawback of the Woodward Lawson method is that it does not allow to control the SLL of the array pattern outside the shaped beam. For this a solution was proposed by H. J. Orchard et al. [105]. Their method is based on the Schelkunoff's unit circle representation of the array polynomial. The pattern SLL were individually controlled by an iterative process but no mutual coupling is considered. The stochastic solutions [106, 107] including mutual coupling [107, 108] are presented for this non linear sector beam synthesis problem for small antenna arrays ($N < 10$).

The goal of this chapter is to overcome the problems with Woodward Lawson technique when used for small discrete arrays by proposing an alternate optimisation solution based on IzBC-PSO for sector beam synthesis with and also without mutual coupling consideration. The problem is divided into two main scenarios based on the choice of array element. In *Scenario I* an array with eight isotropic elements with half wavelength separation is considered. The array pattern is subjected to desired pattern masks while the shaped beam is centred at $\theta_o = 0$ and also $\theta_o = 20^o$ for later example. In later case (while sector is centred at $\theta_o = 20^o$) the beam broadening effect results in violation of the main lobe mask and the re-optimisation is performed to improve the pattern performance. For *Scenario II* the array element is chosen to be BDRA in order to include the mutual coupling. The BDRA array is subjected to the same mask as the isotropic array. The pattern optimisation is performed using the IzBC-PSO. In the following both problem scenarios would be described.

6.2 Scenario I

6.2.1 Problem Setup

In order to model the isotropic array with N elements and $d = 0.5\lambda$ Equation 2.3 is used. The sector beam pattern obtained after applying the Woodward Lawson technique straight to the array with $N = 8$ and $N = 16$ are shown in Figure 6.1. The array with sixteen elements is presented to indicate the issue related to the small discrete antenna array.

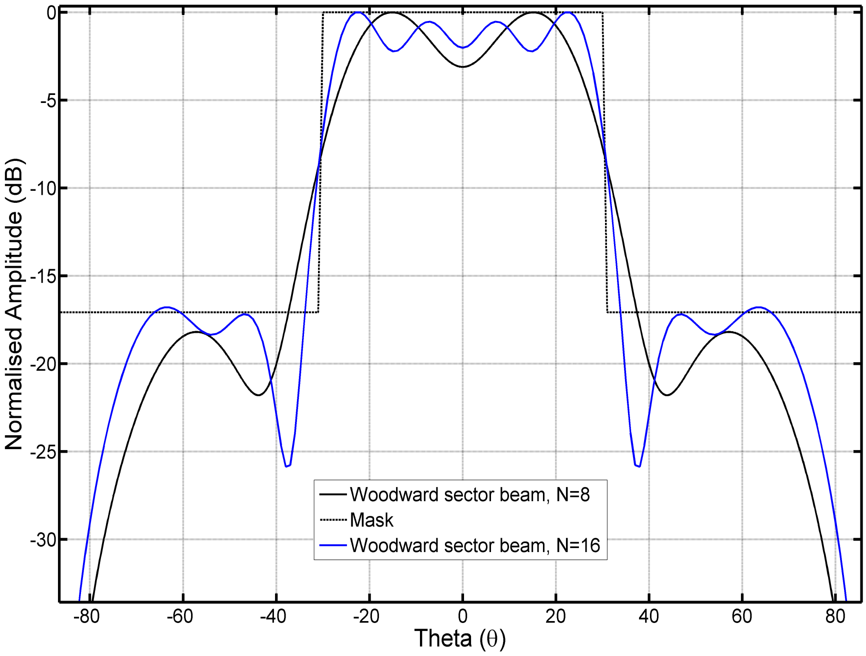

Figure 6.1: The sector beam pattern obtained using the Woodward Lawson method

The Woodward Lawson for $N = 8$ excitation vector is given in Table 6.2. The desired pattern shape was defined by two masks called inner mask (IM) and outer mask (OM). The OM forces the array pattern to have a sector beam for $-30^o < \theta < 30^o$ over a span of 60^o with the reduced SLL. The IM is set to get the ripples in control and to set the HPBW for the sector beam. The IM is set to have a span over 40^o for $-20^o < \theta < 20^o$. With the OM the desired SLL was set to as low as $-16dB$. The target ripple in the main sector beam was set to be $-1dB$.

$$OM = \begin{cases} 0dB & -30 < \theta < 30 \\ -16dB & \text{for all other values of } \theta \end{cases}$$

$$IM = \begin{cases} -1dB & -20 < \theta < 20 \end{cases}$$

The fitness function that is used to meet the mask requirements is shown below;

$$\begin{aligned} fitness = {} & [\varsigma_1(SLL_{des} - SLL_{patt})^2 + \varsigma_2(Patt_{obt}(\theta') - IM(\theta'))^2 \\ & + \varsigma_3(Patt_{obt}(\theta'') - OM(\theta''))^2]^{1/2} \end{aligned} \tag{6.1}$$

Where

SLL_{patt} = the maximum of the radiation obtained for $-90^o < \theta < -30^o$ and $30^o < \theta < 90^o$

$Patt_{obt}$ = obtained pattern

$\theta' = -20^o < \theta < 20^o$

$\theta'' = -30^o < \theta < 30^o$

The contribution multipliers $(\varsigma_1, \varsigma_2, \varsigma_3)$ for the multi-objective function were adjusted such that the problem was simplified as the single objective problem. IzBC-PSO was used to find the optimum results. As it is evident from the fitness function that the optimisation problem is tightly constraint. Which means that the exact target values are required to be met in order to minimise the cost function.

In order to study the sector beam scanning linear phase gradient was applied to Equation 2.3. The sector beam was scanned to $\theta_o = 20^o$. The modified inner and outer masks are given below. The main goal for this study is to improve the sector beam as it scans and mitigate the effect of beam broadening.

$$OM' = \begin{cases} 0dB & -10 < \theta < 50 \\ -16dB & \text{for all other values of } \theta \end{cases}$$

$$IM' = \begin{cases} -1dB & 0 < \theta < 40 \end{cases}$$

The fitness function defined for the scanned sector beam is given by Equation 6.2. All the terms have already defined. The goal is to minimise the fitness function value.

$$\begin{aligned} fitness = {} & [\varsigma_1(SLL_{des} - SLL_{patt})^2 + \varsigma_2(Patt_{obt}(\theta') - IM'(\theta'))^2 \\ & + \varsigma_3(Patt_{obt}(\theta'') - OM'(\theta''))^2]^{1/2} \end{aligned} \tag{6.2}$$

6.2.1.1 Initialising IzBC-PSO

The target OM beamwidth was mapped on the unit circle in z-space starting with the initial root locations corresponding to the uniform excitation vector following the procedure described in chapter 4. The root locations that come under the mask mapping were set for the α bound of 30^o and the bound for other root locations were set to 40^o. The step increments were set to 10^o for each root location in order to improve the optimisation performance. The r bound was defined between 0.1 and 2 for all root locations. The swarm size was set to 30 and the number of iterations were 200 to make the computation total of 6000.

6.2.2 Results & Discussion

The radiation patterns shown in Figure 6.1 compare the performance of Woodward Lawson technique for discrete arrays. In case of $N = 8$ the ripple level is $-3dB$ and mainlobe is violating the outer mask. The radiation pattern performance improves with $N = 16$ as ripples have reduced to $-2dB$ with better

Goal/Parameter	Value
PSLL (dB)	-16
Ripple (dB)	-1
Sector width (Deg)	60
Swarm Size	30
Iterations	200

Table 6.1: Summarising the design objectives and parameters for IzBC-PSO

roll off characteristics compared to the eight element array. The goal here is to show that IzBC-PSO can be used successfully to achieve the desired radiation pattern characteristics with small antenna array of eight elements.

The optimised sector beam synthesis results have been presented in Figures 6.2 and 6.4 for the sector beam centred at $\theta_o = 0^o$ and $\theta_o = 20^o$ respectively. In Figure 6.2 it is shown that IzBC-PSO is successfully used to meet the optimisation objectives. The ripple in main sector is constrained to $-1dB$ which is an improvement of 66.7% compared to the Woodward Lawson sector beam shown in Figure 6.1. The constraint on the main sector beam has been met as well with an improvement of 31.8% compared to the radiation pattern shown in Figure 6.1. The PSLL and average SLL were $-15.5dB$ after optimisation. This was the minimum PSLL obtained subjected to the ripple constraint for eight isotropic element array. The HPBW is noted as 47^o which is 4% narrower compared to the Woodward technique. Figure 6.2 shows best optimisation result. The optimised excitation vector used to obtain the radiation pattern shown in Figure 6.2 is given in the second column of Table 6.2.

In Figure 6.3 the radiation pattern is shown after the optimised excitation vector (used to obtain the radiation pattern shown in Figure 6.2 and given in second column of Table 6.2) was subjected to the linear phase gradient for $\theta_o = 20^o$. No change in the PSLL and average SLL was noted. The ripple was also constraint to $-1dB$. However the beam broadening effect caused the 8% increase in the HPBW as compared to the radiation pattern shown in Figure 6.2. The main sector beam is centred at $\theta_o = 20^o$ but the OM is violated by 21.3%. The optimisation goal was to follow OM and IM as close as possible while maintaining the reduced SLL and ripple constraint.

Figure 6.4 compares both radiation patterns before and after the optimisation once the array was scanned. The excitation vector used to obtain the

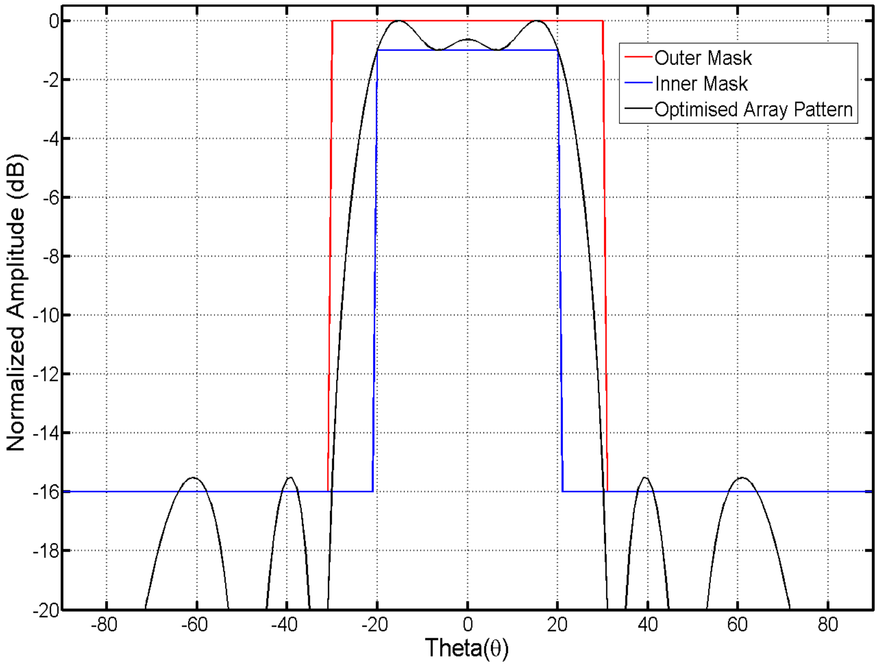

Figure 6.2: The radiation pattern of uniformly spaced linear array (USLA) consisting of eight isotropic elements and the desired outer and inner masks at broadside obtained using PSO

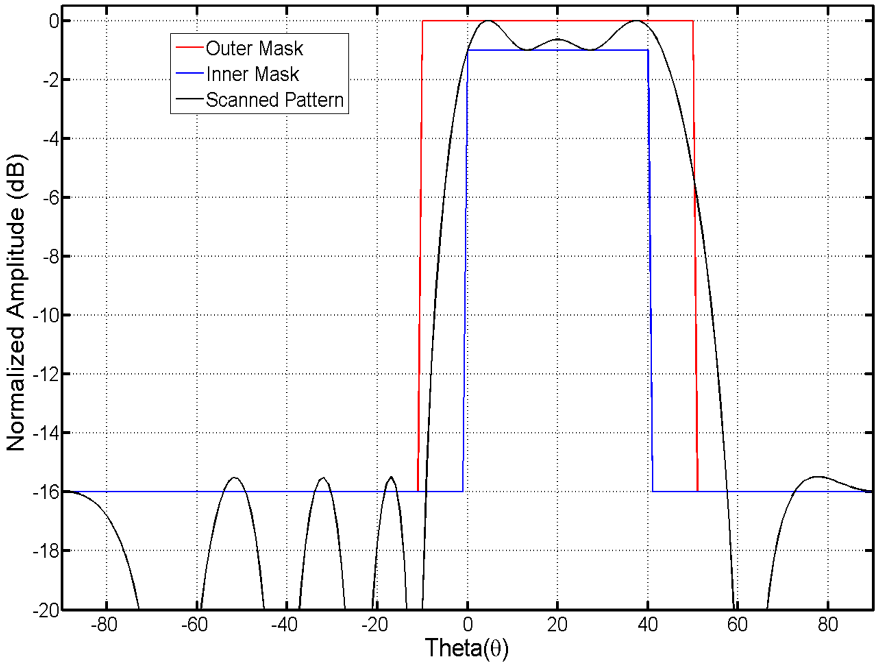

Figure 6.3: The radiation pattern shown in Figure 6.2 scanned to 20^o for $N = 8$

optimised radiation pattern is given in the third column of Table 6.2. It is important to note that to reduce the beamwidth of the sector beam the PSLL/average SLL and the ripple constraint were sacrificed. After the optimisation the mainlobe followed the OM′ but the minimum PSLL and average SLL were found to be $-14.2dB$. This indicates an increase of 8.6% in SLL. The ripple in the main sector beam was found to be $-1.6dB$ which violates the IM′. In order to overcome the beam broadening of the array a trade off exploited that exist for SLL and the mainlobe ripple by using IzBC-PSO. The use of IzBC-PSO has significantly improved the radiation pattern desired characteristics. Only modification performed is to the fitness function and no changes are made to the problem model or algorithm parameters.

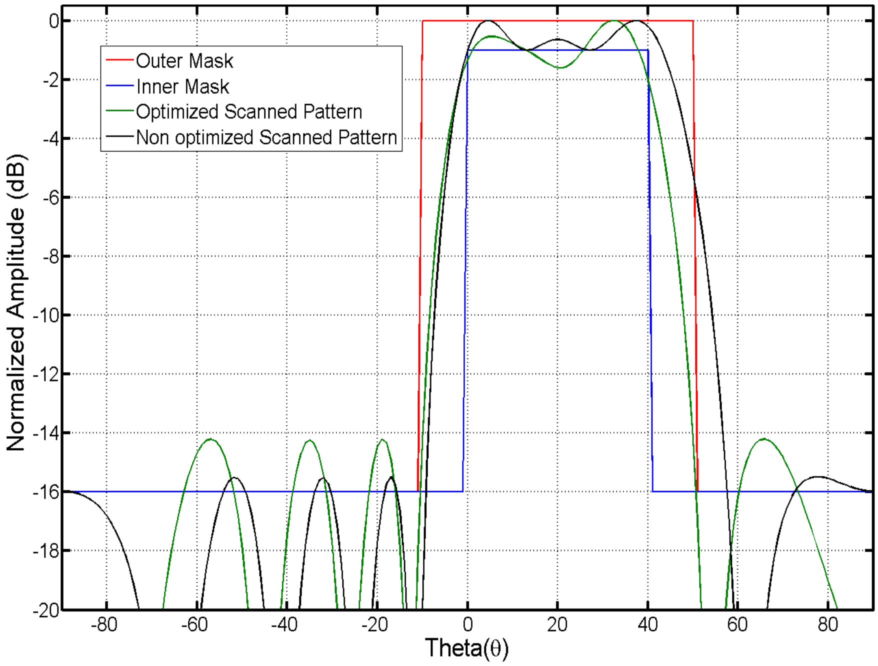

Figure 6.4: The radiation pattern scanned to 20^o obtained after optimization using IzBC-PSO, for $N = 8$

6.3 Scenario II

6.3.1 Problem Setup

For *Scenario II* the isotropic element is replaced by the BDRA element. The array is modelled using Equation 2.5 and the active element patterns. The

Woodward Lawson Excitation Vector		IzBC-PSO for $\theta_o = 0^o$		IzBC-PSO for $\theta_o = 20^o$	
Amplitude	Phase(Deg)	Amplitude	Phase(Deg)	Amplitude	Phase(Deg)
0.20	180	0.25	0	0.24	0
0.15	180	0.10	180	0.21	146
0.22	0	0.33	180	0.33	94
1.00	0	0.28	180	0.18	20
1.00	0	0.28	0	0.32	163
0.22	0	0.87	0	0.87	103
0.15	180	1.00	0	1.00	52
0.2	180	0.68	0	0.71	−3

Table 6.2: The excitation vectors used to obtain radiation patterns shown in Figures 6.1, 6.2 and 6.3

.

element separation is 0.41λ. The goal is to meet the pattern mask requirements for IM and OM described. The Woodward Lawson method was applied to find out the excitation coefficients for $d = 0.41\lambda$ to use in Equation 2.5. The resultant excitation vector is given in Table 6.3 and the radiation pattern is shown in Figure 6.5. The conventional technique was failed to meet the OM requirement. IzBC-PSO was used to optimise the pattern to meet the IM and OM targets as close as possible in the presence of mutual coupling.

All values defined in Table 6.1 hold for the *Scenario II*. The fitness function is given as below;

$$\begin{aligned} fitness = {} & [\varsigma_1(SLL_{des} - SLL_{patt})^2 + \varsigma_2(Patt_{obt}(\theta') - IM(\theta'))^2 \\ & + \varsigma_3(Patt_{obt}(\theta'') - OM(\theta''))^2]^{1/2} \end{aligned} \tag{6.3}$$

All terms have already defined. The same IzBC-PSO initialisation setup was chosen for this scenario. The results of both scenarios are discussed in the following.

6.3.1.1 Initialising IzBC-PSO

The setup used for the sector beam centred at $\theta_o = 20^o$ is the same as *Scenario I*. The root locations on the unit circle are first modified to represent the scanned

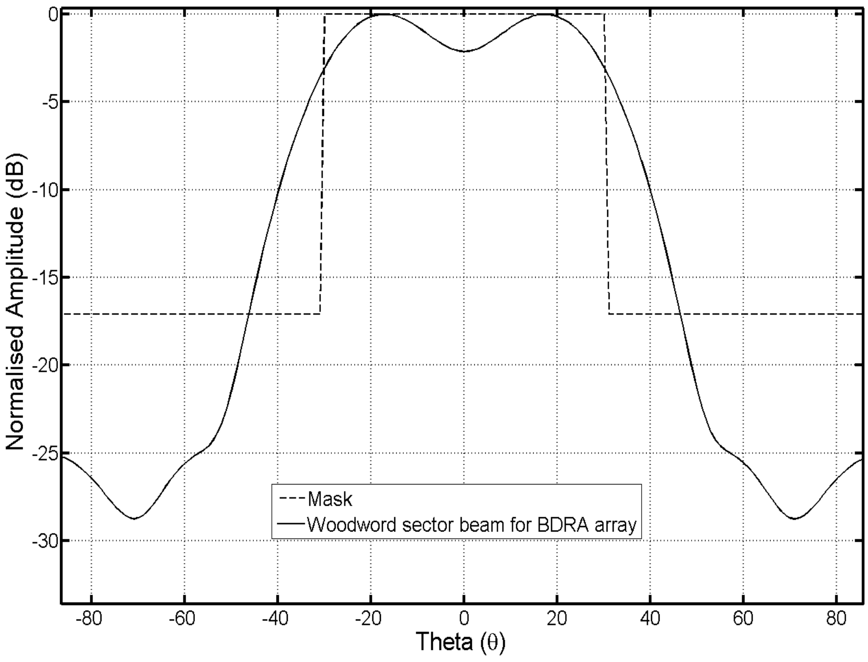

Figure 6.5: The radiation pattern of BDRA array after applying the Woodward Lawson coefficients for $d = 0.41, N = 8$

taper and then mask mapping is performed in the z-space. The optimisation goals and parameters are summarised in Table 6.1. The goal in this case is to find the optimum root locations that correspond to an excitation vector resulting in the radiation pattern that meet the target mask requirements.

6.3.2 Results & Discussion

In this section BDRA array is considered and the mutual coupling effect is highlighted. The results regarding the isolated BDRA element array are compared with the BDRA coupled array. In Figure 6.6 the BDRA array patterns are presented both for the coupled array and the isolated element array while excited by the excitation vector optimised for $\theta_o = 0^o$, given in second column of Table 6.2. The Isolated BDRA element array radiation pattern was obtained using Equation 2.4 and the element pattern shown in Figure 2.18. The mainlobe in case of isolated BDRA element array is 36.7% broader compared to the target OM and the mainlobe ripple is as low as $-0.6dB$. In case of mutual coupling the BDRA coupled array model exhibit the same beam broadening compared to the isolated BDRA element pattern with higher SLL. The optimisation objective in this case was set to contain the mainloabe within OM under the presence of mutual coupling.

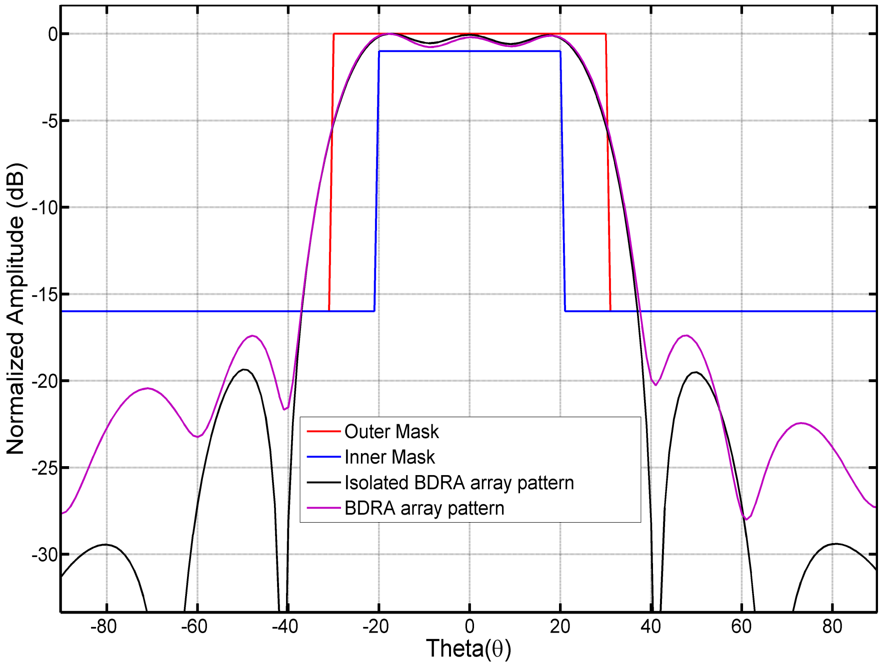

Figure 6.6: Comparison of isolated BDRA element array and BDRA coupled array when excited with the same taper as for the isotropic array radiation pattern shown in Figure 6.2

The IzBC-PSO was applied to the BDRA coupled array and the OM target was met at the cost of higher SLL. Figure 6.7 shows the BDRA array radiation pattern after IzBC-PSO was used to meet the defined IM and OM criteria in the presence of mutual coupling. The optimised excitation vector is given in Table 6.3. The mainlobe ripple was found to be $-0.2dB$. The mainlobe was contained in the OM. The reason for this mainlobe behaviour is that the BDRA element pattern makes the beam broader compared to an isotropic case plus in this case since $d < 0.5\lambda$ therefore mainlobe is broad inherently. In order to fit the mainlobe within the OM constraint the HPBW and SLL are traded compared to the radiation pattern shown in Figure 6.6. The PSLL and average SLL for the radiation pattern shown in Figure 6.7 are $-12.5dB$ and $-13dB$ respectively. On comparing Figures 6.2 and 6.7 the difference between the two optimised solutions is evident. The PSLL has increased by $3dB$ in case of BDRA coupled array with $d = 0.41\lambda$ but mainlobe rippled has reduced by $0.8dB$ compared to an isotropic half wavelength array when the main beam was bound to the same OM. It is shown here that IzBC-PSO was successfully used to achieve the desired main beam with reduced SLL and mainlobe ripple in the presence of mutual coupling.

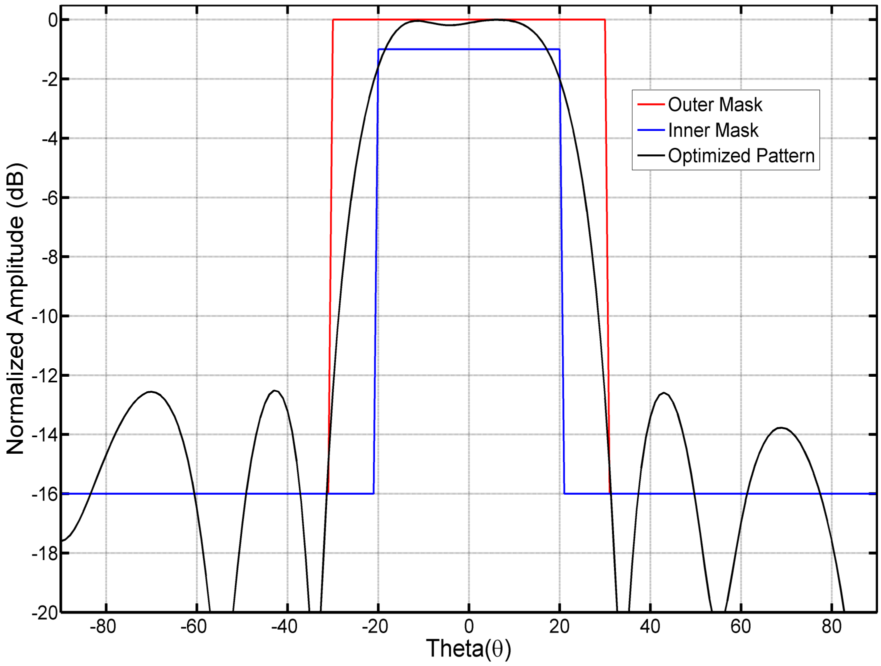

Figure 6.7: The radiation pattern of coupled BDRA array after optimisation using PSO

On comparing the radiation patterns shown in Figures 6.7 and 6.5 the improvement in the sector main beam was found to be 43.4%. The successful implementation of IzBC-PSO not only reduced the ripple from $-2dB$ to $-0.2dB$ but also maintained a reduced SLL. This shows that IzBC-PSO can be effectively used for discrete small arrays in the presence of mutual coupling.

The excitation vector presented in the second column of Table 6.3 was subjected to the linear phase gradient to perform a main beam scan to 20^o. The resultant scanned radiation pattern is shown in Figure 6.8 as Magenta line. The PSLL was noted to be $-10dB$ with the average SLL of $-10.6dB$. The mainlobe violated the OM by 22^o and the beam is not properly centred at the target scan direction. The fitness function given by Equation 6.1 is used in order to achieve the desired main beam characteristics. The re-optimisation of the radiation pattern after scanning 20^o resulted in the pattern shown in Green, Figure 6.8. The excitation vector used to find this plot is given in the second column of Table 6.3.

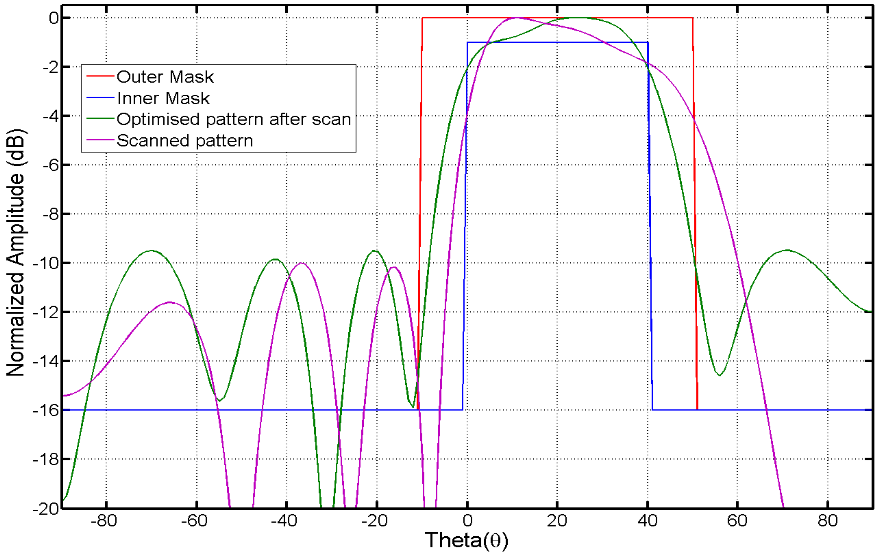

Figure 6.8: The radiation patterns of BDRA array after (Green) and before (Magenta) optimisation using IzBC-PSO scanned to 20^o

Woodward Lawson Taper for d=0.41λ		Optimised Weight Vector ($\theta_o = 0^o$)		IzBC-PSO Weight Vector ($\theta_o = 20^o$)	
Amplitude	Phase	Amplitude	Phase	Amplitude	Phase
0.13	180	0.25	0	0.21	0
0.21	180	0.47	180	0.32	−137
0.26	0	0.22	180	0.19	−112
1.00	0	0.04	0	0.36	31
1.00	0	0.52	0	0.65	−173
0.26	0	1.00	0	0.51	−107
0.21	180	1.00	0	0.89	−85
0.13	180	0.97	0	1.00	−16

Table 6.3: The optimised excitation vectors used to obtain the radiation patterns presented in Figures 6.7 and 6.8

On comparing the two radiation patterns shown in Figure 6.8 it is clear that the mainlobe is successfully contained in the target OM. The improvement in the main beam width is 28.2%. The resultant PSLL and average SLL were found to be $-9.5dB$. The mainlobe intersected the IM at $-2dB$ and there were no ripples. The target shape of the mainlobe was obtained at the cost of higher SLL. Study of the presented scenarios in this section shows the robustness of the IzBC-PSO technique. The proposed technique was utilised under mutual coupling and significant improvements were achieved.

6.4 Chapter Summary

The important results of this chapter are:

- Excitation taper sampling problem is highlighted for the discrete small antenna array that limits the use of conventional techniques (§6.2.1, §6.2.2);
- A nonlinear pattern synthesis problem is solved by using the proposed scheme for both isotropic and non isotropic elements which shows that this scheme is equally effective for practically small discrete arrays (§6.2.2, §6.3.2);
- IzBC-PSO is used successfully to significantly improve the radiation pattern performance of the small discrete antenna array of isotropic element with $N = 8$ and $d = 0.5\lambda$ (§6.2.1.1);
- It is shown that radiation pattern degradation due to array scanning can be improved using the proposed optimisation scheme (§6.2.2);
- The mutual coupling effect is mitigated and radiation pattern synthesis objectives are achieved using the same optimisation model (§6.3.2);
- IzBC-PSO is used successfully to improve the pattern degradation in terms of beam broadening when the mainlobe is scanned to $\theta_o = 20^o$ and reduced SLL (§6.3.2);

Chapter 7

Wideband Phased Array Optimisation

This chapter concerns the wideband performance of small discrete periodic linear phased antenna arrays. The wideband performance optimisation problem is divided into two main scenarios to elaborate the solutions provided for the specific wideband features. The relationship between the frequency variation and the pattern beamwidth is developed in section 7.1.1 of this chapter. It is desirable in some wideband high resolution applications to maintain the main beam HPBW as the frequency varies. In case of periodic linear array the beam naturally broadens as the frequency is decreased. The *Scenario I* of this chapter considers this as the optimisation problem and sets the maintenance of HPBW while reducing the SLL as the problem objective. The IzBC-PSO is used for the optimisation of this problem that provides the suboptimal solution for this problem. The array consisting of isotropic elements is considered for this scenario.

The *Scenario II* considers array mutual coupling effect. In order to simplify the wideband mutual coupling problem an array consisting of a hypothetical wideband element is assumed with $N = 8$. It is assumed that the self impedance of this element and the element pattern does not vary with the frequency. However, the mutual coupling model for this hypothetical element is sensitive to the frequency variation and is identical to the dipole coupling behaviour as modelled in chapter 2 section 2.10.5. The Chebychev taper for SLL=$-30dB$ is applied to this array. The optimisation goal in this scenario is to maintain the target SLL while the main beam is at $\theta_o = 0^o$ and also when scanned to

$\theta_o = 30^o$ [44]. In literature stochastic optimisation techniques have been applied to various wideband array problems [58, 109–112].

7.1 Scenario I

The focus of this problem scenario is on maintaining the HPBW while reducing the SLL across frequency sweep. The problem objectives are presented in the form of a fitness function. This problem is solved by using IzBC-PSO which minimises the defined fitness function. The problem setup used for this scenario and the results obtained are discussed below.

7.1.1 Problem Setup

For this scenario a linear antenna array consisting of eight isotropic elements was considered. The array geometry is the same as described in the chapter 2. This linear is represented mathematically as;

$$AF(\theta) = \sum_{n=1}^{N} w_n e^{j(n-1)kd\sin\theta} \tag{7.1}$$

Which can be further modified as expressed below;

$$AF(\theta) = \sum_{n=1}^{N} w_n e^{j(n-1)(\frac{2\pi f}{c})d\sin\theta} \tag{7.2}$$

Where f is the frequency, c is the speed of light and other terms are already defined. For this example a frequency band between a maximum of $1GHz$ and a minimum of $0.6GHz$ is considered. The array is half wavelength separated at $1GHz$. For isotropic array the mathematical expression to find the half power points is taken from Balanis [3] and modified to suite our array geometry. It is given as;

$$\theta_h = \sin^{-1}\left(\frac{\pm 1.391\lambda}{\pi N d}\right) \tag{7.3}$$

Where θ_h is the half power point of the array radiation pattern. If Equation 7.3 is solved for positive value only then the total HPBW is given by $2 * \theta_h$. Equation 7.3 is further modified in terms of frequency (f) as expressed below;

$$\theta_h = \sin^{-1}\left(\frac{\pm 1.391c}{\pi N d f}\right) \tag{7.4}$$

$$\Rightarrow \theta_h \propto \frac{1}{f} \tag{7.5}$$

Equation 7.5 implies that the HPBW of isotropic array is inversely proportional to the frequency. Therefore with decrease in frequency the HPBW will increase. For this scenario the objective is to maintain the HPBW and reduce the SLL simultaneously across the frequency band. In order to find an optimum solution to this problem IzBC-PSO is used. In the following initialisation of IzBC-PSO is described.

7.1.2 IzBC-PSO Setup

The starting point for this optimisation problem is the uniformly excited antenna array at $1GHz$. The root locations are shown in Figure 7.1. The HPBW is found to be approximately 13^o corresponding to FNBW of 30^o. The goal is to maintain this HPBW as the frequency sweeps down. The frequency varies from $1GHz$ to $0.6GHz$ in the steps of $0.1GHz$ for this scenario. In order to meet this objective the root locations marked as 1 and 7 are adjusted for each frequency considered. These root locations are the first nulls of the radiation pattern in θ space marked as $FNBW_1$ and $FNBW_2$. The FNBW of the radiation pattern in θ space is chosen to be mapped on the unit circle in terms of separation in α between roots 1 and 7 as α_{sep}. The root locations under consideration can be expressed as;

$$z_1 = e^{jkd\sin(FNBW_1)}$$

$$z_1^m = e^{j\frac{2\pi f^m}{c}d\sin(FNBW_1)} \tag{7.6}$$

And for root location number 7;

$$z_7^m = e^{j\frac{2\pi f^m}{c}d\sin(FNBW_2)} \tag{7.7}$$

Where z_1^m and z_7^m are the root locations for root number 1 and 7 as marked in Figure 7.1 in z-space for a sample frequency f^m for m=1,2,..,5 . For each sample frequency value this separation between roots 1 and 7 was determined as given below;

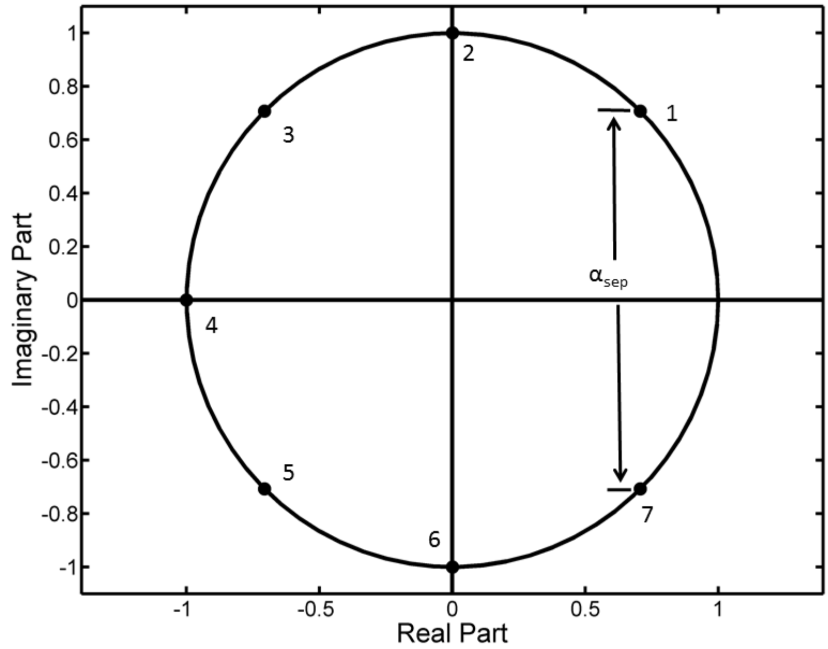

Figure 7.1: Root distribution of the uniform taper in z-space

$$\alpha_m = \frac{2\pi f}{c} d|(\sin(FNBW_1) - \sin(FNBW_2))| \tag{7.8}$$

Where α_{sep} is the separation between roots 1 and 7 as shown in Figure 7.1. Once the corresponding α_{sep} is determined the root locations 1, 7 and 4 are fixed both in α and r domain whereas all other roots have their boundaries defined following the procedure described in chapter 4. The r dimension is bound to vary between 0.5 and 1.5. The starting α bound is set to 20^o with an increment of 10^o. The optimum root locations are determined in order to obtain the reduced SLL while maintaining the FNBW. Since the root locations determining the FNBW are fixed for all the frequency values considered therefore the simplified single objective fitness function is given as below;

$$fitness = \sqrt{(SLL_{des}^{f_m} - SLL_{patt}^{f_m})^2} \tag{7.9}$$

Where $SLL_{des}^{f_m}$ is the desired SLL for m^{th} frequency value under consideration. It is set to $-20dB$ in order to reduce the SLL while maintaining the FNBW for the corresponding f_m. The fitness function defined in Equation 7.9 is used to obtain five independent optimised excitation weight vectors for each frequency value analysed simultaneously. The simulation results are presented and compared in the following section. The discussion is based on comparing the optimised and non optimised radiation patterns and highlighting the advantage of IzBC-PSO.

7.1.3 Results & Discussion

First the effect of the frequency variation on the array radiation patterns is presented in Figure 7.2.

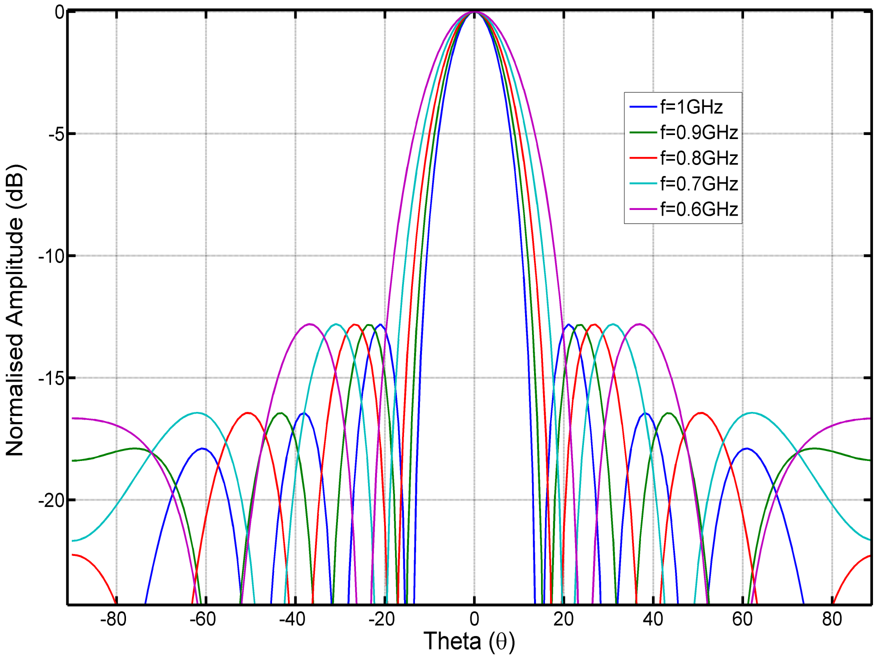

Figure 7.2: The array radiation patterns as the frequency sweeps from $1GHz$ to $0.6GHz$ in steps of $0.1GHz$

The radiation patterns were normalised with respect to $f = 1GHz$ radiation pattern. All radiation patterns have the same value of PSLL and the main lobe peak. The results from Figure 7.2 has been summarised in Table 7.1. The HPBW varies with the frequency variation as shown in the Figure 7.3 that is obtained from Equation 7.4 and verified from the results presented in Figure 7.2.

On comparing the two curves presented in Figure 7.3 before and after optimisation it is evident that IzBC-PSO has improved the HPBW performance significantly. The variation in HPBW for isotropic array is noted as 62.5%.

Frequency (GHz)	PSLL (dB)	Average SLL (dB)	HPBW (Deg)
1.0	−13	−15.8	13.7
0.9	−13	−15.8	15.1
0.8	−13	−17.2	16.9
0.7	−13	−14.6	19.2
0.6	−13	−14.6	22.3

Table 7.1: Tabular summary of the Figure 7.2

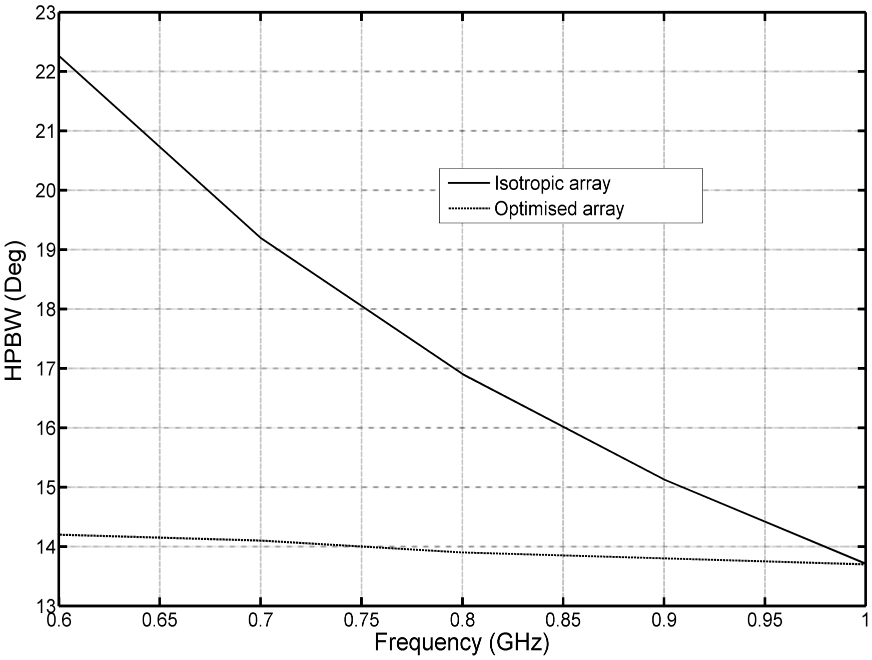

Figure 7.3: The HPBW variation as Frequency sweeps between 1*GHz* and 0.6*GHz* for isotropic array (solid line) and after the optimisation (dashed line)

After optimisation it is significantly reduced to 4% with maximum HPBW at $0.6GHz$ of 14.2^o.

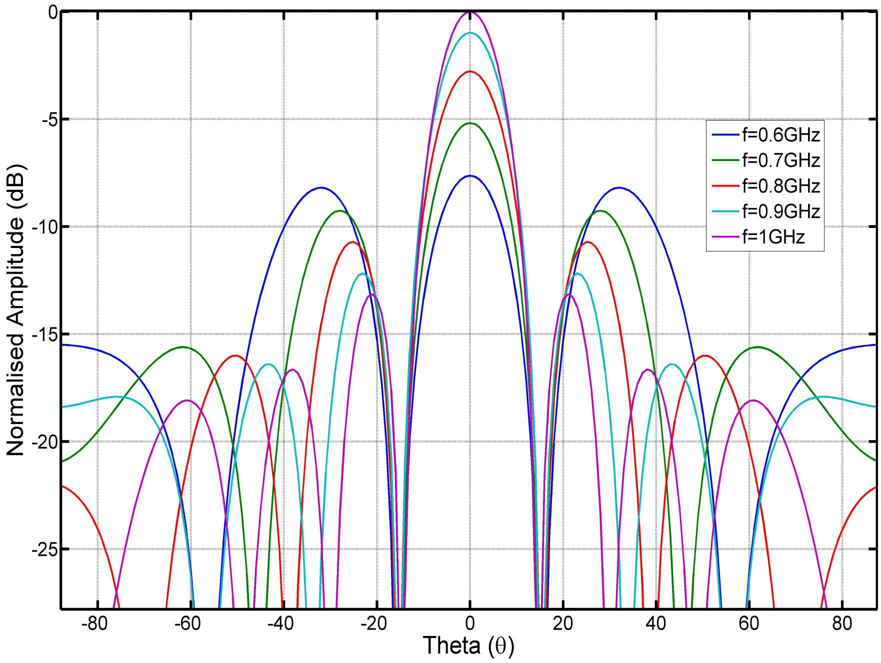

Figure 7.4: The array radiation patterns after fixing the root locations 1 and 7 in z-space to maintain the FNBW

As the first step of the optimisation process the FNBW were modified to maintain the HPBW across the frequency band. The effect of this modification over the SLLs is shown in Figure 7.4. The PSLL has risen from $-13.2dB$ at $1GHz$ to $-0.6dB$ at $0.6GHz$. This indicates a significant rise of $12.6dB$ in the PSLL over the frequency band. The results from Figure 7.4 are presented in Table 7.2. IzBC-PSO is used to obtain the reduced SLL while maintaining HPBW.

Frequency (GHz)	PSLL (dB)	Average SLL (dB)	HPBW (Deg)
1.0	−13.0	−15.8	13.7
0.9	−11.0	−15.1	13.8
0.8	−7.9	−13.5	13.9
0.7	−4.0	−7.2	14.1
0.6	−0.6	−4.2	14.2

Table 7.2: Tabular summary of the Figure 7.4

The optimised results for the reduced SLL are presented in Figure 7.5. The results are summarised in Table 7.3. On comparing the PSLL columns of Table

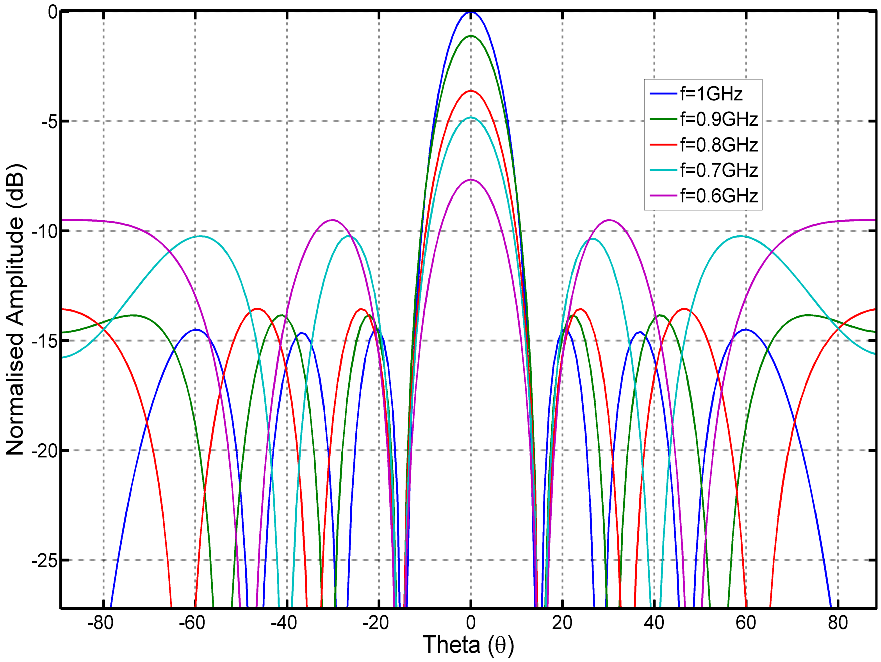

Figure 7.5: The optimised radiation patterns with reduced SLL and constant HPBW

7.2 and 7.3 significant improvement after optimisation is evident. The PSLL at $1GHz$ was reduced by $1.5dB$ while the HPBW was 13.7^o. The improvement in PSLL for $0.6GHz$ was noted to be $1.2dB$ with the HPBW of 14.2^o. The maximum HPBW variation over the target frequency band was 0.5^o. For each frequency considered in the band IzBC-PSO produced the radiation pattern with target HPBW and the reduced PSLL. It is clearly shown that the use of IzBC-PSO has significantly improved the radiation pattern performance. If IzBC-PSO is not used then the resultant patterns shown in Figure 7.4 have higher SLL. The use of IzBC-PSO ensures that the radiation patterns meet the required target HPBW with the reduced SLL. The IzBC-PSO was used to obtain five independent optimised excitation weight vectors corresponding to the frequencies considered in the band.

7.2 Scenario II

In this work wideband performance of a small array consisting of eight wideband elements is investigated with the SLL constraint in the presence of mutual coupling over a frequency band of $0.6 - 1.4GHz$. To simplify the problem it was

Frequency (GHz)	PSLL (dB)	Average SLL (dB)	HPBW (Deg)
1.0	−14.5	−14.5	13.7
0.9	−12.7	−12.7	13.8
0.8	−9.9	−9.9	13.9
0.7	−5.4	−5.4	14.1
0.6	−1.8	−1.8	14.2

Table 7.3: Tabular summary of the Figure 7.5

assumed that the self impedance of the wideband element is not varying over the frequency band under consideration. The mutual coupling characteristics of this assumed wideband element are identical to the dipole element. The mutual coupling model defined in chapter 2 section 2.10.5 is used to determine the coupling at various frequency values in the band. The coupling behaviour shown in Figure 7.6 is only for two dipoles in free space. However the coupling consideration for this work is not limited to two consecutive elements. The current on a given element is the sum of the all the induced currents that have been induced due to the presence of the other active elements as discussed in section 2.10.5.

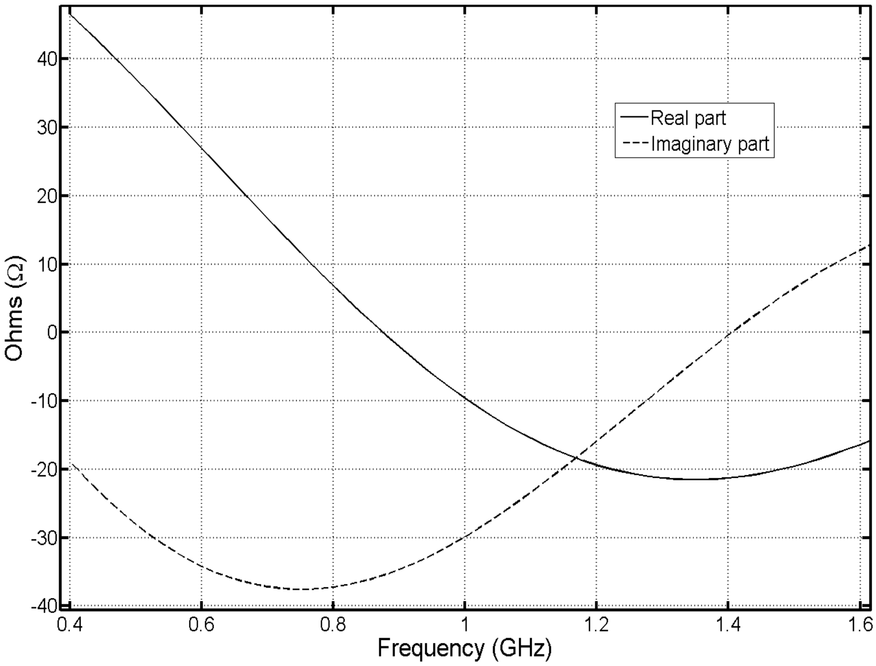

Figure 7.6: The mutual impedance variation of real and imaginary parts against the frequency

As it is well known, mutual coupling limits the performance of wideband and scanning arrays. In order to solve this problem IzBC-PSO is modified to optimise over the frequency band. The optimum complex weights are determined for the uniformly spaced array for broadside and when it is scanned to 30^o without a priori knowledge of mutual coupling while the target PSLL is $-30dB$. The bandwidth performance is compared with the conventional Dolph-Chebychev distribution [6] for eight ($N = 8$) and sixteen element ($N = 16$) array. It is indicated that the bandwidth performance is significantly degraded in small array ($N < 10$) compared to array with $N = 16$. It is shown in [42] that PSO can be used effectively to improve SLL performance in small arrays compared to conventional methods. Schelkunoff's [23] unit circle approach is used to find the optimum weights. This approach was adopted because of fast convergence as it enables IzBC-PSO to define variable boundaries intelligently in solution space.

The goal in this chapter is to obtain a single optimised excitation weight vector that could produce radiation patterns with PSLL within tolerance of $\pm 2dB$ over a band of frequency ($0.6 - 1.4GHz$) for small antenna array. In case of scanned array an additional tolerance criterion is introduced to allow the radiation pattern normalised amplitude in the scan direction to drop as low as $-1dB$.

7.2.1 Problem Setup

A periodic array consisting of eight wideband elements is assumed along the x-axis. The element separation is half wavelength at $1GHz$. Equation 7.2 can be used to define such an array when $\theta_o = 0$. For an arbitrary scan direction θ_o the excitation weight vector is modified as follows;

$$\beta = -\frac{2\pi f}{c} d \sin\theta_o \tag{7.10}$$

$$w_n = a_n e^{j(n-1)\beta} \tag{7.11}$$

The array factor in Equation 7.2 can be modified as shown in Equation 7.11;

$$AF(\theta) = \sum_{n=1}^{N} (a_n e^{j(n-1)\beta}) e^{j(n-1)(\frac{2\pi f}{c})d\sin\theta} \tag{7.12}$$

In order to study the wideband performance of the scanned array linear phase gradient was determined using Equation 7.10. The element separation (d) is set to half wavelength, frequency (f) is set to $1GHz$ and $\theta_o = 30^o$ in Equation 7.10. Once the β was determined it is kept constant across the frequency band. The mutual coupling matrix, Z, was determined by using the MoM based technique described in chapter 2. The mutual coupling effect over the weight vector is given by Equation 7.13.

$$w_n^{'} = Z^{-1} \cdot w_n \tag{7.13}$$

Where $w_n^{'}$ is the coupled excitation vector. For this problem w_n is the $-30dB$ Dolph-Chebychev distribution. The coupled excitation vector is used to determine the array radiation pattern that shows the mutual coupling effect. The Equation 7.2 after including the mutual coupling effect is shown below;

$$AF^{'}(\theta) = \sum_{n=1}^{N} w_n^{'} e^{j(n-1)(\frac{2\pi f}{c})d \sin\theta} \tag{7.14}$$

Where $AF^{'}(\theta)$ is the changed array pattern. Equation 7.14 is used in IzBC-PSO as the coupled array model. The bandwidth performance is compared in terms of PSLL variation and fractional bandwidth (FBW). The mathematical expression used to determine the FBW is given as;

$$FBW = \frac{F_2 - F_1}{F_c} \times 100 \tag{7.15}$$

Where
F_2 = final frequency in the band considered
F_1 = initial frequency in the band considered
$F_c = (F_1 + F_2)/2$

The following section describes the initialisation of the IzBC-PSO.

7.2.2 IzBC-PSO Setup

It is desired to find a single excitation vector that could produce the radiation patterns within acceptable tolerance over the defined frequency band. Therefore it is necessary to evaluate Equation 7.14 over the band. In order to achieve the optimisation objective this problem is solved for the sample frequency values taken form the band simultaneously. To get the effective wideband performance the band ($0.6 - 1.4GHz$) is sampled in steps of $0.2GHz$ therefore five independent radiation patterns are evaluated for the PSLL performance. The PSLL values obtained from these radiation patterns are compared to each other to find maximum PSLL value among these. This maximum PSLL ($PSLL_{max}$) thus found is used to compare it with the target SLL. The main beam direction is also considered at each individual frequency and compared with the target mainlobe direction. The scan direction that has maximum difference is taken into account. The fitness function used for this optimisation problem is given below;

$$fitness = \sqrt{(SLL_{des} - PSLL_{max})^2 + (Scan_{des} - Scan_{patt})^2} \tag{7.16}$$

Where

$SLL_{des} = -30dB$

$PSLL_{max}$ = maximum PSLL obtained when the radiation patterns at sample frequencies are obtained with single weight vector.

$Scan_{des}$ = desired scan directions include $\theta_o = 0^o$ and also for a later consideration $\theta_o = 30^o$

$Scan_{patt}$ = the obtained scan direction after comparing the radiation patterns

The optimisation goal is to minimise the fitness function and find a single weight vector that could produce the radiation patterns with PSLL meeting $\pm 2dB$ tolerance over the frequency band considered

Since a single optimised weight vector is obtained therefore the boundaries were defined following the steps given in chapter 2... The r dimension was bound to vary between 0.5 and 1.5. The starting α bound was set to 20^o with an increment of 10^o. The simulation results are presented and discussed in the next section.

7.2.3 Results & Discussion

To highlight the mutual coupling effect Dolph-Chebychev taper (-30dB) is used in the presence of mutual coupling. Equations 7.13 and 7.14 are used to change the Dolph-Chebychev taper and to obtain the resultant radiation patterns. The array patterns thus obtained are referred to as Dolph-Chebychev array patterns (DCAP). The DCAP at sample frequencies of 0.6*GHz*, 1*Ghz* and 1.4*GHz* are shown in Figure 7.7. The results from Figure 7.7 are summarised in Table 7.4. The PSLL obtained at 0.6*GHz* and 1.4*GHz* are $-27dB$ which is $1dB$ higher compared to the defined PSLL tolerance. At 1*GHz* the PSLL is $0.3dB$ higher compared to the defined tolerance. The Figure 7.8 shows the radiation patterns at the sample frequencies obtained by using the single optimised wight vector found by using the IzBC-PSO. The results are summarised in Table 7.4. At 0.6*GHz* and 1*GHz* the PSLL is $-30dB$ meeting the exact target PSLL requirement. The HPBW in case of the optimised radiation patterns is found slightly greater then the DCAP about 1.4^o at 0.6*GHz* and 0.5^o at 1*GHz*. At 1.4*GHz* the PSLL was $-29.5dB$ with an increase of 0.5 in HPBW compared to DCAP at the same sample frequency. It is clearly shown that IzBC-PSO has successfully used to find the desired optimised weight vector in order to meet the PSLL requirement in the presence of mutual coupling. If matrix inversion technique is used in this case to mitigate the mutual coupling then at each sample frequency an individual set of excitation vector is required which complicates the wideband array feed.

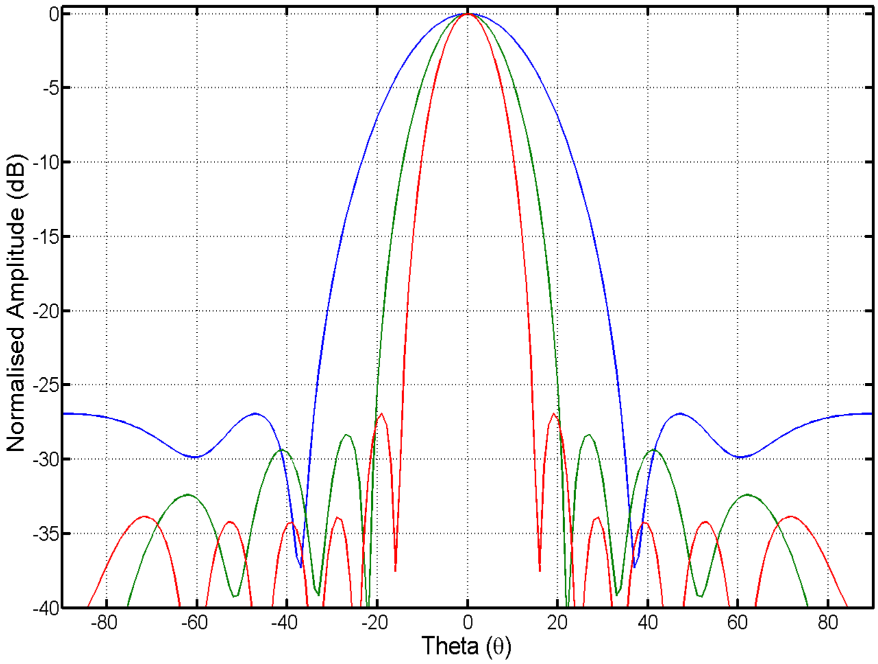

Figure 7.7: The radiation patterns at three sample frequencies obtained by using the Dolph-Chebychev $-30dB$ taper in the presence of mutual coupling

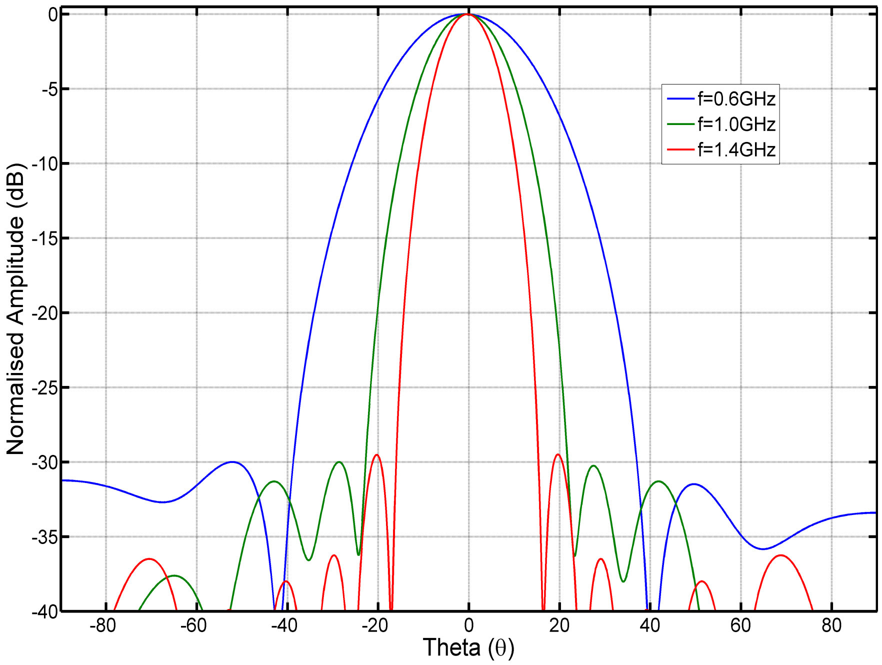

Figure 7.8: The radiation patterns obtained by the single optimised weight vector at sample frequencies in the presence of mutual coupling

Frequency (GHz)	Coupled Dolph-Chebychev Array Patterns		Optimised Array Pattern	
	PSLL (dB)	HPBW (Deg)	PSLL (dB)	HPBW (Deg)
0.6	−27	26.6	−30	28
1.0	−28.3	16.4	−30	17
1.4	−27	11.6	−29.5	12.1

Table 7.4: Tabular summary of the Figures 7.7 and 7.8

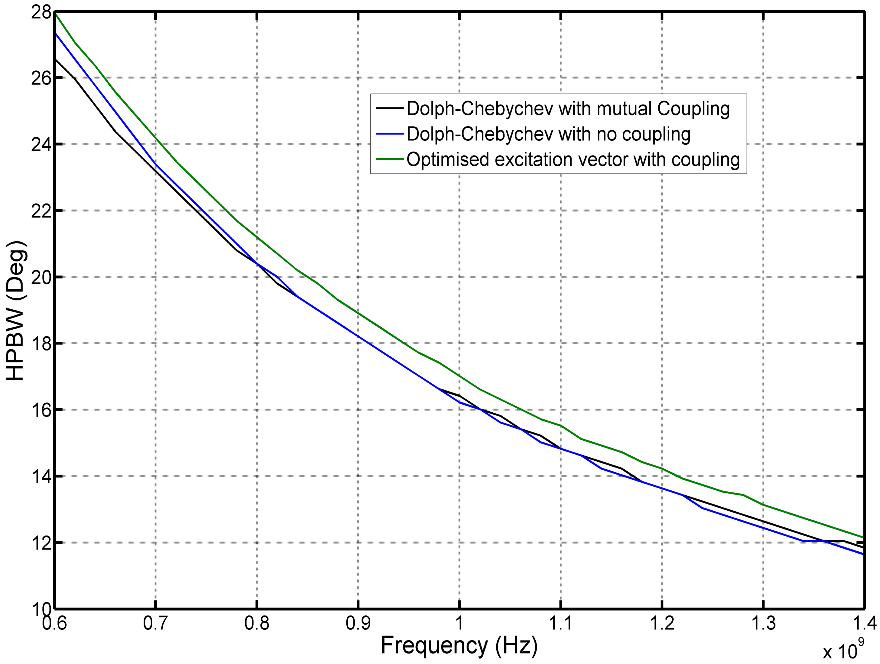

Figure 7.9: The HPBW comparison among the coupled and non coupled Dolph-Chebychev array and optimised array radiation pattern

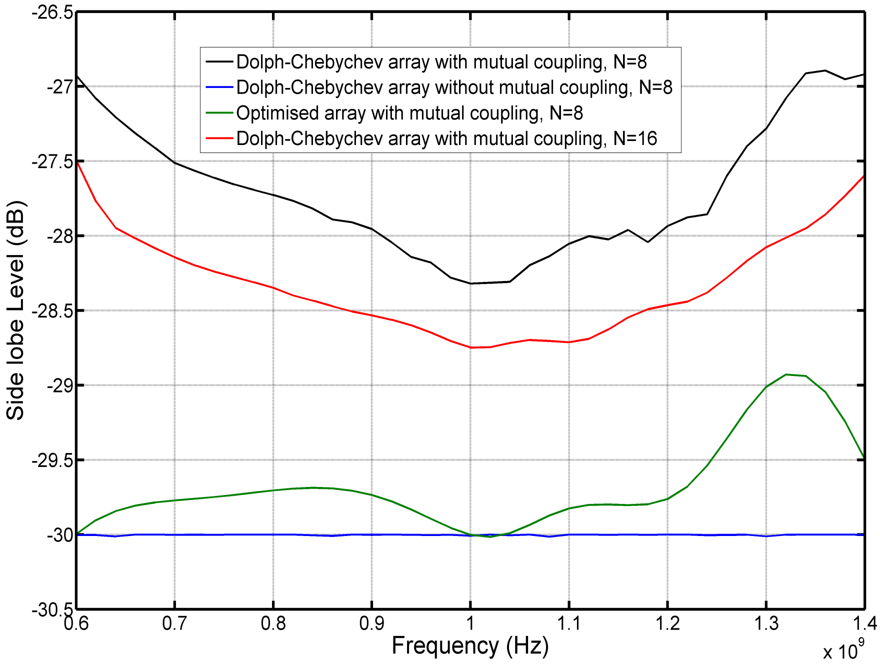

Figure 7.10: The comparison of the PSLL variation across the frequency band for the Dolph-Chebychev (coupled and non coupled) and optimised array patterns in the presence of mutual coupling

The HPBW and PSLL performance for DCAP (coupled and non coupled) and the resultant optimised radiation pattern are shown in Figures 7.9 and 7.10 respectively. To determine these performances the frequency band was sampled with $0.02GHz$ steps. Figure 7.9 shows HPBW over band and that all three radiation pattern types have similar trend. The maximum and minimum difference between the HPBW in case of coupled DCAP and the optimised radiation pattern was found to be 1.4^o at $0.6GHz$ and 0.5^o at $1GHz$ respectively.

The PSLL variation across the frequency band is presented in Figure 7.10 for $N = 8$ and $N = 16$. It is shown that DCAP under no mutual coupling exhibit stable $-30dB$ PSLL across the band. However in the presence of mutual coupling PSLL is not within the defined PSLL tolerance for both array types. The PSLL bandwidth performance for $N = 16$ DCAP is presented to highlight severity of pattern degradation due to mutual coupling in small wideband arrays. In case of $N = 8$ DCAP the minimum PSLL value over the band was $-28.3dB$ which is $1.7dB$ higher then the target PSLL. In order to compare the fractional bandwidth (FBW) over which the Dolph-Chebychev taper without any compensation was able to meet the tolerance, F_1 and F_2 were recorded from Figure 7.10 as $0.91GHz$ and $1.19GHz$. These are the points where PSLL curve for coupled DCAP exceeds the $-28dB$ level. The resultant FBW was determined using the Equation 7.15 to be 26.7%. However the minimum PSLL obtained in case of $N = 16$ DCAP is $-28.8dB$ which is $1.2dB$ higher compared to the target PSLL and shows an improvement of $0.5dB$ over the small array. The FBW for this array with $F_1 = 0.66GHz$ and $F_2 = 1.32GHz$ was found to be 66.7%. It is evident from these results that a large array compared to an array with ($N = 8$) has better bandwidth performance without any compensation for mutual coupling.

The PSLL curve for the optimised radiation pattern has minimum PSLL value of $-30dB$ which is exactly equal to the target PSLL. The single optimised excitation vector used to determine the radiation patterns over the band kept the PSLL successfully under the defined tolerance value over the entire band. The FBW for the optimised weight vector was found to be 80%. This has shown an improvement of 66.2% in bandwidth over the non compensated $N = 8$ DCAP and 19.4% over the non compensated $N = 16$ DCAP.

It is clearly shown here that small arrays are more sensitive to mutual coupling compared to comparatively large arrays over a frequency band. It is further shown here that IzBC-PSO is successfully used to significantly improve the PSLL performance over a range of frequencies in small wideband arrays in the presence of mutual coupling. If IzBC-PSO is not used the mutual coupling changes the radiation patterns at various frequency in the band as evident from Figures 7.7 and 7.10. It is important to note that this wideband performance is achieved with a single excitation weight vector obtained by IzBC-PSO and given in Table 7.5. This shows that IzBC-PSO technique has advantage over the inversion matrix mutual coupling compensation technique as it requires to have different set of excitation weights at different frequencies which complicates the feeding structure of a small wideband array. Furthermore the use of IzBC-PSO for $N = 8$ has outperformed the PSLL bandwidth performance of comparatively large array ($N = 16$ DCAP).

Optimised Excitation Vector	
Amplitude	Phase (Deg)
0.20	0
0.49	−9
0.78	−11
1.00	−10
1.00	−9
0.79	−6
0.50	−2
0.22	11

Table 7.5: The IzBC-PSO excitation vector used to obtain the plots shown in Figures 7.8 and 7.10

The mutual coupling varies with the scan direction [113] and its effect on SLL is shown in Figure 7.11. To obtain the scanned pattern under mutual coupling a linear phase shift was applied for $\theta_o = 30^o$ to Dolph-Chebychev $-30dB$ taper using Equation 7.11 and then Equation 7.13 was used. The mutual coupling has significant effect over the PSLL of the DCAP for $N = 8$. The results are presented at the sample frequencies with steps of $0.2GHz$ over the band. In this situation there are two major degradations to the DCAP one is to the PSLL and the other is to the scan direction as indicated in Figures 7.11 and 7.14. At all the sample frequencies the PSLL for DCAP has violated the defined PSLL tolerance. The grating lobes start to appear at $1.2GHz$. The scan direction varies from 17.7^o to 46.6^o over the frequency band due beam squinting.

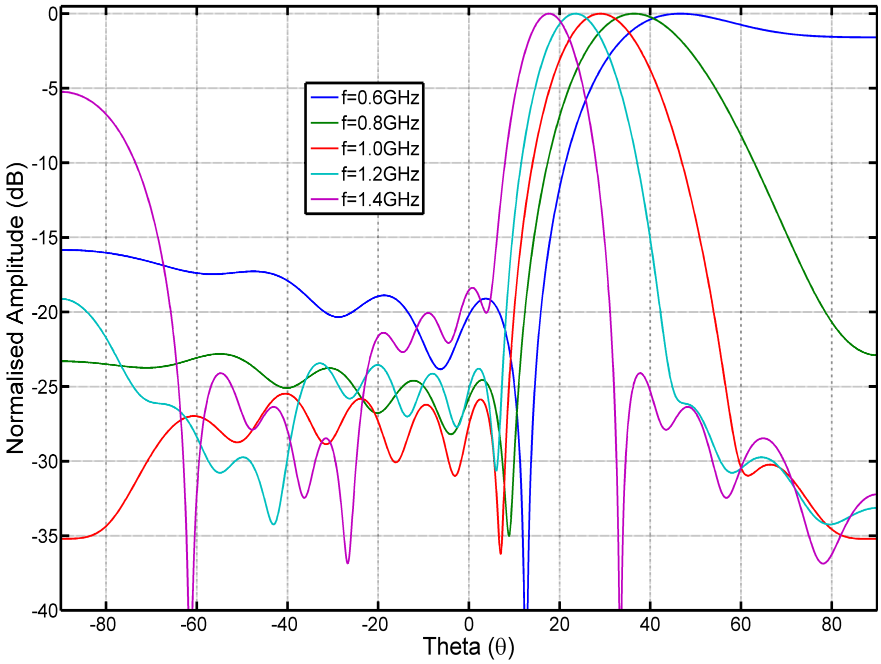

Figure 7.11: The radiation patterns obtained by applying the linear phase gradient to Dolph-Chebychev $-30dB$ taper in the presence of mutual coupling while scanned to $\theta_o = 30^o$

The IzBC-PSO is used to obtain a single excitation weight vector that could maintain the PSLL below the defined tolerance and also improve the mainlobe scan deviation. The results obtained by the optimised weight vector are presented in Figure 7.12. It is evident that the PSLL performance has improved significantly after applying IzBC-PSO. The minimum PSLL obtained for the sample frequencies presented was noted to be $-30dB$ that is exactly equal to the target PSLL. Figure 7.12 proves the significance for using IzBC-PSO in the presence of mutual coupling.

The variation in the PSLL over the frequency band is compared in Figure 7.13 for DCAP ($N = 8$ and $N = 16$) with the optimised radiation patterns obtained using IzBC-PSO. The minimum PSLL in case of $N = 8$ DCAP was $-25.5dB$ at $1GHz$. This values is $2.5dB$ and $4.5dB$ higher then the defined PSLL tolerance and target value. The comparatively larger array with $N = 16$ excited by Dolph-Chebychev $-30dB$ taper has minimum PSLL of $-28.6dB$ at $1GHz$ and it obeys the PSLL tolerance. The FBW for this array with $F_1 = 0.89GHz$ and $F_2 = 1.16GHz$ was found as 26.3%. It is shown that with non compensated for

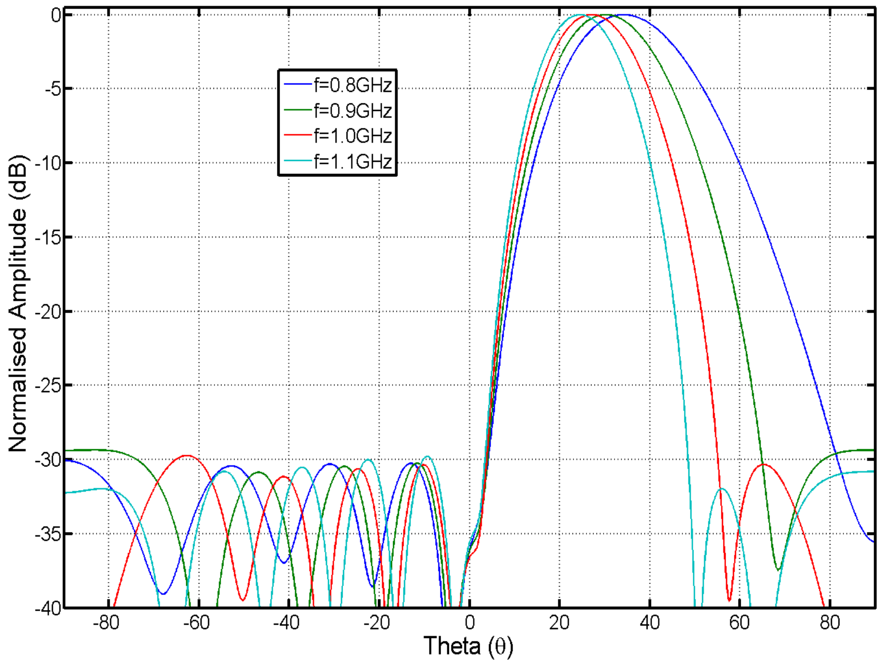

Figure 7.12: The radiation patterns obtained by applying the single IzBC-PSO optimised excitation vector in the presence of mutual coupling while scanned

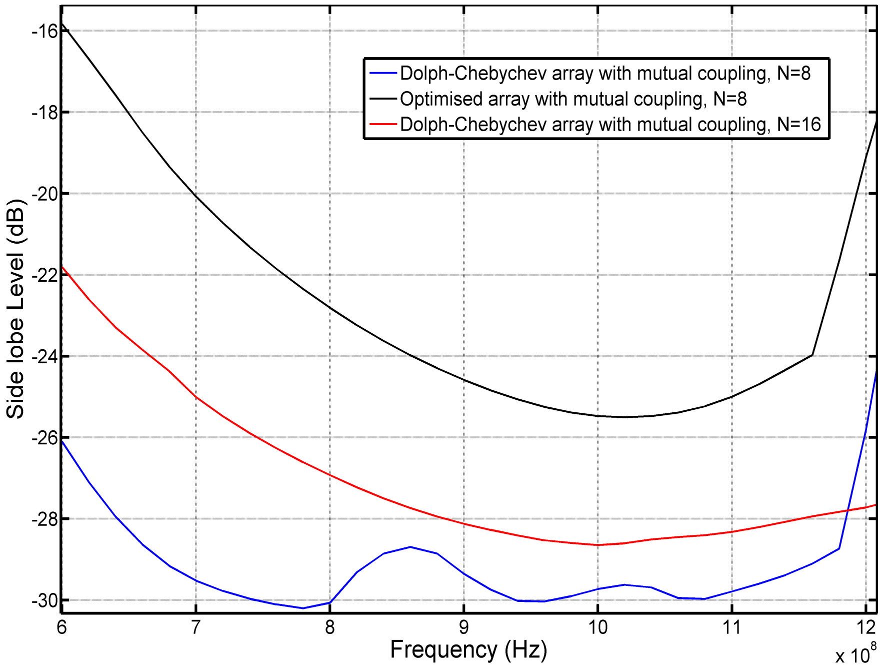

Figure 7.13: Comparing the PSLL bandwidth performance for $N = 8, 16$ DCAP and the optimised patterns while scanned to $\theta_o = 30^o$ in the presence of mutual coupling

mutual coupling Dolph-Chebychev taper comparatively large array behaves better in terms of PSLL bandwidth. For the PSLL curve in Figure 7.13 obtained with the single optimised excitation vector for $N = 8$ the minimum PSLL was found to be $-30.2dB$ at $.78GHz$. The FBW for this curve was recorded as 59.3% with $F_1 = 0.64GHz$ and $F_2 = 1.18GHz$ using the Equation 7.15. The use of IzBC-PSO in the presence of mutual coupling has shown improvement over the comparatively large array. Once again it is shown here that under severe pattern degradations due to mutual coupling IzBC-PSO can be used for small wideband array successfully.

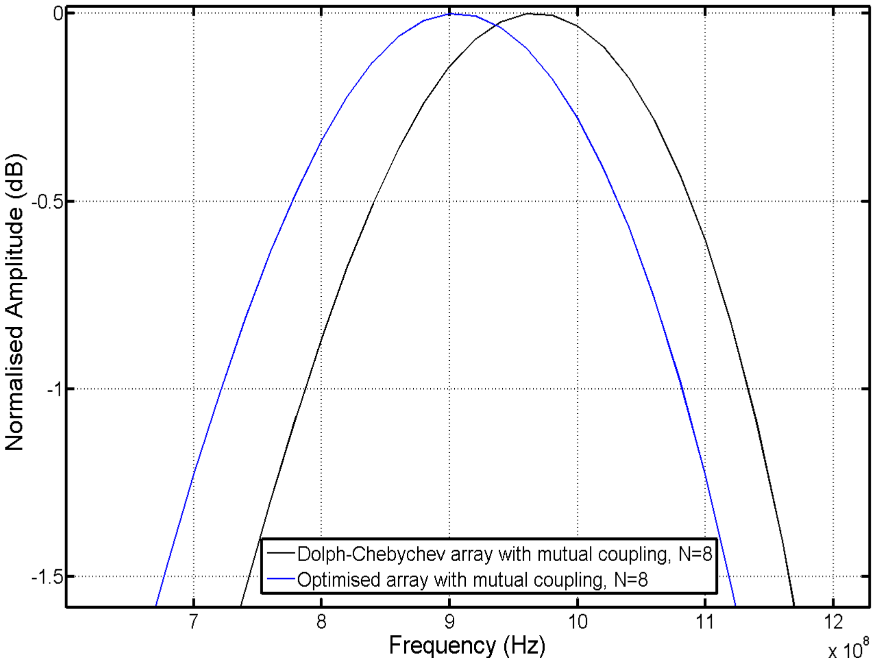

Figure 7.14: The absolute power variation at $\theta = 30^o$ across the frequency band compared for $N = 8$ DCAP and the optimised patterns

The radiation power variation in the desired scan direction as the frequency sweeps is presented in Figure 7.14 for $N = 8$ DCAP and the optimised radiation patterns. The bandwidth criterion for the power level tolerance in the target scan direction was $-1dB$ relative to the peak value. In case of DCAP the mainlobe power FBW was found to be 38%. In case of the optimised pattern the mainlobe power FBW was 40%. IzBC-PSO has the advantage of 5% improvement in the bandwidth over the frequency band considered. Figure 7.15 shows the variation of the HPBW for $N = 8$ DCAP and the optimised radiation patterns over the band. It is observed that both type of radiation patterns have the same HPBW. This highlights another advantage of using the IzBC-PSO as it produces an excitation vector that generates the radiation patterns with PSLL within the defined tolerance having the same HPBW as for non compensated patterns.

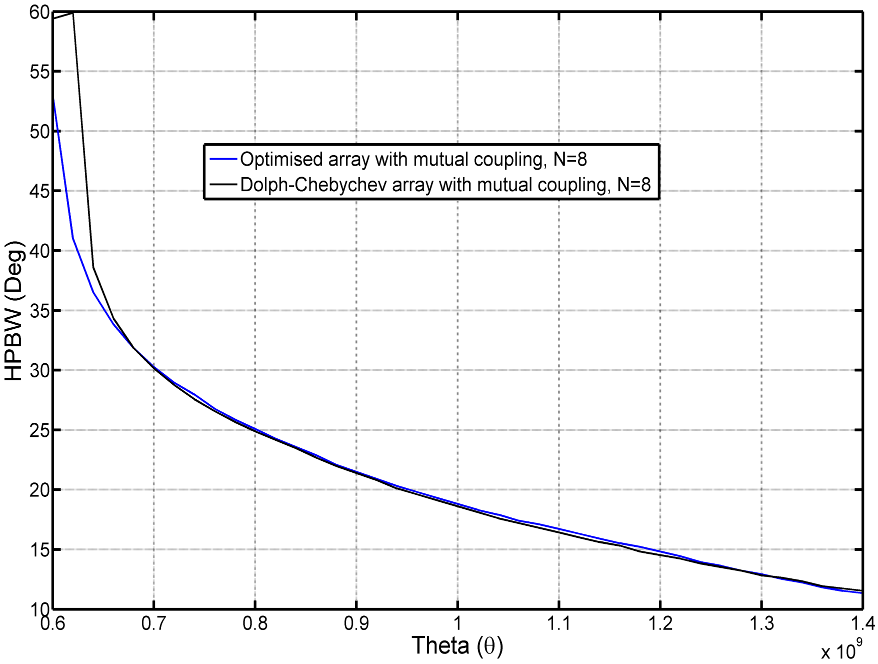

Figure 7.15: The HPBW variation across the frequency band for $N = 8$ DCAP and optimised patterns

It is shown once again here the need of using IzBC-PSO in the presence of mutual coupling to improve the wideband performance of small antenna arrays. The use of IzBC-PSO has significantly improved the PSLL bandwidth compared to non compensated small ($N = 8$) and comparatively large ($N = 16$) arrays while the mainlobe is scanned. The HPBW requirement is the same as that of the non compensated $N = 8$ DCAP yet improved PSLL performance is obtained. All this bandwidth improvement is obtained by using a single optimised excitation weight vector given in Table 7.6.

An interesting aspect of the Schelkunoff's unit circle approach has been considered here. It was observed that by restricting the nulls within the unit circle a bandwidth advantage was obtained. A possible reason for this is that the separation between the nulls is small as compared to the case where nulls are restricted outside the unit circle. As the separation between the nulls decides the SLL of array radiation pattern. If separation between the nulls is

Optimised Excitation Vector	
Amplitude	Phase (Deg)
0.4003	0
0.6486	272.4
0.9040	190.7
1.0	106.0
0.8392	23.4
0.5725	−57.2
0.2825	214.9
0.0885	132.8

Table 7.6: The IzBC-PSO excitation vector used to obtain the plots shown in Figures 7.12 for $\theta_o = 30^o$

greater then the SLL will be higher. Therefore smaller separation between the nulls cause a better SLL (pattern) bandwidth performance. The root locations for the Dolph-Chebychev array for the broadside taper are compared with modified root locations in the presence of mutual coupling in Figure 7.16 at $f = 1GHz$. This relocation due to mutual coupling causes the increase in PSLL. Figure 7.17 shows the optimised root locations that resulted in the optimised excitation vector given in Table 7.5. The optimised excitation vector after applying Equation 7.11 resulted in w_n' and the corresponding roots are shown in Figure 7.17.

In case of the scanned array the corresponding root locations to Dolph-Chebychev $-30dB$ taper with phase gradient applied for $\theta_o = 30^o$ are compared with the modified root locations due to mutual coupling at $f = 1GHz$ in Figure 7.18. The modified root locations have moved off the unit circle outwardly. This root placement explains the sensitivity of the PSLL to the change in frequency. Since the root separation is greater compared to the non coupled situation the SLL are higher. The root locations are modified for each frequency value considered because the mutual coupling is frequency dependent. It is important to note that IzBC-PSO resulted in the optimum root locations shown in Figure 7.19, all roots are placed well inside the unit circle. This resulted in the modified root locations after including the mutual coupling effect at $f = 1GHz$ to be near the unit circle as shown in Figure 7.19. The PSLL is lower compared to the Dolph-Chebychev taper under mutual coupling due to the optimised root

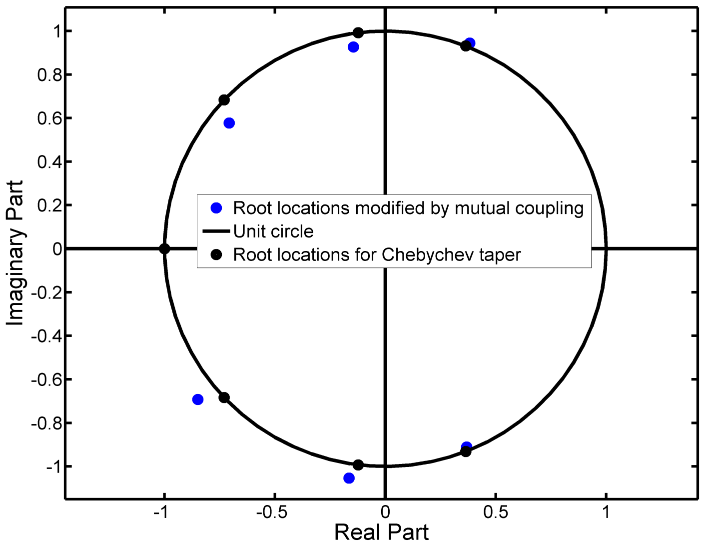

Figure 7.16: Root locations for Dolph-Chebychev $-30dB$ taper with and without mutual coupling effect at $f = 1GHz$

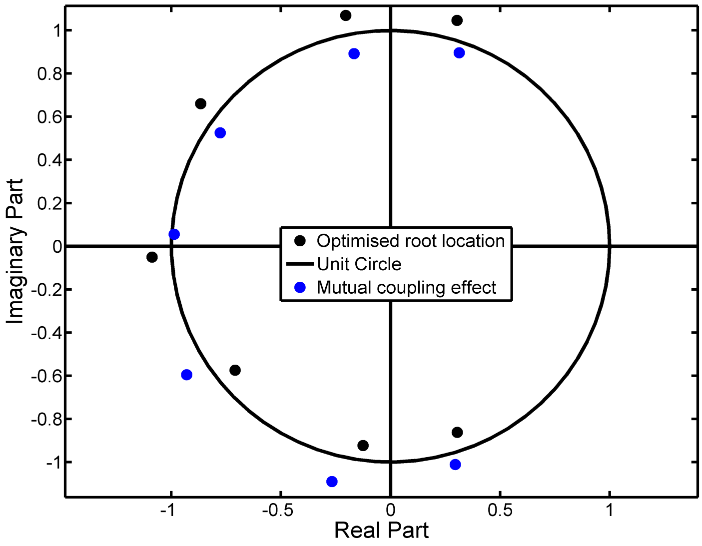

Figure 7.17: Root locations for the optimised excitation vector with and without mutual coupling effect at $f = 1GHz$

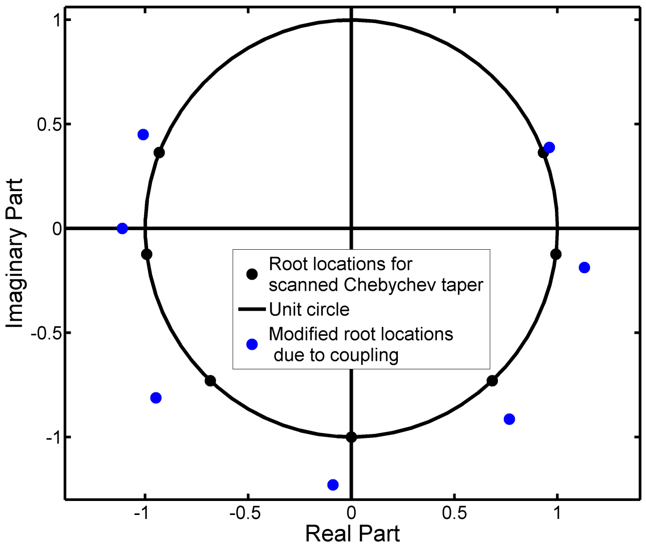

Figure 7.18: Root locations for Dolph-Chebychev $-30dB$ taper with and without mutual coupling effect at $f = 1GHz$ for $\theta_o = 30^o$

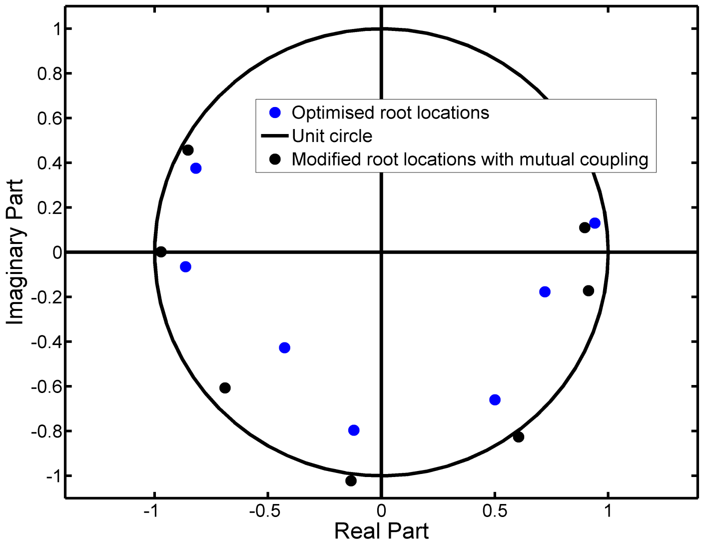

Figure 7.19: Root locations for the optimised excitation vector with and without mutual coupling effect at $f = 1GHz$ for $\theta_o = 30^o$

positioning.

7.3 Chapter Summary

The important results of this chapter are:

- It is shown that the proposed IzBC-PSO can be used successfully for the wideband phased array operation (§7.1.3,§7.2.3)
- A solution based on IzBC-PSO for high resolution wideband arrays is presented and it is demonstrated that the reduced SLL are achieved while maintaining the HPBW of the radiation pattern (§7.1.3);
- The mutual coupling effect over the SLL bandwidth performance of a small wideband array is presented and a solution based on IzBC-PSO is proposed that resulted in a single excitation vector that when applied to the small antenna array gives the desired SLL bandwidth performance over the band ($0.6 - 1.4GHz$) (§7.2.3);
- It is shown that in case of small antenna array ($N = 8$) the SLL bandwidth performance is effected significantly as compared to the comparatively large antenna array ($N = 16$) (§7.2.3);
- While scanning to $\theta_o = 30^o$, the SLL bandwidth performance degrades and the defined tolerance is not achieved without the use of IzBC-PSO (Figure 7.13);
- Better SLL bandwidth performance is achieved for the small antenna array ($N = 8$) using IzBC-PSO compared to the comparatively large array of ($N = 16$) while the small array is excited with a single excitation vector obtained using IzBC-PSO (Figure 7.13);
- The significance of the root placement is discussed and it is found that if roots are placed inside the unit circle the SLL variation over the frequency band is less compared to the case when roots are placed outside the unit circle (Figure 7.19)

Chapter 8

Experimental Verification: Beamforming Setup & Measurements

8.1 Introduction

Beamforming is a general term used to present a wide variety of array pattern synthesis. The basic purpose of beamforming in the antenna arrays is to add the patterns from individual elements constructively and destructively in desired directions. Therefore beamforming is a signal processing technique which enables control of the array pattern by adjusting the input amplitude and phase of each antenna. Conventionally analogue beamforming (ABF) techniques are used. Therefore expensive and application specific hardware, mostly Butler matrix & Rotman lens, is used for the beamforming purposes [5].

The digital beamformer relies on conversion of the received RF signal into digital stream which then can be manipulated. In particular applying a weight becomes a multiply and sum operation. The digital beamforming (DBF) made it possible to be realised at the individual element level. The received signal at each element is usually passed through an analogue chain (containing amplifiers and filters) before sampling. The sampled data is then processed by signal processing techniques often Fast Fourier Transform (FFT). At this stage the received signal could be weighted and summed to produce a desired array pattern [114]. The DBF provides flexible and robust beamforming solution. It allows the run time beamforming with limited features to optimise. Several antenna array systems have been implemented with this technology.

For this research work two different beamformers were used. CASPER's (Centre of Astronomy Signal Processing and Electronics Research) Interconnect Break-out Board (IBOB) was programmed by R. P. Armstrong [69] (University of Oxford) and the Digital Acquisition (DAQ) board designed by the engineers at Jodrell Bank Observatory [70].

The goal of this chapter is to present the measurement setup used and beamforming results obtained using the Vector Network Analyser (VNA), IBOB and DAQ board. The IzBC-PSO based solution is then applied to various array synthesis applications. To incorporate the mutual coupling impedance matrix and active element patterns have been used to model the array. The goal of this chapter is to show that these IzBC-PSO based solutions are applicable in real world applications using digital beamformers with no a priory knowledge of coupling. To demonstrate this active element patterns were measured in the anechoic chamber using Vector Network Analyser (VNA). The simulated results based on VNA measurements are presented and finally the array weights are applied to the digital beamformer to obtain the desired pattern in real-time.

8.2 Experimental Setup

In order to perform any pattern measurements basic instrumentation includes:

- transmitting antenna system
- receiving antenna system
- an environment with low multipath and reflection problems (anechoic chamber)
- positioning system
- data processing and recording system

The positioning system and data processing/recording facility were provided by the University of Oxford. The transmitting antenna was designed at University of Oxford.

8.2.1 Transmitter

The transmitting antenna used in this test was an ultra wideband log periodic antenna. The transmitter setup is shown in Figure 8.1.

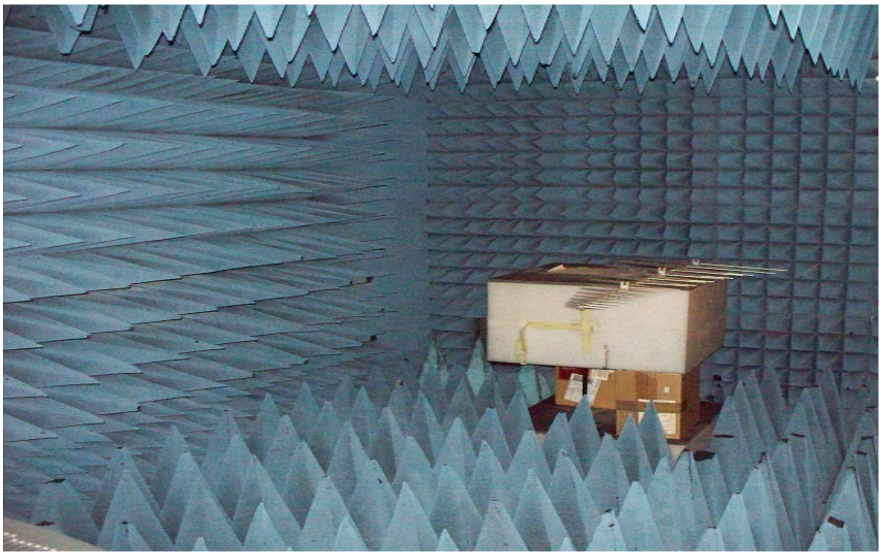

Figure 8.1: Wideband log periodic antenna (transmitter) setup in the anechoic chamber

8.2.2 Receiver: BECA Array

A linear array of eight elements was used for this experiment. The centre four elements were active with two dummy elements on each side. The array consists of Bunny Ear Combline Antenna (BECA) element presented by Y. Zhang et al. [68]. The dummy elements were terminated in the matched load of 169Ω. The active elements were connected to the 50Ω baluns. The elements are half wavelength apart at 882*MHz*.

The measurement of far field antenna array patterns was the objective of this test. In order to fulfil the Fraunhofer farfiled criterion, the distance between the transmitter and the receiving array must be greater than $2D^2/\lambda$, where D is the maximum dimension of the antenna array [3]. Once four elements were connected the active aperture length of four element array was 684*mm*. The total aperture length of the array including dummy elements was 1364*mm*. The wavelength of interest lied between 600*mm* to 429*mm* (500*MHz* to 700*MHz*). It is important to emphasis here that both the active array length and the full array length were larger then the maximum value of the wavelength involved [3]. This condition is required for the valid use of above mentioned farfield criterion. The desired farfield distance was found to lie between 1557mm-2180mm (taking $D = 684mm$). The anechoic chamber used for these measurements provided a distance of approximately 3500mm between transmitter and receiver. It is shown here based on the above calculations that the measurements were performed in the farfield.

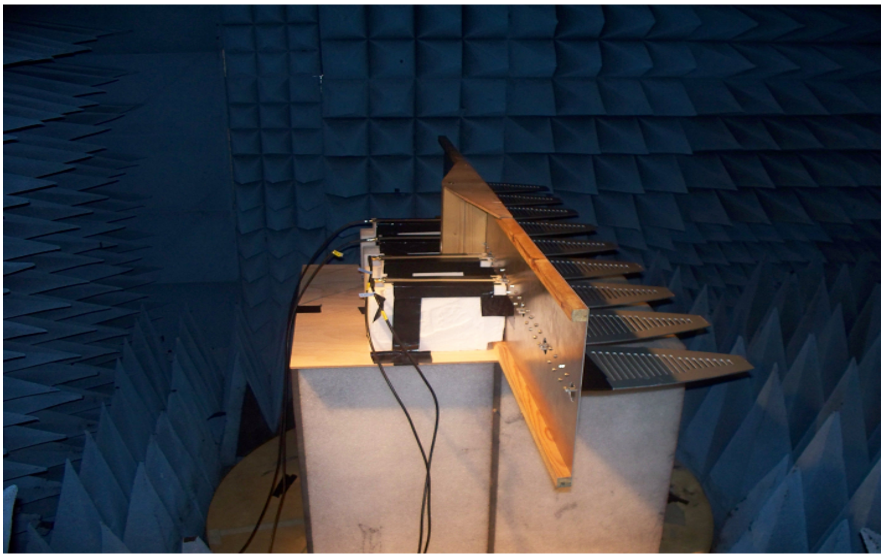

Figure 8.2: BECA array (receiver) setup in the anechoic chamber

The BECA array was setup as shown in the Figures 8.2. This test was divided into two parts. In the first part Vector Network Analyser (VNA) was used to measure active element patterns and the full array pattern. In the second part digital beamformers presented in chpater 8 were used to measure the array pattern and to apply beamforming weights (coefficients).

8.3 VNA Measurements

The purpose of any array pattern synthesis optimiser is to keep the pattern profile as desired under the physical constraints of the array. It has been demonstrated in previous chapters that a IzBC-PSO based high performance optimiser is suitable to use for this purpose. The results presented in those chapters rely on the active element patterns obtained from CST. In this chapter the same optimisation approach is used but measured results are shown. For this purpose standard measurement was made using VNA. First active element patterns were measured and later the full array pattern was measured.

8.3.1 Measuring Active Element Patterns

In this measurement set up the array under test (AUT) consisted of eight elements in total. The centre four elements were used as the active elements while the two elements on each side were used as dummy elements to minimise the severe edge effects. Since the array is of finite size therefore the surroundings of each element could not be assumed symmetric. Therefore, it was necessary to measure individual element patterns to model the array.

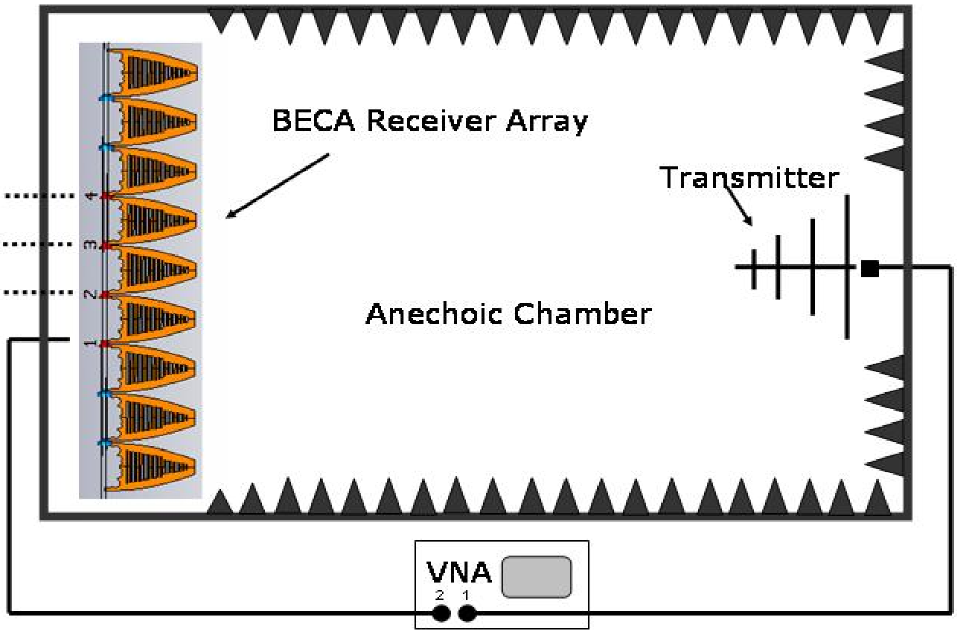

Figure 8.3: Experimental setup used to measure element patterns while array was placed in position 1. The dashed lines connected to ports 2, 3 & 4 show that VNA port 2 connected to these one after the other and always terminated if not under test (Figure is not to scale)

The experimental setup used to measure the individual element patterns is shown in Figure 8.3. This was defined as array position 1. The measurement was performed using a VNA. The transmitter was connected to port one and the element 1 was connected to port two of VNA. The remaining three elements were terminated with 50Ω terminators. The array was then rotated in $\phi = 0$ plane for θ from -90^o to 90^o. After completing a 180^o rotation element 2 was connected to the port two of VNA and element 1 was terminated. The same process was repeated for all four elements.

8.3.2 Measured Pattern Comparison

Under ideal circumstances it is expected that the element patterns for element 1 and 4, 3 and 2 would be mirror image pairs. But as shown in the Figures 8.5 to 8.8, for array position 1, it was not the case. Therefore to isolate the effect of array structure and the anechoic chamber environment further measurements were made.

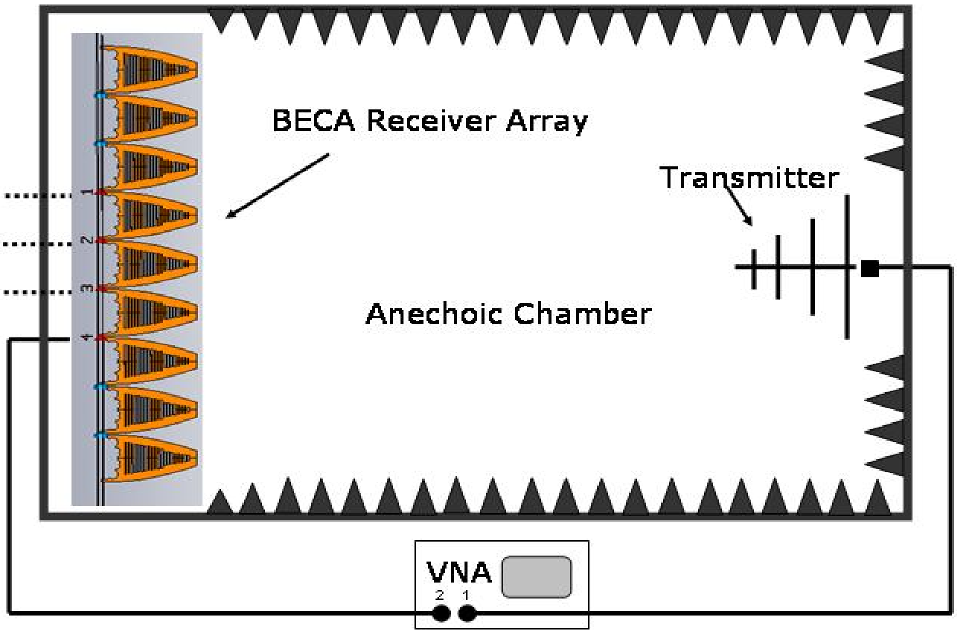

Figure 8.4: Experimental setup used to measure element patterns while array was placed in position 2. Note that the element positions have been swapped. The dashed lines connected to ports 1, 2 & 3 show that VNA port 2 connected to these one after the other and always terminated if not under test (Figure is not to scale)

For this purpose the array was flipped and the element positions were swapped from right to left. This new array arrangement was defined as array position 2. Care was taken to ensure that the electromagnetic environment does not change. The experimental setup is sown in Figure 8.4. The element pattern measurement was performed following the same procedure described above. The results are shown in Figures 8.5 to 8.8 for comparison purposes.

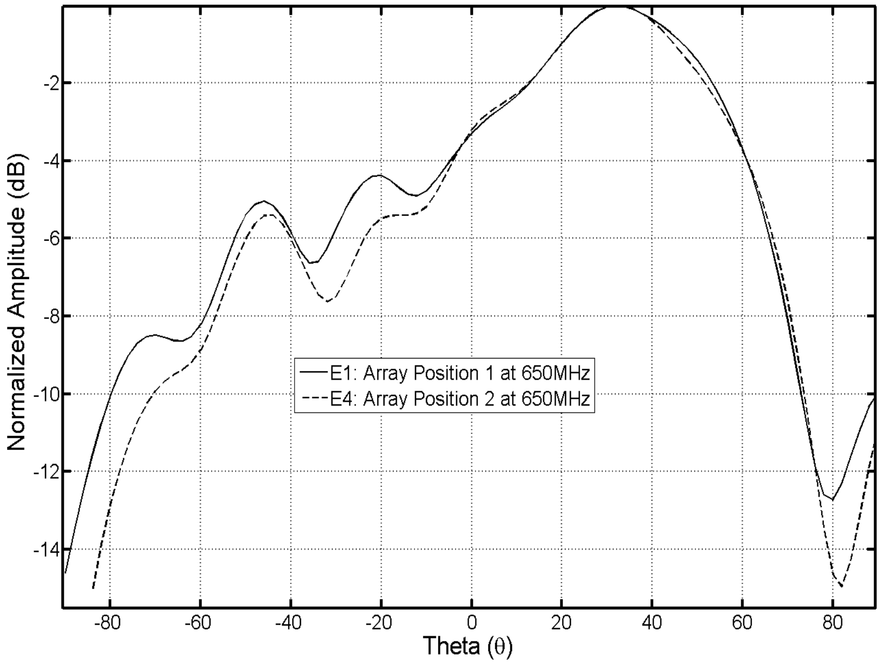

Figure 8.5: Pattern comparison for element 1, the radiation plot in dB

In Figure 8.5 the element 1 pattern in array position 1 is compared to the element 4 pattern in array position 2. The patterns overall follow the similar trends, the main beam of both patterns was well matched however the maximum significant difference in power level observed was $1.3dB$. Figure 8.6 represents the comparison of element 2 in position 1 to the element 3 in position 2. Here main beam was not as well matched as in the previous case. The significant power level difference noted in this comparison was $0.6dB$.

Figure 8.7 shows a comparison of element 3 and 2 in position 1 and position 2 respectively. A significant power level difference was observed at 26^o of magnitude $0.3dB$. In Figure 8.8 the element patterns for element 4 and element 1 in position 1 and position 2 are compared. Significant power level difference of $0.7dB$ was observed.

Therefore the pattern asymmetries observed in these results are due to the radiating structure not the electromagnetic environment. Being unable to

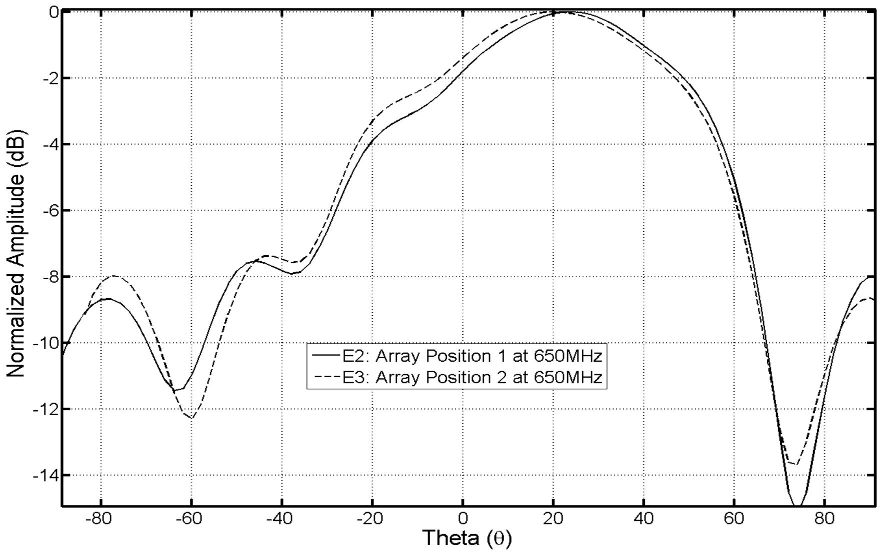

Figure 8.6: Pattern comparison for element 2, the radiation plot in dB

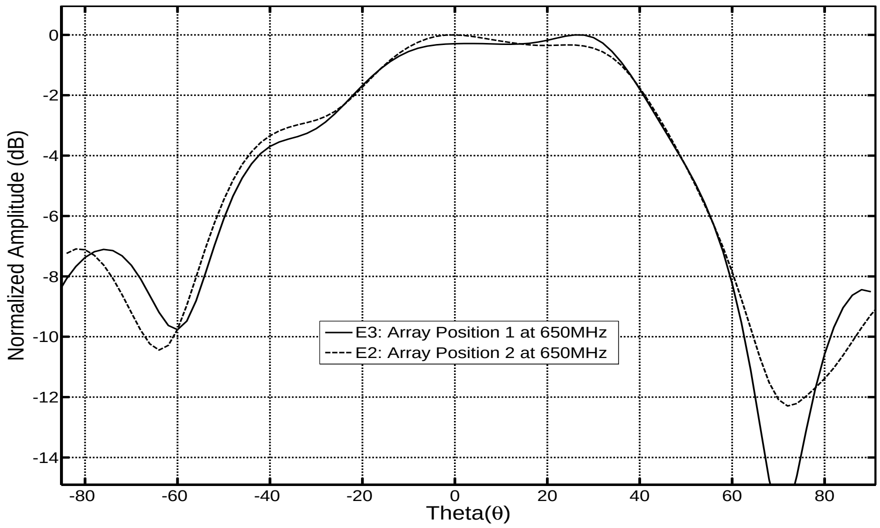

Figure 8.7: Pattern comparison for element 3, the radiation plot in dB

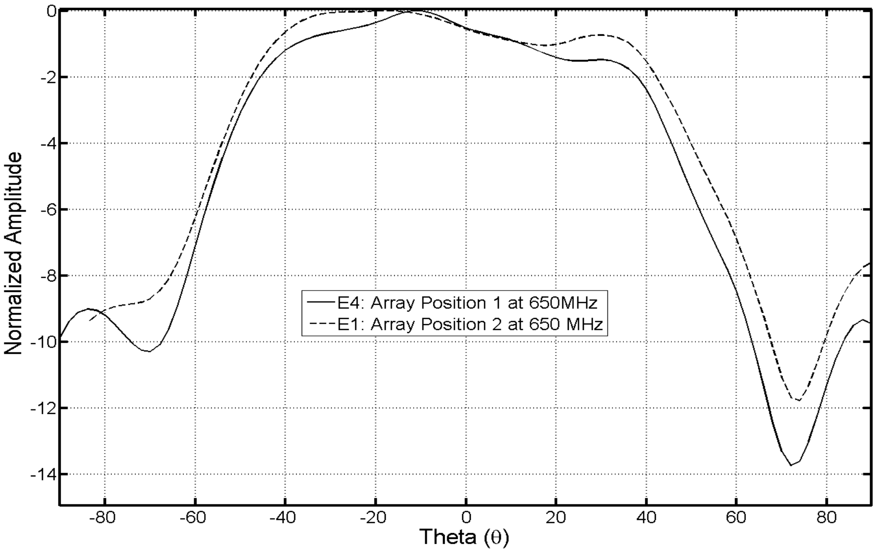

Figure 8.8: Pattern comparison for element 4, the radiation plot in dB

intervene with physical array design no modification was made to the array.

The differences observed in power level of measured patterns could be a result of fringe electromagnetic reflections or small changes in the environment as the array flipped over. Since the absorbers used in the chamber were carbon loaded and they are most effective at the frequencies greater then $1GHz$ [5].

8.3.3 Measuring Array Pattern

After performing the individual element pattern measurements the array pattern was measured. Experimental setup is shown in Figure 8.9 The four array elements were connected to a four port power combiner (ZFSC-4-1) from $Mini - Circuits^{®}$.

The port 5 (sum port) of the power combiner was then connected to the port 2 of the VNA. The VNA port 1 was connected to the transmitter. The same measurement procedure was repeated to measure the full array pattern. The comparison of the measured array pattern and the array pattern obtained after performing vector addition of the individual element patterns (Array Radiation Pattern (ARP)) is presented in Figure 8.10 at $650MHz$. Uniform weights were applied to the ARP. It is shown as:

$$ARP(\theta) = \sum_{n=1}^{4} w_n * E_n(\theta) \tag{8.1}$$

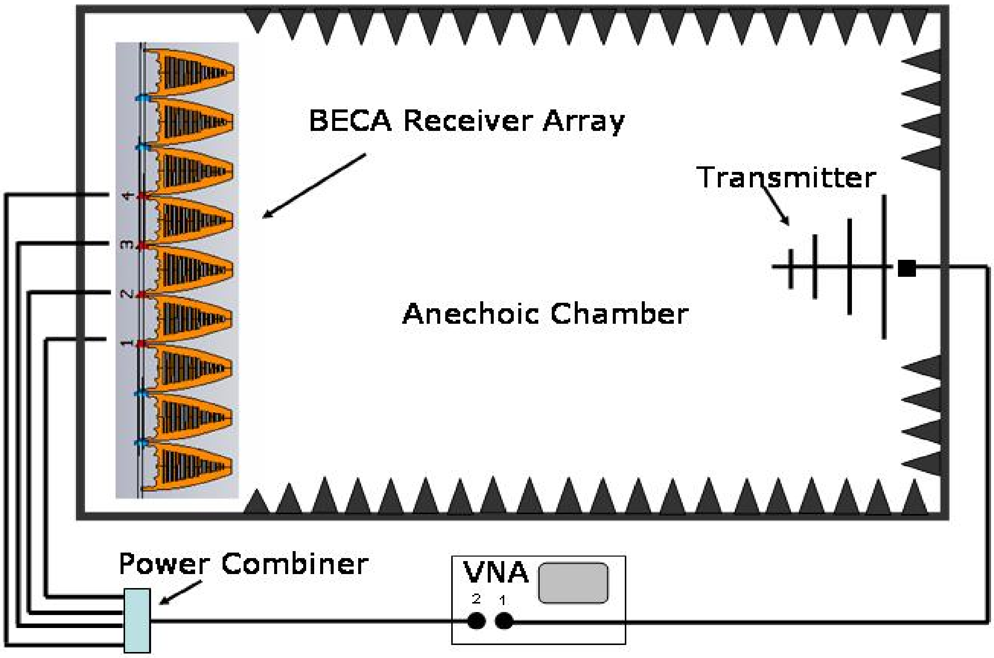

Figure 8.9: Experimental setup used to measure the array pattern. The four elements were connected to the power combiner and power combiner output was connected to port 2 of VNA (Figure is not to scale)

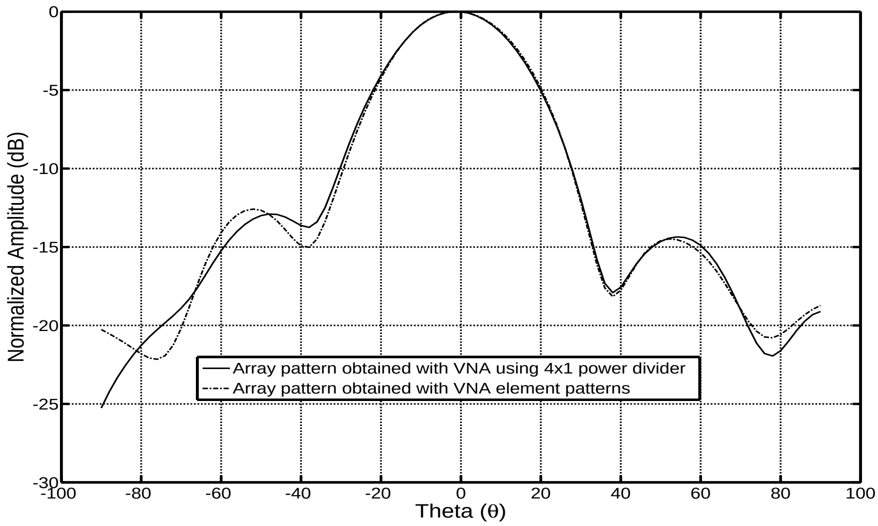

Figure 8.10: The array pattern measured using VNA is compared with the Array Radiation Pattern (ARP) at 650MHz

Where E_n is the n^{th} element pattern and w_n is the complex excitation (weight) value assigned to n^{th} element. It was assumed that the power combiner used would add the received power at four ports all multiplied by the same attenuation constant without introducing any phase differences.

The two patterns were generally matched. The maximum significant difference observed was 0.88dB at 54^o. The pattern difference observed could be a result of reflections in the chamber as discussed in the previous section.

8.4 Array Pattern Synthesis

In this section the IzBC-PSO discussed in chapters 3 and 4 will be used to obtain desired array patterns by modifying w_n in Equation 8.1. At 650MHz the effective separation between the elements was 0.37λ. Therefore this is the case of closely packed array which adds to the mutual coupling of the array generally.

8.4.1 Broadside Pattern Synthesis

In the Figure 8.11 array patterns obtained with three different tapers are presented for the broadside scan. The array pattern with uniform taper has a maximum SLL of $-12.54dB$ with the beamwidth of 34^o. It is shown in the same Figure that the Chebychev taper for $-25dB$ SLL was unable to produce the desired result. The maximum SLL obtained was $-17.52dB$ with half power beamwidth of 40^o. This emphasis that under strong coupling conditions conventional methods could not produce expected results. Also the array separation was less then half wavelength therefore Dolph-Chebychev taper was unable to produce the optimum result.

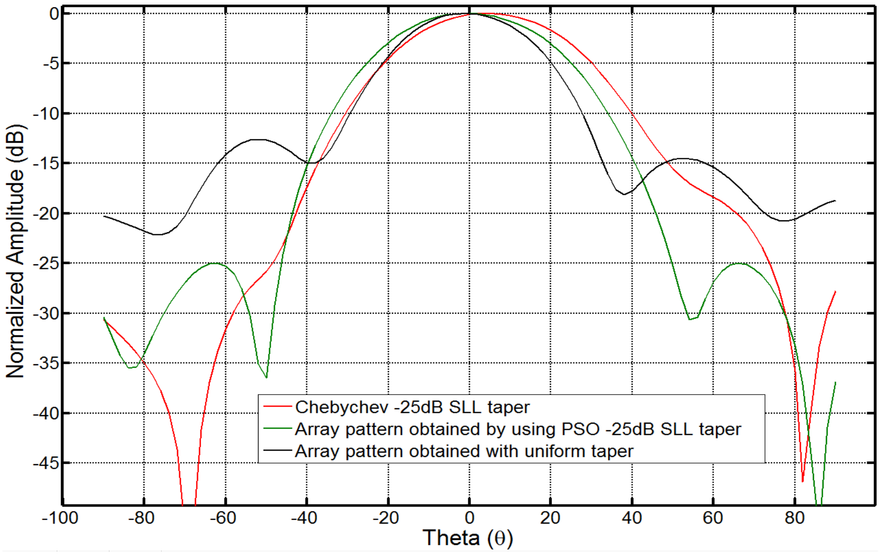

Figure 8.11: The array pattern measured using VNA are compared at $650MHz$

For IzBC-PSO maximum SLL was set to $-25dB$ as the goal. The results are presented in Figure 8.11. The maximum SLL obtained for ARP after modifying w_n with the optimised weights was $-25dB$ with the half power beamwidth of 40^o. It is shown here that the IzBC-PSO based optimisation scheme was able to obtain the desired pattern shape under non ideal conditions. The results have been summarised in Table 8.1.

The taper values used to modify w_n in Equation 8.1 to obtain the patterns discussed are given in Table 8.2. Clearly the optimised amplitude taper has asymmetric distribution across the array aperture. This is the result of the asymmetric behaviour of the array elements identified earlier in this chapter. The optimiser also provides the correct excitation phase to achieve the goal accurately.

Taper Applied	$-3dB$ Beamwidth (Deg)	PSLL (dB)
Uniform	34	-12.5
Chebychev	40	-20.2
Optimised	40	-25

Table 8.1: Peak sidelobe level (PSLL) and beamwidth are compared for the three sets of taper applied to the measured patterns of the array

Number of Element	Dolph-Chebychev -25dB Taper		Optimised Taper	
N	Mag	Phase (Deg)	Mag	Phase (Deg)
1	0.48	0	0.32	0
2	1	0	0.90	-32
3	1	0	1.00	-41
4	0.48	0	0.64	-35

Table 8.2: The amplitude and phase values applied to the array for Chebychev and the optimised taper

8.4.2 Scanned Pattern Synthesis

In Figure 8.12 the scanned performance of the AUT is examined. The array pattern shown in dotted line is obtained by applying the uniform linear phase gradient. The main beam is scanned to the desired scan direction i.e. 30^o away from the broadside. The maximum SLL observed was $-12.25dB$ with the half power beamwidth (HPBW) of 32^o. Now this is a multi-objective optimisation problem. The gaol is to achieve a minimum possible SLL while keeping the same beamwidth as with the uniform taper and maintaining the scan direction. The optimisation procedure used for this type of multi-objective problem is defined in chapter 5.

The resultant optimum pattern had the same HPBW as the uniform taper pattern but the SLL is improved by $4.86dB$. This is 40% improvement in SLL performance while maintaining the scanned direction. Table 8.3 summarises the results.

The amplitude and phase tapers corresponding to the results shown in Figure 8.12 are given in Table 8.4. As for the linear phase gradient a consistent

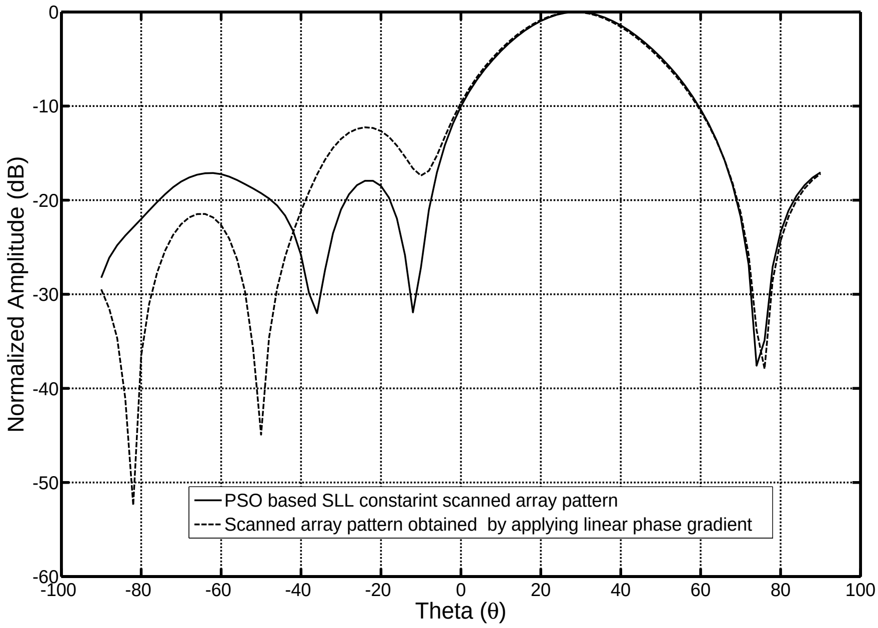

Figure 8.12: The array pattern measured using VNA are compared at 650*MHz*

Taper Applied	$-3dB$ Beamwidth (Deg)	Peak Sidelobe Level (dB)
Uniform Taper	32	-12.2
Optimised Taper	32	-17.1

Table 8.3: Peak sidelobe level (PSLL) and beamwidth comparison of the linear phase gradient and the optimised taper for a scan angle of 30^o

phase progression is observed but the optimised weights showed non linear but monotonic phase progression across the array.

8.4.3 Null Pattern Synthesis

Three independent null pattern synthesis examples are presented and discussed in this section. It is assumed that in three cases the interference source is located at -30^o, -50^o and -70^o of θ respectively. Figure 8.13 represents the ARPs with nulls at -30^o, -50^o and -70^o. The optimisation goal for each pattern synthesised and presented in Figure 8.13 was to place the pattern null at a desired look direction while the main beam is scanned to 30^o. The SLL were constrained for the same HPBW in all three cases only on left side of main beam.

Number of Element	Uniform Taper		Optimised Taper	
N	Mag	Phase (Deg)	Mag	Phase (Deg)
1	1.00	0	0.95	0
2	1.00	66	1.00	71
3	1.00	133	1.00	113
4	1.00	−161	0.92	−141

Table 8.4: Amplitude and phase values for uniform linear phase gradient and the optimised taper

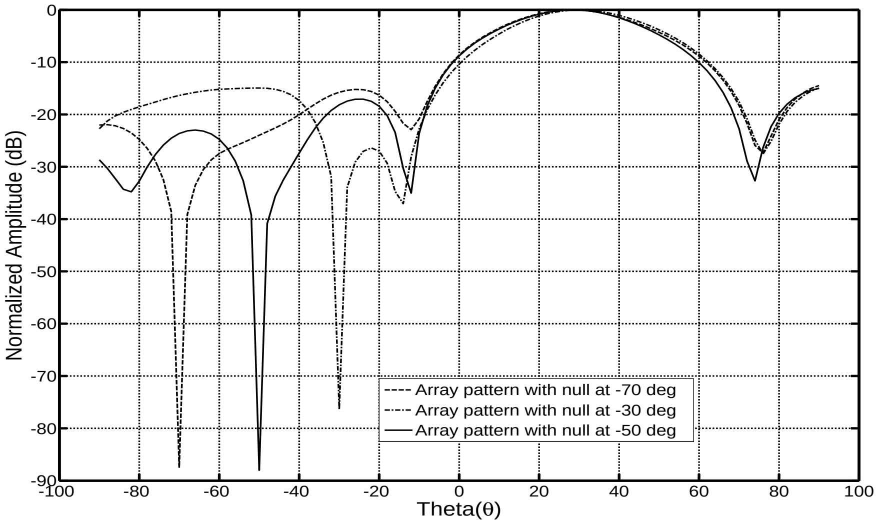

Figure 8.13: The array pattern measured using VNA are compared at 650*MHz*

Null Position (Deg)	$-3dB$ Beamwidth (Deg)	Null Depth (dB)	Minimum Sidelobe Level (dB)
−30	34	−76.32	−14.94
−50	34	−84.67	−16.01
−70	34	−84.43	−15.21

Table 8.5: A comparison of optimised tapers used to obtain the null at a desired angular position while constraining the sidelobe levels and the main beam scan direction

Number of Element	Taper for Null at −30 deg		Taper for Null at −50 deg		Taper for Null at −70 deg	
N	Mag	Phase (Deg)	Mag	Phase (Deg)	Mag	Phase (Deg)
1	0.8838	0	0.6798	0	0.623	0
2	1	90	1	46	1	55
3	0.7615	120	0.9046	117	0.431	130
4	0.6132	−121	0.6720	−156	0.4783	−164

Table 8.6: Amplitude and phase of optimised tapers used to obtain the null at a desired angular position while constraining the sidelobe levels and the main beam scan direction

The pattern comparison is summarised in Table 8.5. It is shown that the HPBW is maintained at 34^o however the null depth and the SLL are not the same for three cases. The null depth was used as a trade off to obtain a minimum possible SLL under constraints i.e SLL, HPBW, scan direction and null depth. The target null depth was set to $-100dB$. The maximum SLL achieved in three cases was $-14.94dB$. The taper values used to modify w_n are shown in Table 8.6. It was observed that the tapers used were significantly different in terms of the amplitude and phase values.

8.5 Interconnect Break-out Board (IBOB)

Interconnect Break-out Board (IBOB) has a Xilinx Virtes-II Pro 2VP50 FPGA. The FPGA was programmed using Python programming language. The DBF could be performed either in time domain or in frequency domain. For this work frequency domain technique was implemented because of its ease of calibration. The four element linear array beamforming hardware used for this research work is shown in Figure 8.14.

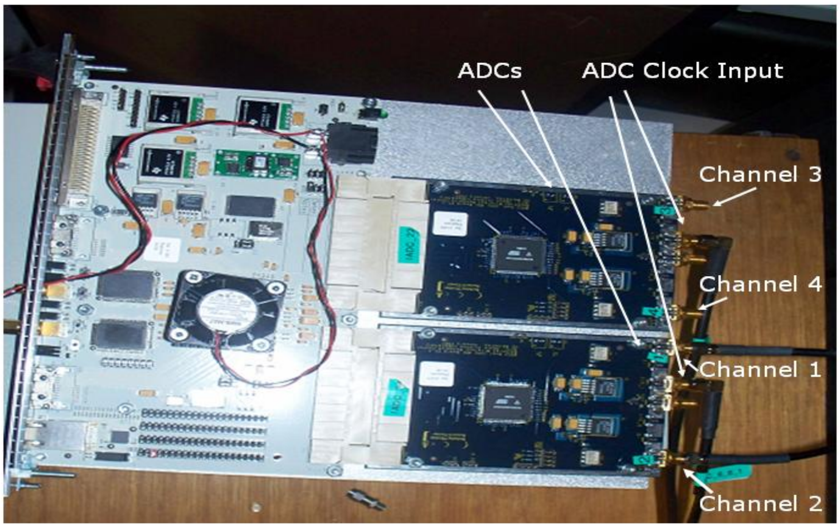

Figure 8.14: The Interconnect Break-out Board used

The schematic of the implemented beamforming system is shown in Figure 8.15. The hardware and the interfacing software code were provided by R. P. Armstrong, University of Oxford. The beamforming weights are produced using the optimiser developed for this research work described in chapters 3 and 4. The main steps involved in beamforming using IBOB are summarised below.

8.5.1 Sampling

This is the first key step involved in any digital beamforming operation. The received RF signal was sampled at, $F_s = 800MSa/sec$ with eight bit precision. This sampling frequency gives a Nyquist bandwidth of $400MHz$ symmetric about DC as shown in Figure 8.16. For this experiment RF frerquency range was from $500MHz$ to $700MHz$ giving a bandwidth of $200MHz$. According to the Nyquist Sampling theorem for the given sampling rate continuous signal must be band limited to $400MHz$. Therefore it was necessary for the received RF signal to be down converted to Nyquist bandwidth.

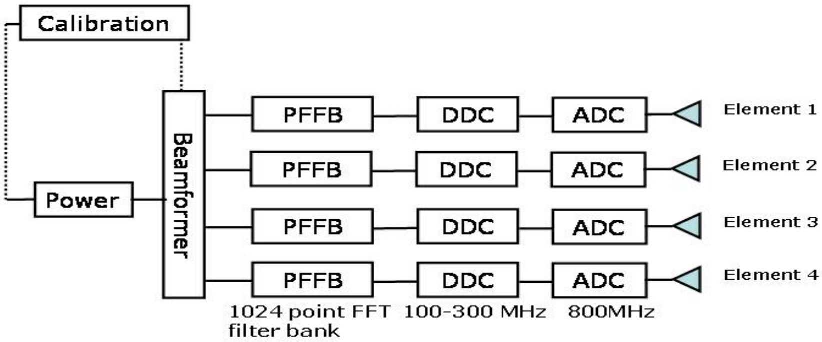

Figure 8.15: Schematic of four element IBOB beamformer used for this measurement

8.5.2 Digital Down Conversion

A digital down converter (DDC) is equivalent to analogue mixer. It has advantages of operational stability and control over its analogue counter part. In order to band limit the desired signal within the Nyquist bandwidth DDC is used immediately after the ADC. The sampled signal was multiplied by a complex sinusoidal signal at $600MHz(\frac{3}{4} * F_s)$. This resulted in the RF signal bandwidth mapped to $-100Mhz$ to $100MHz$ shown by the shaded portion in the Figure 8.16. The signal bandwidth is shifted symmetrically about DC to minimise the required sampling rate as the maximum negative frequency is similar to the maximum positive frequency. The time domain real signal is now converted to a complex sampled signal. The complex arithmetic is used in FPGA after DDC because it help to identify the negative frequencies.

8.5.3 Polyphase FFT Filter Bank (PFFB)

For efficient performance of the wideband digital system channelisation is very important. In case of a beamformer it allows to maintain defined goals over a wide frequency band by treating the channels individually e.g. associating a unique set of excitation vector with each channel. This channelisation in digital domain could be achieved by applying N point Discrete Fourier Transform

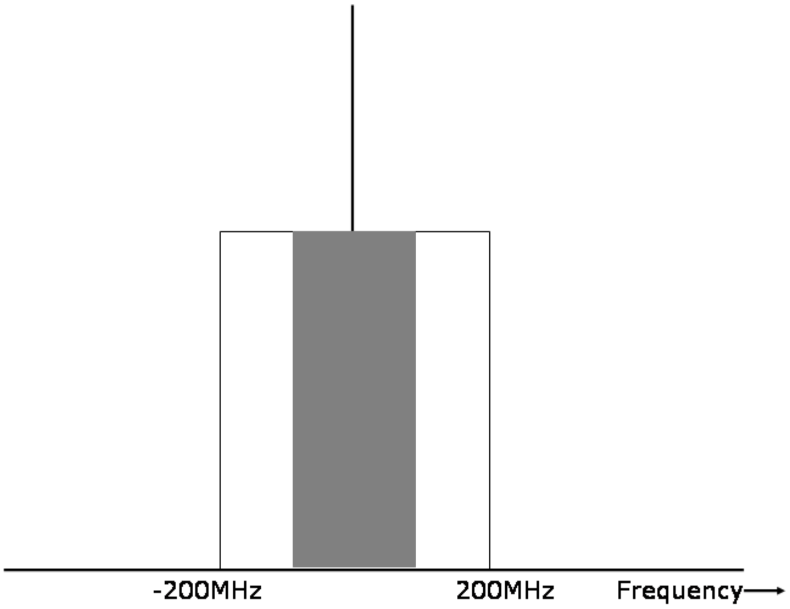

Figure 8.16: Nyquist spectrum and the digitally down converted RF spectrum (shaded)

(DFT) which divides the frequency spectrum in N channels. Fast Fourier Transform (FFT) algorithm is often used to speed up DFT computations. This straight forward channelisation suffers from the spectral leakage (poor spectral isolation). In order to overcome this issue the sampled data was passed through a polyphase filter bank. That improved the spectral isolation. After that 1024 point FFT was performed over the sampled data. The process is shown in Figure 8.17.

8.5.4 Beam Summation

The beam summation process is summarised in Figure 8.18. The four arms represent the digitised data coming from the four array elements. The w_n is the optimised complex multiplier for the n^{th} arm. The complex weights are determined using the IzBC-PSO. After the optimisation process the excitation vector (weights) are multiplied to a preselected digitised channel corresponding to a desired frequency. The multiplied digitised signals are then summed up to form a radiation pattern.

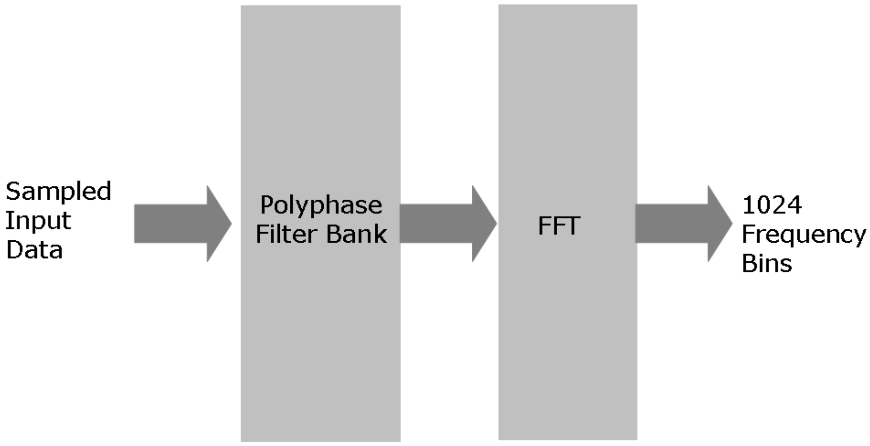

Figure 8.17: Polyphase filter bank and FFT implementation

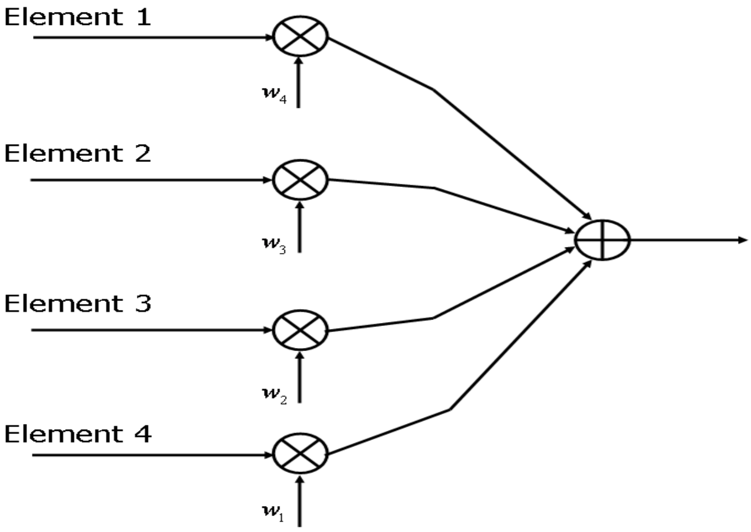

Figure 8.18: The beam summation process

8.5.5 Experimental Setup

The experimental setup is shown in Figure 8.19. Four elements of the BECA array were connected directly to the Analog to Digital Converters (ADCs) on the IBOB. The IBOB was interfaced with the desktop PC using a RJ45 cable. The rotating stage was interfaced with the same desktop PC through a 9 pin serial port. The rotating stage was controlled in 2^o steps. The transmitting antenna was connected to the signal generator and the signal frequency was set to $650MHz$.

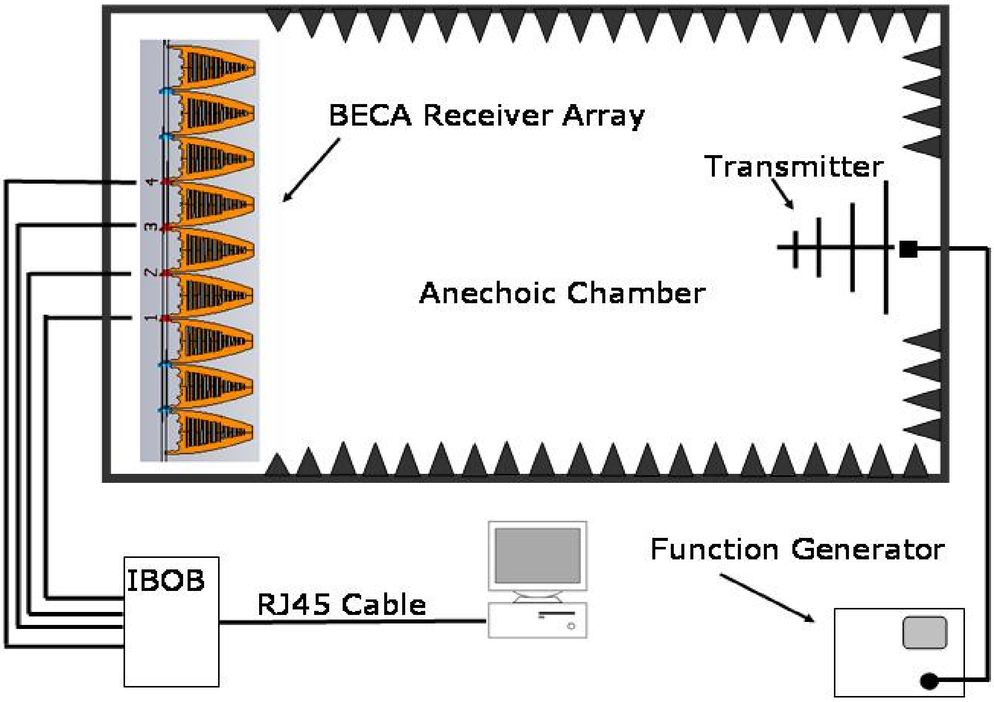

Figure 8.19: Experimental setup used to measure array pattern using the IBOB.

Python script was used to communicate with the FPGA. The code was used to update the beamforming coefficients in magnitude and phase format. These coefficients were obtained by the IzBC-PSO algorithm described earlier. The coefficients were then multiplied by the individual sampled signals before summation. The complex optimized taper was uploaded using this software to see the online optimized results.

8.5.6 Calibration

In a beamformer to achieve correct phase and gain values it is necessary to compensate for the phase and gain errors in the system. These errors could be mainly caused by the structural characteristics (manufacturing tolerance) of the antenna array, environment or the feeding circuitry mismatch. The effect of all these on the received phase and gain values should be calibrated for the desired array operation. In this measurement setup there was no analogue chain involved so only far field calibration was performed [69].

The following calibration procedure is useful for the broadband operation. To each frequency channel an individual complex weight obtained by this procedure could be applied.

First, the BECA array was locked in the broadside position and a mono tune signal of $650MHz$ was transmitted from the transmitter that impinged the array at $\theta = 0^o$. Then element 1 was chosen as the reference for this calibration process. The phase of element 2, ϕ_2, was swept for 2π while phase of element 1 was fixed and all other elements were multiplied by zero. The output power of the DBF was recorded for later comparison. The maximum output power value and the phase value was recorded as the individual element correction phase $\phi_n^{'}$. This procedure was repeated for element 3 and 4 and the correction phases were determined. After this for each element except element 1 the phase correction value $e^{j\phi_n^{'}}$ was uploaded where $n = 2, 3, 4$ [69].

8.5.7 Results & Discussion

After performing the calibration the IBOB beamformer was ready to use. The calibration coefficients were uploaded using the Python script running on desktop PC as shown in Figure 8.19. The array was swept with calibration coefficients as the only channel multipliers. The resultant array pattern at $650MHz$ is shown in Figure 8.20 and compared with the VNA measured pattern. The two patterns follow the similar trends with in very small error. The significant difference of $1.81dB$ at 42^o was observed between the IBOB measured pattern and the VNA measured pattern sidelobe levels of $-10.57dB$ and $-12.38dB$ respectively.

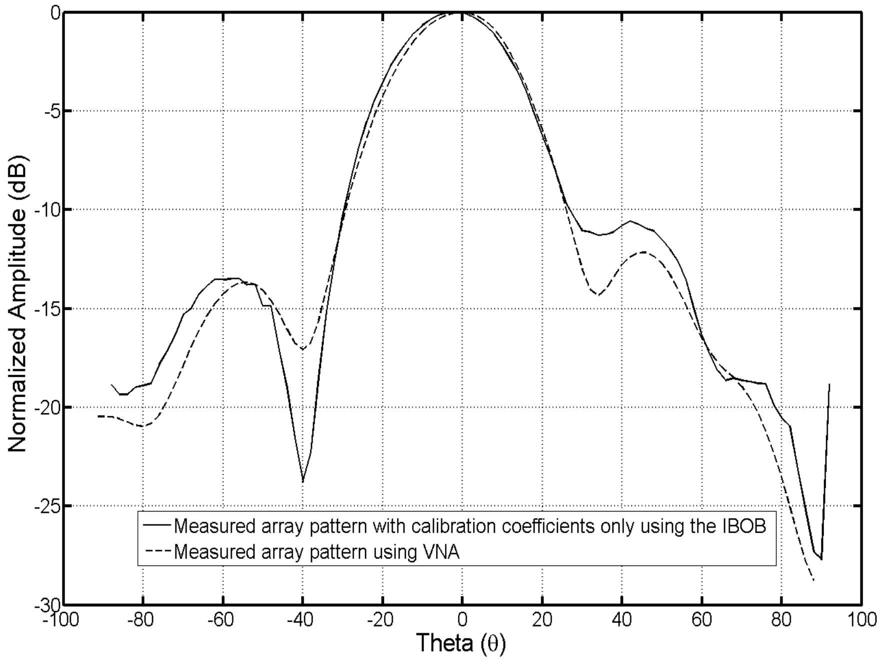

Figure 8.20: The array pattern measured using the IBOB is compared with those obtained by the VNA measurements

8.5.8 Beamforming Taper

In Figure 8.21 the effect on the power pattern measured after applying the beamforming weights to the IBOB beamfoprmer is shown. The MATLAB model based on Equation 8.1 was used to determine the expected radiation pattern for the optimisation purposes. Three sets of the tapers were applied including $-20dB$ SLL Chebychev, optimized tapers generated by the hybrid PSO for target $-20dB$ (IzBC-PSO set 1) and the $-25dB$ (IzBC-PSO set 2) SLLs. The tapers used for this measurement set are given in the Table 8.8. It is evident from the results shown in Figure 8.21 that the optimised IzBC-PSO tapers outperformed the conventional Chebychev.

With Chebychev taper the maximum SLL obtained was $-13.54dB$ with 40^o HPBW also the radiation pattern is not symmetric. The $-20dB$ IzBC-PSO taper resulted in $-19.87dB$ maximum SLL with 34^o HPBW and relatively symmetric pattern. This shows the improvement of $6.33dB$ over the Chebychev taper. The Chebychev taper suffered from the coupling and due to the fact that element separation is less then half wavelength and Chebychev is not optimum. The significant improvement after applying the optimised taper proves the need for an optimisation scheme like one proposed in this study to compensate for

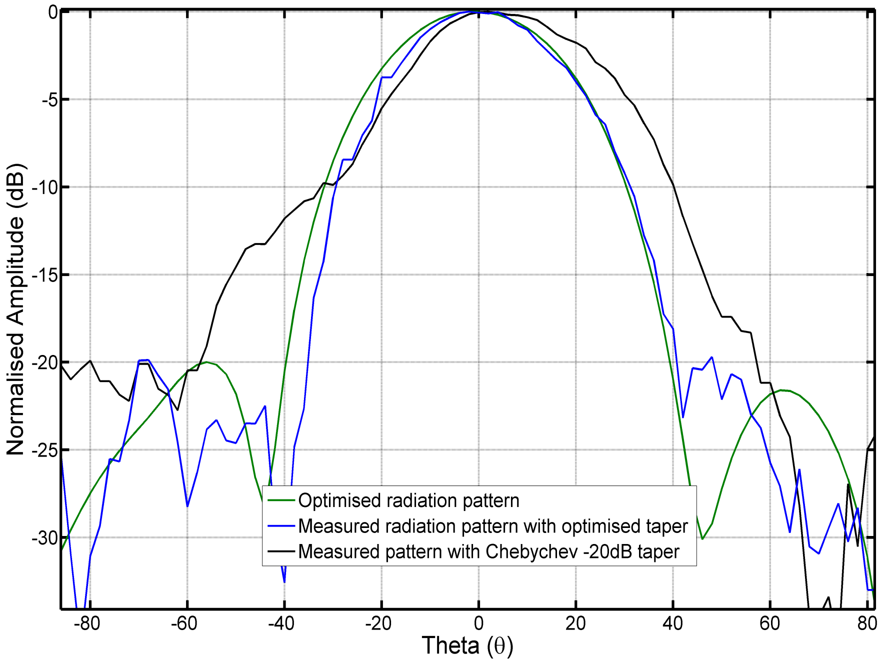

Figure 8.21: The array patterns measured after applying Dolph-Chebychev $-20dB$ and IzBC-PSO weights to IBOB are compared to the optimised radiation pattern (patterns are presented after performing offline calibration)

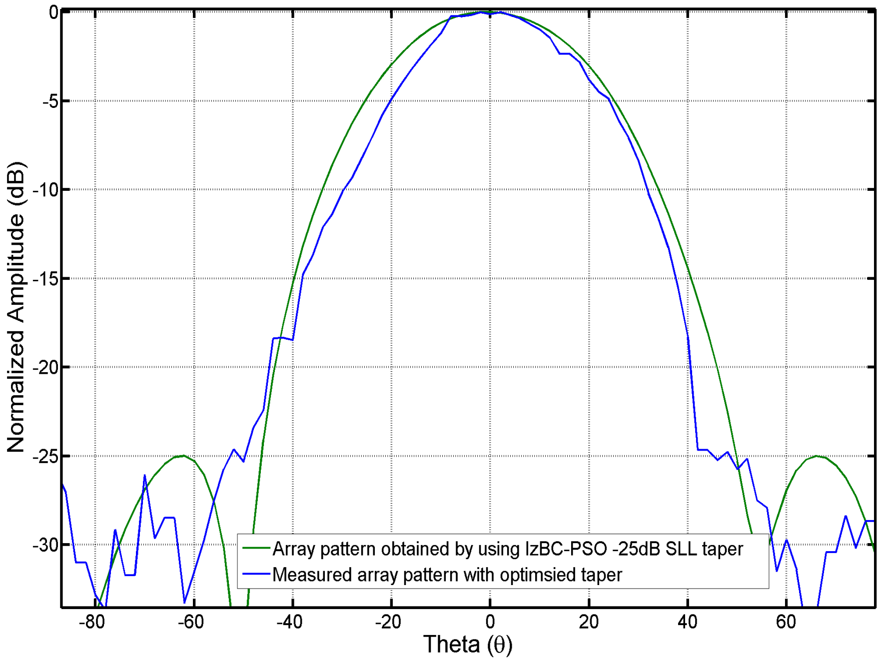

Figure 8.22: The array patterns measured after applying IzBC-PSO weights to IBOB are compared with the optimised results (patterns are presented after performing offline calibration)

Taper Applied	$-3dB$ Beamwidth (Deg)	Peak Sidelobe Level (PSLL) (dB)
-20dB Chebychev	40	-13.5
-20dB IzBC-PSO	34	-19.9
-25dB IzBC-PSO	34	-24.8

Table 8.7: Minimum sidelobe level (SLL) and beamwidth are compared for the three sets of taper applied with IBOB and the patterns are shown in Figures 8.21 and 8.22

Number of Element	Chebychev Taper for $-20dB$ SLL		PSO Taper for $-20dB$ SLL		PSO Taper for $-25dB$ SLL	
N	Mag	Phase (Deg)	Mag	Phase (Deg)	Mag	Phase (Deg)
1	0.5761	0	0.7331	0	0.5997	0
2	1	0	0.9630	-19.6066	1	33.3863
3	1	0	1.0000	1.8507	0.9798	52.3855
4	0.5761	0	0.7370	-7.4198	0.3059	52.8267

Table 8.8: Amplitude and phase of the Chebychev & the optimised tapers used to obtain the target SLL with the IBOB

mutual coupling and other structural non linearity as observed in this case. The conventional pattern synthesis taper is unable to produce the optimum results for practical small antenna arrays.

In the second instance the IzBC-PSO was used for the $-25dB$ target SLL. The resulted power pattern is shown in Figure 8.22. The PSLL observed was $-24.8dB$ with HPBW of 34^o. This proves the ability of the IzBC-PSO to obtain the low SLL for the given number of elements. The pattern presented in comparison was obtained by using the measured element pattern using VNA and was optimised using IzBC-PSO as discussed in sections 8.3.3 and 8.4 of this chapter. The significant improvement in SLL is obtained using the proposed optimised scheme. These results show that the proposed scheme can be implemented with the practical small antenna arrays for the robust beamforming and lower SLLs.

8.5.9 Scanned Pattern Synthesis

IzBC-PSO was used to find out the optimised taper to achieve a scanned beam ($\theta_o = 30^o$) while minimising the PSLL. The MATLAB model based on Equation 8.1 was used to determine the expected radiation pattern for the optimisation purposes. The PSLL was reduced to $-16.5dB$ for the expected radiation pattern with HPBW of 34^o. The optimised taper is given in Table 8.9. This taper was applied to IBOB beamformer and the radiation pattern was measured. The expected and measured radiation patterns are shown in Figure 8.23 and the results are summarised in Table 8.10. The scan direction was accurately achieved as expected. The region on left of the mainbeam is taken for PSLL consideration. The difference between the measured and expected pattern PSLL was found to be $2dB$.

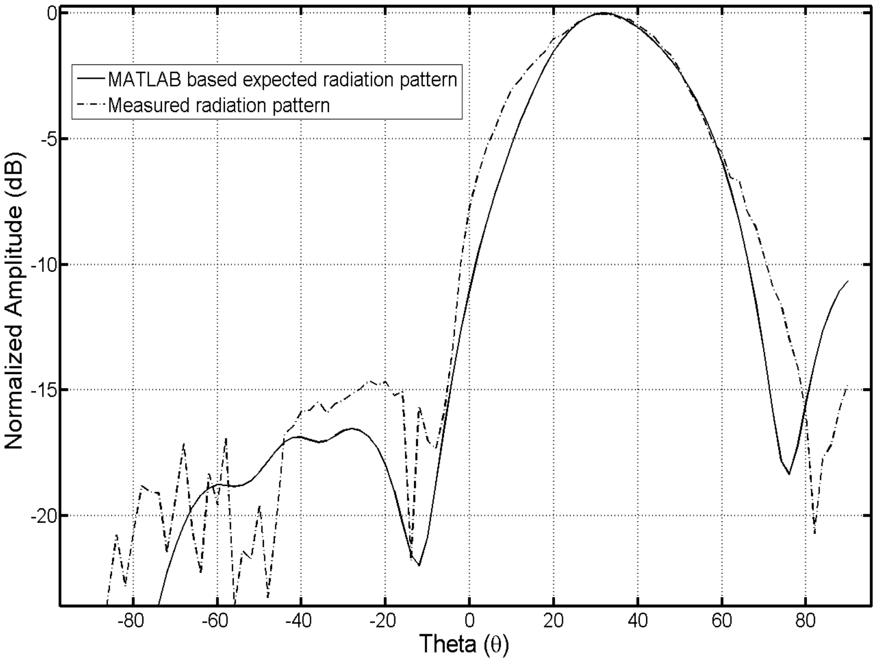

Figure 8.23: Comparison of the scanned array pattern measured by using IBOB after applying IzBC-PSO generated weights and that predicted by MATLAB model. (patterns are presented after performing offline calibration)

From these results it can be concluded that IzBC-PSO has offered significant performance improvement for small antenna array pattern synthesis. The IBOB was used to measure the radiation pattern with the optimised weights applied to observe the online effect of optimised taper. It is shown that the measurements follow the expected results closely and if IzBC-PSO is not used

Number of Element	PSO Taper for 30^o Scaned beam	
N	Mag	Phase (Deg)
1	0.8140	0
2	1	99
3	0.6654	170.3
4	0.1986	−127.3

Table 8.9: Amplitude and phase of the scanned optimised tapers used to obtain the target SLL with the IBOB

Pattern Type	$-3dB$ Beamwidth (Deg)	Peak Sidelobe Level (dB)
Measured	42	−14.6
MATLAB	36	−16.5

Table 8.10: Peak sidelobe level (SLL) and beamwidth are compared for the three sets of taper applied with IBOB and the patterns are shown in Figure 8.23

the radiation patterns are effected due to mutual coupling and the structural non linearity.

8.6 Data Acquisition (DAQ) Board

This is completely independent set of hardware that was used for the beamforming measurements. This equipment has more bandwidth as compared to the IBOB. The IBOB based beamformer provides the online beamforming. Whereas with DAQ offline beamforming was performed. The hardware setup that includes ADCs, FPGA and $1GHz$ sample clock was designed by the engineers at Jodrell Bank Observatory [70]. The basic beamforming setup used with DAQ is shown in Figure 8.24.

The offline beamformer required to use with the DAQ board was designed by this author. That also includes data processing and analysis tools development. The major components of this beamforming setup are summarised below.

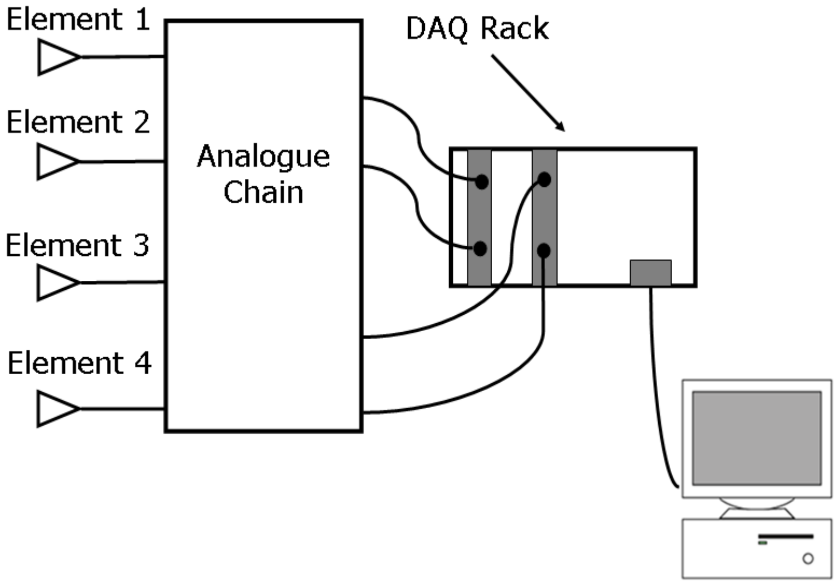

Figure 8.24: Block diagram of DAQ setup used for measurements

8.6.1 Analogue Chain

With this beamformer analogue chain was connected to each RF channel shown in Figure 8.27. The block diagram of the single analogue chain used is shown in Figure 8.25.

The low noise amplifier (LNA) and anti aliasing filter are the essential components of any RF receiver. The target frequency range for this wideband beamformer was chosen from $500MHz$ to $1GHz$. All the components used in the analogue chain were $Mini-Circuits^{®}$ product. The received RF signals were connected directly to the low noise amplifier (LNA $ZX60-33LN+$). This LNA gives a typical gain of $18.8dB$ at $1GHz$. The amplified signal was then passed through high and low pass filter to band limit the signal for Nyquist sampling. The high pass filter ($BHP-500+$) with pass band from $500Mz-3.2GHz$ was used. To keep the signal bandwidth in the required limits a low pass filter ($BLP-850+$) was connected immediately after the high pass filter. The analogue chain, once assembled, was tested individually for each channel.

The measured results are presented in Figure 8.26. The maximum significant difference among the chain gains observed was $0.93dB$ at $630MHz$. The maximum gain obtained was $16.03dB$ at $588MHz$. The maximum and minimum

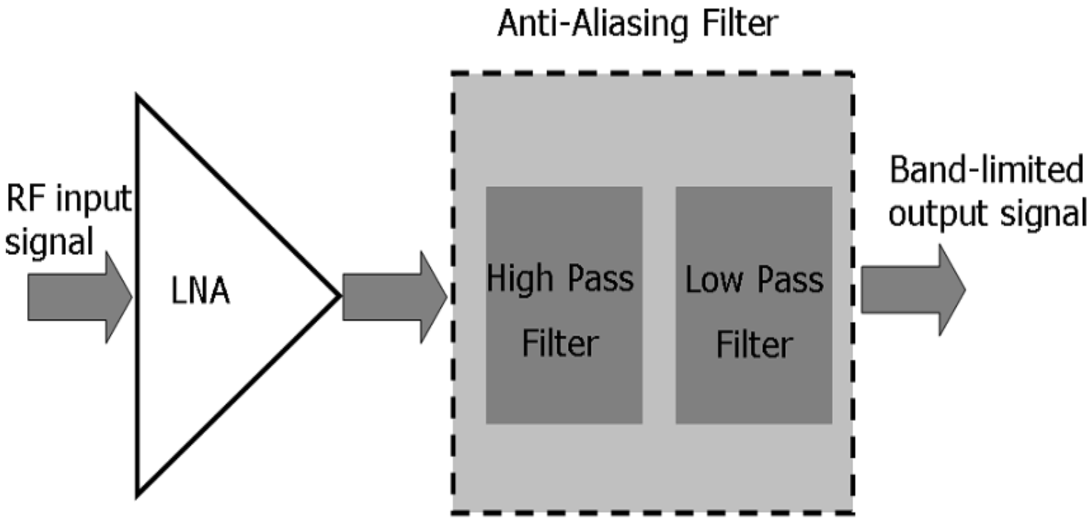

Figure 8.25: Block diagram of the single analogue chain

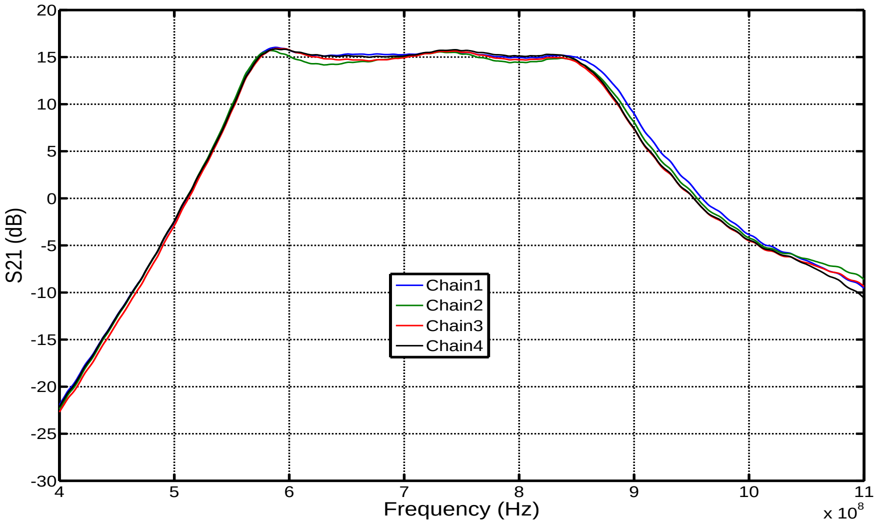

Figure 8.26: The frequency response of the analogue chains

measured $-3dB$ bandwidths were $315MHz$ and $302MHz$ ranging from $561MHz$ to $876MHz$ and $563MHz$ to $865MHz$ for chain 1 and chain 2 respectively.

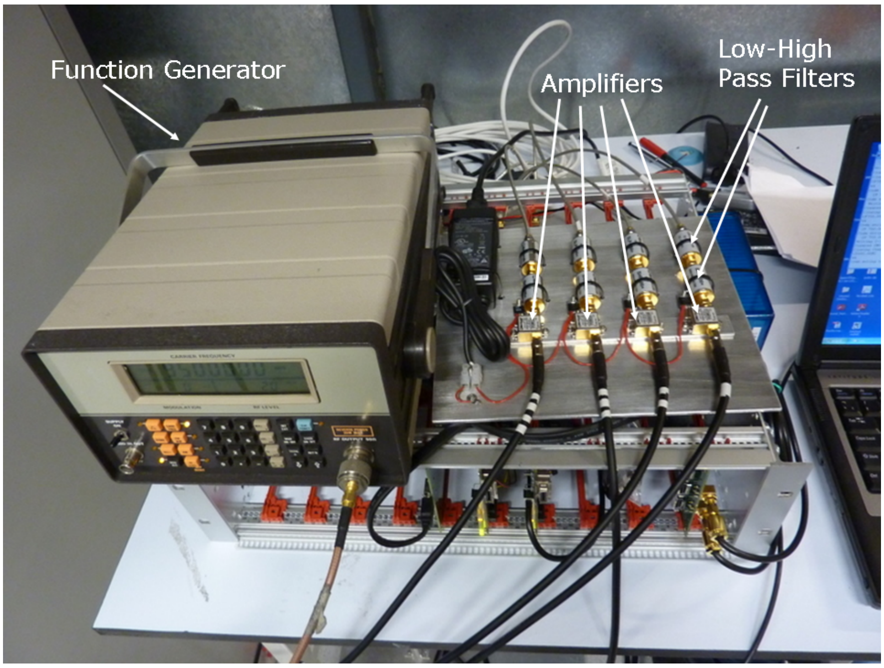

Figure 8.27: Analogue chain used with the DAQ setup

8.6.2 Sampling

As a result of the anti-aliasing filter the input RF signal was bandlimited to $500MHz$ in the upper Nyquist band. This was necessary because the sampling clock was $1GHz$ and the operational frequencies range from $500MHz$ to $1GHz$. According to the Nyquist sampling theorem the signal to be sampled should be bandlimited to half of the sampling frequency to avoid aliasing.

8.6.3 Data Transfer

The sampled and recorded data was transferred from the FPGA (Xilinx Virtex-5 XC5VLX110T) to the desktop machine. Here the FPGA was used to buffer the high rate ADC (ADC08D1500) data. A buffer size of $4KB$ was chosen. The data was read and saved on desktop PC as hexadecimal data files. For a single set of measurement there were 4096 samples ($4KB$) each of 8 bits for each channel. This hexadecimal data was converted to decimal values using MATLAB based code.

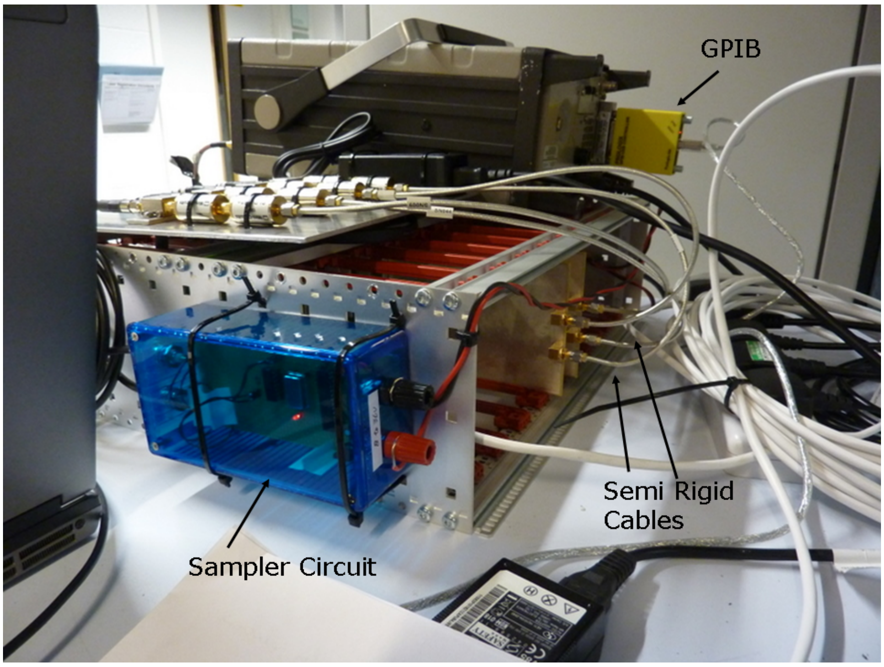

Figure 8.28: Analogue chain connected to the antennas on one end and the DAQ on the other end

8.6.4 Data Processing & Analysis

The time domain sampled data at four channels is shown in Figures 8.29(a) and 8.29(b) for a single test measurement instance. A set of four test measurements was obtained using the setup shown in Figure 8.30.

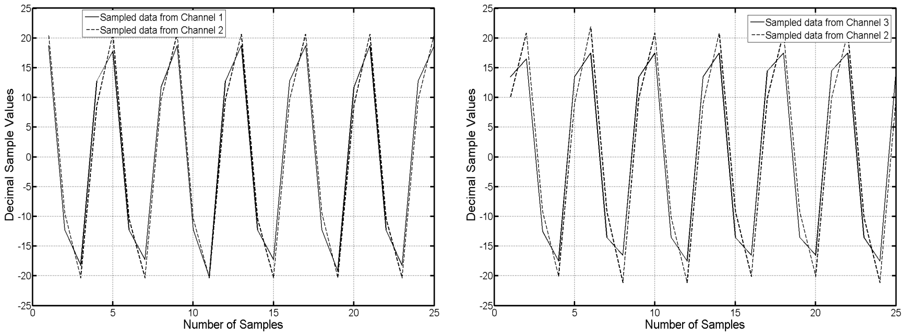

(a) Channel 1 and Channel 2

(b) Channel 3 and Channel 4

Figure 8.29: Sampled data at 750*MHz*

The measurements were performed at five frequency values 550*MHz*, 745*MHz*, 750*MHz*, 755*MHz* and 950*MHz*. Discrete Fourier Transform (DFT) was applied directly to the sampled data of each channel. For DFT calculations the Fast

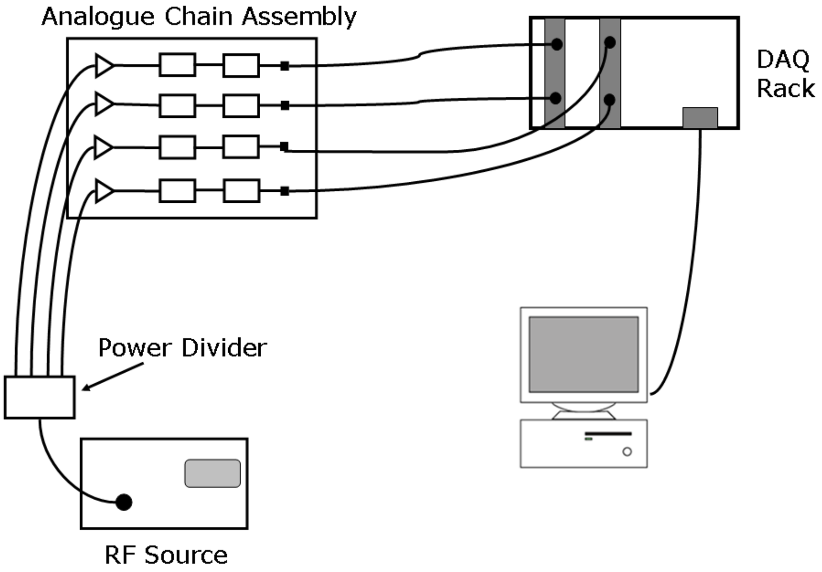

Figure 8.30: Hardware setup for the test measurements

Fourier Transform (FFT) algorithm was used on the full data set of 4096 values. The resultant 4096 point FFT on four channels, shown in Figures 8.31 & 8.32, gives a resolution of 122.1*KHz* over 500*MHz* bandwidth. The possible error with this resolution for each RF frequency measured is negligible.

Since for this experiment a narrow-band signal was used therefore there was no need to apply any sort of filter bank to isolate the frequency bins. The target FFT spectrum bin was the one with maximum power. Because of the good frequency resolution the target bin frequency and the frequency of the RF signal were aligned within some error. Since the percentage error is tolerable for this experiment therefore no bin alignment technique was implemented.

MATLAB based codes were developed as the part of this research work to process and analyse the data.

8.6.5 Software Beamforming

The block diagram of the complete offline software beamforming system, developed as a part of this research study, is shown in the Figure 8.33.

In order to measure the full array radiation pattern all four channels were connected to the four elements of the array under test (AUT) as shown in Figure

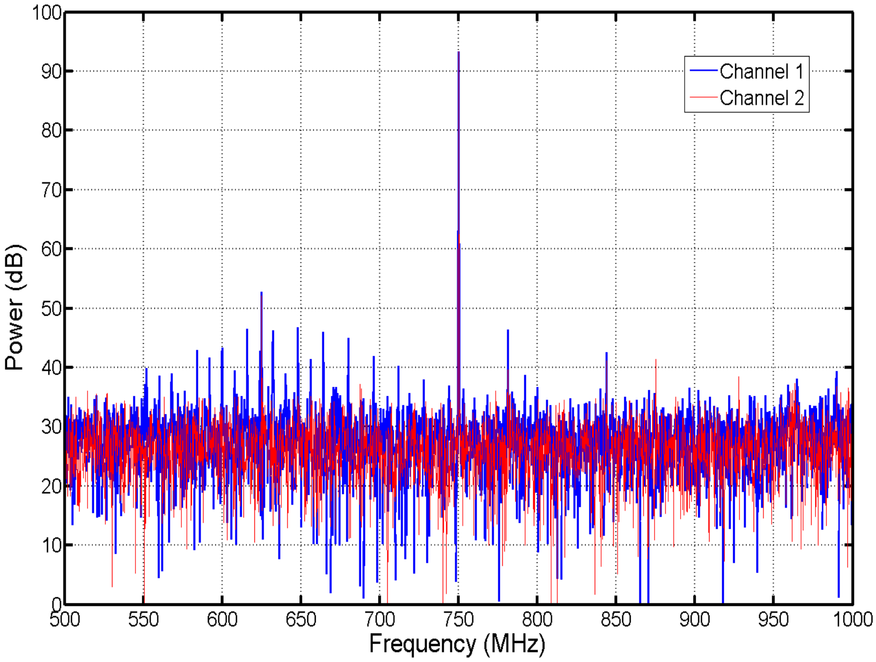

Figure 8.31: Fast Fourier Transform Spectrum at 750MHz

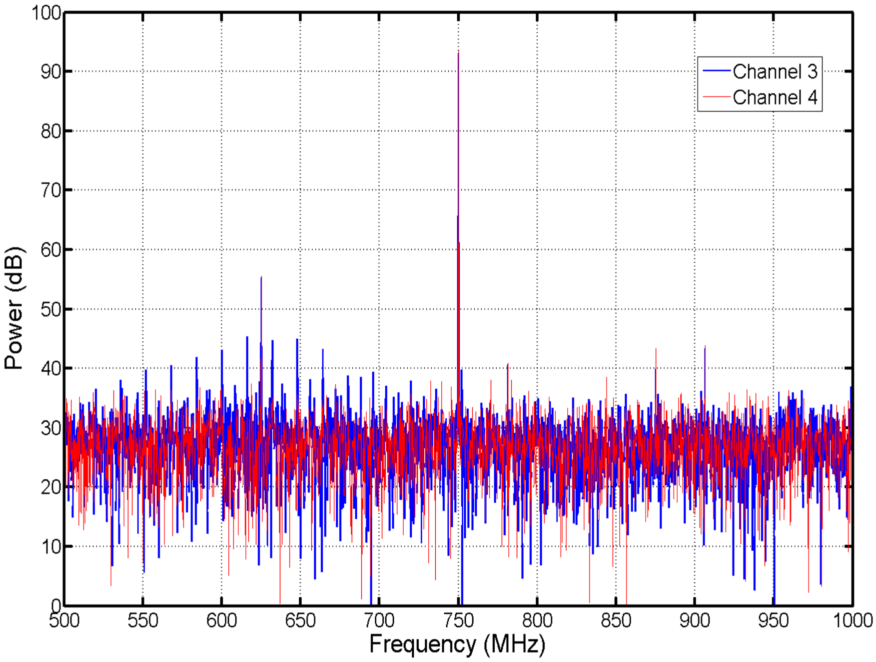

Figure 8.32: Fast Fourier Transform Spectrum at 750MHz for a single look direction

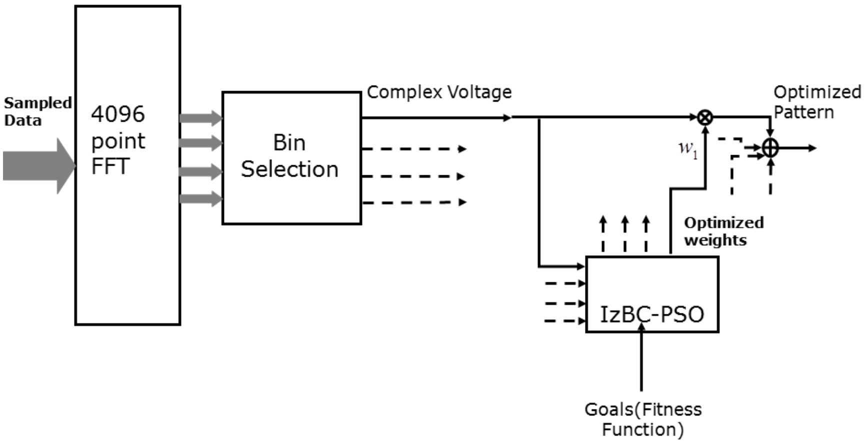

Figure 8.33: The offline beamformer programmed in MATLAB

8.24. The array was rotated along θ (-90^o to 90^o) in steps of 2^o resulting in 91 measurements. The block diagram Figure 8.33 represents the beamforming operation once the data is collected for all 91 measurements. The basic digital signal processing applied to this data is the same as explained in the section 8.6.4 for test data. After the bin selection the corresponding FFT complex voltage ($V = Re + j * Img$) is used to find the radiation pattern for the array as shown in Figure 8.33 after adding all the four channels. The phase information is extracted from the VNA measured element pattern for each element. The VNA measurements were performed at the same look directions as that for the DAQ board. The complete radiation pattern is obtained by multiplying the power data obtained by the DAQ board sampling to the phase term obtained by the VNA at the same frequency.The Figure 8.33 only show the single channel in dark line as active. The dashed lines are represented that for the other channels same process implied. The mathematical expression representing the complex voltage received to each channel at each look direction is given by;

$$V_n(\theta_q) = V'_n(\theta_q)e^{j\phi_n^q} \tag{8.2}$$

Where $q = 1, 2, 3, ...91$, $V_n(\theta_q)$ is the complex voltage value at each q^{th} look direction for each n^{th} channel, $V_n^{'}(\theta_q)$ is the voltage amplitude value obtained from the DAQ board data at each look direction q for the n^{th} channel and ϕ_n^q is the corresponding phase value obtained by the VNA. The total pattern for n^{th} channel would be given by a data array $V_n(\theta) = [V_n(\theta_1), V_n(\theta_2), ..., V_n(\theta_{91})]$. The antenna array radiation pattern (RP) is given by;

$$RP(\theta) = \sum_{n=1}^{4} w_n * V_n(\theta) \tag{8.3}$$

Where w_n is the optimized complex weight multiplier for the n^{th} channel. The complex weights were determined by using the IzBC-PSO algorithm as shown in the Figure 8.33. The individual element (channel) power patterns were fed to the optimiser and total radiation pattern was obtained by applying Equation 8.3. The optimiser then computed for the best solution for the given pattern synthesis goals and produced a set of optimized weights. These weights were multiplied by the individual element (channel) pattern and then summed as shown in Figure 8.33.

In a modified version of the this software digital beamformer the voltages received at only $\theta = 0$ for each channel are measured. These voltages are fixed and the digital sweep is applied to find the predicted radiation pattern (PRP) without physically scanning the array. It is equivalent to fix the physical array structure in one direction say broadside or $\theta = 0$ and applying the progressive phase sweep for $-90 \leq \theta \leq 90$ to the elements. This does not give the actual radiation pattern but it allows to predict the correct scan direction, the target null position and the sidelobe level. It does not require the physical stage rotation and no delays are involved required to measure the individual element patterns yet a feedback is established for the optimisation predictions. The mathematical model is given expression is;

$$PRP(\theta) = \sum_{n=1}^{4} w_n(\theta) * V_n(0^o) \tag{8.4}$$

Where $w_n(\theta) = a_n e^{-jkd(n-1)\sin\theta}$. The beamforming results are presented in the next section.

8.6.6 Results & Discussion

The digital beamforming system based on DAQ is described in chapter 8. The offline beamformer developed as a part of this research work is based on the DAQ measurements. The measurement setup is described below.

8.6.7 DAQ Setup & Processing

BECA array was connected to the analogue chain and each element was connected to the amplifier first as depicted in Figure 8.24. To find the full array radiation pattern all four elements were connected to the DAQ board through analogue chain. The RF signal received at each channel was recorded for the offline processing and no coefficient multiplications were performed at this stage. The recorded data is then processed to find the element patterns. These patterns were then integrated to the IzBC-PSO scheme to run the optimisation process. The optimised weights were then used as the beamforming multiplying coefficients.

In this study offline beamforming is used to predict the full array radiation pattern with only one set of measurement as described in section 8.6.5. This is the measure of voltage received at all four channels when the array is physically directing to the transmitter. With this single set of measurement the predicted radiation pattern (PRP) is determined by using Equation 8.4. This PRP is then used as a feedback for the IzBC-PSO scheme which enables effective reduction of SLL, scanned direction and the pattern null placements as shown below.

8.6.8 Sidelobe Level Reduction

The goal in this section is to produce the radiation patterns with reduced SLL using IzBC-PSO in conjunction with PRP. As a starting point both the PRP and the full array radiation patterns are shown in Figure 8.34 both excited with uniform taper. The full array radiation pattern is obtained by multiplying the excitation weight vector to each channel as shown in Figure 8.33 once the DAQ has finished data recording for a complete 180^o sweep. The radiation patterns are compared with the MATLAB expected patterns. The MATLAB expected patterns are based on the element patterns that are measured using the VNA as described in section 8.3.2.

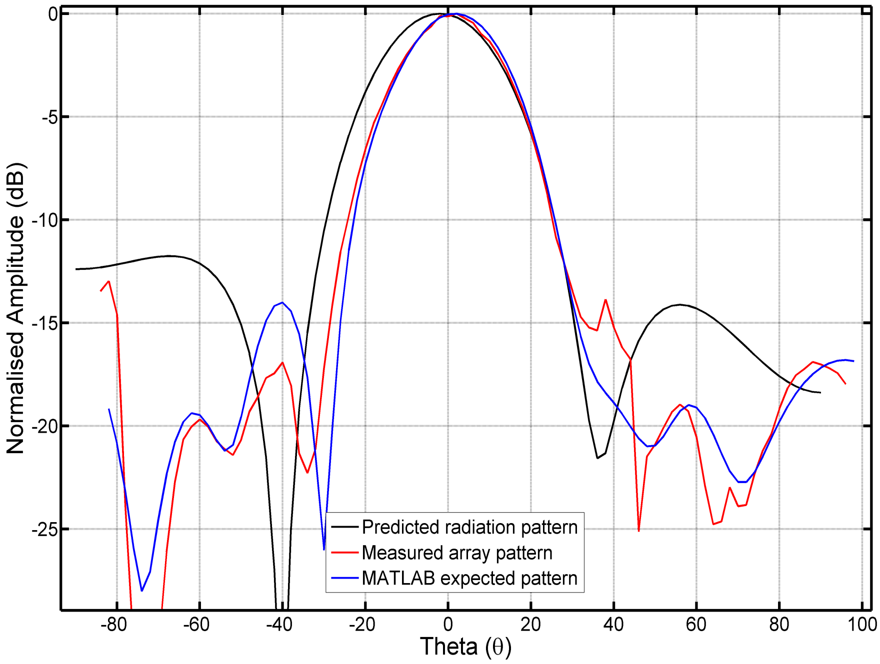

Figure 8.34: Array patterns compared, obtained at $750MHz$ for uniform taper

The DAQ measured pattern and the MATLAB expected pattern follow the general trend although the two patterns are not exactly the same. The predicted pattern has different SLL and it is not expected that predicted radiation pattern would follow the DAQ measured pattern. This pattern is used for mere comparison and to simplify the optimisation requirement of knowing the full element pattern in order to synthesise an optimum array pattern. This idea is used successfully in this study as shown in Figure 8.35.

The proposed optimisation scheme is run to obtain a radiation pattern with target SLL of $-20dB$. The difference between this problem scenario and the other scenarios presented in chapter 5 and earlier in sections 8.4 and 8.5.8 of this chapter is that in this case only PRP is used instead of full radiation pattern. It is shown that the PRP reflected the SLL property desired in the radiation pattern. The DAQ measured radiation pattern has a PSLL of $-21dB$. This result is not accurate compared to those already presented in earlier sections due to the simplification of the array model involved here. This shows that PRP can be used as an indication for the problem objective while performing the optimisation using the proposed scheme, IzBC-PSO.

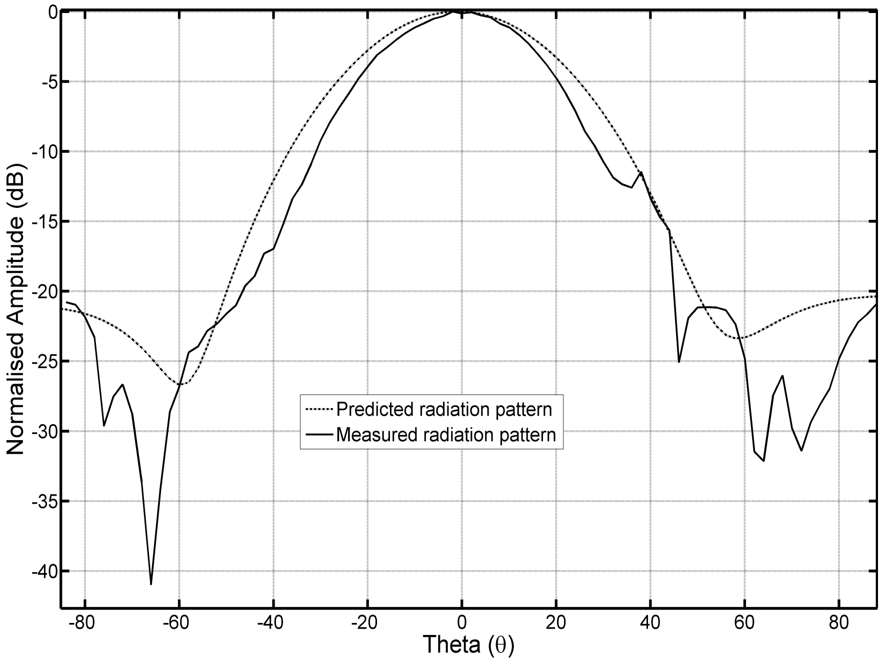

Figure 8.35: Array patterns compared, obtained at $750MHz$ for $-20dB$ SLL

8.6.9 Array Scanning

This section concerns with the investigation of predicting the array scanning behaviour with accurate scan direction and reduced SLL. The optimisation goal was set to obtain a radiation pattern with main beam scanned to $\theta_o = 30^o$ while having reduced SLL for the target HPBW of 32^o. This objective is implemented on the simplified array model (PRP) and the resulted excitation taper is then applied to the DAQ measured data to obtain the full array radiation pattern.

It is evident from Figure 8.36 that the target scan direction is achieved as predicted. The PSLL is reduced to $-15.3dB$ compared to the measured radiation pattern obtained with the linear progressive phase taper. This shows a significant improvement of $3dB$. It is observed that SLL topology is not accurately predicted, however, the main beam scan direction is accurate as both excitation amplitude and phase are determined by using IzBC-PSO.

8.6.10 Null Pattern Synthesis

An important application of the antenna arrays is to mitigate the interference from a known direction. This objective is achieved by placing a null in the direction of interfering source. BECA array with the DAQ digital beamforming

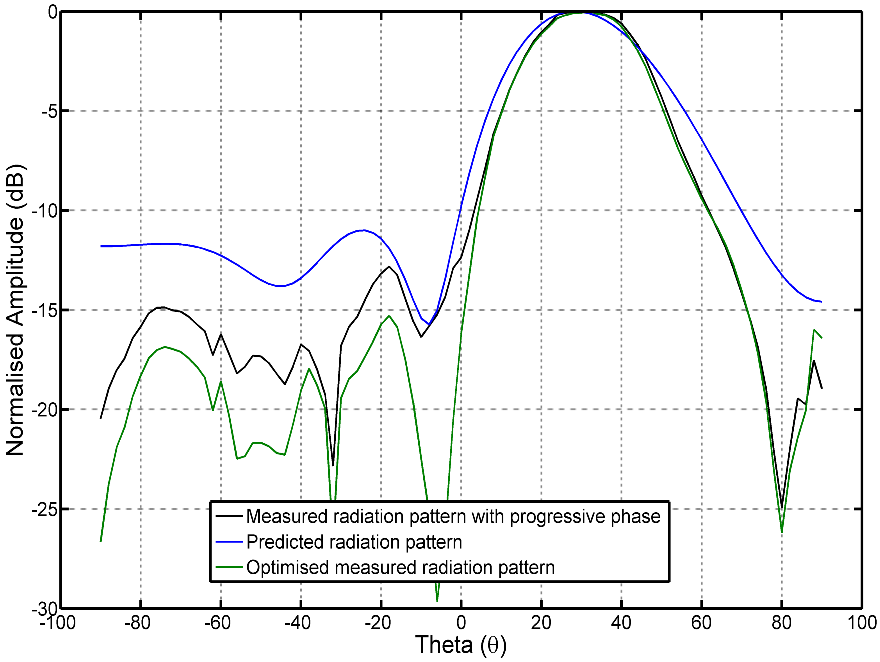

Figure 8.36: Array patterns compared, obtained at 750MHz for mainbeam scanned to $\theta_o = 30^o$

setup is used to demonstrate this ability. The multi objective fitness function used for this problem considers the null depth in a target direction, scan direction and SLL reduction. The optimisation procedure described in earlier chapters. The only difference in the optimisation model here is the use of PRP to predict the correct null and scan direction. The target null depth was set to $-40dB$ at $\theta = 50^o$ and the mainlobe was required to scan to $\theta = -30^o$. The results are given in Figure 8.37 comparing the PRP and the measured results.

It is shown that the scan direction of the mainbeam and null direction were correctly predicted. The null depth of the measured was found to be $-25.8dB$ opposed to predicted $40dB$. The SLL are found below $-15dB$.

It is shown through these test cases that this simplified optimisation model based on a single broadside measurement can be used to predict important pattern characteristics such as scan direction and null placement direction. The radiation power magnitude prediction is, however, not accurate. It is shown that IzBC-PSO has significant performance advantages for the small phased array considered in this study while used with the simplified array model.

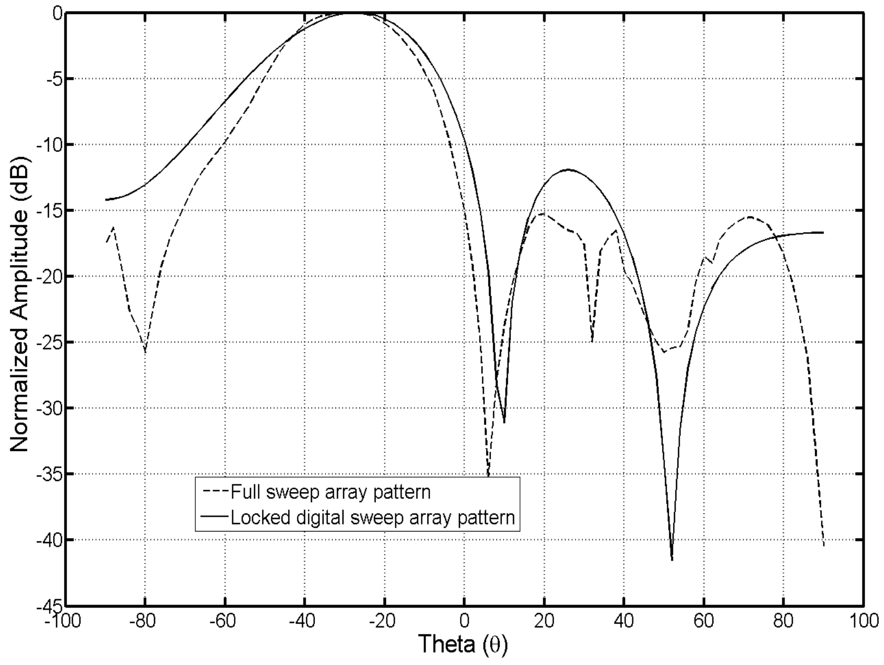

Figure 8.37: Array patterns compared, obtained at $750MHz$ for null at $\theta = 50^o$ and main beam scanned to $\theta = -30^o$

8.7 Chapter Summary

The important results of this chapter are:

- The experimental setup used for the measurements including the digital beamformers is described and depicted in (§8.3, 8.5, 8.6);
- The measured element patterns are presented for BECA array of four elements and it is shown that the asymmetric behaviour is not due to the electromagnetic environment but due to the array structure (section 8.3.2);
- A MATLAB based array model is developed that uses measured element patterns to find the expected full array radiation pattern and it is shown that this expected pattern is in close agreement with the measured full array radiation pattern (section 8.3.3);
- Radiation pattern synthesis is performed on the MATLAB based array model and results are presented for broadside, scanned and null placements, demonstrating the significant advantage of using IzBC-PSO over conventional method (section 8.4);

- The array radiation pattern measurements with IBOB digital beamformer are presented to show that the proposed optimisation scheme is capable of online radiation pattern improvement for small antenna array (section 8.5.7);
- IzBC-PSO has shown significant improvements to the radiation patterns measured online for the broadside and also when the main beam is scanned (section 8.5.8);
- Offline beamforming setup based on DAQ board is used to develop a simplified array model to predict the radiation pattern characteristics (section 8.6.7);
- IzBC-PSO is successfully used with the simplified array model to obtain the optimised array behaviour for reduced SLL, scanned array and for interference jammer applications (sections 8.6.8-8.6.10)

Chapter 9

Conclusion & Future Work

This chapter is intended to present a brief summary of the research work presented in this thesis followed by the conclusions and possible future work avenues.

9.1 Summary of Work

The performance of phased arrays is sensitive to many factors including element type, element separation, array configuration, frequency of operation, bandwidth etc. In this thesis, these factors are modelled as the mutual coupling matrix and active element patterns and it is shown that the radiation performance is significantly degraded for various examples. It is necessary to mitigate the effect of these factors to obtain target radiation performance of an antenna array, this need is highlighted in chapters 5,6,7 and 8. The optimisation scheme, IzBC-PSO, proposed in this thesis to mitigate the effect of above mentioned factors is based on the intelligently defined solution space and the PSO. The narrow band pencil beam patterns are considered in chapter 5 and it is shown that for high resolution low gain scanning antenna arrays, in the presence of mutual coupling, a compensation is essential. The same chapter addresses the limitations of the scanning difference pattern array and the advantage of using the preferred solution is highlighted. A monopulse array is presented in chapter 5 with target sum and difference patterns obtained by phase only modification. In cellular communication systems the sector beams are widely used. In chapter 6 the linear array is considered for its application as sector beam array in the presence of mutual coupling. The resultant radiation pattern has unacceptable ripple and HPBW, which is contained within the defined mask by using the IzBC-PSO. A wideband excitation taper for optimal performance of PSLL bandwidth is determined using the proposed optimisation scheme presented in chapter 7. When main beam scans away from the broadside mutual coupling has significant on the radiation performance and an excitation taper is proposed to improve the PSLL bandwidth.

Convergence and consistency of the IzBC-PSO is tested by comparing it with UoM-PSO and GA based optimisers. The IzBC-PSO has better convergence for all the example problems considered in this thesis. In some cases GA has performed well to produce a single instance of good convergence out of 10 trails but it has poor consistency. The UoM-PSO performed better compared to GA in terms of consistency and convergence but it could not beat the IzBC-PSO. The proposed technique has limitations as its fast convergence and consistency is due to the intelligently defined solution space. It is the Scehlkunoff's unit circle approach that enabled to define such boundary conditions, as this z-space transformation of the array factor can not be used directly for aperiodic arrays or non linear arrays. Also in case of large antenna arrays due to large number of unknowns involved obtaining better convergence and consistency would be a challenge. This issue is addressed in future work section.

9.2 Conclusion

This thesis investigates the performance improvement to the radiation patterns of small linear periodic phased arrays offered by a single optimisation scheme, for a range of pattern synthesis problems. The proposed optimisation scheme, IzBC-PSO, is based on the Particle Swarm Optimiser [21,22,27] and Schelkunoff's [23] unit circle approach. It is shown that the proposed optimisation scheme is capable of achieving the radiation pattern objectives in the presence of mutual coupling for a sum pattern while the mainbeam is at broadside. If no mutual coupling mitigation is applied then the radiation performance is reduced in terms of gain and SLL. The optimisation scheme is capable of simultaneously mitigating the effects of mutual coupling and natural mainbeam broadening while the sum pattern mainbeam is scanned. It is shown that the gain, reduced SLL and other performance metrics have been improved significantly for sum patterns presented. An improvement of $2dB$ in PSLL for a reduced HPBW of 55^o (compared to 73^o) for scanned array is recorded. In case of difference pattern it is shown that the IzBC-PSO has effectively improved the difference pattern slope and SLL in the presence of mutual coupling. A significant degradation in the SLL and the difference pattern twin beam while scanned in the presence of mutual coupling is well known. The PSLL is improved by $6.6dB$ and the difference pattern slope has increased by 4.8 compared to the uncompensated radiation pattern when IzBC-PSO is used. It is shown that the desired array performance is obtained in the presence of mutual coupling and with small array length ($d = 0.4\lambda$). The proposed optimisation scheme has shown to achieve a simplified feed for a monopulse array by using a simple 180^o phase only change in the weights, while meeting the radiation pattern objectives. The sum pattern is obtained with the target average SLL of $-20dB$ while the difference pattern PSLL is maintained at $-15dB$ with the main pattern null depth of $-40dB$ (chapter 5).

Convergence performance comparisons have shown that the preferred scheme, IzBC-PSO, is faster, consistent and more accurate then its variant (UoM-PSO) and GA. Therefore IzBC-PSO technique should be preferred over the competitive techniques for these pattern synthesis problems. It is important to note that the intelligently defined boundaries result in over 30% faster convergence in all cases considered. The issues related to the sampling of the continuous tapers (Taylor, Bayliss, Woodward) have also been resolved by using the preferred scheme (chapter 5).

The IzBC-PSO is also used for sector beam synthesis. The limitations of the Woodward Lawson technique have been overcome by using the preferred technique. Significant pattern improvements are shown with the isotropic and non-isotropic arrays for both broadside and scanned beam situations. In case of isotropic array the main beam ripples are reduced from $-3dB$ (Woodward Lawson Method) to target ripple value of $-1dB$ and the mainbeam is contained in the defined mask by using IzBC-PSO. The target masks are met as close as possible in case of mutually coupled array. The significant beamwidth reduction is shown while the main beam is scanned (chapter 6).

The wideband array performance has improved by using the optimisation schemes UoM-PSO and IzBC-PSO. The frequency sensitivity of HPBW is addressed over a band of frequencies. The optimum solution obtained using

IzBC-PSO results in high resolution beam with reduced SLL. The HPBW is maintained at 13.5^o over a band of frequencies from $0.6GHz$ to $1.0GHz$ (chapter 7).

Improvements have shown in the PSLL bandwidth performance if the proposed optimisation scheme is used, while the mainbeam is at broadside and also when it is scanned. It is important to note that only one set of optimised excitation taper is required to maintain the PSLL under the tolerance level for wideband operation. For a broadside scan the PSLL has improved over $3dB$ for a fractional bandwidth of 80% by using the proposed solution. The effect of mutual coupling becomes severe with the scanning and resulted in higher SLL. The PSLL bandwidth performance is improved with a single optimised excitation taper obtained after re-optimisation for the scanned beam. It is evident if no mitigation is applied the PSLL bandwidth performance is unacceptable for both scenarios considered. The use of IzBC-PSO has improved the PSLL by $10dB$ over a 59% fractional bandwidth (chapter 7).

An important point is that the improved radiation performance is obtained with small arrays for a wide range of pattern synthesis problems by using a single optimisation scheme. No parameter changes are applied to the basic algorithm or to the problem model. Each different problem scenario is translated in terms of a fitness function that is used to determine the performance. The multi objective problems dealt in this thesis are solved as single objective problems with carefully selected weighting (contributing) multipliers. It is not the objective of this thesis to find the best possible solution for a given problem. The goal is to achieve a solution within some acceptable error for reduced number of fitness function evaluations by using a single optimisation scheme that can be applied to all problems presented here. The proposed scheme, IzBC-PSO, fulfils these requirements. It has produced better results with consistency and require less fitness function evaluations as compared to UoM-PSO and GA.

The farfield array radiation pattern measurements are performed to test the proposed scheme for its application in real digital beamforming system. To perform these measurements online and offline digital beamforming setups are used. The results have proven the effectiveness of this technique in the presence of mutual coupling and asymmetric array behaviour. A significant improvement of $6dB$ in PSLL over uncompensated Dolph-Chebychev is observed if IzBC-PSO is used for any array with $d = 0.37\lambda$ (closely packed array). Therefore it is necessary to use the proposed optimisation scheme to obtain a target optimum performance with a small array (in terms of number of elements and array length).

9.3 Future Work

There are a number of applications to which this proposed optimisation scheme can be extended. A well known problem that hinders the application of powerful heuristic optimisation techniques to the large antenna arrays is the number of variables involved. The IzBC-PSO presented for small antenna arrays in this thesis can be applied to large arrays using the concept of sub-arrays.

An interesting topic would be to study the radiation pattern performance of the antenna arrays consisting of non-identical elements. Due to the implementation nature of this technique it can be extended directly to solve the pattern synthesis problems associated with these arrays.

Another logical step forward is the extension of the optimisation scheme to periodic planar array geometry. In case of planar arrays the antenna elements have strong mutual coupling which would limit the performance of conventional pattern synthesis techniques. Therefore, it would be of interest to observe the performance improvements in planar arrays in the presence of mutual coupling and asymmetric array behaviour.

In case of real systems accumulated errors in measuring equipment or other digital errors may degrade the array radiation performance. It would be of interest to improvement the array radiation performance in the presence of noise. Due to the random nature of the noisy environment, conventional optimisation schemes would fail. Since the proposed optimisation scheme is based on a heuristic algorithm therefore it would have an advantage under such conditions.

For improved bandwidth performance and to avoid natural limitations of wideband phased arrays, including beam squinting etc, time delay arrays are used. Therefore, it would also be of interest to model an optimisation scheme for time domain arrays.

It is also of the author's interest to study the possible modifications required for effective implementation of the proposed scheme with active arrays. This would provide the advantages of calibration and better radiation performance.

Bibliography

[1] *IEEE Standard Definitions of Terms for Antennas.*, IEEE Std. 145-1993, 1993.

[2] R. J. Mailloux, *Phased array antenna handbook.* Artech House, INC., 2005.

[3] C. A. Balanis, *Antenna Theory Analysis and Design.* John Wiley & Sons, 2005.

[4] R. S. Elliott, *Antenna Theory and Design.* IEEE Press, John Wiley and Sons, 2003.

[5] C. A. Balanis, *Modern Antenna Handbook*, C. A. Balanis, Ed. John Wiley & Sons, 2005.

[6] C. Dolph, "A current distribution for broadside arrays which optimizes the relationship between beam width and side-lobe level," *Proceedings of the IRE*, vol. 34, no. 6, pp. 335 – 348, June 1946.

[7] T. T. Taylor, "Design of line source antenna for narrow beamwidth and low sidelobes," *Antenna Propagation, IRE Transactions on*, vol. 3, no. 1, pp. 16–28, January 1955.

[8] P. Woodward, "A method of calculating the field over a plane aperture required to produce a given polar diagram," *Electrical Engineers - Part IIIA: Radiolocation, Journal of the Institution of*, vol. 93, no. 10, pp. 1554 –1558, 1946.

[9] P. Woodward and J. Lawson, "The theoretical precision with which an arbitrary radiation-pattern may be obtained from a source of finite size," *Electrical Engineers - Part I: General, Journal of the Institution of*, vol. 95, no. 93, p. 405, September 1948.

[10] E. T. Bayliss, “Design of monopulse antenna difference patterns with low side lobes,” *Bell System Tech. J*, no. 47, pp. 623–40, 1968.

[11] C. L. Dolph, “Discussion on ”a current distribution for broadside arrays which optimizes the relationship between beam width and side-lobe level” (),” *Proceedings of the IRE*, vol. 35, no. 5, pp. 489–492, 1947.

[12] A. Villeneuve, “Taylor patterns for discrete arrays,” *Antennas and Propagation, IEEE Transactions on*, vol. 32, no. 10, pp. 1089 – 1093, October 1984.

[13] I. J. Gupta, J. R. Baxter, S. W. Ellingson, H.-G. Park, H. S. Oh, and M. G. Kyeong, “An experimental study of antenna array calibration,” *Antennas and Propagation, IEEE Transactions on*, vol. 51, no. 3, pp. 664–667, 2003.

[14] D. M. Pozar, “The active element pattern,” *IEEE Transactions on Antennas and Propagation*, vol. 42, no. 8, pp. 1176–1178, 1994.

[15] Y.-W. Kang and D. Pozar, “Correction of error in reduced sidelobe synthesis due to mutual coupling,” *Antennas and Propagation, IEEE Transactions on*, vol. 33, no. 9, pp. 1025 – 1028, September 1985.

[16] H. Steyskal and J. Herd, “Mutual coupling compensation in small array antennas,” *Antennas and Propagation, IEEE Transactions on*, vol. 38, no. 12, pp. 1971 –1975, December 1990.

[17] D. F. Kelley and W. L. Stutzman, “Array antenna pattern modeling methods that include mutual coupling effects,” *Antennas and Propagation, IEEE Transactions on*, vol. 41, no. 12, pp. 1625–1632, 1993.

[18] P. N. Fletcher and M. Dean, “Derivation of orthogonal beams and their application to beamforming in small phased arrays,” *IEE Proceedings -Microwaves, Antennas and Propagation*, vol. 143, no. 4, pp. 304–308, 1996.

[19] I. Salonen, A. Toropainen, and P. Vainikainen, “Linear pattern correction in a small microstrip antenna array,” *IEEE Transactions on Antennas and Propagation*, vol. 52, no. 2, pp. 578–586, 2004.

[20] D. Pozar, Y.-W. Kang, D. Schaubert, and R. McIntosh, “Optimization of the transient radiation from a dipole array,” *Antennas and Propagation, IEEE Transactions on*, vol. 33, no. 1, pp. 69 – 75, January 1985.

[21] J. Kennedy and R. Eberhart, "Particle swarm optimization," *IEEE International Conference on Neural Networks Proceedings*, vol. 4, pp. 1942–1948, 1995.

[22] ——, "A new optimizer using particle swarm theory," *Proceedings of the Sixth International Symposium on Micro Machine and Human Science*, pp. 39–43, 1995.

[23] S. A. Schelkunoff, *A mathematical theory of linear arrays*. Bell System Tech, 1943.

[24] H. Lebret and S. Boyd, "Antenna array pattern synthesis via convex optimization," *IEEE Transactions on Signal Processing*, vol. 45, no. 3, pp. 526–532, 1997.

[25] T. Isernia and G. Panariello, "Optimal focusing of scalar fields subject to arbitrary upper bounds," *Electronics Letters*, vol. 34, no. 2, pp. 162–164, 1998.

[26] A. Sabharwal, D. Avidor, and L. Potter, "Sector beam synthesis for cellular systems using phased antenna arrays," *IEEE Transactions on Vehicular Technology*, vol. 49, no. 5, pp. 1784–1792, 2000.

[27] K. Parsopoulos and M. Vrahatis, *Particle Swarm Optimization and Intelligence: Advances and Applications*. Information Science Reference, 2010.

[28] J. Holland, "Genetic algorithms and the optimal allocation of trials," *SIAM Journal on Computing*, vol. 2, 1973.

[29] G. E. Liepins and M. R. Hilliard, "Genetic algorithms: foundations and applications," *Annals of Operations Research*, vol. 21, no. 1-4, pp. 31 – 57, November 1989.

[30] K.-K. Yan and Y. Lu, "Sidelobe reduction in array-pattern synthesis using genetic algorithm," *IEEE Transactions on Antennas and Propagation*, vol. 45, no. 7, pp. 1117–1122, 1997.

[31] F. Ares and S. R. e. a. Rengarajan, "Application of genetic algorithms and simulation annealing technique in optimizing the aperture distribution of antenna arrays," *Antenna and Propagation Society International Symposium*, pp. 806–809, 1996.

[32] D. Marcano, M. Jiminez, and O. Chang, "Synthesis of linear array using schelkunoff's method and genetic algorithms," in *Proc. AP-S Antennas and Propagation Society Int. Symp. Digest*, vol. 2, 1996, pp. 814–817.

[33] W. C. Wen-Chia Lue and F. Hsu, "Use of b-spline curves and genetic algorithms to reduce the sidelobe level in array-patterns," *Microwave and Optical Technology Letters*, vol. 38, pp. 308–11, 2003.

[34] D. W. Boeringer, D. W. Machuga, and D. H. Werner, "Synthesis of phased array amplitude weights for stationary sidelobe envelopes using genetic algorithms," in *Proc. IEEE Antennas and Propagation Society Int. Symp*, vol. 4, 2001, pp. 684–687.

[35] A. Recioui and A. Aznar, "Use of genetic algorithms in linear and planar antenna array synthesis based on schelkunoff method," *Microwave and Optical Technology Letters*, vol. 49, pp. 1619–23, 2007.

[36] M. Rattan, M. S. Pattern, and B. S. Sohi, "Synthesis of aperiodic linear antenna arrays using genetic algorithm," in *Proc. 19th Int. Conf. Applied Electromagnetics and Communications ICECom 2007*, 2007, pp. 1–4.

[37] D. Gies and Y. Rahmat-Samii, "Particle swarm optimization for reconfigurable phase-differentiated array design," *Microwave and Optical Technology Letters*, vol. 38, pp. 168–75, 2003.

[38] ——, "Reconfigurable array design using parallel particle swarm optimization," in *Proc. IEEE Antennas and Propagation Society Int. Symp*, vol. 1, 2003, pp. 177–180.

[39] M. Bataineh and J. Ababneh, "Synthesis of aperiodic linear phased antenna arrays using particle swarm optimization," *Electromagnetics*, vol. 26, pp. 531–41, 2006.

[40] M. Mussetta, P. Pirinoli, S. Selleri, and R. Zich, "Differentiated meta-pso techniques for antenna optimization," *2007 International Conference on Electromagnetics in Advanced Applications*, pp. 1029–32, 2007.

[41] W. Li, X. Shi, and Y. Hei, "An improved particle swarm optimization algorithm for pattern synthesis of phased arrays," *Progress in Electromagnetics Research*, vol. 82, pp. 319–32, 2008.

[42] A. A. Khan and A. K. Brown, "Sidelobe improvement in small arrays using z-plane transform and particle swarm optimizer," in *Proc. 3rd European Conf. Antennas and Propagation EuCAP 2009*, 2009, pp. 3011–3013.

[43] ——, "Difference pattern synthesis using a particle swarm optimizer," in *Proc. Loughborough Antennas & Propagation Conf. LAPC 2009*, 2009, pp. 329–332.

[44] ——, "Wideband scanning small linear arrays in presence of mutual coupling," *Electronics Letters*, vol. 46, no. 4, pp. 270–271, 2010.

[45] D. W. Boeringer and D. H. Werner, "A comparison of particle swarm optimization and genetic algorithms for a phased array synthesis problem," in *Proc. IEEE Antennas and Propagation Society Int. Symp*, vol. 1, 2003, pp. 181–184.

[46] S. Baskar, A. Alphones, and P. N. Suganthan, "Concurrent pso and fdr-pso based reconfigurable phase-differentiated antenna array design," in *Proc. CEC2004 Evolutionary Computation Congress*, vol. 2, 2004, pp. 2173–2179.

[47] J. Robinson, S. Sinton, and Y. Rahmat-Samii, "Particle swarm, genetic algorithm, and their hybrids: optimization of a profiled corrugated horn antenna," in *Proc. IEEE Antennas and Propagation Society Int. Symp*, vol. 1, 2002, pp. 314–317.

[48] D. Boeringer and D. Werner, "Particle swarm optimization versus genetic algorithms for phased array synthesis," *Antennas and Propagation, IEEE Transactions on*, vol. 52, no. 3, pp. 771 – 779, March 2004.

[49] H. Unz, "Linear arrays with arbitrarily distributed elements," *Antennas and Propagation, IRE Transactions on*, vol. 8, no. 2, pp. 222 –223, March 1960.

[50] Y. T. Lo, *Antenna Handbook: Theory, Applications, and Design*, Y. T. Lo and S. W. Lee, Eds. Van Nostrand Reinhold, 1993.

[51] B. P. Ng, M. H. Er, and C. Kot, "Linear array geometry synthesis with minimum sidelobe level and null control," *IEE Proceedings -Microwaves, Antennas and Propagation*, vol. 141, no. 3, pp. 162–166, 1994.

[52] M. M. Khodier and C. G. Christodoulou, "Linear array geometry synthesis with minimum sidelobe level and null control using particle swarm optimization," *IEEE Transactions on Antennas and Propagation*, vol. 53, no. 8, pp. 2674–2679, 2005.

[53] L. Cen, Z. L. Yu, and W. Ser, "Antenna array synthesis in presence of mutual coupling effect for low cost implementation," *ISIC-2009 - 12th International Symposium on Integrated Circuits, Proceedings*, pp. 360–363, 2009.

[54] L. Cen, W. Ser, Z. L. Yu, and S. Rahardja, "An improved genetic algorithm for aperiodic array synthesis," in *Proc. IEEE Int. Conf. Acoustics, Speech and Signal Processing ICASSP 2008*, 2008, pp. 2465–2468.

[55] P. J. Bevelacqua and C. A. Balanis, "Minimum sidelobe levels for linear arrays," *IEEE Transactions on Antennas and Propagation*, vol. 55, no. 12, pp. 3442–3449, 2007.

[56] J. Robinson and Y. Rahmat-Samii, "Particle swarm optimization in electromagnetics," *Antennas and Propagation, IEEE Transactions on*, vol. 52, no. 2, pp. 397 – 407, February 2004.

[57] S. Selleri, M. Mussetta, P. Pirinoli, R. Zich, and L. Matekovits, "Some insight over new variations of the particle swarm optimization method," *Antennas and Wireless Propagation Letters, IEEE*, vol. 5, no. 1, pp. 235 –238, December 2006.

[58] M. Mussetta, P. Pirinoli, and R. E. Zich, "Metapso-based design of the frequency behavior of a beam scanning linear array," in *Proc. IEEE Antennas and Propagation Society Int. Symp*, 2007, pp. 1605–1608.

[59] M. Clerc and J. Kennedy, "The particle swarm - explosion, stability, and convergence in a multidimensional complex space," *IEEE Transactions on Evolutionary Computation*, vol. 6, no. 1, pp. 58–73, 2002.

[60] D. Bratton and J. Kennedy, "Defining a standard for particle swarm optimization," *Swarm Intelligence Symposium, 2007. SIS 2007. IEEE*, pp. 120 –127, April 2007.

[61] A. Monorchio, S. Genovesi, S. Bertini, and A. Brizzi, "An efficient interpolation scheme for the synthesis of linear arrays based on schelkunoff polynomial method," *IEEE Antennas Wireless Propag. Lett.*, vol. 6, pp. 484–487, 2007.

[62] M. Mismar, T. Ismail, and D. Abu-Al-Nadic, "Analytical array polynomial method for linear antenna arrays with phase-only control," *AEU-International Journal of Electronics and Communications*, vol. 61, pp. 485–92, 2007.

[63] F. J. Ares-Pena, J. A. Rodriguez-Gonzalez, E. Villanueva-Lopez, and S. R. Rengarajan, "Genetic algorithms in the design and optimization of antenna array patterns," *IEEE Transactions on Antennas and Propagation*, vol. 47, no. 3, pp. 506–510, 1999.

[64] D. Marcano, M. Jimenez, F. Duran, and O. Chang, "Synthesis of antenna arrays using genetic algorithms," in *Proc. First IEEE Int Devices, Circuits and Systems Caracas Conf*, 1995, pp. 328–332.

[65] D. Marcano and F. Duran, "Synthesis of antenna arrays using genetic algorithms," *IEEE Antennas and Propagation Magazine*, vol. 42, no. 3, pp. 12–20, 2000.

[66] M. J. Buckley, "Synthesis of shaped beam antenna patterns using implicitly constrained current elements," *IEEE Transactions on Antennas and Propagation*, vol. 44, no. 2, pp. 192–197, 1996.

[67] L. Z. Thamae and Z. Wu, "Broadband bowtie dielectric resonator antenna," *IEEE Transactions on Antennas and Propagation*, vol. 58, no. 11, pp. 3707–3710, 2010.

[68] Y. Zhang and A. K. Brown, "Integrated aperture array antenna design for radio astronomy," *Widefield Science and Technology for the SKA*, pp. 317–321, 2009.

[69] R. Armstrong, K. Adami, and M. Jones, "A digital broadband beamforming architecture for 2-pad," *Widefield Science and Technology for the SKA*, pp. 273–277, 2009.

[70] T. Ikin, P. Wilkinson, A. Faulkner, and et al, "Progress on analogue front end for 2pad," *Widefield Science and Technology for the SKA*, pp. 267–272, 2009.

[71] R. C. HANSEN, *Phased Array Antennas*, K. CHANG, Ed. John Wiley & Sons, Inc., 1998.

[72] W. L. Stutzman and G. A. Thiele, *Antenna Theory and Design*. John Wiley & Sons, 1998.

[73] S. Zhang, S. N. Khan, and S. He, "Reducing mutual coupling for an extremely closely-packed tunable dual-element pifa array through a resonant slot antenna formed in-between," *IEEE Transactions on Antennas and Propagation*, vol. 58, no. 8, pp. 2771–2776, 2010.

[74] T. T. Zhang and W. Ser, "Mutual coupling effect of antenna array communications systems for portable medical devices," in *Proc. 4th IEEE Conf. Industrial Electronics and Applications ICIEA 2009*, 2009, pp. 549–553.

[75] F. Wang, X. Liu, and M. E. Bialkowski, "Performance of mimo beamforming transmission scheme in the presence of mutual coupling," in *Proc. Int Communications and Mobile Computing (CMC) Conf*, vol. 2, 2010, pp. 122–126.

[76] H. Wang, D. G. Fang, and P. Ge, "Mutual coupling reduction between two conformal microstrip patch antennas," in *Proc. 5th Asia-Pacific Conf. Environmental Electromagnetics CEEM 2009*, 2009, pp. 176–179.

[77] M. Sonkki, E. Antonino-Daviu, M. Ferrando-Bataller, and E. Salonen, "Optimal dimensions of two microstrip patch antennas for low mutual coupling at 5.8 ghz," in *Proc. 3rd European Conf. Antennas and Propagation EuCAP 2009*, 2009, pp. 3515–3518.

[78] A. H. Mohammadian, L. M. Golovanevsky, S. S. Soliman, and M. A. Tassoudji, "Prediction of mutual coupling between base station antenna arrays," in *Proc. IEEE Radio and Wireless Conf. RAWCON 2002*, 2002, pp. 153–156.

[79] A. Ludwig, "Mutual coupling, gain and directivity of an array of two identical antennas," *IEEE Transactions on Antennas and Propagation*, vol. 24, no. 6, pp. 837–841, 1976.

[80] A. Kerkhoff and H. Ling, "A simplified method for reducing mutual coupling effects in low frequency radio telescope phased arrays," *IEEE Transactions on Antennas and Propagation*, no. 99, 2011, early Access.

[81] E. M. Friel and K. M. Pasala, "Effects of mutual coupling on the performance of stap antenna arrays," *IEEE Transactions on Aerospace and Electronic Systems*, vol. 36, no. 2, pp. 518–527, 2000.

[82] X.-D. Cai and G. I. Costache, "Numerical analysis of mutual coupling effects in linear and circular arrays," in *Proc. IEEE Antennas and Propagation Society Int. Symp. AP-S. 1992 Digest. Held in Conjuction with: URSI Radio Science Meeting and Nuclear EMP Meeting*, 1992, pp. 641–644.

[83] T. S. Bird, "Analysis of mutual coupling in finite arrays of different-sized rectangular waveguides," *IEEE Transactions on Antennas and Propagation*, vol. 38, no. 2, pp. 166–172, 1990.

[84] L. Tsai, "A numerical solution for the near and far fields of an annular ring of magnetic current," *Antennas and Propagation, IEEE Transactions on*, vol. 20, no. 5, pp. 569–576, 1972.

[85] R. F. Harrington, "Field computation by moment method," *Macmillan, New York*, no. 2, 1968.

[86] R. Poli, "An analysis of publications on particle swarm optimisation applications," *Journal of Artificial Evolution & Applications*, 2008.

[87] J. Kennedy and W. M. Spears, "Matching algorithms to problems: an experimental test of the particle swarm and some genetic algorithms on the multimodal problem generator," in *Proc. IEEE World Congress Computational Intelligence. Conf. The 1998 IEEE Int Evolutionary Computation*, 1998, pp. 78–83.

[88] R. Eberhart and Y. Shi, "Evolving artificial neural networks," *Proc. 1998 Int. Conf. on neural networks and brain*, 1998.

[89] *MATLAB Optmisation Toolbox documentation*.

[90] S. YANG, Z. NIE, and Y. Wu, "A practical array pattern synthesis approach including mutual coupling effects," *Electromagnetics*, vol. 27, pp. 53–63, 2007.

[91] P. Demarcke, H. Rogier, R. Goossens, and P. De Jaeger, "Beamforming in the presence of mutual coupling based on constrained particle swarm optimization," *IEEE Transactions on Antennas and Propagation*, vol. 57, no. 6, pp. 1655–1666, 2009.

[92] J. Kennedy, "The behavior of particle," in *Proc. 7th Annu. Conf. Evol. Program*, 1998.

[93] V. Kadirkamanathan, K. Selvarajah, and P. J. Fleming, "Stability analysis of the particle dynamics in particle swarm optimizer," *IEEE Transactions on Evolutionary Computation*, vol. 10, no. 3, pp. 245–255, 2006.

[94] R. Hansen, "Aperture efficiency of villeneuve $\bar{n}$ arrays," *IEEE Transactions on Antennas and Propagation*, vol. 33, no. 6, pp. 666–669, 1985.

[95] D. McNamara, "Direct synthesis of optimum difference patterns for discrete linear arrays using zolotarev distributions," *Microwaves, Antennas and Propagation, IEE Proceedings H*, vol. 140, no. 6, pp. 495 –500, December 1993.

[96] D. A. McNamara, "Performance of zolotarev and modified-zolotarev difference pattern array distributions," *IEE Proceedings -Microwaves, Antennas and Propagation*, vol. 141, no. 1, pp. 37–44, 1994.

[97] O. M. Bucci, M. D'Urso, and T. Isernia, "Optimal synthesis of difference patterns subject to arbitrary sidelobe bounds by using arbitrary array antennas," *IEE Proceedings -Microwaves, Antennas and Propagation*, vol. 152, no. 3, pp. 129–137, 2005.

[98] F. Ares, S. R. Rengarajan, A. Vieiro, and E. Moreno, "Optimisation of aperture distributions for difference patterns," in *Proc. AP-S Antennas and Propagation Society Int. Symp. Digest*, vol. 4, 1995, pp. 1826–1829.

[99] M. D'Urso and T. Isernia, "Solving some array synthesis problems by means of an effective hybrid approach," *IEEE Transactions on Antennas and Propagation*, vol. 55, no. 3, pp. 750–759, 2007.

[100] P. Lopez, J. A. Rodriguez, F. Ares, and E. Moreno, "Subarray weighting for the difference patterns of monopulse antennas: joint optimization of subarray configurations and weights," *IEEE Transactions on Antennas and Propagation*, vol. 49, no. 11, pp. 1606–1608, 2001.

[101] R. C. Hansen, "Array pattern control and synthesis," *Proceedings of the IEEE*, vol. 80, no. 1, pp. 141–151, 1992.

[102] S. Ali Hosseini and Z. Atlasbaf, "Optimization of side lobe level and fixing quasi-nulls in both of the sum and difference patterns by using continuous ant colony optimization (aco) method." *Progress in Electromagnetics Research*, no. 79, pp. 321–37, 2008.

[103] P. Rocca, L. Manica, and A. Massa, "Synthesis of monopulse antennas through iterative contiguous partition method," *Electronics Letters*, vol. 43, no. 16, pp. 854 –856, February 2007.

[104] M. Alvarez-Folgueiras, J. Rodriguez-Gonzalez, and F. Ares-Pena, "Synthesising taylor and bayliss linear distributions with common aperture tail," *Electronics Letters*, vol. 45, no. 1, pp. 18 –19, January 2009.

[105] H. J. Orchard, R. S. Elliott, and G. J. Stern, "Optimising the synthesis of shaped beam antenna patterns," *IEE Proceedings H Microwaves, Antennas and Propagation*, vol. 132, no. 1, pp. 63–68, 1985.

[106] D. J. Sadler, "Sector beam synthesis using antenna arrays," in *Proc. 2nd IEE/EURASIP Conf DSPenabledRadio (Ref. No. 2005/11086)*, 2005.

[107] S. Kundukulam and K. Beenamole, "Design of a linear array antenna for shaped beam using genetic algorithm," *International Journal of RF and Microwave Computer-Aided Engineering*, vol. 18, pp. 410–16, 2008.

[108] R. Shavit and I. Taig, "Array pattern synthesis using neural networks with mutual coupling effect," *IEE Proceedings -Microwaves, Antennas and Propagation*, vol. 152, no. 5, pp. 354–358, 2005.

[109] H. M. Elkamchouchi and M. M. Wagih, "Synthesis of wideband array patterns via particle swarm optimization," in *Proc. ITI 5th Int. Conf. Information and Communications Technology ICICT 2007*, 2007, pp. 109–113.

[110] P. Bevelacqua and C. Balanis, "Geometry and weight optimization for minimizing sidelobes in wideband planar arrays," *Antennas and Propagation, IEEE Transactions on*, vol. 57, no. 4, pp. 1285 –1289, April 2009.

[111] G. Cardone, G. Cincotti, and M. Pappalardo, "Design of wide-band arrays for low side-lobe level beam patterns by simulated annealing," *Ultrasonics, Ferroelectrics and Frequency Control, IEEE Transactions on*, vol. 49, no. 8, pp. 1050 – 1059, August 2002.

[112] G. Cardone, G. Cincotti, P. Gori, and M. Pappalardo, "Optimization of wide-band linear arrays," *Ultrasonics, Ferroelectrics and Frequency Control, IEEE Transactions on*, vol. 48, no. 4, pp. 943 –952, July 2001.

[113] L. Kurtz, R. Elliott, S. Wehn, and W. Flock, "Mutual-coupling effects in scanning dipole arrays," *IRE Transactions on Antennas and Propagation*, vol. 9, no. 5, pp. 433–443, 1961.

[114] D. E. Dudgeon, "Fundamentals of digital array processing," *Proceedings of the IEEE*, vol. 65, no. 6, pp. 898–904, 1977.

Appendix I

Taylor $\bar{n}$ Line-Source

The space factor defined by Taylor is given as [3, chapter 7];

$$SF(u, A, \bar{n}) = \frac{\sin(u)}{u} \frac{\prod_{n=1}^{\bar{n}-1}\left[1-\left(\frac{u}{u_n}\right)^2\right]}{\prod_{n=1}^{\bar{n}-1}\left[1-\left(\frac{u}{n\pi}\right)^2\right]} \tag{A.1}$$

Where $u = \pi \frac{l}{\lambda}\cos\theta$, $A = \frac{1}{\pi}\cosh^{-1}(R)$, R is the voltage ratio and line source is assumed along z-axis. Taylor defines a scaling factor σ that moves the inner nulls accordingly.

$$\sigma = \frac{\bar{n}}{\sqrt{A^2 + \left(\bar{n} - \frac{1}{2}\right)^2}} \tag{A.2}$$

The null locations can be found as;

$$u_n = \pi \frac{l}{\lambda}\cos\theta_n = \begin{cases} \pm\pi\sigma\sqrt{A^2 + \left(n - \frac{1}{2}\right)} & 1 \le n \le \bar{n} \\ \pm n\pi & \bar{n} \le n \le \infty \end{cases} \tag{A.3}$$

The normalised line-source distribution, which yields the desired pattern, is given by

$$I(z') = \frac{\lambda}{l}\left[1 + 2\sum_{p=1}^{\bar{n}-1} SP(p, A, \bar{n})\cos\left(2\pi p \frac{z'}{l}\right)\right] \tag{A.4}$$

The coefficients $SP(p, A, \bar{n})$ can be found as;

$$SF(p, A, \bar{n}) = \begin{cases} \frac{\left[(\bar{n}-1)!\right]^2}{(\bar{n}-1+p)!(\bar{n}-1-p)!}\prod_{m=1}^{\bar{n}-1}\left[1-\left(\frac{\pi p}{u_m}\right)^2\right] & |p| < \bar{n} \\ 0 & |p| \ge \bar{n} \end{cases} \tag{A.5}$$

Appendix II

Dolph-Chebychev Array

The excitation coefficients for the Dolph-Chenychev array are determined by using the following mathematical equations [3, chapter 6];

$$a_n = \begin{cases} \displaystyle\sum_{q=n}^{M} (-1)^{M-q} (z_o)^{2q-1} \frac{(q+M-2)!(2M-1)}{(q-n)!(q+n-1)!(M-q)!} & \textit{for even elements} \\ \displaystyle\sum_{q=n}^{M+1} (-1)^{M-q+1} (z_o)^{2(q-1)} \frac{(q+M-2)!(2M)}{\varepsilon_n (q-n)!(q+n-2)!(M-q+1)!} & \textit{for odd elements} \end{cases} \tag{B.1}$$

Where

$$z_o = \frac{1}{2}\left[\left(R+\sqrt{R^2-1}\right)^{\frac{1}{N-1}} + \left(\left(R-\sqrt{R^2-1}\right)^{\frac{1}{N-1}}\right)\right] \tag{B.2}$$

$$\varepsilon_n = \begin{cases} 2 & n = 1 \\ 1 & n \neq 1 \end{cases} \tag{B.3}$$

R is the voltage ratio between the main lobe and the minor lobe.

Appendix III

Genetic Algorithm

Genetic algorithm works on the concept of survival of the fittest Darwinian Theory. It involves all major steps that are suggested by the Theory to evolve from one generation to the next. The flowchart for the Genetic algorithm is given as;

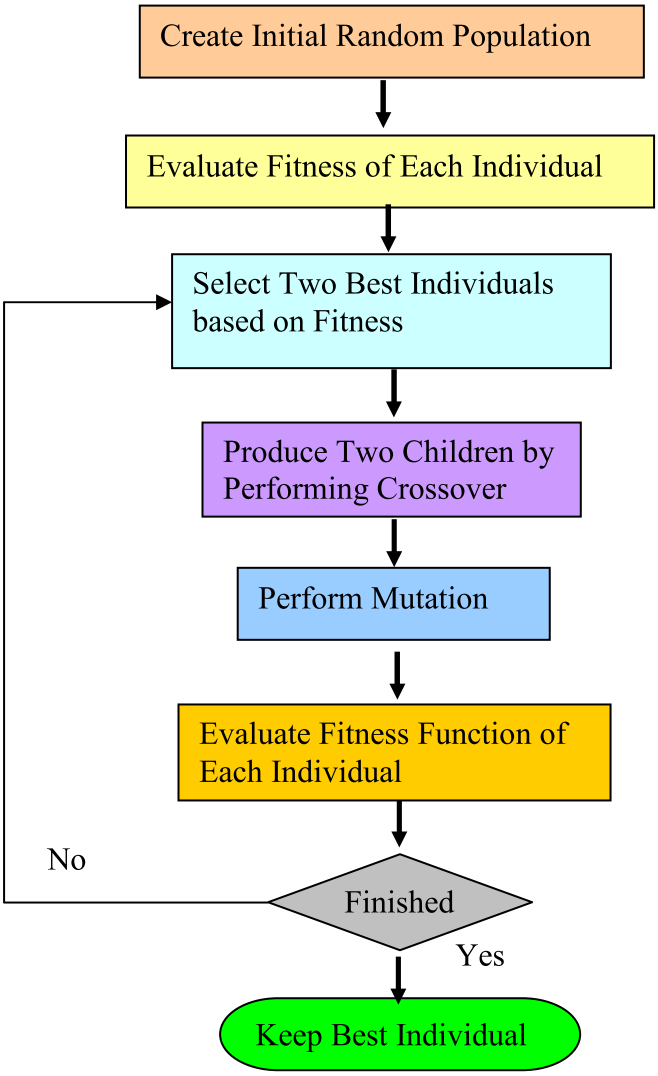

Figure C.1: Flowchart of the typically used Genetic Algorithm (GA)

The GA can be summarised in the following major steps [27-28].

C.1: Population Initialisation

This step involves with the setting a starting point for the algorithm. Generally random values are assigned to the individuals in a given population set.

C.2: Evaluate Fitness Function

The optimisation problems are translated form the problem space to the optimiser in the form of fitness function. Fitness function may consist of multiple terms each representing a constraint or an optimisation objective. These terms of fitness function are evaluated to judge the ‘goodness’ of a proposed solution.

C.3 Selection Process

This process depends on the performance of the individuals in terms of their fitness function evaluations. The best parents are selected on the basis of their respective fitness scores.

C.4 Reproduction

This step involves creating children for best parents from the previous generation. It works on the idea that stronger parents will lead to stronger children.

C.5 Mutation

This process involves some random modifications in the individuals which provide genetic diversity and enables the search for solution in broader space.

C.6 Crossover

Crossover combines the two individuals to make a new individual for the next generation.